Singlet Oxygen Luminescence Detection

Konstantinos Tsimvrakidis MSc, BSc

Submitted in fulfillment of the requirements for the Degree of

Doctor of Philosophy

James Watt School of Engineering

Division of Electronics and Nanoscale Engineering

University of Glasgow

April 2020

Abstract

The detection of a single photon at 1270 nm wavelength allows the direct monitoring of Singlet Oxygen ($^1O_2$), making Singlet Oxygen Luminescence Detection (SOLD) a powerful dosimetry technique for photodynamic therapy in the treatment of cancer. However, the direct detection of $^1O_2$ emission at 1270 nm wavelength is extremely challenging as the $^1O_2 \rightarrow {}^3O_2$ transition in biological media has very low probability and short lifetime due to the high reactivity of singlet oxygen with biomolecules. Recent advances in single photon detection providing high detection efficiency, low noise single-photon detectors are an important innovation in the development of a practical SOLD system for eventual clinical use. In this thesis I present a compact fibre coupled SOLD system, using a supercontinuum pump source to precisely target exact photosensitizer absorption peak wavelengths and single-photon detectors for near-infrared detection by benchmarking a superconducting and a semiconductor photon counting detector. Both pump laser and detector are intrinsically fibre-coupled making them ideally suited for the development of practical singlet oxygen sensor head. The SOLD system was used to carry out a series of singlet oxygen time-resolved measurements in solution and in live cells. These measurements offer information on the photosensitized generation and deactivation of singlet oxygen generated by different photosensitizers and microenvironments at the 1270 nm wavelength and a first investigation of the 1590 nm singlet oxygen luminescence signal is presented.

Table of Contents

List of tables

List of figures

List of equations

Acknowledgments

The completion of this work could have not been possible without the help, support, guidance, and efforts of many people.

Firstly, I would like to express my gratitude to my supervisor Prof. Robert H. Hadfield for the continuous support, motivation, and encouragement throughout my PhD study. His valuable guidance all along helped me complete my research work and write this thesis. I am most grateful to Dr Nathan R. Gemmell for the continuous help, insightful advice, and guidance. I am also grateful to Dr Nikolaj Gadegaard and Dr Marie Cutiongco for their assistance and collaboration. Lastly, I would like to thank all my PhD colleagues.

A very special thank you goes to my dearest friend Aggelos F. who has been patiently supporting me throughout these years and to Daphne who has always been there for me. Special thanks to all my friends Eleni, Andreas S., Andreas C., Aggelos M., Rodanthi and Takis for their unconditional friendship and all the good times we had together.

Finally, I would like to acknowledge my family, my parents, and my brother. Thank you for your support and encouragement, without which I would not have come so far.

Author's declarations

I, KONSTANTINOS TSIMVRAKIDIS, declare that this thesis titled, 'Singlet Oxygen Luminescence Detection' and the work presented in it are my own. I confirm that:

- This work was done wholly while in candidature for a research degree at this University.
- Where any part of this thesis has previously been submitted for a degree or any other qualification at this University or any other institution, this has been clearly stated.
- Where I have consulted the published work of others, this is always clearly attributed.
- Where I have quoted from the work of others, the source is always given. With the exception of such quotations, this thesis is entirely my own work.
- I have acknowledged all main sources of help.
- Where the thesis is based on work done by myself jointly with others, I have made clear exactly what was done by others and what I have contributed myself.

Konstantinos Tsimvrakidis MSc, BSc

List of publications

- Tsimvrakidis K, Gemmell N, Erotokritou K, Miki S, Yabuno M, Yamashita T, Hirotaka T, Hadfield R. Enhanced Optics for Time-Resolved Singlet Oxygen Luminescence Detection. IEEE Journal of Selected Topics in Quantum Electronics. 2019;25(1):1-7.

- Gemmell N, Hills M, Bradshaw T, Rawlings T, Green B, Heath R, Tsimvrakidis K, Zwiller V, Dorenbos S, Crook M, Hadfield R. A Miniaturized 4 K Platform for Superconducting Infrared Photon Counting Detectors. Superconductor Science and Technology. 2017;30(11):11LT01

List of abbreviations

ADC	Analog to digital converter
ALA	5-aminolevulinic acid
APC	Angled physical contact
APD	Avalanche photodiode
BCS theory	Bardeen, Cooper and Schrieffer theory
CFD	Constant fraction discriminator
cps	counts per second
CW	Continuous wave
DCR	Dark count rate
DMSO	Dimethyl Sulfoxide
FBS	Fetal Bovine Serum
FC	Ferrule connector
FDA	Food and Drug Administration
FL	Focal Length
FTIR	Fourier-transform infrared
FWHM	Full width at half maximum
GM	Gifford-McMahon
GQD	Graphene Quantum Dot
HC-PCF	Hollow core photonic crystal fibre
HpD	hematoporphyrin derivative
I-V	Current-voltage
J-T	Joule-Thompson
LED	Light emitting diode
LIDAR	Light detection and ranging
MPcs	Metallophthalocyanines
mTHPC	meta-tetra(hydroxyphenyl)chlorin
NIR	Near-infrared
OPO	Optical parametric oscillator
PC	Physical contact
PDT	Photodynamic Therapy
PMT	Photomultiplier Tubes

PNR	Photon number resolution
PS	Photosensitizer
QD	Quantum Dot
QE	Quantum efficiency
QKD	Quantum key distribution
RFL	Reflected focal length
ROI	Reactive oxygen intermediates
ROS	Reactive oxygen species
SFQ	Single flux quantum
Si-CMOS	Silicon complementary metal-oxide semiconductor
Si-SPAD	Silicon single photon avalanche photodiode
SMF	Single mode fibre
SNAP	Superconducting nanowire avalanche photodetector
SNR	Signal to noise ratio
SNSPD	Superconducting nanowire single photon detector
SOLD	Singlet oxygen luminescence dosimetry
SPAD	Single photon avalanche photodiode
SPD	Single photon detector
SQUID	Superconducting quantum interference device
TAC	Time to amplitude converter
TCSPC	Time correlated single photon counting
TES	Superconducting transition edge sensor
TRPD	Time resolved phosphorescence detection
UCN	Upconversion nanoparticles
UV	Ultraviolet
WCP	Weak coherent pulses
ZnPc	Zinc Phthalocyanine

Chapter 1 – Introduction

This PhD thesis presents work carried out for the engineering of a next-generation optical setup that will potentially be implemented in Photodynamic Therapy (PDT) for the treatment of cancer. Clinical photodynamic treatments lack efficient dosimetry techniques, something that singlet oxygen's direct monitoring aim to play a key role. Direct monitoring of singlet oxygen is accomplished by detecting its weak signature in the 1270 nm wavelength, which was enabled by the utilization of advanced single-photon detectors in the near-infrared. Singlet oxygen is efficiently generated by molecular oxygen undergoing a photodynamic process with the help of organic dyes with specific optical properties. Generation of singlet oxygen and detection of its near-infrared luminescence are carried out by using a supercontinuum laser source for the activation of oxygen and the detection of its emission by superconducting nanowire single-photons detectors and InGaAs single-photon avalanche diodes, while the delivery and collection of the light is controlled by a carefully engineered fibre-coupled optical head.

1.1 Thesis Structure

Chapter 2 consists of a comprehensive introduction and literature background on all the aspects of this project. It includes details of the singlet oxygen generation and deactivation pathways and kinetics, the organic dyes' optical properties and their role in photodynamic therapies, the dosimetry techniques, and the importance of singlet oxygen direct dosimetry technique. Also, a brief review is given on the single-photon detectors emphasizing on the single-photon avalanche diodes and the superconducting nanowire single-photon detectors, as well as on the time correlated single photon counting technique that is later mentioned for the data acquisition.

Chapter 3 describes the experimental setup used throughout the project. Includes information on the light source, the engineering and optimization of the optical head describing the selection of each component, the single-photon detectors' specifications with the characterization setups followed by a comparison between the two types. Lastly, the time correlated single photon

counting module used for the acquisition of the singlet oxygen signal is described and is given information on the fitting of the acquired singlet oxygen decay curves that is used for the extraction of lifetimes.

The solution-based singlet oxygen luminescence results are presented in Chapter 4. It starts with an overview of the different dyes used for the excitation of molecular oxygen and continues describing the singlet oxygen luminescence detection mechanisms and equations. Then singlet oxygen luminescence measurements are presented in both 1270 nm and 1590 nm wavelengths, including comparison plots between different dyes and various concentrations, providing information on the detected signal and its lifetimes. Lastly, singlet oxygen measurements in the presence of a well-established singlet oxygen quencher are presented.

In Chapter 5 are presented follow-up experiments in a somewhat more biological environment. Singlet oxygen measurements in the presence of an optical phantom simulating the scattering of human tissue and the direct detection of singlet oxygen from inside normal and cancer cells are the main focus of this chapter. Efficient detection of singlet oxygen in a more physiological environment is the ultimate test before advancing to real clinical-based measurements.

Chapter 6 is a summary of the conclusions from the experimental chapters giving an overview of all the results presented. Also, an outlook is given on the possibility of further work, discussing clinical trials, a singlet oxygen microscope, alternative singlet oxygen decay pathways and next-generation infrared single-photon sensors optimized for singlet oxygen luminescence dosimetry.

Chapter 2 – Background and Literature Review

2.1 Molecular Oxygen and Reactive Oxygen Species

Molecular oxygen (or dioxygen) O_2 first appeared in the Earth's atmosphere roughly 2.5 billion years ago [1, 2]. Oxygen made its appearance due to oxygenic photosynthesis, an evolutional need for aerobic respiration by early cyanobacteria, which lead to more complex eukaryotic organisms [2]. Since then, molecular oxygen plays an important role in the maintenance of life on Earth as it is the main molecule in cellular inspiration for all living aerobic organisms, as well as in mechanisms that lead to life extinguishing [3]. The reason molecular oxygen exhibits such behavior and properties is due to its unique electronic structure. O_2 is a paramagnetic biradical molecule with an open-shell electronic structure and an even electron number (two oxygen atoms bound together with 6 outer electrons for each atom) and, unlike most molecules, has by default the electronic ground state in a spin triplet state ($O_2(X^3\Sigma_g^-)$) [3, 4, 5, 6], thus in chemical reactions, oxygen is common to exhibit radical-like behaviour. Ground state molecular oxygen has two unpaired electrons in its electronic configuration, as shown in Figure 2.1, which follow Hund's rule and occupy different molecular orbitals [6, 7]. When excited, molecular oxygen's excited electronic states are singlet, with the two lowest energy singlet states being the $O_2(a^1\Delta_g)$ and $O_2(b^1\Sigma_g^+)$ with excitation energies of 7882 cm^{-1} and 13121 cm^{-1} respectively [8, 9]. The superscript "1" and "3" indicate the molecular electronic state (singlet or triplet), the "g" subscript (from the German word *gerade*) indicate that the molecule's symmetry is even, meaning that the inversion through the centre of symmetry of the molecule does not result in a change of sign for the molecular orbital, while the Greek letters "Δ" and "Σ" correspond to the orbital angular momentum (M_L), with M_L equal to 2 and 0 for "Δ" and "Σ" respectively [7, 10].

Since the 1950s, where Gerschman *et al.* first noticed that toxic effects in aerobic organisms were caused due to oxygen-bearing free radicals, a lot of research has been done in this reactive class of oxygen species [7, 11, 12]. These highly reactive, endogenous oxygen-containing species have been widely called ROS (reactive oxygen species) or ROI (reactive oxygen intermediates). ROI include

all the species that have been formed chemically by incomplete reduction of molecular oxygen, such as the peroxide ($\cdot O_2^{-2}$), hydrogen peroxide (H_2O_2), superoxide radical anion ($\cdot O_2^-$), hydroxyl anion (OH^-) and its neutral form, the hydroxyl radicals ($\cdot OH$), while with the term ROS, all ROI are included along with singlet oxygen ($^1\Delta_g$) and ozone (O^3) [13]. By some, ROS also include compounds such as peroxyl ($\cdot ROO$), carobonate radicals ($\cdot CO^{3-}$), alkoxyl ($\cdot RO$), organic hydroperoxides (ROOH), hypochlorous (HOCl), hypoiodous acids (HOI), semiquinone ($\cdot SQ^-$) and hypobromous (HOBr) [14, 15]. ROS can also be separated in free radicals and non radicals [15, 16]. A photophysical process where reactive oxygen species are formed via electron transfer actions is characterized as Type I process, while the excitation of molecular oxygen molecules and the generation of singlet oxygen via energy transfer from a nearby excited molecule (typically photosensitizer dyes) is referred to as a Type II photochemical process [4, 17].

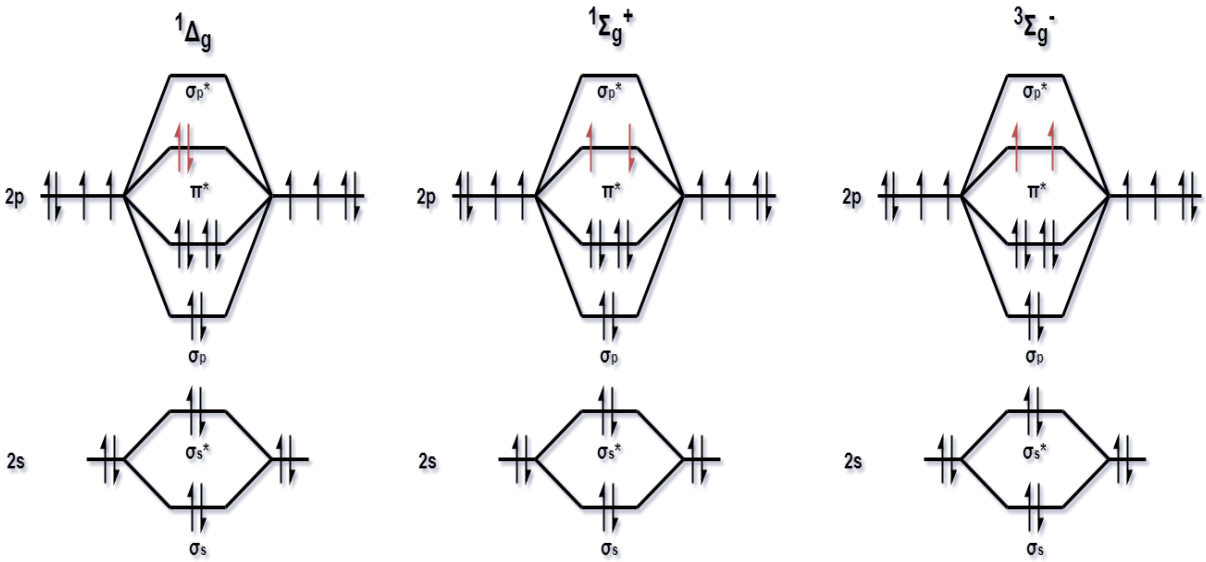

Figure 2.1. Diagram illustrating the molecular orbital of ground-state triplet molecular oxygen $^3\Sigma_g^-$ and the first two excited singlet states $^1\Delta_g$ and $^1\Sigma_g^+$.

2.1.1 Singlet Oxygen

The term Singlet Oxygen is commonly used for the $^1\Delta_g$ state, the first electronic excited state of the molecular oxygen. It was Ellis and Kneser who first observed absorption of liquid O_2 at ~1261 nm showing the optical transition from

the ground state ($^3\Sigma_g^-$) to the first excited state ($^1\Delta_g$) [6, 18]. The relatively low excitation energy required for the pairing of the electrons in the same orbital and forming the singlet oxygen is about 94 kJ mol^{-1} (0.98 eV) [4, 7]. However, this occupation of the same orbitals with a change in the electron spin, alongside with selection rules based on symmetry, parity and angular momentum show that the transitions between the electronic states of oxygen are not very probable [4, 19]. This is mainly the case for the electronic transitions of an unperturbed oxygen molecule. In the case of collision with other molecules or atoms, the perturbed oxygen molecule gains some freedom in the transitions as this radiative transition forbiddeness is weakened for both absorption and emission [6]. In addition, the perturbation of O_2 also introduce to the molecule new non-radiative deactivation pathways, such as electronical to vibrational energy transfer and the charge transferred induced quenching which are calculated to be very effective processes in the deactivation of the excited singlet states [6]. Along with the molecular studies of the oxygen molecule, over the last decades, several ways of generating singlet oxygen have been proposed and researched, such as the direct excitation of the oxygen molecules, via chemical reactions or the photosensitized generation of singlet oxygen [4, 20-23].

In a direct excitation of molecular oxygen into a singlet state, a laser is used to directly pump into the first or the second electronic excited states, either at ~1270 nm ($O_2(X^3\Sigma_g^-) \rightarrow O_2(a^1\Delta_g)$) or at ~765 nm ($O_2(X^3\Sigma_g^-) \rightarrow O_2(b^1\Sigma_g^+)$). While these transitions are of very low probability, in collision dependent perturbations caused by the solvents used each time, these transitions appear to be more probable [20, 24]. However, direct pumping at 765 nm is preferred over the 1270 nm excitation wavelength as there is still need for easily accessible fast pulsed lasers in the 1270 nm region, but more importantly, there is a spectral window in the 765 nm region where absorption by biological compounds and molecules like chromophores, or water, is weak [20]. In 2015, a quantified direct excitation of molecular oxygen in a time-resolved study was presented by Mikkel Bregnhøj *et al.*, using Ti:sapphire femtosecond lasers at 765 nm producing up to 60 mW of optical power, PMT detectors for the detection of the 1270 nm phosphorescence signal, while for the oxygen containing solutions, solvents known for their ability to generate long-lived singlet oxygen were used, such as toluene, D_2O, acetonitrile and benzonitrile [20]. As for the generation of singlet oxygen through chemical

reaction, different pathways have been proposed like the reaction of hypochlorite with hydrogen peroxide, the decomposition of hydrogen peroxide, superoxide ions, endoperoxides and triphenyl phosphate ozonide, or through the calcium peroxide diperoxohydrate which can be easily prepared from hydrogen peroxide and calcium chloride [21, 25-29]. However, generating singlet oxygen via chemical reactions usually is very complicated, the quantum yield is not as high as singlet oxygen generated through other methods, and sometimes the side reactions occurred can be a major drawback.

The third method of singlet oxygen generation mentioned above is the photosensitized excitation of the molecular oxygen, and is the method used and studied throughout this research. The main concept of this photosensitized excitation lies on the electronic energy transfer from an excited dye molecule, a so-called photosensitizer (or simply sensitizer), to the ground state oxygen molecules. More specifically, the photosensitizer molecule is illuminated with light usually from the ultra-violet to the deep-red spectral region and is excited (typically achieved via one-photon transition) to a higher energy singlet electronic state where there is a chance to undergo intersystem crossing generating a triplet electronic state. From this long-lived triplet state, it will decay back to ground state via phosphorescence, while there is a chance (depending on the structure and properties of each photosensitizer) to transfer energy to ground state oxygen molecules and excite them into one of its reactive singlet states [6, 17, 22]. This process is favored by the long-lived triplet state of the sensitizer (decay from the sensitizer triplet state to ground state is a “forbidden” transition due to quantum selection rules). So, this microsecond lifetime (compared to nanoseconds for the de-excitation of a sensitizer singlet state) provides enough time for interaction with a colliding oxygen molecule.

A triplet state photosensitizer can react in both ways with the molecular oxygen. In Type I reaction free radicals are generated from this excited photosensitizer state which interact with oxygen and produce active oxygen species such as the superoxide radical anion and others that were mentioned earlier. In the case of the Type II mechanism, the triplet state photosensitizer slowly decays on the time scale of microseconds and transfers energy to molecular oxygen, generating singlet oxygen states [4, 22]. From these excited singlet state,

different decay wavelengths occur as it emits near-infrared photons and relaxes back to ground state, as shown in Figure 2.2 [30].

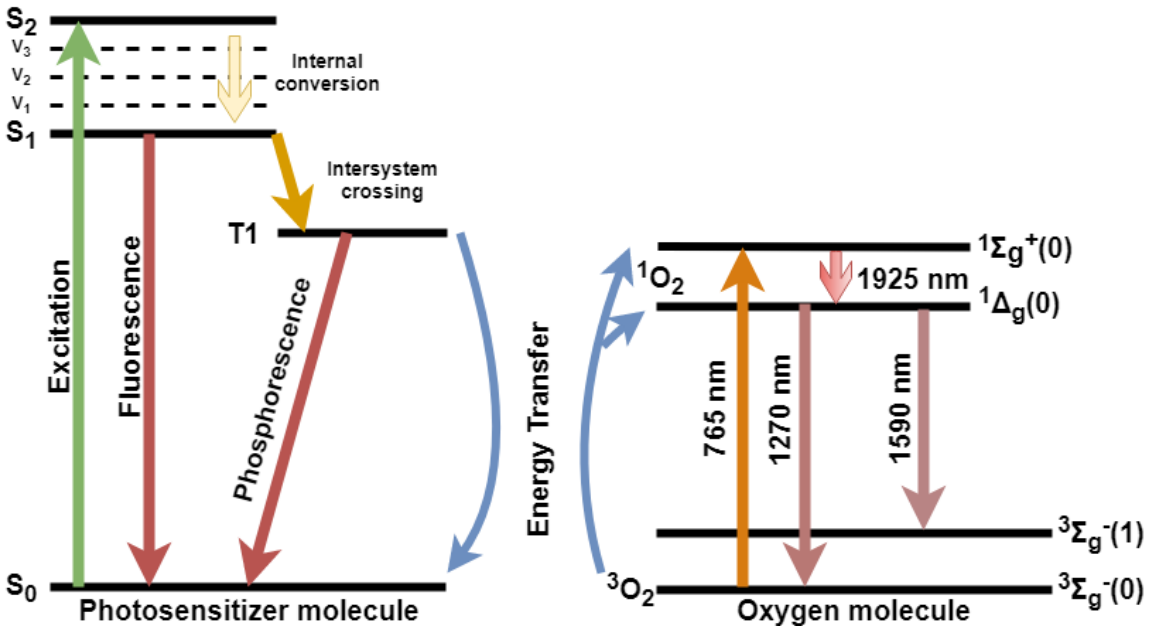

Figure 2.2. Schematic showing the Jablonski diagram of the excitation and luminescence of the photosensitized dye and its transferred energy to molecular oxygen, exciting it into singlet states.

The ~1590 nm emission shown in Figure 2.2 corresponds to the transition from the first excited electronic state $^1\Delta_g$ to the first vibrational ground state $^3\Sigma_g^-$ (v = 1). This photosensitized luminescence of $^1O_2$ was first observed and studied by Khan in 1980 [31], and later that year by Salokhiddinov *et al.* [32] who managed to carry out measurements on the 1270 nm and 1588 nm luminescence spectra and lifetimes. The latter using a Ge photodetector and a monochromator managed to record the band intensities of each emission, showing that 1588 nm emission is approximately 60 times weaker than that of 1270 nm. Due to the very weak emission intensity, extensive experiments involving the 1588 nm luminescence are difficult to carry out, even to this day. In the next chapters, experiments involving time-resolved measurements of the $^1\Delta_g \rightarrow {}^3\Sigma_g^-$ (v = 1) at 1588 nm luminescence are presented, discussed and compared to the standard $^1\Delta_g \rightarrow {}^3\Sigma_g^-$ (v = 0) at 1270 nm.

The kinetics for the generation and decay of the singlet oxygen in a homogenous system have been reviewed [33] and are described below in simplified

steps categorised in three main process groups: a) photosensitizer excitation and generation of its triplet state, b) photosensitizer's triplet state decay and generation of excited oxygen molecules, and c) singlet oxygen's decay and quenching.

a) For the excitation of the photosensitizer molecule from ground singlet state to an electronic excited singlet state the kinetics are the following:

$$PS + h\nu_{exc} \rightarrow {}^1PS \quad (1)$$

$${}^1PS \rightarrow PS + h\nu_F \quad (2)$$

$${}^1PS \rightarrow PS \quad (3)$$

$${}^1PS \rightarrow {}^3PS \quad (4)$$

b) For the processes regarding the triplet state of the photosensitizer and the generation of singlet oxygen:

$${}^3PS \rightarrow PS + h\nu_P \quad (5)$$

$${}^3PS \rightarrow PS \quad (6)$$

$${}^3PS + O_2 \rightarrow PS + {}^1O_2 \quad (7)$$

$${}^3PS + O_2 \rightarrow Other \quad (8)$$

c) Finally, for the processes regarding the quenching and decay of singlet oxygen:

$${}^1O_2 \rightarrow O_2 + h\nu \quad (9)$$

$${}^1O_2 \rightarrow O_2 \quad (10)$$

$${}^1O_2 + Q \rightarrow O_2 + Q \quad (11)$$

$${}^1O_2 + Q \rightarrow Other \quad (12)$$

Other quantities describing the quantum yields for the production of triplet state photosensitizer molecules and singlet oxygen, as well as their lifetimes are determined by the equations below [34].

Production quantum yield of the ^{3}PS:

$$\Phi_T = \frac{k_{isc}}{k_F + k_{ic} + k_{isc}} \quad (13)$$

Where k_{isc}, k_F and k_{ic} are the rate constants for intersystem crossing, the fluorescence from the excited state of the sensitizer and the internal conversion, respectively.

The ^{3}PS lifetime in the absence of molecular oxygen, considering equations 5 and 6:

$$\tau_T^0 = 1/k_T^0 = \frac{1}{k_P + k_{T,NR}} \quad (14)$$

Where k_P and $k_{T,NR}$ are the rate constants for the photosensitizer phosphorescence and the triplet state non-radiative decay, respectively.

The ^{3}PS lifetime in the presence of molecular oxygen, determined by equations 7 and 8 as:

$$\tau_T = 1/k_T = \frac{1}{k_T^0 + k_{T,q}^{O_2}[O_2]} \quad (15)$$

Where $k_{T,q}^{O_2}$ is the sum of $k_{T,\Delta}^{O_2}$ and $k_{T,other}^{O_2}$ which are the rate constants for the energy transfer to molecular oxygen and all the other processes occurring in the presence of triplet state photosensitizer and oxygen. $[O_2]$ is the concentration of the oxygen.

The proportion of the oxygen quenching of the ^{3}PS molecules:

$$P_T^{O_2} = \frac{k_{T,q}^{O_2}[O_2]}{k_T^0 + k_{T,q}^{O_2}[O_2]} = 1 - \frac{\tau_T}{\tau_T^0} \quad (16)$$

The fraction of $P_T^{O_2}$ that gives singlet oxygen molecules:

$$f_{T,\Delta}^{O_2} = \frac{k_{T,\Delta}^{O_2}}{k_{T,q}^{O_2}} \quad (17)$$

The quantum yield for the production of the singlet oxygen molecules:

$$\Phi_{\Delta}(\,^3PS) = \Phi_T \times \frac{k_{T,\Delta}^{O_2}[O_2]}{k_T^0 + k_{T,q}^{O_2}[O_2]} = \Phi_T \times P_T^{O_2} \times f_{T,\Delta}^{O_2} \quad (18)$$

And lastly, the lifetime of the singlet oxygen:

$$\tau_{\Delta} = 1/k_{\Delta} = \frac{1}{k_{\Delta}^0 + \sum_i \left(k_{\Delta,q}^{Q}[Q]\right)_i} \quad (19)$$

Where k_{Δ}^0 is the sum of the rate constants for the radiative and non-radiative decay of the singlet oxygen, and $k_{\Delta,q}^{Q}$ is the sum of the rate equations for the physical quenching of singlet oxygen and all the other processes involved. $[Q]$ is the quencher concentration, while *i* represents all possible quenchers.

2.1.2 The "other" Singlet Oxygen

As mentioned earlier, the term singlet oxygen is widely given to the first electronic excited state, $^1\Delta_g$ (also called singlet delta) [35]. Nevertheless, the upper excited state ($^1\Sigma_g^+$), is also a singlet state and is the second electronic excited state above $^1\Delta_g$, also referred to as "singlet sigma" [35, 36]. Singlet sigma ($^1\Sigma_g^+$) is ~63 kJ/mol higher in energy than the singlet delta state, therefore more energetic which led to extended studies in the pursuit of a better understanding of this state [35, 36]. Transitions between any two of the ground triplet state and the excited singlet states are forbidden for electric dipole radiation processes by the selection rules, and while transitions between the ground triplet state to any of the excited singlet states are also spin forbidden leading to long lifetimes, the transition between the singlet sigma and singlet delta states is spin allowed making the upper excited state short lived [37]. Minaev *et al.* proposed a theoretical model (that later was experimentally proven by Fink *et al.*) for the transition $^1\Sigma_g^+ \rightarrow {}^1\Delta_g$. In the case of the isolated molecule this transition is forbidden as of magnetic dipole, while when collision perturbations occur the

transition is highly affected, getting a more favorable dipole character resulting in an intensity enhancement [37-40]. Additionally, the transition probability in the perturbed molecule is 6 orders of magnitude larger than the isolated oxygen molecule [6]. The lifetime τ_Σ from singlet sigma to singlet delta is also highly affected by the environment with lifetimes ranging from a few picoseconds for solvents like water and deuterized water, up to hundreds of nanoseconds for CCl_4 and C_2Cl_4 [6, 35, 41]. Singlet sigma's main deactivation pathway is non-radiatively to $^1\Delta_g$ state with efficiency close to unity, while in the chance of radiative deactivation to the lower singlet state $^1\Delta_g$, it emits near-infrared photons ~1925 nm and ~765 nm wavelength when decaying to the ground triplet state with lifetimes in the timescale of seconds in room temperature [6, 30, 36, 42, 43]. More accurately, the $^1\Sigma_g^+ \rightarrow {}^1\Delta_g$ emission has a measured red peak maximum wavelength ranging from 1908 nm (5241 cm^{-1}) for oxygen in the gas phase up to 1936 nm (5165 cm^{-1}) in CS_2 [42]. This indicates how the solvent affects the $^1\Sigma_g^+ \rightarrow {}^1\Delta_g$ emission maximum with a max difference of 28 nm, compared to the much smaller shift of ~8.8 nm for the $^1\Delta_g \rightarrow {}^3\Sigma_g^-$ transition [42, 44-47], while due to the different spectral bands the difference in the transition energies is somewhat equivalent as the energy gap for $^1\Sigma_g^+ \rightarrow {}^1\Delta_g$ is 76 cm^{-1} and 54 cm^{-1} for the $^1\Delta_g \rightarrow {}^3\Sigma_g^-$ [42, 44, 45, 48]. The width of this emission, however, is a controversial subject. Noxon indicated that the bandwidth of the emission cannot exceed 5.5 cm^{-1} at the peak half-maximum, while later Fink *et al.*, Chou and Frei and Weldon *et al.* claimed that the emission bandwidth at half-maximum is much broader with values up to ~90 cm^{-1} [40, 42, 49, 50].

2.2 Photosensitizers

Photosensitizers (PS) are organic molecules that are able to absorb light energy and transfer it efficiently to neighboring molecules and act as the intermediate agent required in phototherapy processes. This process in its early state has been known since 1400 BC where sunlight or artificial light later on (UV – Visible) was used in the treatment of skin diseases [51]. Phototherapy treatments include various dermatological treatments where the photosensitizers are not always needed, such as psoriasis, eczema, vitamin D deficiency, in Parkinson's

disease to ease the symptoms, cutaneous T-cell lymphoma and many more [52 - 54]. In phototherapy treatments where the photosensitizers are employed (Photochemotherapy), these are usually UV light activated (5-Methoxypsoralen, 8-Methoxypsoralen, Trioxsalen) and the medical arena is capable of treating psoriasis, mycosis fungoids, HIV- associated dermatoses, pityriasis lichenoides, vitiligo and many more dermatological diseases [55, 56]. The combination of light and photosensitizer was initially examined as a potential treatment process in the early 1900s [57]. This is when the Photodynamic therapy (PDT), a type of photochemotherapy, started to emerge. In PDT, the photosensitizer is excited by a light source and through its triplet state, it transfers energy to adjacent oxygen molecules exciting them into the highly reactive singlet oxygen (as described in paragraph 2.1.1). However, photodynamic therapy was not available until the 1990s when Photofrin (porfimer sodium, a sensitizer in the porphyrin group) was clinically approved for the treatment of bladder cancer in Canada. The sensitizers mainly used for PDT come from the porphyrinoid group, such as the porphyrin, chlorin, texaphyrin, phthalocyanine, pheophorbide and other structures related to these dye compounds [56, 58]. Their chemical molecular structures are shown in Figure 2.3. Other non-porphyrin photosensitizers are the xanthenes, cyanines, anthraquinones, phenothiazines, and curcuminoids [56].

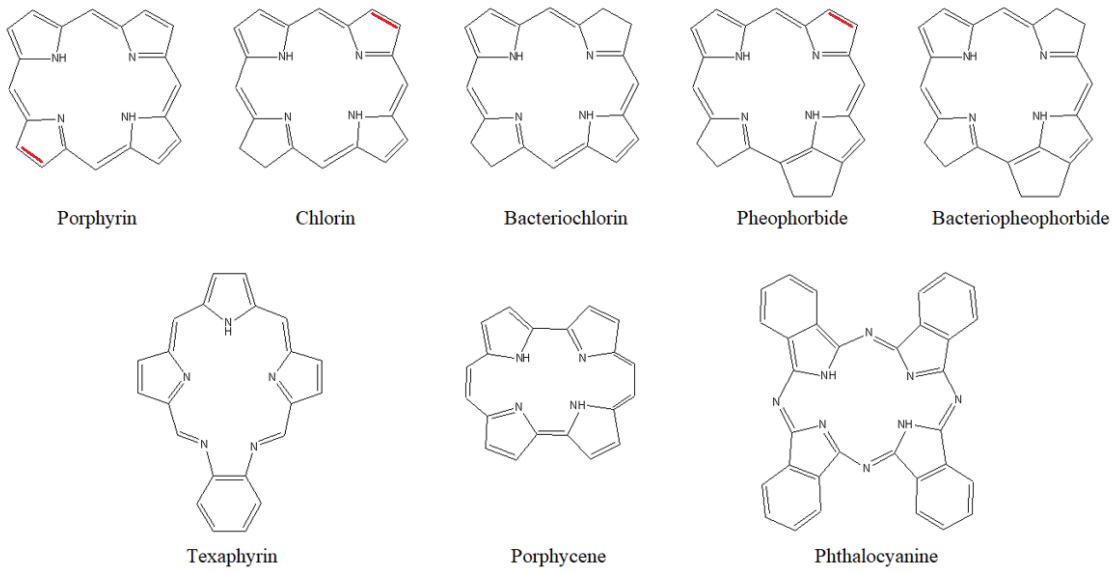

Figure 2.3. Chemical molecular structures of the porphyrinoid group dye sensitizers and other related structures.

To understand better the use and selection of the PSs, first, we need to list all the favorable properties a sensitizer should have in order to be ideal for PDT. Firstly, the PS should be able to accumulate and stick efficiently in the tumour tissue while it should be excreted from the normal tissue rapidly after the treatment. Also, an important property is the ability to highly absorb light with wavelengths above 700 nm and high molar extinction coefficient (ε_{max} = 50.000-100.000 M^{-1} cm^{-1}). The light above 700 nm (in the near infrared) is weakly absorbed by endogenous molecules like the hemoglobin (a protein in red blood cells), therefore the excitation light has a deeper penetration into the targeted tissue. An ideal photosensitizer should have negligible dark-toxicity, meaning that it is not cytotoxic in the absence of the activation light, high photostability, high triplet state quantum yield (Φ_T > 0.4) with triplet energies $E_T \geq 95$ kJ mol^{-1}, a long enough triplet lifetime (τ_T > 1 μs) so that interaction with oxygen molecules is more probable and sufficient reactive oxygen species are generated, and of course high singlet oxygen quantum yield (Φ_Δ as close to unity as possible). Amphiphilicity is also very important so that the sensitizer chemical can efficiently travel in the system to the targeted tumour, for which some hydrophilicity is required, while in order to diffuse through lipid barriers and bind in the tumour endocellular sites, some degree of lipophilicity is necessary [56, 59]. Other favorable properties would be the chemical purity of the compound for easier clinical approval, as well as minimum manufacturing cost for large-scale production and easy reproducibility [22, 56, 59, 60]. Taking into consideration all these requirements, it can be deduced that manufacturing such photosensitizer is not an easy task. However, many of the photosensitizers available are clinically approved without fully satisfying all the requirements, while most of them are currently being tested in clinical trials [59].

Photosensitizers are categorized into three main groups. The first generation PSs are mainly porphyrin-based PSs developed in the 1970s, like the hematoporphyrin derivative (HpD) and porfimer sodium [59]. While these first generation PSs showed that they can efficiently destroy the tumour, were water-soluble which is important for intravenous delivery, with negligible dark-toxicity and very useful for the initial clinical trials, they had some important deficiencies they could not overcome. The problem with these PSs were the poor bioavailability (the fraction of an administered drug that reaches the systemic circulation), the

weak absorption in the red spectral range where the light penetration in tissue is deeper, the low extinction coefficients that required larger amounts of the drug, accumulation in tumour tissue was not optimal with prolonged photosensitivity requiring the patient to avoid sunlight and other high-energy light for more than 48 hours [59, 61, 62]. These severe drawbacks of the first generation photosensitizers led to the development of new or improved compounds. The second generation, mostly developed in the late 1980s, included not only a big range of new and improved porphyrinoid compounds and porphyrin-based structures (shown in Figure 2.3), but also some non-porphyrinoid compounds. In the second generation, are also included the metallated derivatives of existing photosensitizers such as the Si(IV)-naphthalocyanine (SiNC), the aluminium phthalocyanine tetrasulfonate ($AlPcS_4$), zinc phthalocyanine (ZnPc) and tin ethyl etiopurpurin ($SnET_2$) without, however, always providing a more efficient photodynamic effect [63]. The 2nd generation PSs were developed aiming to overcome the deficiencies of the 1st generation and showed improved $^1O_2$ quantum yields, higher extinction coefficients and peak absorption wavelengths above 630 nm. Also, the higher-to-normal tissue concentration and time accumulation of the drug led to faster treatments and shorter photosensitivity periods [59]. The 3rd generation consists of the development of photosensitizers that focus on the longer excitation wavelengths, better tumour selectivity and shorter photosensitivity periods. Therefore, much research focusses on the improvement of the existing 2nd generation photosensitizers by modifying them with biological conjugates (peptides, antibody, antisense) that will assist in the specific targeting of the tumour, or by encapsulating them into delivery carriers that will transport the PS through the blood and release it on the targeting tumour [59, 64 - 66]. So far, however, their low vivo selectivity has prevented them from actual clinical trials [67].

Some of the limitations of the existing photosensitizers can be overcome with the help of nanoparticles. Nanoparticles with typical sizes of 1 - 100 nm can be designed to assist existing PSs that are insoluble or hydrophobic by delivering them onto the targeted site, transfer the appropriate amount of energy to the PS or even act as the PS itself [59, 60]. Depending on the role of the nanoparticles in the process of the photodynamic effect, are categorized as active or passive nanoparticles [59, 68 – 70]. The nanoparticles offer large surface to volume ratios

which lead to an increased amount of PS on the targeted tumour [71, 72], can be designed to bestow increased amphiphilicity to the PS and to avoid the early release of the PS in the body reducing this way the accumulation of the drug in normal tissue, and therefore reduce the overall photosensitivity [73, 74]. Also, their surface and can be further engineered to carry various components simultaneously like chemotherapy drugs or targeting ligands [68]. Lately, the use of certain nanoparticles as downconverting PSs is researched with their ability to act as the PS itself and produce ROS. Examples of these downconverting nanoparticles are the fullerenes, titanium dioxide (TiO_2) and zinc oxide (ZnO). Fullerenes (a carbon allotrope in spherical shape usually composed by 60 or 70 carbon atoms) offer good photostability, effective generation of Type I and Type II ROS, low photobleaching and they do not break down [75]. Some of their disadvantages, though, is their excitation wavelength that is not optimal for deep tissue penetration and their insolubility in water require their attachment to other ligands [59, 76-80]. Titanium dioxide (or titania, TiO_2) is examined as a potential effective PS due to its low toxicity, very good biocompatibility, and photocatalytic activity [81]. Titanium dioxide has been tested *in vitro* and *in vivo* in animals showing promising results, with a major drawback its photoactivation with short-wavelength UV light [82-90]. Similar to the TiO_2 nanoparticles are the zinc oxide (ZnO) nanoscaled particles. ZnO nanoparticles studied in various sizes (up to 100nm) have similar band gap to TiO_2, photocatalytic activity and phototoxic effects [59, 91, 92]. Zinc oxide has also been used in combination therapies acting also as an anticancer drug delivery agent [93]. Similar behaviour is offered by certain nanoparticles characterized as energy-transducers. These nanoparticles not only are carriers for the PS but also assist in the energy transfer to the PS allowing the photoactivation of the PS by light at wavelengths far from the absorption region of the photosensitizer. Examples of such nanoparticles are the X-ray activatable nanoparticles, upconverting nanoparticles, and semiconductor quantum dots [59]. Chen et al. in 2006 proposed a different way of activating porphyrin-based PSs in the visible at around 400 nm where the production of ROS is much more probable, instead of the weak absorption at 600-800 nm where light penetrates deeper into tissue [94]. The idea was to attach to the PSs scintillation or persistent luminescence nanoparticles such as BaFBr:Eu^{2+}, Mn^{2+}, LaF3:Ce^{3+}, and LaF3:Tb^{3+}, that can be activated with X-ray luminescence (utilizing the practically

unlimited penetration of X-rays in the tissue) and emit in the visible at 400 nm, 500 nm, and 650 nm matching the strong absorption peaks of the porphyrins [59, 94, 95]. Upconversion nanoparticles (UCN) are also proposed as potential assistants to classical sensitizers. UCN are nanosized particles usually comprised of ceramic materials doped with actinides, transition metals, or lanthanide ions like Er^{3+}, Yb^{3+}, and Tm^{3+}, and have the ability to convert low energy light (e.g. near-infrared light with good tissue penetration) to higher energy light, absorbing simultaneously multiple low energy photon and emitting in the visible via the anti-Stokes emission process. These nanoparticles can be used either as efficient PS carriers or as an intermediate to activate the chosen PSs located deep into the tissue [59, 96, 97]. Lastly, the approach of the quantum dots (QDs) in the activation of the PSs and the efficient generation of $^1O_2$ holds great promise. QDs usually in the size of just a few nanometres (from 1 to 6 nm) are particles that depending on their tunable size and composition can have unique optical properties. Therefore, their emission can also be tuned from the UV spectral range all the way to the infrared region precisely matching the peak absorption wavelength of the selected photosensitizer. Moreover, by altering and modifying their surface, better water-solubility and biocompatibility can be achieved for PDT applications. Various QDs have been proposed the last years, most of them semiconductors such as CdSe, CdS, ZnS, and graphene in zero-dimension confinement [59, 98 – 104]. Graphene quantum dots (GQDs) offer a rather versatile solution to the low singlet oxygen quantum yields by having a very broad tunable absorption band up to the visible region and strong emission at around 680 nm, good aqueous dispersibility, low photobleaching, great photostability (superior to protoporphyrin IX), and an ideal pH stability. Also, the large Stokes shift of 205 nm allows the GQDs to self-absorb the emitted light minimizing the interferences between the excitation and scattered light. The unique optical properties of the GQDs result in a large enough energy gap between the excited singlet state and the triplet state, offering an extra $^1O_2$ generation pathway through the intersystem crossing, with a combined quantum yield >1 [104].

2.3 Photodynamic Therapy and Dosimetry

The term 'Photodynamic Therapy' (PDT) originates from the term '*photodynamische Wirkung'* (that means photodynamic effect) conceived by the German pharmacologist Hermann von Tappenier in the early 1900s [105]. PDT is an emerging treatment of cancer and other diseases (dermatological, skin disorders, etc.) where a photosensitizer is applied to the patient systematically or topically accumulating on the targeted tissue. The sensitizer is then photo-activated *in situ* by a wavelength tuned light source that matches the photosensitizer's peak absorption spectrum and by energy transfer to adjacent oxygen molecules, the generated reactive oxygen species act as lethal agents to destroy or modify tissue and cells [22, 106, 107]. This photodynamic process was described in more detail in paragraph 2.1.1. PDT offers a big advantage over other cancer therapies and that is the very accurate tissue destruction limiting the effect only to targeted cancer tumours leaving the rest of the normal tissue intact. The effect on the tumours is threefold: a direct destruction of the tumour cells by the ROS, tumour infarction by damaging the tumour-associated vasculature, and a possible immune response activation against the cancer cells [108, 109]. However, despite the great cancer cell accuracy and the negligible side-effects, PDT is restricted from being widely clinically applied by the difficulty of shining light onto the tumour and calculating the right treatment dose for each individual treatment. Complex interactions between each patient's biomolecules, correct treatment light, photosensitizer and tissue oxygen concentrations make dose quantification difficult, especially for each individual patient. Currently, there are four PDT dosimetry methodologies that prevail: a) *explicit dosimetry*, a technique involving the measurement of each PDT component and their incorporation into a dose model. However, accurate measurements in light, photosensitizer drug and oxygen are not simple and dynamic interactions varying from patient to patient and different tumour environments, may alter each one of these measurements during the treatment [30, 110 – 115], b) *implicit dosimetry*, which also requires the measurement of at least two of the treatment parameters. These are incorporated into a single metric that will preclinically predict the damage on the tumour and, therefore, the treatment outcome [30, 112]. Examples of implicit dosimetry are the fluorescence spectroscopic measurement of the photoproducts

[116 - 118], and more commonly, the photosensitizer photobleaching which is based on the monitoring of its fluorescence [112, 119]. Implicit dosimetry based on the PS fluorescence and photobleaching is a relatively practical and easy to apply dosimetry method which has shown promising results by accurate predictions of the singlet oxygen dose and the treatment outcome, however cannot be applied to all treatments due to the different properties and singlet oxygen generation efficacies of each photosensitizer [120]. c) *biophysical/biological tissue response monitoring* which also require monitoring of the treatment so it can predict the damage on the tissue, such as vascular shutdown. In this method, it is necessary to observe tissue changes during or right after the treatment for the adjustment of the light dose induced and/or the photosensitizer dose [121 – 125]. d) *direct dosimetry* is one of the most promising dosimetry methods and is considered the 'gold standard' of PDT dosimetry. Unlike the complexity of the indirect techniques, in direct dosimetry it is involved only one PDT parameter, the measurement of $^1O_2$ that is causing the tumour damage [30]. The prevailing method to apply direct $^1O_2$ dosimetry is by the time-resolved measurement of $^1\Delta_g \rightarrow {}^3\Sigma_g^-$ transition emitting at 1270 nm, which is the main focus of this project [30, 126 – 129]. Other ways to detect $^1O_2$ have been proposed, such as the frequency-domain measurement of the 1270 nm transition, the dimol emission measurement at 634 nm and by monitoring the $^1\Delta_g \rightarrow {}^1\Sigma_g^+$ transition at 1925 nm either by its fluorescence or time-resolved Fourier-transform infrared (FTIR) spectroscopy [130 – 132]. However, these means have not been proven sufficient and even less practical than the direct 1270 nm singlet oxygen luminescence detection (SOLD). The $^1O_2$ luminescence at 1270 nm has been very challenging to detect *in vivo* due to the high reactivity with the biomolecules, with short lifetimes of < 1 μs and very low probability at ~ 10^{-7} [127, 133]. Groups attempting SOLD have reported results using different types of single photon detectors [30, 128, 134]. However, the quantum efficiency of these detectors was poor at 1270 nm (<1 % for photomultiplier tubes and ~25% for single photon avalanche diodes), while the dark count rates were too high even when cooled down. Such weak and low probability emission requires a very sensitive near-infrared detector operating at the single photon level, along with the appropriate optical components for the delivery of the excitation light and the collection of the 1270 nm photons. A more sophisticated "SOLD setup" has been carefully

engineered in this project and is described in detail in § 3, utilizing state of the art NIR single photon detectors (SPDs) and a fast TCSPC (time correlated single photon counting) card module.

2.4 Single Photon Detection

Quantization of light was first proposed by Einstein in 1905 when explaining the photoelectric effect [135], which later led to the term 'photon'. Since then, light detection and manipulation technologies keep advancing to a point where we are able to generate and detect these single light quanta. Nowadays, single photon systems have extended the light detection from the visible to the deep infrared region of the electromagnetic spectrum [136]. The relationship between energy, *E*, and wavelength, λ, as shown below is:

$$E = \frac{hc}{\lambda} \tag{20}$$

Where *h* is Planck's constant and c the speed of light in vacuum. As shown in equation 20, energy and wavelength are inversely proportional meaning that the energy of a single photon is decreasing as we move towards the infrared region. High energy photons are easier to detect, in comparison to low energy infrared photons which require sensitive single photon detectors. Detection beyond the visible region was not possible, until the introduction of the NIR Photomultiplier Tube (PMT) and later the Single-Photon Avalanche Diode (SPAD) and Superconducting Nanowire Single-Photon Detector (SNSPD). Such advances in single photon detection have paved the way to novel applications, such as depth imaging, quantum key distribution systems, quantum information and in life sciences, like the singlet oxygen luminescence detection [129, 136].

In order to characterize a single photon detector, first we need to quantify its performance by establishing some parameters. The main parameters commonly used are detection efficiency, dark count rate, timing jitter, spectral range, dead time and photon number resolution [136, 137].

The **detection efficiency (η)** is one of the primary and most obvious performance metrics and is the probability that an incident photon on the detector will be registered as an output signal. However, in practice the detection efficiency is lower than 100% as the overall system detection efficiency (η_{sde}) consists of the coupling efficiency ($\eta_{coupling}$) – the photon losses due to the absorption, scattering or reflection that prevent photons from reaching the detector within the experimental environment, the absorption efficiency ($\eta_{absorption}$) – depending on the material and geometry of the detector, and the registering probability ($\eta_{registering}$) – a probability that the detector will generate an electrical output signal after the photon absorption. Considering these contributions, the overall system detection efficiency (η_{sde}) is:

$$\eta_{sde} = \eta_{coupling} \times \eta_{absorption} \times \eta_{registering} \tag{21}$$

The intrinsic device detection efficiency (η_{dde}) is:

$$\eta_{dde} = \eta_{absorption} \times \eta_{registering} \tag{22}$$

Subsequently, the value of η_{sde} and η_{dde} can only be equal when $\eta_{coupling} = 1$. In actual single photon counting experiments the optical coupling is not perfect, therefore the term quantum efficiency of the detector is widely used for the overall system detection efficiency (η_{sde}).

The **dark count rate (DCR)** is the rate at which a detector will generate a false count. False counts can be produced by various noise sources, either internal caused by the type of the detector or external such as unwanted stray light from a light source. Usually DCR is measured in counts per second (cps) or Hertz (Hz). It is important to keep dark count rate low so that the false events are limited, and the overall error rate is low contributing in a higher signal to noise ratio (SNR) [137].

Timing jitter *(Δt)* is defined as the uncertainty in the detection response. This variation in time Δt of the absorption of the incident photon and the generation of the output electrical pulse is typically given as the Full Width at Half Maximum (FWHM) of the distribution, as shown in Figure 2.4.

The **spectral range** of the detector is the region of the electromagnetic spectrum in which it is sensitive and capable of detecting photons. It is important that the detector is very sensitive at a wavelegth range that will satisfy the needs of the experiment.

The **dead time (τ_d)** is the time that the detector needs to reset itself after a detection event. In this recovery time the detector is blind and incapable of registering true events. Ideally, a detector should have very short dead time as this will affect the maximum count rate.

Photon number resolution (PNR) is the ability of a single photon detector to distinguish between one or more absorbed photons that are incident simultaneously. This can be achieved either by producing a pulse which is proportional to the number of the absorbed photons (e.g. superconducting transition edge detectors [138]), or by spatially multiplexing conventional detectors in an array and generating an output signal combining all the outputs of the array of detectors [139-141]. PNR can be an important asset when it comes to quantum photonics applications that advantage from multi-photon states [142]. However, most conventional SPDs operate in a binary response meaning that they can only distinguish between zero photons or one-or-more photons.

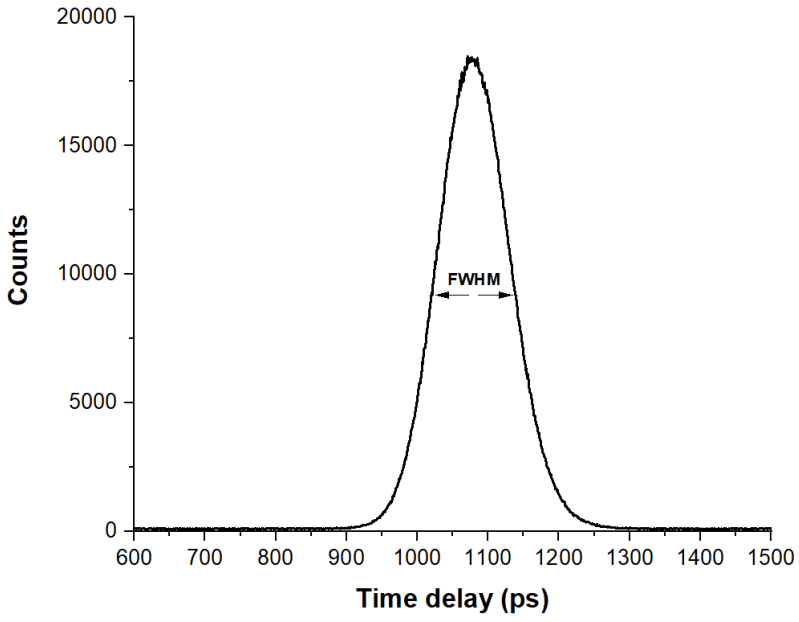

Figure 2.4. Example histogram demonstrating the timing jitter in full width at half maximum peak height of a SNSPD detection system. Measured timing jitter is 118.6 ps.

2.4.1 Photomultiplier Tubes

The Photomultiplier tube (PMT) was first demonstrated in 1935 and is the first single photon photocathode-based detector that is used until today in various applications as the most established photon-counting technology [143, 144, 145]. A PMT is a vacuum tube with a photocathode, a series of dynodes and an anode. The photocathode absorbs the photon and an electron is emitted via the photoelectric effect. This electron is then accelerated in an electric field created by the voltage applied towards the first dynode and on collision further electrons are released towards the next dynode (biased at a higher voltage than the previous) where more electrons are ejected. This repeated process on the dynodes creates an electron cascade that reaches the anode and generates a large current pulse [146]. The number of the electrons that are ejected from each anode is dependent on the energy of the accelerated electrons. Therefore, by biasing the dynodes in high voltages the electrons receive greater acceleration and higher amplification to a factor of the order of 10^6. The advantage of a PMT unit is its very large active detection area (diameter > 10 mm) [136]. An example of a PMT design is shown in Figure 2.5.

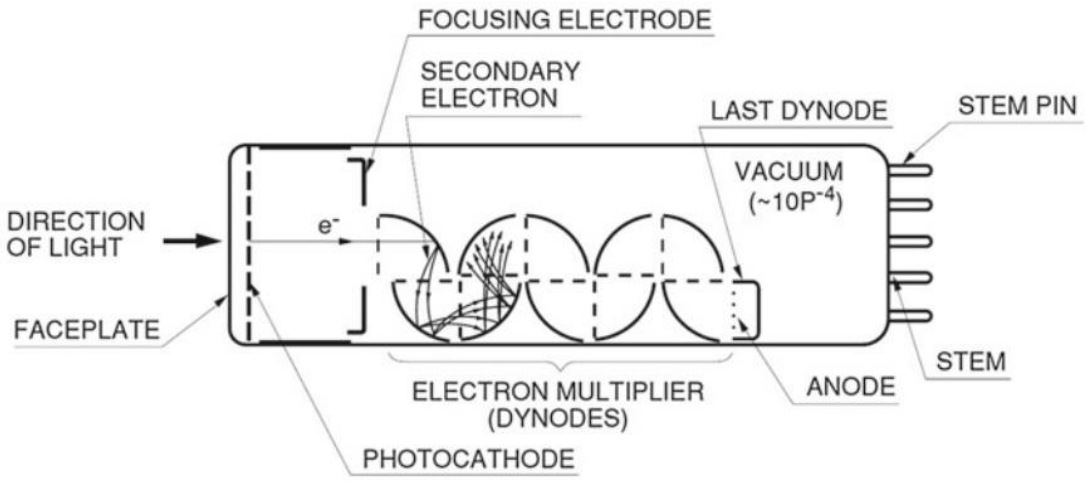

Figure 2.5. Typical design of a photomultiplier tube [145].

There are also various PMTs' designs with emphasis on the different types of dynode configuration. Schematics of the different dynode geometries are illustrated in Figure 2.6. The type of the dynode along with the size of the photocathode and the focusing system are those that define the electrical properties of the PMT. The PMT characteristics vs the dynode geometry is shown in Table 2.1.

Dynode Type	**Rise Time (ns)**	**Fall Time (ns)**	**Pulse Width (ns)**	**Electron transit time (ns)**	**Transit time spread (ns)**	**Photoelectron Collection Efficiency**
Linear-focused	0.7 to 3	1 to 10	1.3 to 5	16 to 50	0.37 to 1.1	Good
Circular-cage	3.4	10	7	31	3.6	Good
Box-and-grid	<7	25	13 to 20	57 to 70	<10	Very good
Venetian Blind	<7	25	25	60	<10	Poor
Fine mesh	2.5 to 2.7	4 to 6	5	15	<0.45	Poor
Metal channel	0.65 to 1.5	1 to 3	1.5 to 3	4.7 to 8.8	0.4	Good

Table 2.1. Photomultiplier tube characteristics vs dynode geometry [146].

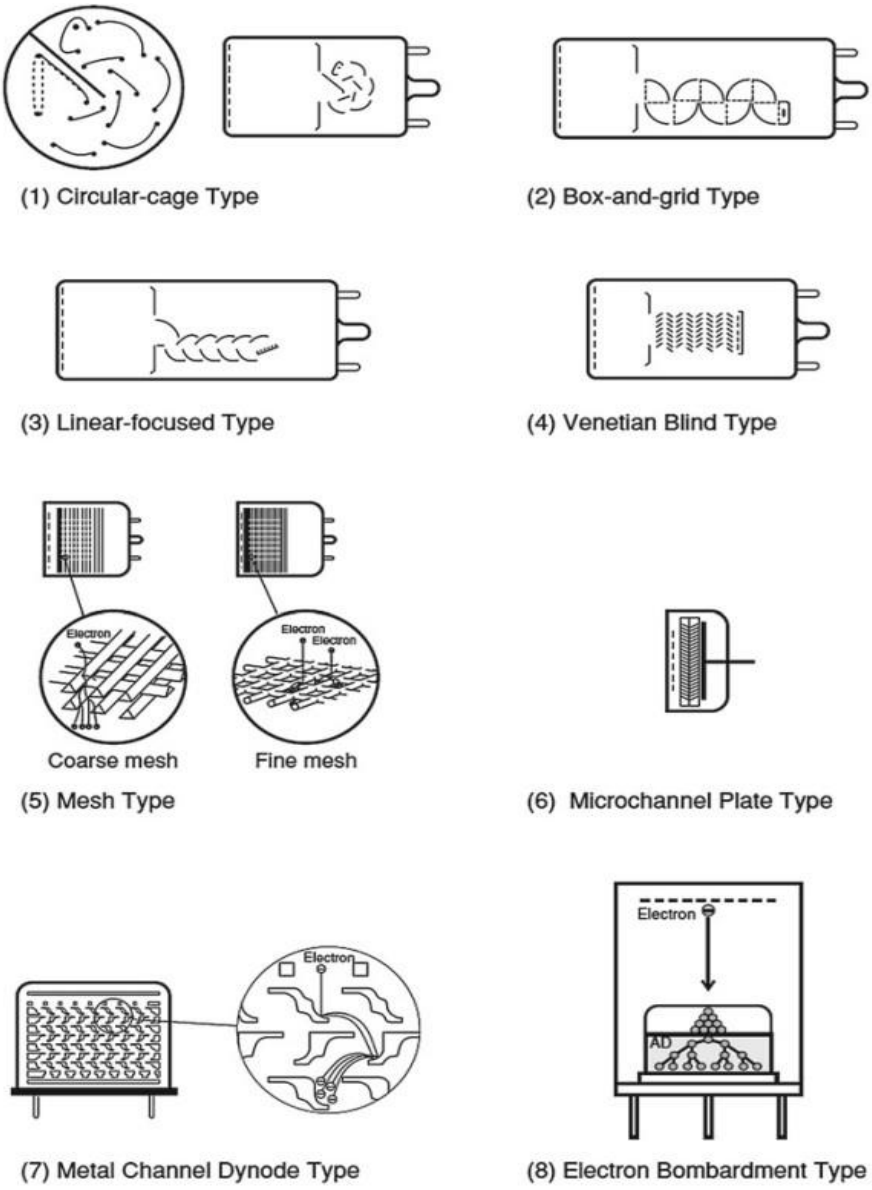

Figure 2.6. Schematics of dynode geometries inside the photomultiplier tube [145].

The spectral range of the PMTs is determined by the material of the photocathode used and the thickness uniformity of the photocathode layer that affects the sensitivity area of the PMT. Materials like Cs-I, Sb-Cs and Cs-Te cover the UV spectral window. Bialkali (Sb-Rb-Cs, Sb-K-Cs), high temperature bialkali (Na-K-Sb) and multialkali (Na-K-Sb-Cs) best operate in the visible region, while alloys like GaAs(Cs), GaAsP(Cs), InP/InGaAs(Cs) and InP/InGaAsP(Cs) offer quantum sensitivity in the near-infrared spectral region. Most PMTs offer good quantum efficiency in the UV and visible region. An example is the GaAsP(Cs)-based photomultiplier tube with peak single photon detection efficiency ~40% at

580 nm at ~ 100 cps dark count rate and 300 ps timing jitter at FWHM, while the maximum count rate can be up to 10 MHz [146]. Detection in the near-infrared region has also been achieved with focus on the telecommunications wavelengths (1310 nm and 1550 nm). The reported quantum efficiency at 1550 nm with an InP/InGaAs PMT is about 2% when cooled down to 200 K [146].

2.4.2 Single-Photon Avalanche Diodes

The single-photon avalanche diode (SPAD) is a well-established alternative to PMTs in the detection of single photons in the visible and the near-infrared. SPADs are based on semiconductor materials, with the first SPADs being developed in the early 1980s made of silicon [147]. Its operation is based on the change of the conducting properties of the semiconductor material with the absorption of a photon. When a photon is absorbed, an electron is excited from the valence band into the conduction band, leaving a 'hole' in its place (Figure 2.7). The creation of this electron-hole pair acts as a charge carrier and provides a method for photo-detection.

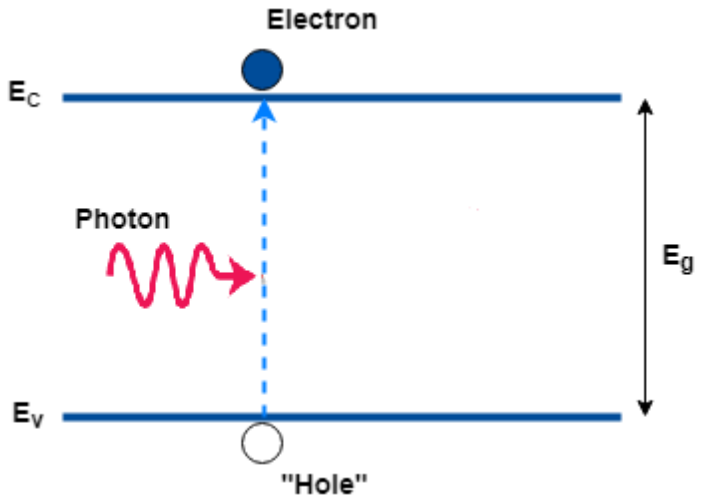

Figure 2.7. Schematic example illustrating the generation of an electron-hole pair with the absorption of a photon. The photon's energy excites the electron into the conduction band, leaving a "hole" in the valence band.

In a photodiode, the application of an electric field accelerates the charge carriers and creates a measurable photocurrent value. The photodiode structure is based on a p-n or p-i-n junction (p-type semiconductor material is positive with an excess of 'holes', n-type is negative with an excess of electrons and 'i' stands for the intrinsic or undoped region which is sandwiched between 'p' and 'n'). This layer of undoped semiconductor (intrinsic) between the two other doped regions in p-i-n junctions provide greater carrier mobility, greater absorption depths, while decrease the transit times and reduce the capacitance of the device. The avalanche photodiode (APD) structure, which SPADs are based on, has a voltage applied so that the n-type semiconductor is at a higher potential than p-type. This way, the junction is reverse biased. In a SPAD, the avalanche diode operates in Geiger mode meaning that it is reverse biased above its break-down voltage. When a photon is absorbed, the carriers that are generated undergo an avalanche gain (impact ionization) resulting in a macroscopic breakdown of the junction [136, 148]. After the detection event, the avalanche is stopped and the device resets by lowering the bias voltage below the break-down voltage passively or with the help of a quenching circuit, getting ready for subsequent photon detection events [136, 147, 149, 150]. In the case of a single photon APD, a single carrier can undergo multiplication and trigger a complete break-down of the diode.

The spectral photodetection range is dependent on the absorbing material. SPADs have been demonstrated operating from the UV up to the mid-infrared, with their cut-off wavelength being determined by the energy band gap (E_g) of the material, as shown in Table 2.2. Silicon SPADs have been used for many decades as silicon covers a broad area from 400 nm up to 1000 nm [147]. To extend the sensitivity to the telecommunication optical wavelengths, SPADs made of semiconductors like germanium (Ge) and indium gallium arsenide (InGaAs) have been an active area of development [151 – 156].

Material	Band gap (eV)	Cut-off wavelength (μm)
Si	1.14	1.09
Ge	0.67	1.86
GaAs	1.43	0.87
InP	1.35	0.92
InGaAs	0.75	1.66
InAs	0.35	3.56
InSb	0.18	6.93
HgCdTe	$0 < E_g < 1.44$	$0.86 < \lambda < \infty$

Table 2.2. Energy band gaps (E_g) and cut-off wavelengths of common semiconductor materials in room temperature (300 K).

Silicon SPADs (Si-SPADs) have been widely used because of their useful wavelength range in the visible up to near-infrared, as determined by silicon's energy band gap of 1.1 eV, shown to achieve excellent optical characteristics. The Si-SPAD structure can be either based on a thick or shallow junction (Figure 2.8). A thick junction structure is optimized for higher detection efficiency and low dark count rate, while a shallow junction structure emphasizes on the low timing jitter and the low bias voltage requirements [157, 158]. Thick junction Si-SPADs have shown quantum efficiencies of up to ~77% at ~800 nm, dark count rates as low as 5 Hz, while FWHM timing jitter is typically at ~400 ps [150, 157, 159, 160]. Shallow junction Si-SPADs have a peak quantum efficiency at 550 nm of ~49% and those which are blue-shifted can achieve ~30% at 400 nm [161, 162]. The main advantage, though, of shallow junction Si-SPADs is their timing properties, achieving a timing jitter of 35 ps full width at half maximum [163 – 165]. Si-SPADs have also been integrated in Si-CMOS (Silicon complementary metal-oxide-semiconductor) processes resulting in sensitive large Si-SPAD arrays with

integrated electronics, a technology with high impact and usefulness in big technological industries like automotive and smartphone manufacture [166 – 170].

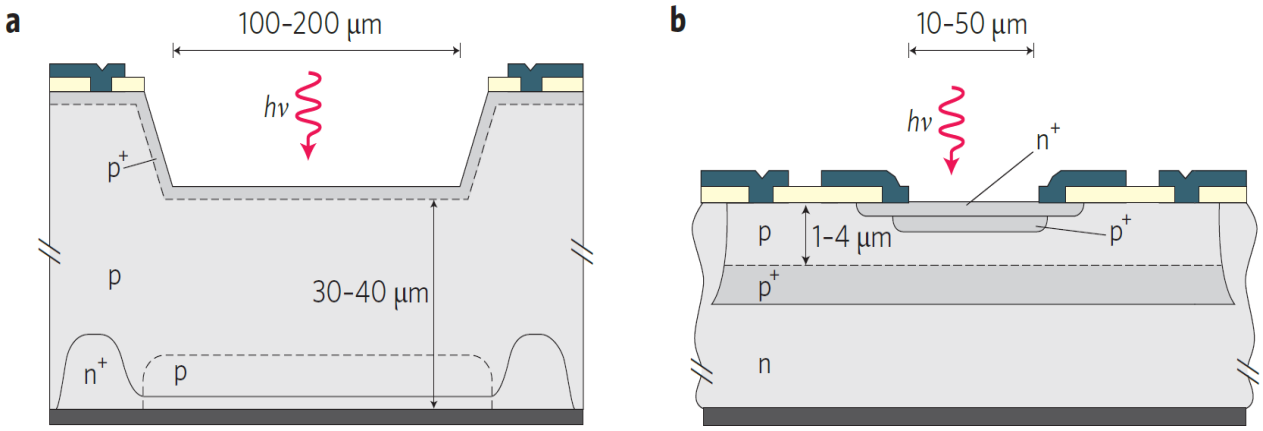

Figure 2.8. Cross section of **a)** thick junction SPAD structure, and **b)** shallow junction SPAD [158].

To extend the photon absorption sensitivity beyond silicon's 1000-1100 nm cut-off, there is need for semiconductor materials with smaller energy band gaps like indium gallium arsenide (InGaAs) and germanium (Ge). As shown in Table 2.2, InGaAs has a 0.75 eV band gap with about 1660 nm cut-off wavelength. The most widely used SPAD detector for the short-wave infrared region is the InGaAs/InP detector, capable of achieving up to 50% quantum efficiency in the telecommunication wavelengths (25-40% at 1550 nm and 50% at 1310 nm), with timing jitter values down to 30 ps at FWHM [171 – 174]. InGaAs/InP SPADs' operation is very similar to Si-SPADs but usually they suffer from afterpulsing effects and high dark count rates that significantly reduce the overall SNR. To overcome this problem, they typically operate in a gated Geiger mode, in which the detector is biased only when a photon is expected to arrive (in short 'gates'). Nowadays, there are commercial InGaAs SPADs operating in a free-running mode, while dark counts remain low by utilizing a Peltier cooler to keep the device at 183K [175]. In addition, these detectors can be fabricated to have large active detection areas (62.5 μm diameter). Single photon InGaAs SPAD arrays are also an active area of research with end goal the design of an efficient multi-pixel single-photon camera [176]. Pioneering this field is Princeton Lightwave Inc., recently

bought by Ford Motor company to incorporate this technology to automotive LIDAR (Light detection and ranging) systems [177].

Similarly, Ge-SPADs have a narrow band gap at 0.67 eV and their sensitivity fades out beyond 1300 nm. However, Ge-SPADs did not show similar characteristics to InGaAs-SPADs, suffering from low quantum efficiencies, very high dark count rates, afterpulsing effects and poor timing resolution [155, 178]. In the last decade, Ge-on-Si SPADs have been examined as a potential InGaAs alternative. Work by Lu *et al.*, Aminian *et al.,* and Warburton *et al.* has shown improved quantum efficiency and timing jitter, but still suffering from high dark count rates even when in gated mode [179 - 181]. Most recently, work by Vines *et al.*, has demonstrated an improved Ge-on-Si SPAD with higher quantum efficiency and significantly reduced afterpulsing effects. The detector was cooled down to 125 K, operating in a Geiger mode with 50 ns 'gates' and achieving a quantum efficiency in the order of 38% at 1310 nm telecom wavelength but still struck by MHz order of magnitude DCR [182]. The decrease in detector's temperature also results to a higher Ge energy band gap and therefore a shorter wavelength cut-off. At 125 K, germanium's band gap corresponds to 0.84 eV and a wavelength cut-off at about 1.48 μm.

2.4.3 Superconducting Detectors

Superconductivity is a state in which a material has zero resistance and exhibits perfect diamagnetism. It was discovered in 1911 by H. Kamerlingh Onnes who while studying the resistances of pure metals at low temperatures using liquid helium, observed the sudden drop of mercury's resistance at 4.2 K [183]. The transition to superconducting state of mercury is shown in Figure 2.9. The maximum temperature at which a material allows the electrical current to flow with no resistance is called the critical temperature (T_c). Above that value the material will return to its normal resistive state. Critical temperatures of known superconductor elements and compounds are shown in Table 2.3. However, there is also a maximum value of electrical current density (critical current I_c) which can keep the material in superconducting state while below critical temperature. As the current density moves towards its critical value, the kinetic inductance (L_k)

of the material also increases. Additionally, there is a maximum magnetic field (critical field B_c) that can be applied to the material before losing its superconducting properties. Superconductors (materials that are in superconducting state) can be distinguished in Type I and Type II superconductors. Their main difference is that in Type I the transition from normal to superconducting state happens instantly while in Type II this phenomenon occurs "slower" – below critical temperature the superconducting properties increase as the temperature is decreased. Also, in Type I superconductors the magnetic field is completely excluded up to a critical field, while in Type II some magnetic field lines may penetrate through the superconductor. This diamagnetism in Type I superconductors was demonstrated in 1933 by Meissner and Ochsenfeld ("Meissner Effect") [184]. The observation of the Meissner Effect was described by the London brothers ("London Theory") in 1935 and was further expanded in 1950 by the "Ginzburg-Landau" theory [185, 186].

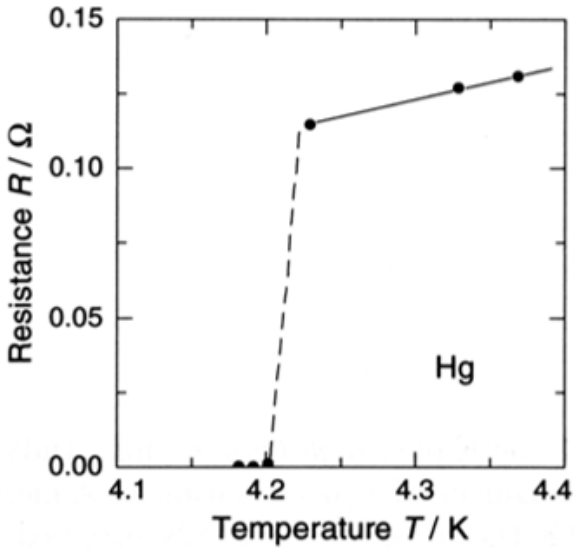

Figure 2.9. Mercury's sudden resistance drop when cooled to 4.2 K, measured by Onnes [183].

A different approach to the superconducting phenomenon was given by Bardeen, Cooper, and Schrieffer ("BCS theory") in 1957. According to BCS theory, superconductivity is explained with the help of the electron-phonon interaction forming the so-called "Cooper pairs" [187]. When cooled down below the critical temperature, electrons can overcome the Coulomb repulsion and form electron

pairs that can travel through the material lattice with no resistance. The material must be kept below the critical temperature and critical current for the pairs to remain bonded. When temperature or current density exceed their maximum value, the Cooper pairs break, superconductivity is destroyed, and the material returns to its normal resistive state.

Utilizing the superconductivity theories and exploiting these unique properties, have led to the fabrication of novel sensitive single photon detectors that have been an active area of research for the last 20 years. Various superconducting detector concepts have been demonstrated, among them the superconducting transition edge sensor (TES) and the superconducting nanowire single photon detector (SNSPD).

Element	T_c (K)	Compound	T_c (K)
Al	1.19	NbN	16
Be	0.026	NbTiN	10.6-11.8
Cd	0.55	Nb_3Sn	18.1
Ga	1.09	Nb_3Ge	23.2
Hf	0.13	Cs_3C_{60}	19
Hg	4.15	MgB_2	39
In	3.4	MoSi	7.5
La	4.8	$PbMo_6S_8$	15
Mo	0.92	YPd_2B_2C	23
Nb	9.1	$HoNi_2B_2C$	7.5
Np	0.075	TiN	6
Os	0.65	WSi	4
Pa	1.3	UPt_3	0.5
Pb	7.2	UPd_2Al_3	2
Re	1.7	$(TMTSF)_2ClO_4$	1.2
Rh	0.0003	$(ET)_2Cu[Ni(CN)_2]Br$	11.5
Ru	0.5	$La_{1.83}Sr_{0.17}CuO_4$	38
Sn	3.75	$YBa_2Cu_3O_{6+x}$	93
Ta	4.39	$Bi_2Sr_2Ca_2Cu_3O_{10+x}$	107
Tc	7.8	$Tl_2Ba_2Ca_2Cu_3O_{10+x}$	125
Th	1.37	$HgBa_2Ca_2Cu_3O_{8+x}$	135
Ti	0.5	$Hg_{0.8}Tl_{0.2}Ba_2Ca_2Cu_3O_{8.33}$	134
Tl	2.39		
U	0.2		
V	5.3		
W	0.012		
Zn	0.9		
Zr	0.55		

Table 2.3. Critical temperature of known superconductor elements and compounds.

The superconducting transition edge sensor (TES) is a very sensitive bolometer with excellent optical detection characteristics. Its operation is based on a superconducting film that is kept at its transition stage, where a slight change in temperature will result in a change in resistance [188]. When an incident photon is absorbed into the film, the device (biased with constant voltage) gets heated leading to a resistance change, such that a current pulse can be read out by a SQUID (superconducting quantum interference device) amplifier electronics. A schematic of the operation of the TES is illustrated in Figure 2.10. This change in the device's resistance is proportional to the energy absorbed, and therefore to the wavelength of the photon absorbed. So, the sensor is able to provide single photon spectral resolution or photon number resolution when a fixed wavelength is used [189].

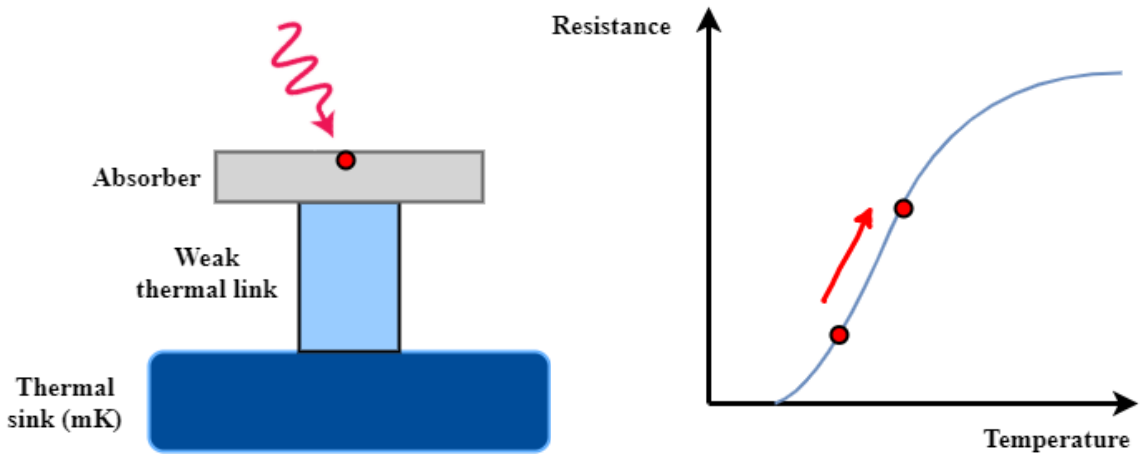

Figure 2.10. (a) Schematic illustrating the operation of a TES, and (b) when a photon is absorbed with the film, the change in temperature leads to a change in resistance.

Tungsten-based TESs offer very high quantum efficiency, up to 98% at 1550 nm when enclosed to a tuned optical cavity, with photon number resolution and negligible dark count rates [190 - 192]. However, in actual experiments DCR may be higher due to room temperature black-body radiation [193]. Timing properties are relatively poor, with typically about 100 ns timing jitter at FWHM and dead time in the order of micro-second as it is limited by the thermal time constant of the element itself. Improved timing jitter values at FWHM (4 – 10 ns) and dead

times (100 ns) have been reported using films with higher transition temperatures in cooperation with faster read-out SQUID electronics [194, 195]. TES detectors may be difficult to implement in an actual experiment due to their need of sophisticated and expensive cryogenics (operate at 50 – 100 mK), however, they have already carried out long distance QKD (Quantum key distribution) and quantum optics experiments [193, 196, 197].

Superconducting nanowire single-photon detectors (SNSPDs or SSPDs) were first introduced by G. Gol'tsman in 2001 and since then have been implemented in numerous experiments, offering great single-photon sensitivity at wavelengths from the visible up to the mid-infrared, sub-Hz dark count rates, pico-second timing jitters and short recovery times [136, 198]. The detector is made of a thin ~5 nm layer deposited onto a substrate (sapphire, MgO or SiO_2), patterned by electron beam lithography and then etched (usually via reactive ion etch RIE) into 100 – 200 nm wide nanowires (typical SNSPD nanowires are made of Nb, NbN, NbTiN or the amorphous WSi and MoSi) usually patterned into a boustrophedonic meander (up to 20x20 μm^2) which increases the active area of the detector and assists in the efficient optical coupling [199 - 201]. A typical SNSPD meander is shown in Figure 2.11.

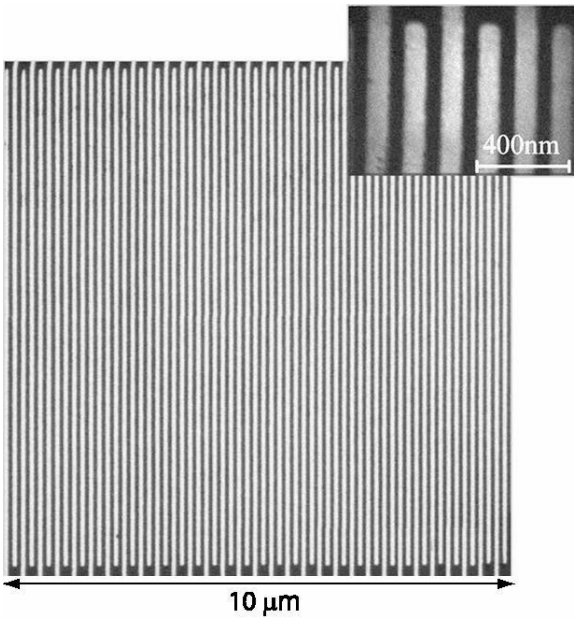

Figure 2.11. The active area of a 4 nm thick and 120 nm wide NbN nanowire patterned into a 10 µm x 10 µm meander [202].

However, this kind of pattern means that the detection efficiency is directly dependent on the polarization of the incident light, as nanowires are more likely to absorb photons that are polarized parallel rather than those polarized perpendicular to them [203]. To negate this effect there have been patterns demonstrated that are able to efficiently absorb light in more than one orientation [204, 205]. Examples of these patterns are shown in Figure 2.12. Whatever the pattern used each time, it is reasonable to aim for large active areas by increasing the overall length of the nanowire. However, there are nanowire constrictions that prevent that. Due to the increased risk for fabrication errors as the nanowire length increases, long nanowires are shown to have limited sensitivity because of the smaller cross-sectional area, restricting the ability of the nanowire to carry high currents [206]. Also, increased nanowire length means an overall increase in the kinetic inductance and therefore longer detector dead times and lower count rates [207]. As a result, most SNSPDs are limited to 10-15 μm^2 active areas to match with the core diameter of a single-mode fibre for infrared wavelengths.

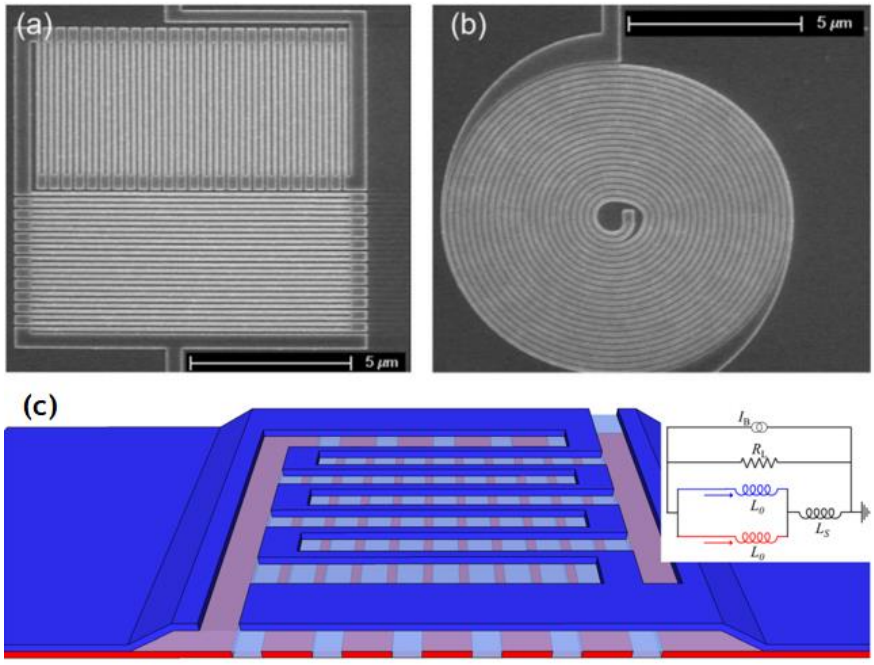

Figure 2.12. SNSPD patterns with polarization independent light absorption. (a) a wire patterned in two orthogonally oriented meanders, (b) a spiral pattern and, (c) a 3D illustration of two meanders stacked orthogonally and its equivalent electrical circuit diagram. (a) and (b) from ref. [204], (c) from ref. [205].

Designs that overcome some of the constraints have also been demonstrated. An example is the superconducting nanowire avalanche photodetector (SNAP) design, shown in Figure 2.13. SNAP devices are basically a series of biased superconducting nanowires connected in parallel that when one of the nanowires become resistive due to an incident photon, the current will be distributed to the rest of the nanowires resulting into a cascade of resistance [208-210].

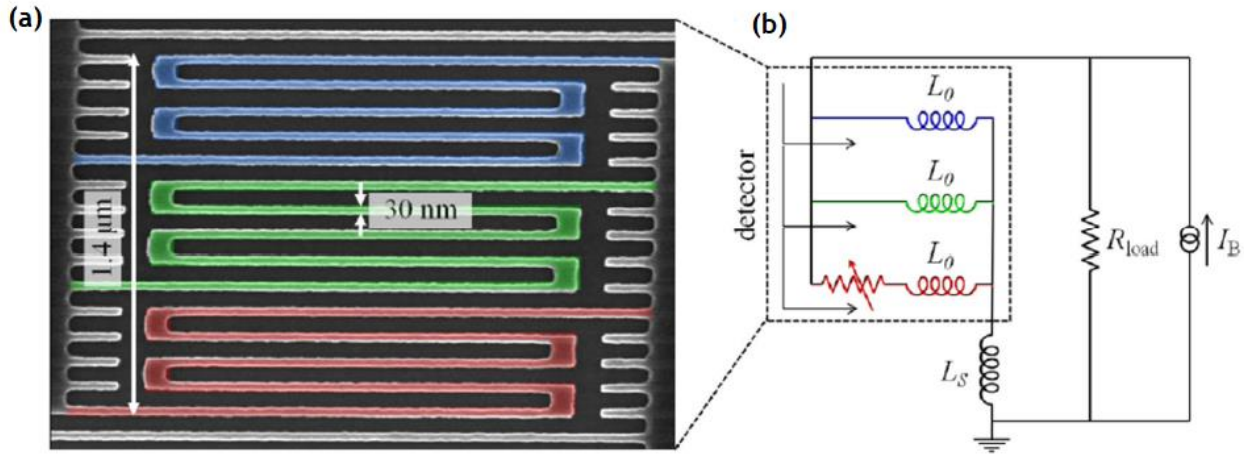

Figure 2.13. (a) A SNAP device with each nanowire distinguished by a different colour and, (b) the equivalent electrical circuit [210].

The operation of SNSPDs is also based on the transition of a superconductor to its normal resistive state to create a detection event. More specifically, a superconducting nanowire is used and biased below, but close to, its critical current I_c while being cooled well below the transition temperature T_c. When an incident photon is absorbed, the energy transferred to the superconducting nanowire will force local Cooper pairs split apart and form a local resistive "hotspot", which due to the continuous supercurrent that flows through the nanowire, will instantly trigger the current density around the "hotspot" to a point above its critical current limit of the nanowire, forming that way a growing resistive strip along the nanowire as a result of Joule heating. This resistive strip generates a voltage drop and a measurement of that drop across the device

signifies a detection event. Then, the current is 'switched' out of the detector with the help of a low resistance shunt resistor which is connected in parallel to the device setup and, due to the electron-phonon scattering, the 'hot' electrons are diffused away of the resistive strip to lose their extra energy restoring the area to the superconducting state waiting for the next detection event [198, 211 – 213]. A schematic of the basic operation principle of the SNSPD is shown in Figure 2.14.

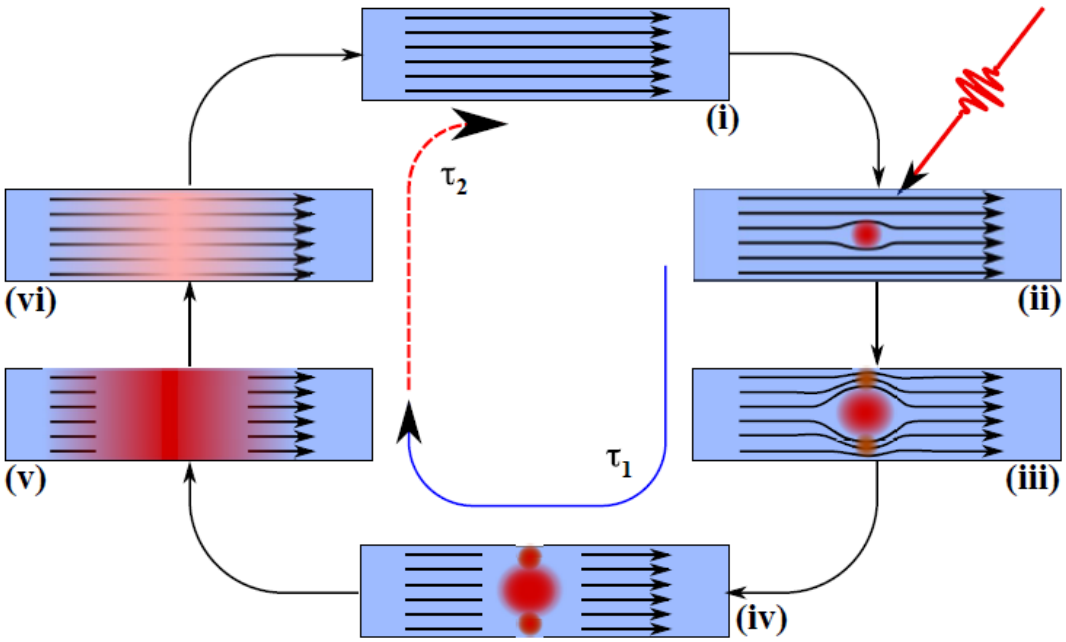

Figure 2.14. The basic operation principle of a SNSPD [137, 212, 213] in two times, τ_1 for detection event and τ_2 for recovery of the nanowire. (i) nanowire in superconducting state and current biased just below its critical current. (ii) Incident photon creates a "hotspot". (iii) Supercurrent incapable of flowing through the resistive hotspot, increases the current density above the critical value. (iv) Creation of a resistive region across the width of the nanowire. (v) Electron-phonon scattering expands the resistive region along the nanowire and current flow is completely blocked. (vi) Bias current is shunted, and nanowire is restored to the superconducting state. From [137].

While this basic phenomenological device operation model is understood across the SNSPD community, recently more sophisticated theoretical modelling

has been undertaken, leading to improved understanding and enabling engineering of improvements in device performance. These refined models are based on the assumption that vortex-antivortex pairs are responsible for the phase transition. Holzman and Ivry state that either a) the nanowire gets heated by the photon absorption causing a drop in the energy barrier, so that a vortex can penetrate the nanowire and since it is biased with current, the vortex penetrates across the width of the nanowire disrupting the superconductivity and , b) a vortex-antivortex pair is generated with the absorption of a photon and as the nanowire is current biased, a Lorentz force is applied on both vortex and antivortex in opposite directions. This pair is split when Lorentz force exceeds a certain value, causing the nanowire to become resistive and create a measurable detection event [214]. However, none of the models can completely explain the detection mechanism, as different mechanisms may be undergoing for different materials, photon energies and device geometries.

Continuous progress in the field has established SNSPD as an excellent choice in most quantum sensing applications and experiments offering excellent detector characteristics. Marsili *et al.* in 2012 demonstrated 93% quantum efficiency at 1550 nm telecommunication wavelength with sub-Hz DCR and low timing jitter (<100 ps) [215] and *Reddy et al.* in 2019 achieved a quantum efficiency >96% also at 1550 nm [216], while Shibata *et al.* in 2015 showed that a SNSPD can have extremely low DCR in the order of 10^{-4} cps (counts per second) [217]. In terms of timing properties, SNSPDs have the clear lead with timing jitter of 4.6 ps in the near-infrared and 2.7 ps in the visible at 400 nm at FWHM and reset time values at 119 ps at telecom wavelengths [218, 219]. As a drawback, compared to other single photon detecting technologies, is considered the expensive and sophisticated cryo-cooling systems required for cooling at temperatures below 5 K for Nb-based alloys and below 2 K for MoSi or WSi. Moreover, in the pursuit of efficient near-infrared and mid-infrared cameras, but also SNSPDs with larger active areas, SNSPD arrays have been demonstrated of up to 64 pixels with great uniformity and large active areas (up to 160 x 160 μm) [220, 221]. An example of a 64-pixel SNSPD array is shown in Figure 2.15. However, apart from the fabrication complexity, a multi-pixel array also faces increased heating problems from the extra room-temperature electronics and cables for each SNSPD device in the array requiring better cooling systems. The most serious

limitation, though, is as the number of SNSPDs increase there is a need of design and more complex read-out electronic circuits. Solving these problems, reported designs have been attempting to overcome these limitations utilizing SFQ-logic (single flux quantum) digital electronic devices [222].

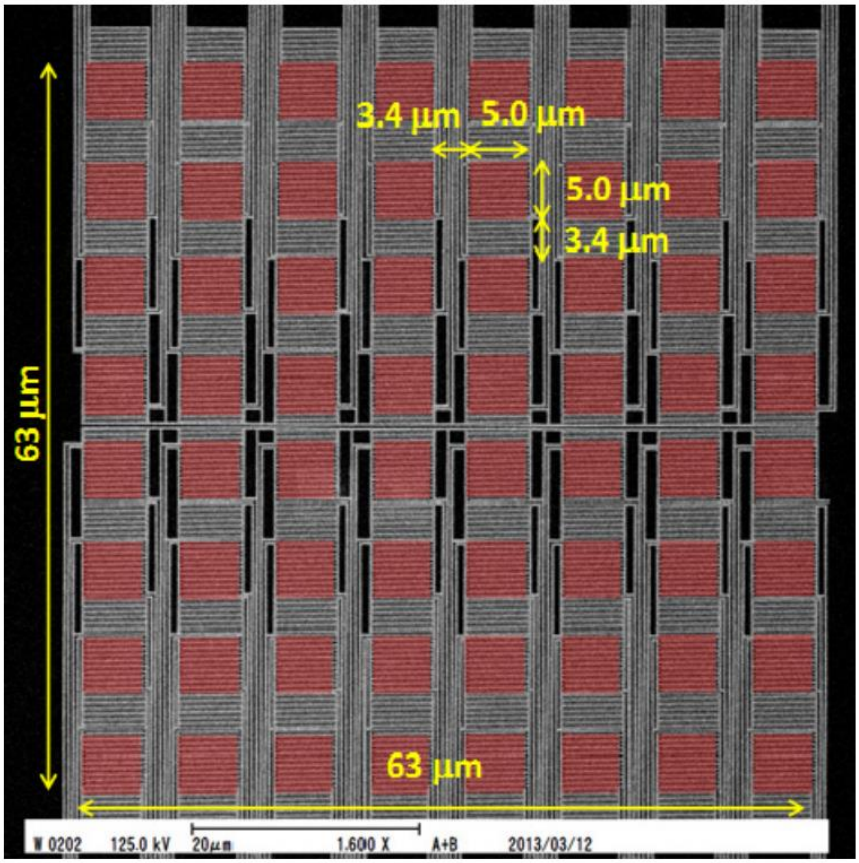

Figure 2.15. SEM image of a 64-pixel NbTiN SNSPD array covering a total of 63µm^2 [220].

2.5 Time Correlated Single Photon Counting

Time correlated single photon counting (TCSPC) is a single photon detection-based measurement technique in which the arrival times of individual photons are counted with the help of single photon detector. In TCSPC single photons are detected from a periodic light signal, the time of their detection is registered, and a waveform is constructed from these time measurements [223]. An illustration of a typical TCSPC architecture is shown in Figure 2.16.

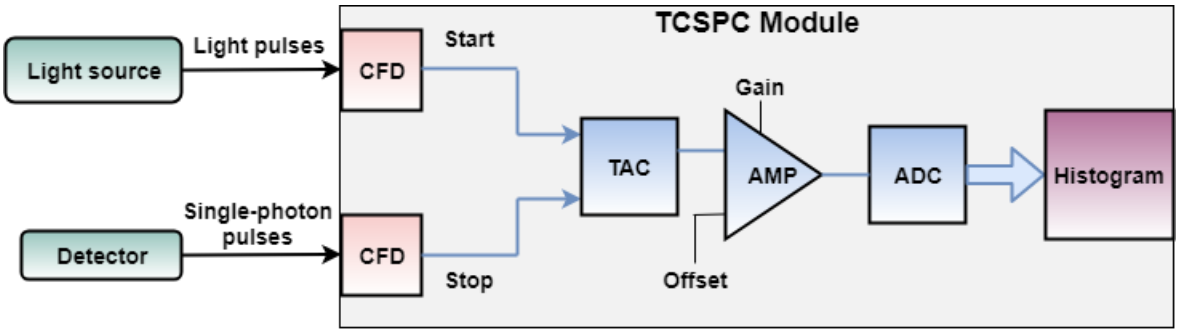

Figure 2.16. Illustration of a TCSPC setup.

The light source sends repetitive pulses into the TCSPC module that act as a start signal, while single photon detection events enable the detector to send pulses as stop events. Both signals go through Constant Fraction Discriminators (CFDs) that trigger at a constant fraction of the pulse amplitude, eliminating all amplitude fluctuations and pulse timing jitters. The outputs from the CFDs are sent to a Time-to-Amplitude converter (TAC) that generates an output signal by linearly charging a capacitor proportional to the arrival time of the start and stop signals. Next, the output voltage from the TAC is amplified by a biased amplifier, utilizing a variable gain and offset to adjust to the preferred time window. Then the amplified TAC signal is sent to an Analog-to-Digital converter (ADC), where a digital output is generated equivalent to the registered time of the photon detection event. The amplified signal from TAC is resolved in multiple “bins” (time channels) of the same width and is important that the ADC is of high precision to avoid noise and distortions in the output histogram. Nowadays, TCSPC devices have reduced significantly the timing drifts and jitters operating steadily in the sub-ps region [224]. Finally, the output signal from ADC when there is a photon detection event, stores the information of the time arrival of the photon into a data memory location. As continuous ADC signals are stored in memory locations, a final histogram is built up of the photon distribution over time, as shown in Figure 2.17. Ideally, all photons emitted by the light source are detected by the detector and recorded. However, due to the timing jitter of the electronics and dead time of the detector, only one photon (stop pulse) can be registered for each start pulse. Usually this is enough for an accurate histogram measurement. Sometimes, though, when the light intensity is too high, it is possible that after

an excitation pulse period multiple photons are detected in the same period. As a result, after the first photon, subsequent photons may be lost leading to a distorted waveform. This “pile-up” effect is a serious drawback of TCSPC following the Poisson detection probability formulas. A Poisson process is described by the rate of detection events in time. To avoid distortions and lifetime errors, the detection count rate must not be higher than the 5% of the excitation repetition rate. For example, if the light source emits photons at 20 MHz repetition rate, the count rate of the detector must be limited to 1 MHz. Usually pile-up effect is the main problem of experiments that implement slow light sources (repetition rates in the range of kHz) in combination to efficient detectors with long dead times.

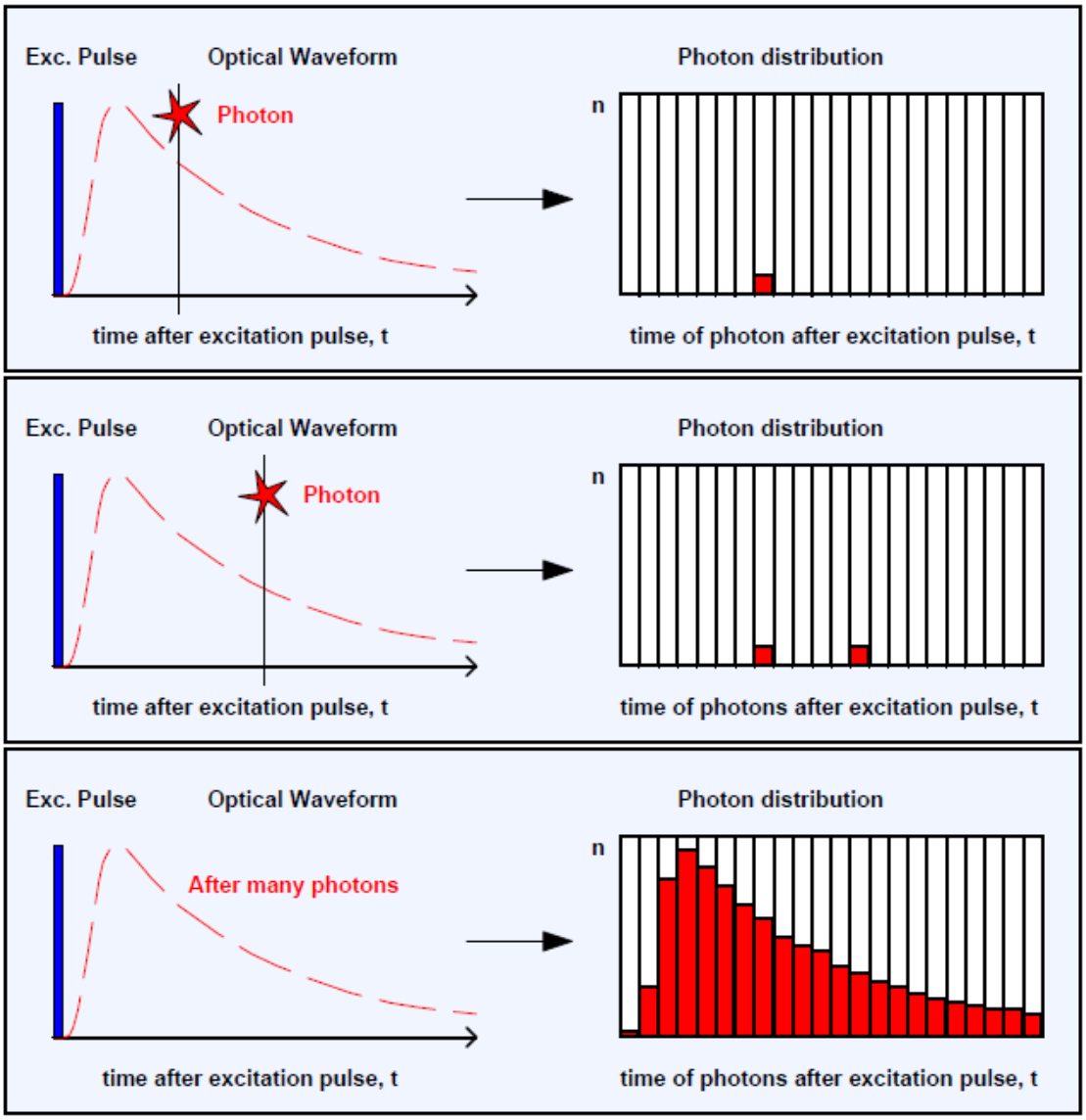

Figure 2.17. TCSPC illustration explaining how the measurement of individual photon times construct the output histogram [224].

Chapter 3 – Experimental methods

3.1 Introduction

The theoretical background of molecular oxygen, photosensitizers, single photon detectors and TCSPC was given in § 2. This chapter describes how all these elements are combined to form a sophisticated SOLD setup with emphasis on the engineering part of this project. The complete SOLD setup can be categorized in four main components: a) the laser source which is required for the precise excitation of the chosen photosensitizer, b) the optical setup including all the optical components for the manipulation and control of the illumination (delivery) light and the near-infrared singlet oxygen (collection) light, c) the detection of the singlet oxygen luminescence emission by a single photon detector and, d) the TCSPC module that correlates the laser signal with the detection signal to generate histograms of the acquired singlet oxygen emission. A schematic of the overall SOLD setup is presented in Figure 3.1.

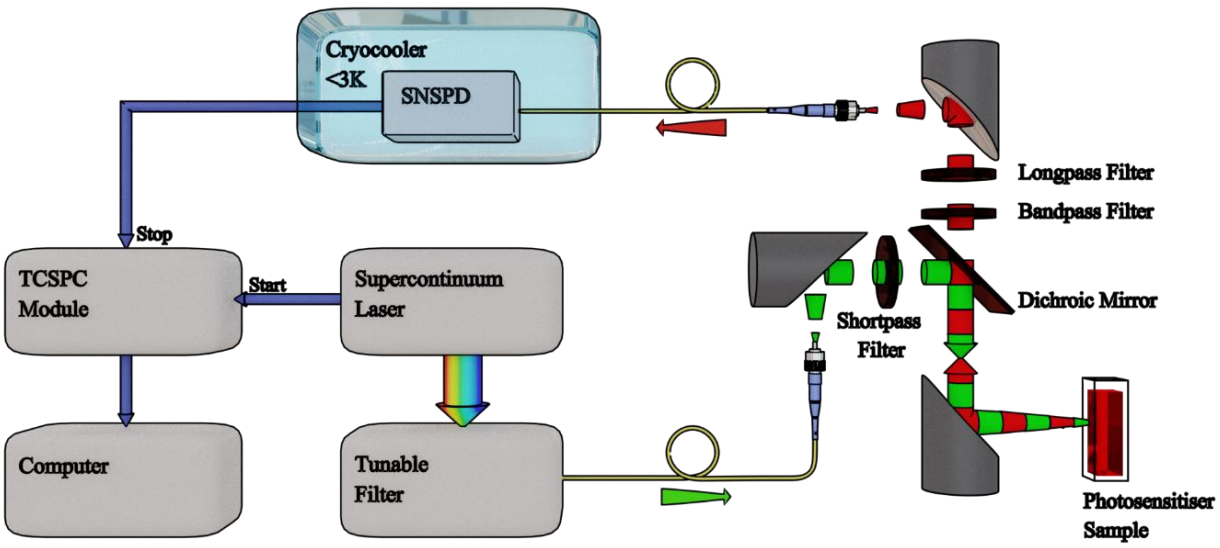

Figure 3.1. A schematic of the SOLD setup. Designed by Dr. Nathan R. Gemmell.

More specifically, a detailed description will be given of the laser source selection, the selected optical components, and the chosen configuration for the generation of singlet oxygen and the collection of its near-infrared emission as discussed in paragraph 2.1.1. Also, the various single photon detectors used will be analyzed along with their characterization processes and information, and lastly the TCSPC module characteristics and data acquisition.

3.2 Excitation source

Light source systems play an important role in the PDT and in the dosimetry techniques as the light properties must be carefully considered in order to efficiently excite the photosensitizer and make most efficient use of the delivered optical power, generating as many singlet oxygen molecules as possible. Earlier PDT and SOLD studies have been utilizing both laser-based systems and non-laser systems. Laser-based systems include argon/dye lasers, metal vapor lasers, solid state lasers, optical parametric oscillators (OPOs) lasers and semiconductor diode lasers, while non-laser systems are consisted of tungsten filament quartz halogen lamps, xenon arc lamps, metal halide lamps, phosphor-coated sodium lamps, fluorescence lamps and light emitting diodes (LEDs) [225, 226]. Argon lasers are typically coupled to a dye for specific PDT outputs focused on the 630 nm wavelength, generating up to 200 mW/cm^2 of continuous wave (CW) optical power density. Metal vapor lasers with or without being coupled to an external dye have a short pulse duration operating as quasi-CW operating from UV to 750 nm (depending on the dye) and providing up to 10 W/cm^2 and 500 mW/cm^2. Solid state lasers such as Nd:YAG and KTP:YAG lasers have similar timing and spectral characteristics to metal vapor lasers. Solid state OPOs stand out for their ability to operate at wavelengths from 250 nm up to 2000 nm and the optical power they produce reach the 1 W/cm^2. Semiconductor lasers can only be fibre coupled, offer PDT-accepted emission wavelengths at 600-950 nm and they can offer up to 700 mW/cm^2 of CW light. Non-laser light sources can also produce a few hundreds of mW/cm^2 optical power density like lasers, but they typically have a much broader emission spectrum which often require the use of additional optics and filters.

The light sources mentioned above are perfect candidates for PDT therapies, being able to excite a specific clinical photosensitizer and apply a large amount of optical power. They are also suitable for most SOLD studies and experiments, but they are far from ideal as they have minimum wavelength tunability, are CW and/or cannot easily tune their repetition rate and optical power. For these reasons, the selected light source for this project is a supercontinuum laser source from NKT Photonics (SuperK compact supercontinuum laser). In a supercontinuum laser, the supercontinuum generation is the process where the laser light is converted to a very broad spectral bandwidth light. The optical spectral range of the laser is 450 – 2400 nm with total output power at ~110 mW, tunable repetition rates up to 24 kHz with optical output pulses <2 ns wide. The supercontinuum laser is coupled to a single line filter from NKT Photonics (SuperK Varia tunable single line filter) with tunable wavelength from 450 – 800 nm, variable wavelength bandwidth from 10 nm up to 100 nm and collimated to a single mode FC-APC fibre. The NKT Photonics supercontinuum laser and the single line filter are shown in Figure 3.2. The selection of the specific laser and single line filter allows the precise selection of the peak absorption wavelength of the chosen photosensitizer, an ideal solution for singlet oxygen experiments as most photosensitizers have their excitation peaks in the region of 500 - 700 nm.

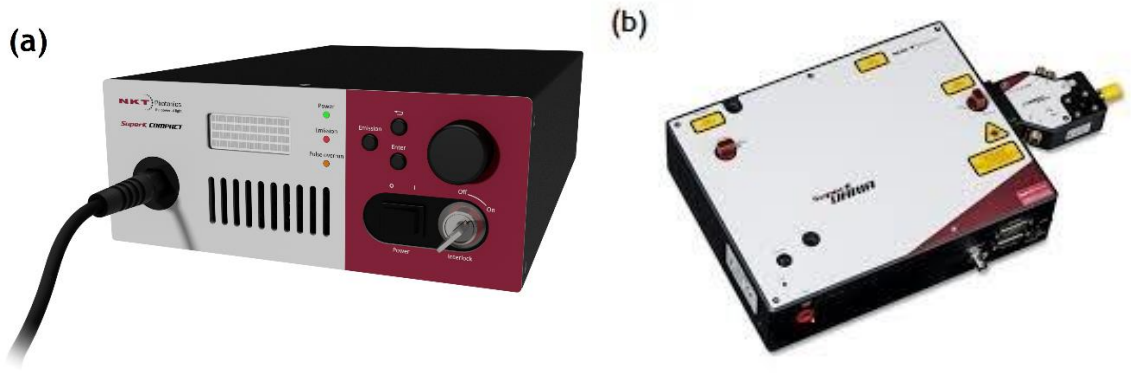

Figure 3.2. (a) SuperK compact supercontinuum laser and, (b) SuperK Varia single line filter for 450 – 800 nm wavelength. From [227].

In addition, the low repetition rate matches the needs of the experiment enabling the acquisition histograms in a 42 μs detection time window after the excitation pulse, a lifetime usually longer than singlet oxygen's lifetime in most solvents. The output optical power after the coupling with the single line filter is up to 2 mW, depending on the centre wavelength and bandwidth as shown in Figure 3.3. The optical power reaching the photosensitizer may be weaker than most semiconductor CW diodes or other laser sources used in SOLD experiments, but still the optical power is sufficient for the efficient generation of singlet oxygen and the unique characteristics a supercontinuum source offers can overcome this small flaw. The light from the single line filter is directed to the optical setup through a metallic single mode FC-APC fibre. The analog pulse signal output is transferred from the supercontinuum laser to the TCSPC module's sync channel giving the 'start' signal, as described in paragraph 2.5. Additionally, the laser is connected to a PC unit via USB for the easy tuning of all the parameters in a software with user interfaces for both laser and single line filter.

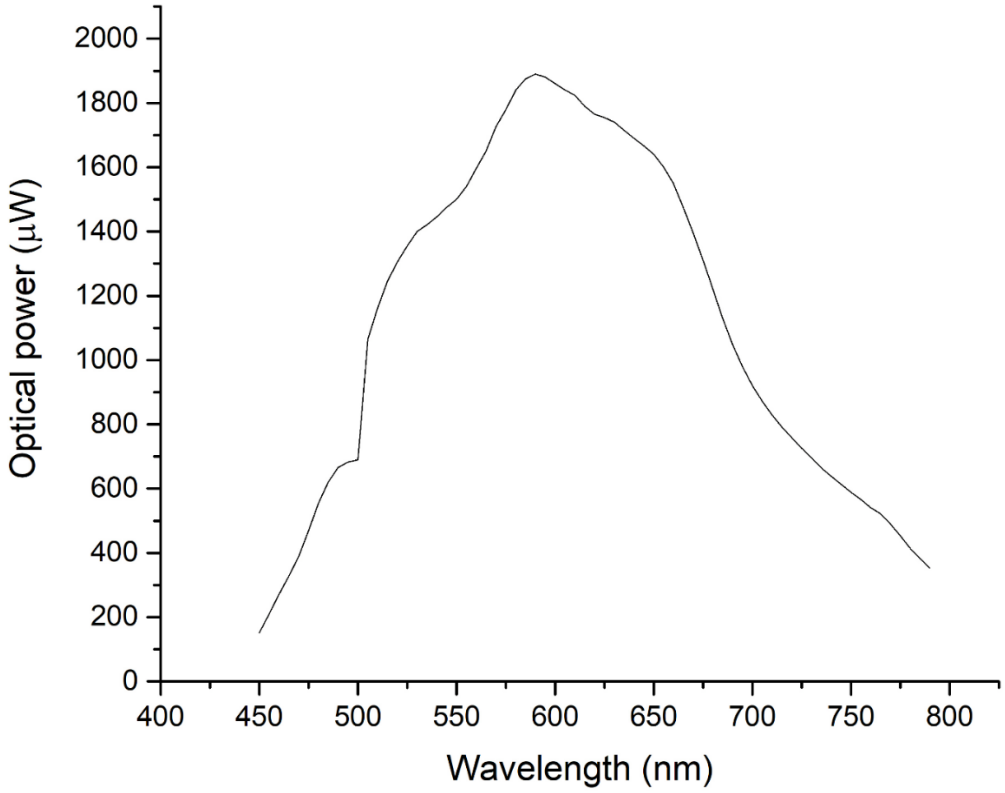

Figure 3.3. The total optical power emitted by the single line filter as a function of wavelength.

3.3 Optical Setup

The optical setup was built by carefully selecting the optical parts and continuously tweaking and upgrading over the years. An illustration of the optical setup is shown in Figure 3.4. The optical setup was not designed in a conventional L-configuration of the excitation and the emission collection, it was rather designed and built to excite and collect from the same spot. This way the alignment of the two beams (excitation visible light and NIR singlet oxygen light) was very accurate and by choosing the appropriate optical filters the excitation light was blocked from reaching the detector.

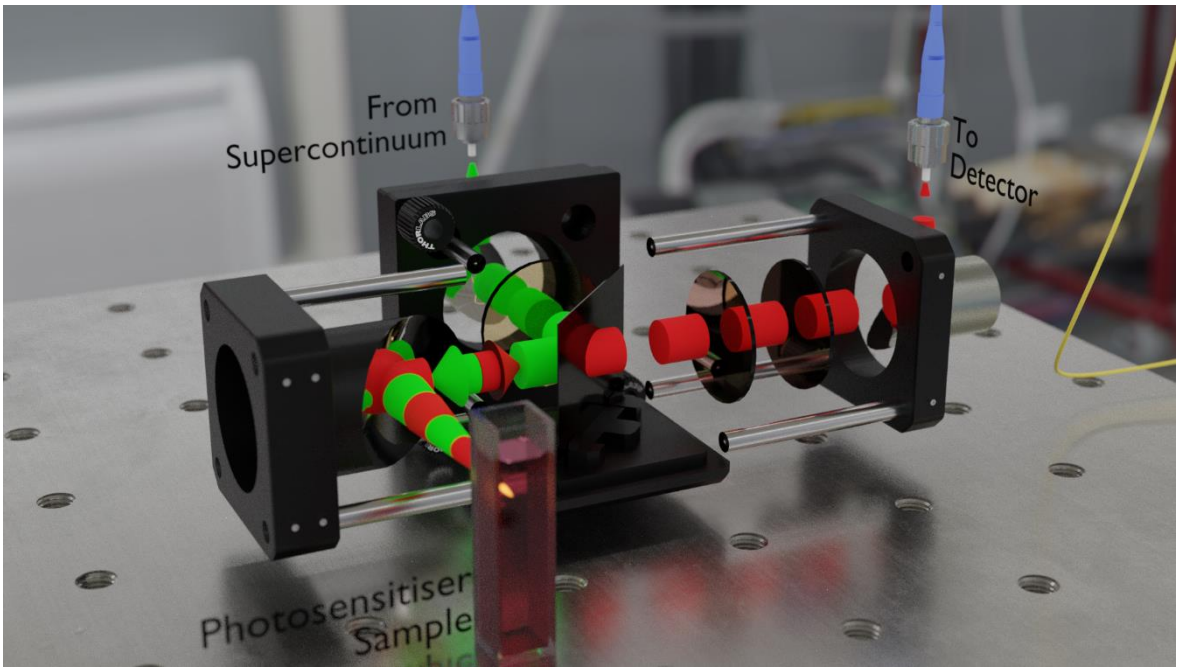

Figure 3.4. 3D illustration of the optical head. Designed by Dr. Nathan R. Gemmell.

The optical fibre from the supercontinuum laser (9 μm core size diameter) is coupled to a reflective collimator (Thorlabs RC08FC-P01 - protected silver reflective collimator 450 nm – 20 μm, 8.5 mm collimated beam) with 33 mm reflected focal length (RFL). The visible light from the laser is then filtered by two short pass filters with cut-off wavelengths shorter than the generated singlet oxygen photons. The first is a hard-coated short pass filter from Thorlabs

(FESH0950) with cut-off wavelength at 950 nm and the second is a KG-1 Heat absorbing glass from Edmund Optics with wavelength transmission allowance from 400 nm up to ~1 μm. Both filters allow visible light pass through while they block most of the infrared light that may come from the broad laser emission or stray ambient light. The filtered visible light is then sent through a dichroic beam splitter (Thorlabs DMLP950 – long pass dichroic mirror) which is set at a 45° angle with 950 nm cut-on wavelength. Excitation light is diverted by the 45° angle dichroic mirror and then focused by an 90° angle off-axis parabolic mirror (Thorlabs MPD129-P01 – 90° Off-axis silver protected Parabolic mirror, RFL 50 mm) on the side of 4 ml quartz cuvette (Sigma Aldrich – Hellma absorption cuvette) filled with photosensitizer. Peak excitation wavelength for the photosensitizers used is centred at 522 nm, 540 nm, 645nm, 660 nm and 689 nm. More on the photosensitizers is discussed in § 3. The optical power at each wavelength was measured by a power meter, while the diameter of the beam spot size on the cuvette and the optical power density is calculated as below and are presented in Table 3.1:

$$Beam\ spot\ size\ (\mu m) = Fiber\ core\ (\mu m)\frac{FL\ of\ Reflective\ mirror\ (mm)}{FL\ of\ Collimation\ package\ (mm)} \quad (23)$$

and,

$$Power\ Density\left(\frac{W}{mm^2}\right) = \left(\frac{Beam\ spot\ size(\mu m)*10^{-3}}{2}\right)^2 * Optical\ power(mW) * 1000 \quad (24)$$

With 9 μm fibre core diameter, 33 mm collimator focal length (FL) and 50 mm focal length of the reflective mirror, the diameter of the beam spot size from eq.23 is 13.64 μm.

PS centre wavelength	Optical power (mW)	Optical power density (W/mm^2)
522 nm	1.2	0.175
540 nm	1.4	0.204
645 nm	1.8	0.263
660 nm	1.6	0.234
689 nm	1.1	0.161

Table 3.1. Chosen PS peak excitation wavelengths and the optical power and power density applied to the PS sample.

The focused beam enters the cuvette with the photosensitizer and the photodynamic process generates singlet oxygen which emits 1270 nm and 1590 nm photons following the decaying pathways. These near-infrared photons are reflected by the same 90º off-axis parabolic mirror towards the dichroic beam splitter, where this time the light passes through the dichroic mirror. The parabolic mirrors ensure that the focal length of both routes, illumination and collection, is the same for optimum overlap. Also, these mirrors ensure that the optical setup do not vary as the wavelengths change in either illumination or collection. Then the NIR beam is filtered by a long pass filter and a band pass filter to block all the unwanted light that may pass through the previous optics. For the 1270 nm emission detection the filtering consists of a long pass filter with cut-on wavelength at 1200 nm (Thorlabs FELH1200 – premium long pass filter) and a band pass filter centred at 1270 nm (Omega Optical – custom ordered Band pass filter, 90% transmission at 1270 nm ± 4 nm). For further 1270 nm emission measurements, four more band pass filters were used around the 1270 nm wavelength: two custom ordered band pass filters at 1240 nm ± 4 nm and 1300 nm ± 4 nm from Omega Optical and two band pass filters centred at 1200 nm ± 2 nm and 1340 nm ± 2 nm from Thorlabs (FB1200-10, FB1340-12).

For the 1590 nm emission detection similar filtering was used with a long pass filter with cut-on wavelength at 1500 nm (Thorlabs FELH1500 – Premium Long

pass filter) and a band pass filter centred at 1590 nm ± 2.4 nm (Thorlabs FB1590-12 – Band pass filter). Similarly to 1270 nm measurements, four more band pass filters around the 1590 nm wavelength were used for additional measurements: band pass filters with centre wavelength at 1560 nm ± 2.4 nm, 1620 nm ± 2.4 nm, 1520 nm ± 2.4 nm and 1650 nm ± 2.4 nm from Thorlabs (FB1560-12, FB1620-12, FB1520-12, FB1650-12). Finally, the filtered NIR light is collimated by a collimation package with 7 mm focal length (Thorlabs RC02FC-P01 – protected silver reflective collimator 450 nm – 20 μm, 2 mm collimated beam) coupled to a fibre leading to the single photon detector. The collection fibre selection depends on the single photon detector used. For measurements with SNSPDs a standard SMF28e fibre with ~ 9 μm core diameter was used (Thorlabs P1-SMF28e-FC-2 – single mode patch cable, 1260 – 1625 nm, FC/PC, 3 mm Jacket, 2 m long). For measurements utilizing the InGaAs detector, the fibre used was a multimode fibre with 62.5 μm core diameter provided by the company. The transmission data for the filters and mirrors mentioned above are included in Appendix A.

The overall size of this optical head setup is 20 cm x 15 cm x 5 cm. This size is relatively small for a bench-based experiment. However, if it was to be used in a clinical therapy, the whole optical sensor head could be further optimized for size without sacrificing the collection efficiency, down to the size of a pen.

3.4 Single-Photon Detectors

The detection of the singlet oxygen luminescence was accomplished by two types of single photon detector: a superconducting nanowire single photon detector (SNSPD) and a single photon avalanche diode (SPAD). SPAD is a well-established technology for single photon detection experiments in the visible and the near infrared, while SNSPD is a newer alternative to existing single photon detector achieving incredibly high quantum efficiency and ultra-low timing jitter values while keeping the dark count rate low, as described in paragraph 2.4. Both detectors can be fibre-coupled and are excellent candidates for singlet oxygen luminescence detection experiments, offering great timing properties and high quantum efficiency at the desired singlet oxygen emission wavelengths. Experimental data are acquired by both detector technologies. Several SNSPDs

were used during this project, most of them fabricated by Prof. Robert Hadfield's group and collaborators, while the SPAD used is a commercial InGaAs SPAD acquired during the last months of the project as the big increase in the overall active detection area coupled to a multimode fibre would increase the collection signal more than a SNSPD of higher efficiency. The quantum efficiency of all SNSPD detectors was measured at two wavelengths based on the available laser sources emitting at standard telecommunication wavelengths 1310 nm and 1550 nm (close to the desired 1270 nm and 1590 nm singlet oxygen luminescence). The characterization of the SPAD was accomplished using a tunable laser source with extended emission from 1340 nm up to 1650 nm. The quantum efficiency of the detectors was calculated following the equations below:

$$E_{one\ photon}(J) = \frac{h*c}{\lambda} \tag{25}$$

Where $E_{one\ photon}$ is the energy of one photon in Joule, h is the Planck constant with value 6.62607015 * 10^{-34} J * s, c is the speed of light that equals to 299792458 m/s and, λ is the wavelength of the incident photon in nanometers.

$$Photons\ per\ second = \frac{Input\ power(W)}{E_{one\ photon}(J)} \tag{26}$$

$$Photons\ after\ att. = 10^{\frac{10*(log_{10}\ Photons\ per\ second) - attenuation\ (dB))}{10}} \tag{27}$$

$$Quantum\ Efficiency = \frac{Photon\ counts - dark\ counts}{Photons\ after\ att.} \tag{28}$$

Attenuation of the laser output is necessary for the characterization of the single photon detectors, as the laser sources used are not true single photon sources. The laser pulses are attenuated to generate weak coherent pulses (WCP) so that the mean number of the photons produced per laser pulse is smaller than 1 [162]. The number of photons in each pulse follows the Poissonian statistics and the equation that gives the arrival probability is:

$$P(n,\mu) = \frac{\mu^{n} * e^{-\mu}}{n!} \quad (29)$$

Where $P(n,\mu)$ is the probability of a pulse to be attenuated to a specific value of μ containing n photons [228, 229].

3.4.1 Superconducting nanowire single photon detector system

SNSPD systems used in this project were based on NbN and NbTiN chips. To operate in their superconducting state, they had to be cooled down below their critical temperature. The cooling system is a closed-cycle Gifford-McMahon (GM) refrigerator consisted of a 1.5 kW Sumitomo CNA-11C indoor air-cooled compressor and a Sumitomo RDK-101D cold-head. The heat transferral medium is high purity helium gas, which flows inside two successive GM stages. The first stage reaches 40 K and the second is further cooled to about 4 K. The cold-head provides 0.1 W of cooling power at 4.2 K and is able to reach temperatures < 3 K [230], as shown in Figure 3.5. The compressor is 40 cm x 32 cm x 45 cm placed under the bench or in a service room, being separated from the cold-head and connected to the base of the refrigerator by two flexible gas lines. The SNSPD devices are placed on the cold-head, while thermometers are installed and monitor both GM stages and cold-head temperature. The whole refrigerator is housed inside a cylindrical vacuum chamber of ~25 cm diameter and 60 cm tall, while the overall weight does not exceed 20 kilograms.

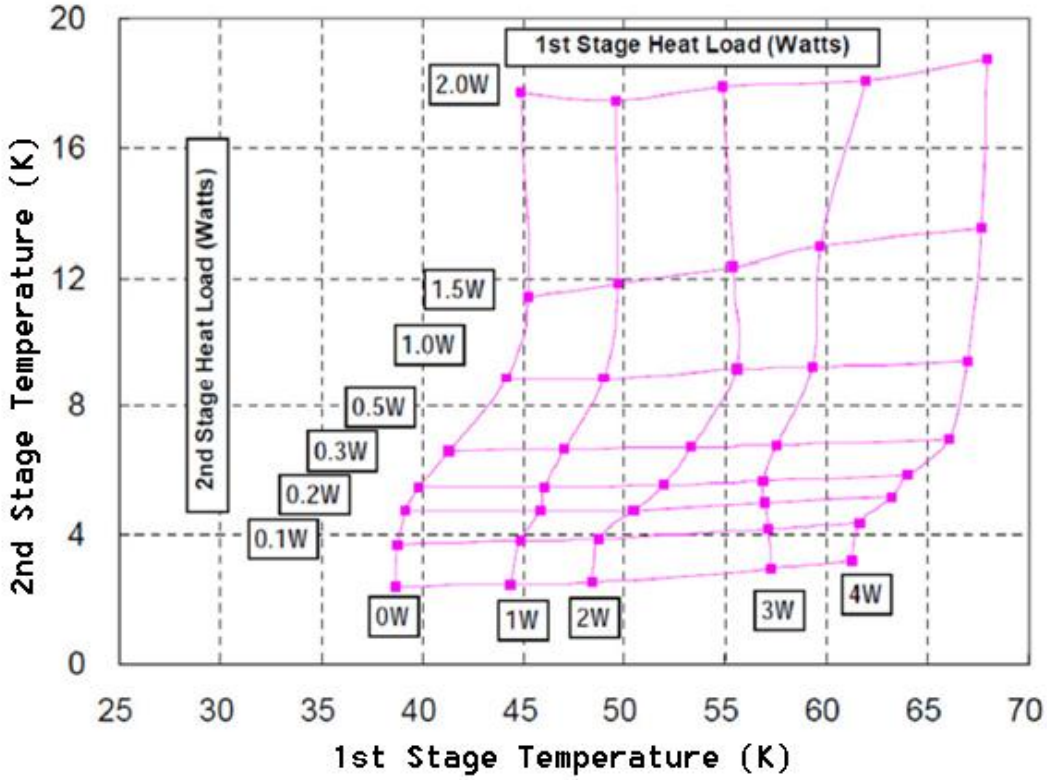

Figure 3.5. Heat load map for the two-stage Sumitomo RDK-101D cold head. Adapted from [231].

Experiments were also made using a first of a kind miniaturized closed-cycle refrigerator for the needs of its proof of concept validation. Among other practical experiments, singlet oxygen luminescence detection was accomplished by a SNSPD mounted and cooled inside this cooling platform. This was a demonstrator produced by Dr Nathan Gemmell in collaboration with STFC Rutherford Appleton Laboratory for the QuantIC quantum technology hub. The cooling system is the prototype for the European Space Agency Planck space telescope. The miniaturized cooling system consists of two Stirling stages and a Joule-Thompson (J-T) stage on top, reaching a minimum temperature of 4.2 K. The cooling power at 4.7 K is 4 mW operating with ^{4}He gas [232]. The miniaturized cooling platform in shown in Figure 3.6.

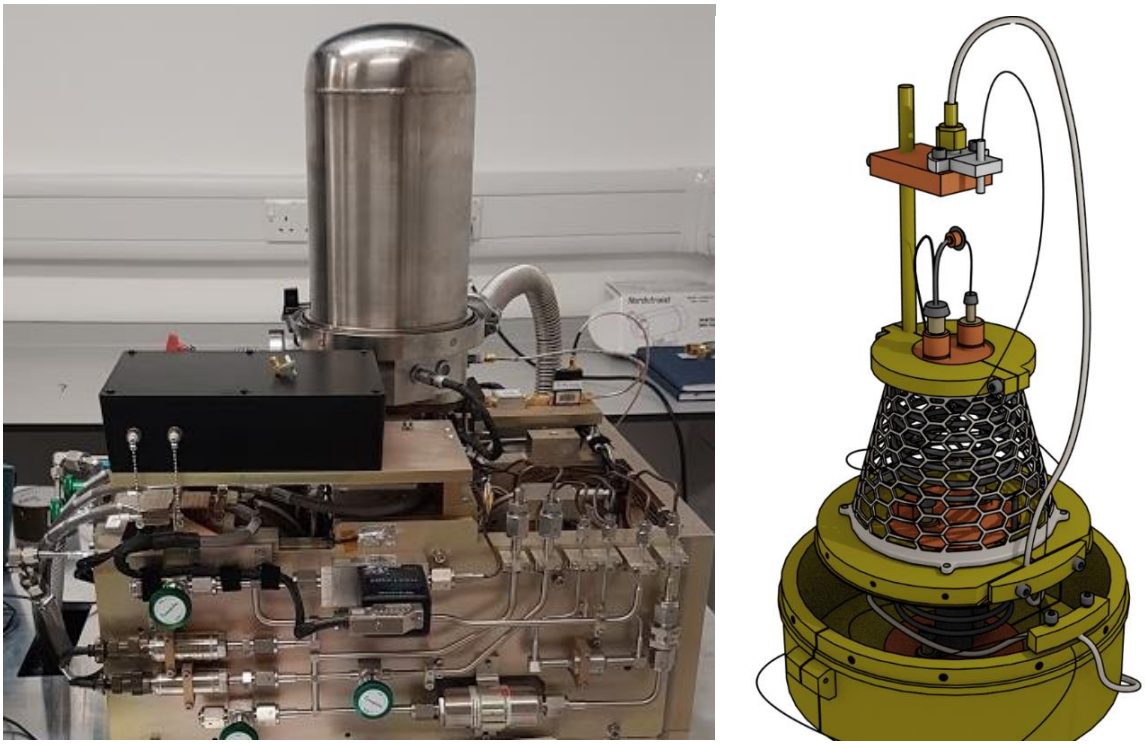

Figure 3.6. a) The whole miniaturized cooling platform and, b) a 3D model of the top stage with a SNSPD device mounted, fibre coupled and electrically connected (provided by Dr Nathan R. Gemmell).

SNSPD based experiments were carried out by various devices available during the time of the project. The SNSPDs were characterized by acquiring their current-voltage (I-V) curve, the overall quantum efficiency (QE) and their timing jitter. Timing jitter is a negligible parameter for the singlet oxygen luminescence experiments but as a part of the general characterization of the device that was also used in other experiments, it needed to be carried out. Once the SNSPD is cooled down to <3 K an I-V curve is required to define the performance of the device and help us know at which current value will bias the device to be approaching the critical current. The electrical setup for the acquisition of the I-V curve, as shown in Figure 3.7, is with the help of a load resistance (typically ~100 kΩ) that defines the current supplied to the SNSPD ($I = V_{voltmeter} / R_{load}$). The bias voltage supplied by a SIM 900 voltage is varied as the resistance and current is monitored, up to a value that will exceed the critical current I_c. A Python script assisted in the monitoring and recording of each value and in generating the I-V curve. The shunt resistance that is connected in parallel to the SNSPD is typically

much smaller than the device resistance and is added to prevent the device from remaining in the resistive state once the superconductivity is destroyed (latching). The shunt resistance diverts the current away and helps the device recover its superconducting state.

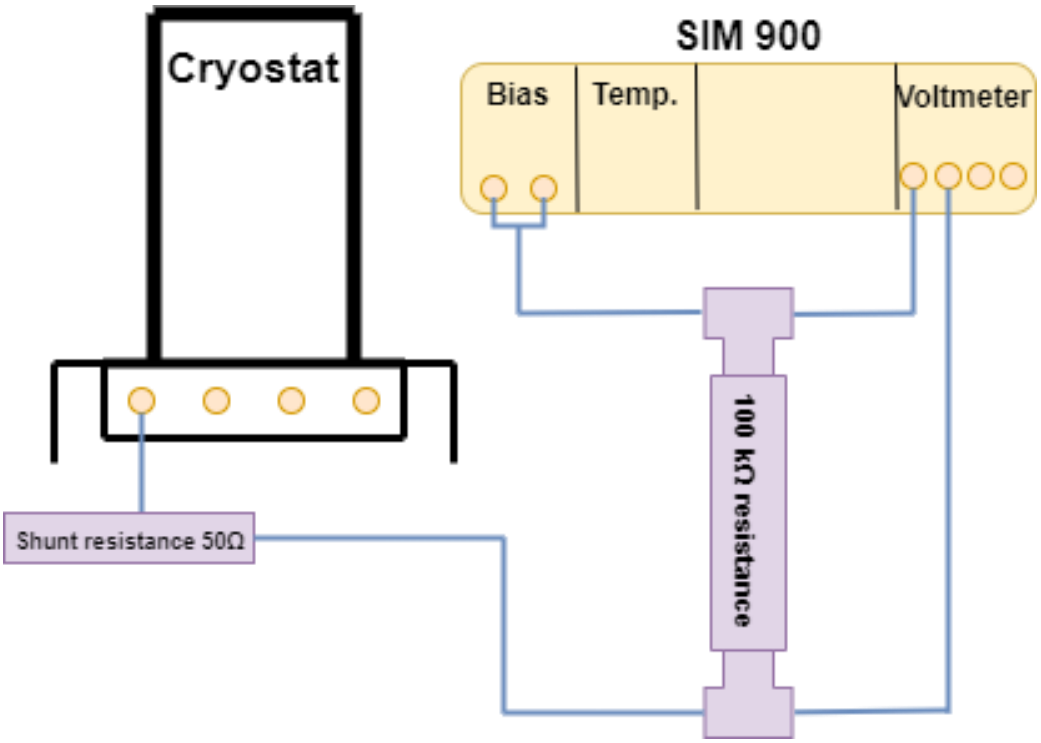

Figure 3.7. Experimental setup for the I-V characteristics of the SNSPD.

An example of the I-V characteristic graph of a SNSPD cooled down to 2.3K is shown in Figure 3.8, with a 50 Ω shunt resistance in parallel and a 100 kΩ load resistance. In the graph, the transition from the superconducting state to the normal resistive state is happening at ~ 20 μA. That means that the SNSPD device must be biased just below the critical current of 20 μA in order to operate as a single photon detector at 2.3 K.

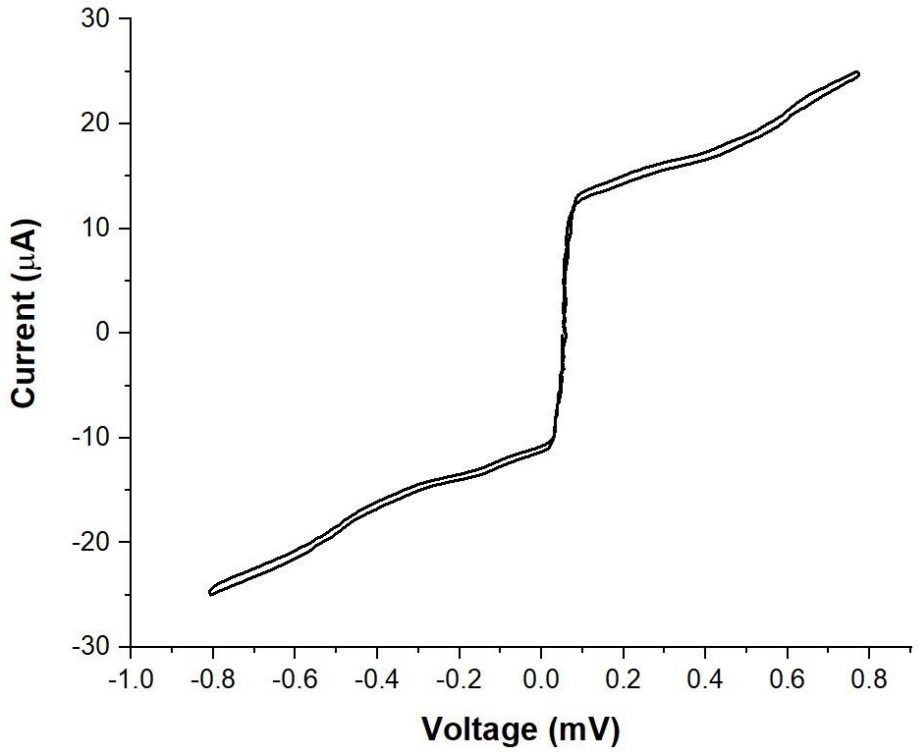

Figure 3.8. I-V characteristics of a SNSPD measured at 2.3 K with a 50 Ω shunt resistor.

Next, the system detection efficiency (η_{SDE}) is calculated using a calibrated light source and optically attenuating the output so that it emits weak coherent pulses in the single photon level, controlling the incident power reaching the detector. By knowing the input power and the wavelength the light source emits, quantum efficiency is easily calculated using equations 26 to 28. The experimental setup (Figure 3.9) is based on a diode laser source driven by a pulse pattern generator (PPG) that its optical pulse output is heavily attenuated by two programmable optical attenuators to enter the single photon emission regime and control the photon flux onto the active region and a fibre polarizer that may tune the polarization of the incident light so that the detector is absorbing as much as possible. At the same time, the SNSPD is current biased at a fixed value and through a standard readout circuit consisted of a bias tee, a 100 kΩ resistance, a 50 Ω shunt resistance and a room-temperature amplifier chain the output signal pulses from the detector are recorded in a photon counter. While the laser is blocked, a certain number of photons for each bias value are still being detected and recorded in the photon counter. These values are the dark counts generated

by internal or external noise contributions. Subtracting these values from the total detected counts and dividing by the total incident photons fed to the detector, as in equation 28, the system detection efficiency is calculated.

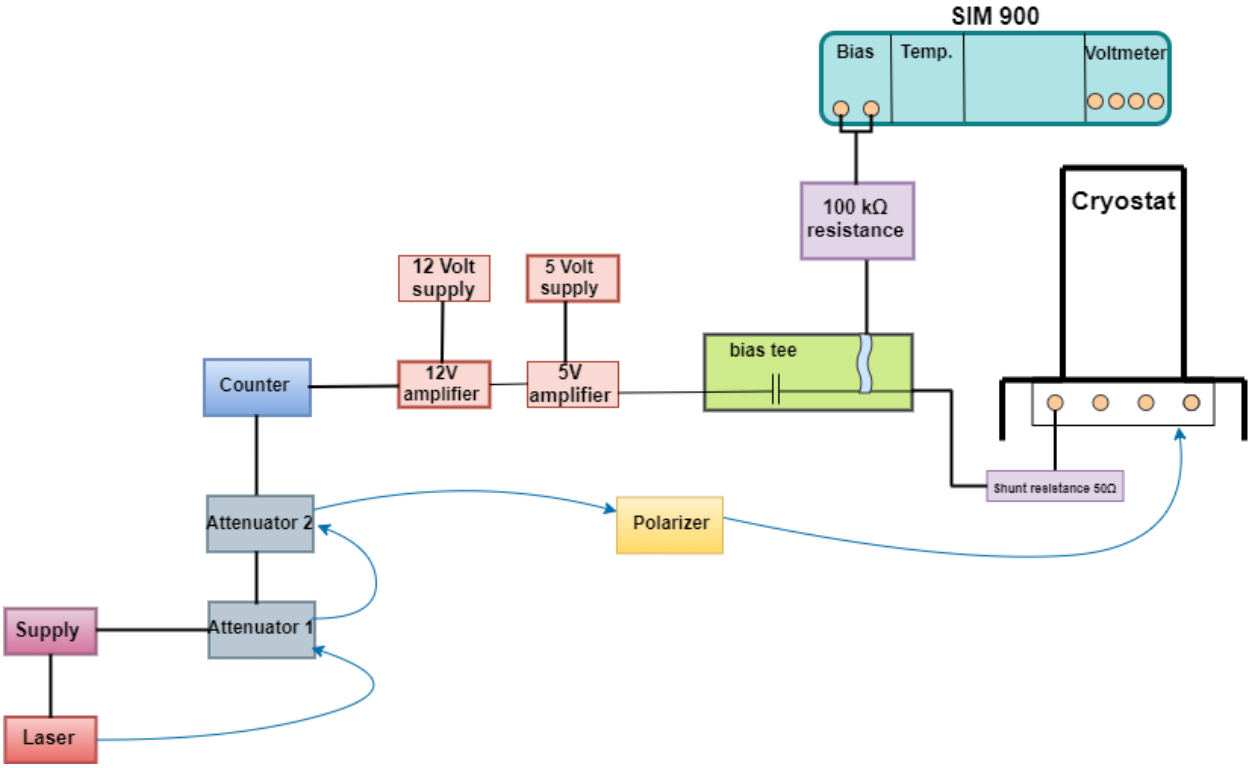

Figure 3.9. Illustration of the experimental setup used for the measurement of the system detection efficiency. Black connections illustrate the electrical connectivity between the components, while the blue arrows represent the fibre connectivity for the travel of light from the laser light source onto the detector.

In Figure 3.10a an example measurement of the quantum efficiency at 1550 nm of a SNSPD is shown, in comparison to the corresponding dark count rate for each bias point. The quantum efficiency has a steep increase at lower bias points and then it tends to reach a plateau, while the dark count rate is slowly increasing at low current values and then shows a sharp rise. For practical experiments, a system quantum efficiency value is typically accepted if it does not exceed 1000 dark counts per second. In Figure 3.10b, it is clear that at the bias point where the dark count rate reaches the 1000 cps, the respective quantum efficiency is at ~25%.

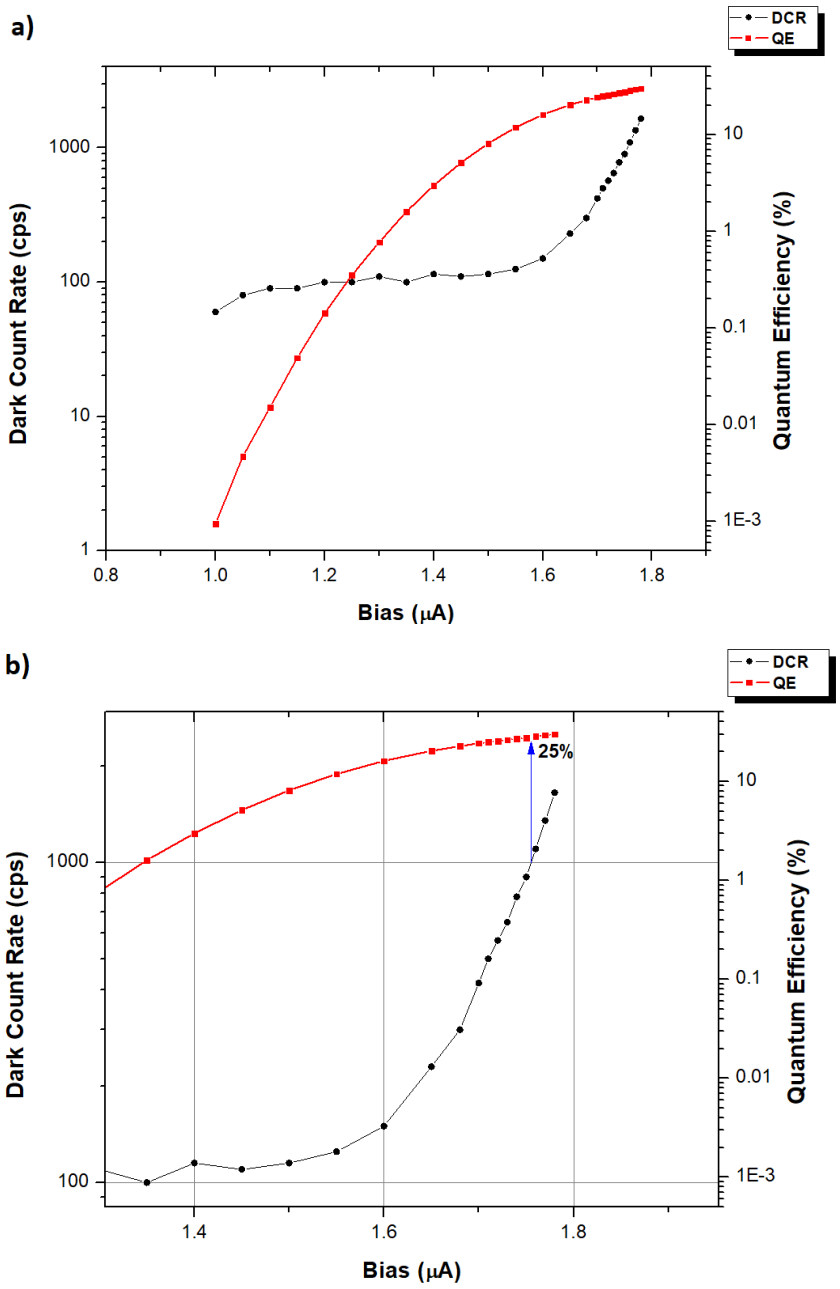

Figure 3.10. a) Quantum efficiency and dark count rate versus bias current plot of a SNSPD device and, b) same plot, zoomed in at bias points around 1000 dark counts per second with the corresponding quantum efficiency value.

The timing jitter (Δ_t), briefly explained in paragraph 2.4, gives the timing uncertainty between the detection of a single photon and the generation of an electrical output pulse in a practical system. Measurement of the timing jitter of a detector gives timing resolution information such as the maximum count rate. The experimental setup for the acquisition of the timing jitter value is shown in

Figure 3.11. A femtosecond mode-locked fibre diode laser generating narrow optical pulses (KPhotonics CNT-1550-TK laser, 50 MHz repetition rate, centre wavelength λ = 1560 nm) is connected to a 90:10 beam splitter. The 10% optical output is coupled to an InGaAs photodiode (Thorlabs, DET08CFC InGaAs, λ = 800-1700 nm, <70 ps rise time). The input light detected by the photodiode generates an electrical output pulse sent to the SYNC port of a TCSPC module. The 90% optical output of the beam splitter sends the light through two programmable optical attenuators so that the pulses are attenuated to a single-photon regime. The attenuated light is then detected by the SNSPD and an electrical output signal is sent to the timing (input) port of the TCSPC card. The TCSPC card is a PicoQuant PicoHarp 300 capable of recording pulses within a 4 ps time bin. Recording the sync signal pulses and the input signal pulses from the SNSPD, a histogram is formed and from the Gaussian fit on the histogram the FWHM timing jitter is extracted. Example of the histogram generated and the FWHM value was shown earlier in § 2 (Figure 2.4).

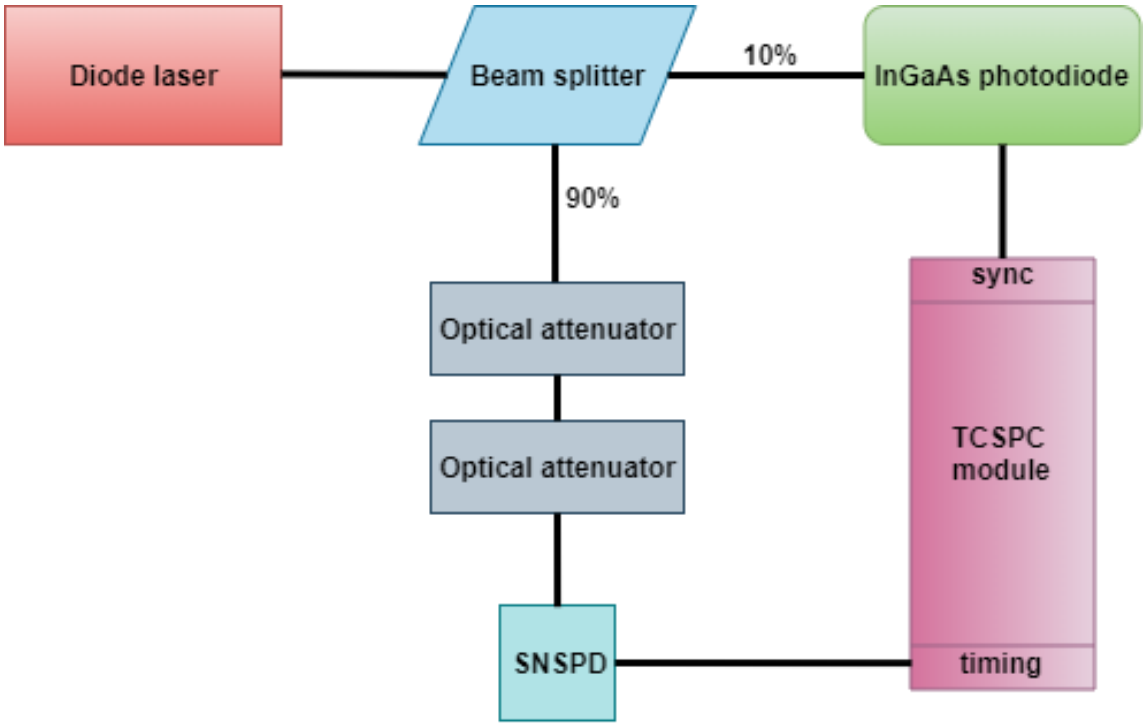

Figure 3.11. The apparatus for the acquisition of the timing jitter of a SNSPD.

3.4.2 Single photon avalanche photodiode

The SPAD used for the detection of singlet oxygen luminescence is a commercial ID230 InGaAs SPAD from IDQuantique. The operation of SPAD and its optical and timing characteristics were discussed in paragraph 2.4.2. The SPAD operates in a free-running mode and with the help of a Peltier cooler it can be cooled down to 183 K in order to minimize the dark count rate. The overall detector active area is 125 μm in diameter, split in half and fibre-coupled to two 62.5 μm multimode fibres. The SPAD unit connects to a PC and through the IDQ software the user can tune the SPAD's dead time and set the operation temperature to either -50 ºC, -70 ºC or -90 ºC, and the quantum efficiency to 10%, 15%, 20% or 25%. Depending on the chosen quantum efficiency point, the timing jitter of the device can be as low as 180 ps FWHM. The operation wavelength of InGaAs SPADs ranges from 0.9 μm – 1.7 μm, which makes it ideal for singlet oxygen luminescence experiments, offering high detection efficiencies in the desired 1270 nm and 1590 nm wavelengths. Figure 3.12 is reproduced from IDQ's ID230 datasheet, showing the quantum efficiency over the whole wavelength operation region. When operation efficiency at 1550 nm is set to 25%, the corresponding efficiency at 1270nm is roughly at 29%.

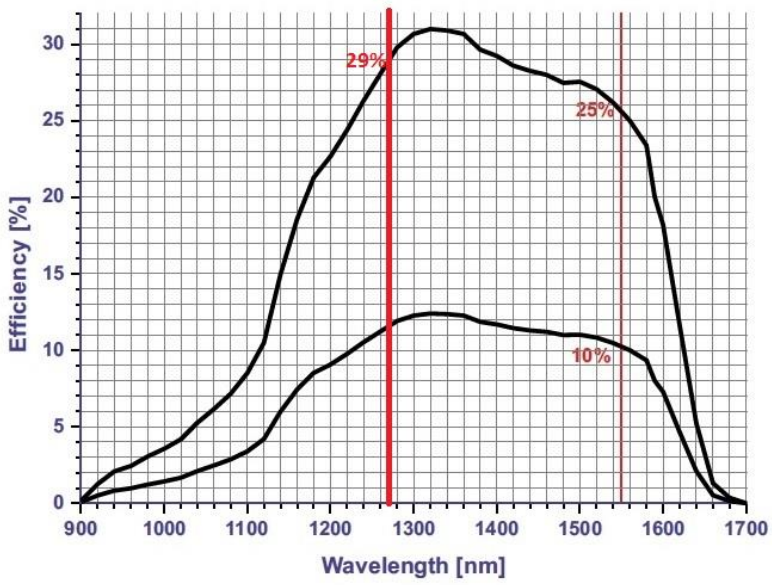

Figure 3.12. ID230 InGaAs SPAD quantum efficiency versus wavelength. Maximum efficiency at 1550 nm is 25% and at 1270 nm is 29%. Reproduced from [175].

The SPAD underwent further characterization in terms of quantum efficiency and dark count rate at different operation temperatures and over a wavelength range. The dead time of the SPAD was always set to 42 μs to match the histogram time defined by the laser repetition rate. The quantum efficiency from 1340 nm up to 1650 nm comparison between the three different operation temperatures is shown in Figure 3.13, while the dark count rate for all four QE values and operation temperatures is shown in Table 3.2. As expected, the lower the temperature SPAD is cooled at, the lower the dark count rate. This means that cooling the SPAD at –90 °C the dark count rate is significantly reduced compared to –50 °C and –70 °C and is optimum temperature. Dark count rate is also affected by the quantum efficiency point as for higher quantum efficiency values; the device is biased at higher voltages leading to increased dark counts. Therefore, setting the SPAD's quantum efficiency at the maximum value of 25%, may give higher detection sensitivity but at the cost of the increased dark count rate. However, in most cases, the dark count rate at 25% QE is still low enough and with strong luminescence signal the SNR is not greatly affected.

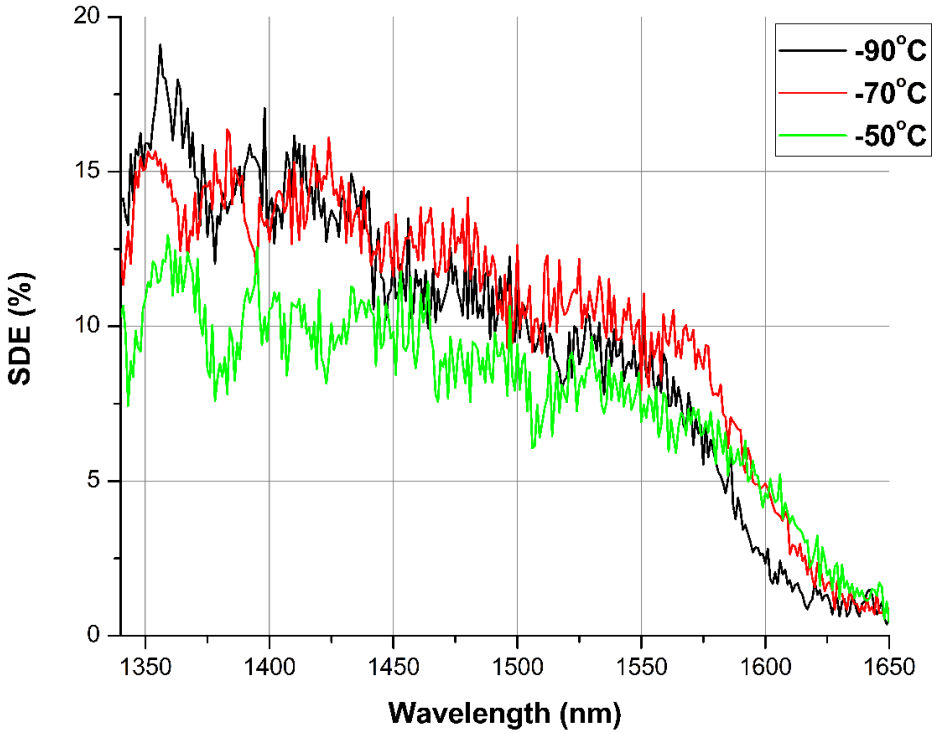

Figure 3.13. Quantum efficiency scan from 1340 nm to 1650 nm for all three SPAD temperatures.

Quantum efficiency	Dark Count Rate (cps) at stated temperature		
	-50 ºC	-70 ºC	-90 ºC
10%	731.1	76.4	11.2
15%	1513.3	171.1	27.7
20%	-	366.7	52.3
25%	-	558.9	80.5

Table 3.2. Dark count rate in cps for all SPAD's operation temperatures and quantum efficiencies. SPAD operating at -50 ºC was unable to operate biased at high values.

By looking at Figure 3.13, the SPAD's quantum efficiency operating at -70ºC is very close to that of -90 ºC. However, the dark count rate at -90 ºC is much lower than that at -70 ºC making the former the obvious selection for the experiments that followed. At -50 ºC, the dark count rate is much higher even when the selected quantum efficiency at 1550 nm is 10% or 15%. Operation at 20% and 25% could not be achieved at -50 ºC. In Figure 3.14, the default quantum efficiencies are compared over the same wavelength range for each temperature point. The actual quantum efficiencies at 1550 nm are very close to the expected as indicated by the default quantum efficiency values. The actual quantum efficiency trend is also similar to the one provided by the company with the highest peak being around 1350 nm. Based on that, it is safe to assume that the maximum quantum efficiency that can be achieved at 1270 nm is about 29-30%. With these quantum efficiency values at 1270 nm, along with the very low dark count rate and the big collection area offered by the size of the chip coupled to a multimode fibre, the SPAD is a very good choice for singlet oxygen luminescence experiments.

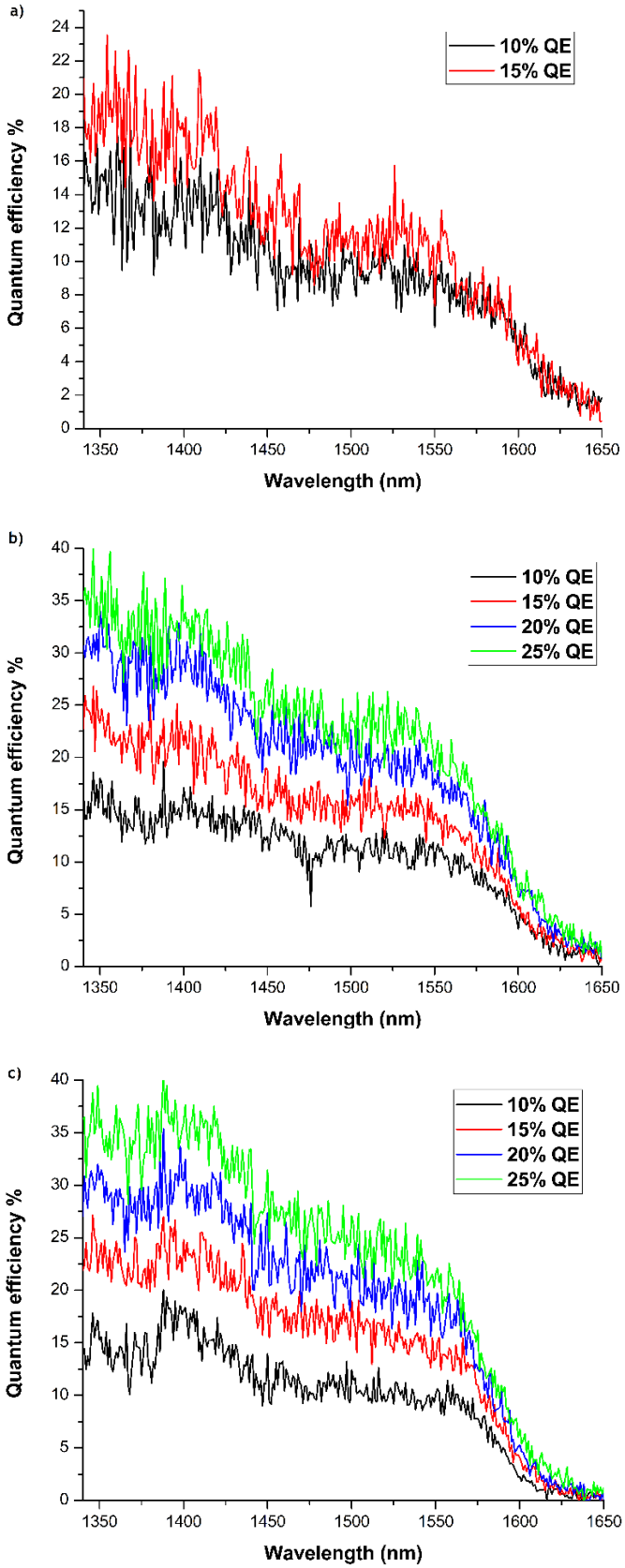

Figure 3.14. Quantum efficiency scans from 1340 nm to 1650 nm wavelength with SPAD's default QE at 1550 nm set to 10%, 15%, 20% and 25%. Operation temperature is set at a) -50 ºC, b) -70 ºC and, c) -90 ºC.

3.5 TCSPC Module

The TCSPC module is a PicoQuant PicoHarp 300 card with a single input channel. The supercontinuum laser is connected to the sync channel of the TCSPC card and the single photon detector to the timing channel. While running in the histogrammer mode, the card correlates signals from the laser and the detector and generates histograms proportional to the laser's repetition rate. Therefore, with the supercontinuum laser's repetition rate of ~24 kHz, the histograms generated are in a 42 µs time window. Additionally, the probability of a detection event has to be kept low compared to the excitation rate (typically below 5%) to avoid pulse pile-up effects. Thus, with the supercontinuum laser running steadily at 24 kHz, the overall count rate needs to be up to 1.2 kHz. The bin width of the histogram can be adjusted and can be as small as 4 ps. Small bin widths increase the curve resolution but as less counts are recorded per bin, the intensity of the bins is much smaller and may lead to less distinguishable shapes. An example histogram with bin resolution at 65 ns and acquisition over 60 seconds (646 bins) is shown in Figure 3.15.

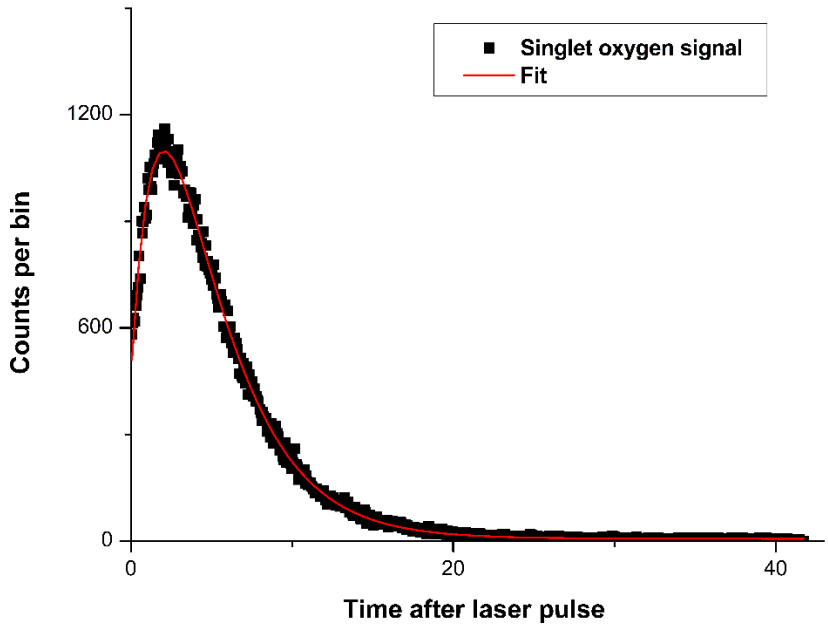

Figure 3.15. Histogram generated over 60 seconds of acquisition time with 65536 ps bin width size.

The biexponential decay curves arising from the singlet oxygen signal detected are fitted using a singlet oxygen equation involving the two lifetimes, the singlet oxygen lifetime, and the photosensitizer triplet state lifetime. The fitting of the decay curves allows the extraction of the two lifetime values. The formula used to best fit the data set of the recorded singlet oxygen signal is:

$$A * \frac{t_2}{t_1 - t_2} * \left(e^{-\frac{t+B}{t_1}} - e^{-\frac{t+B}{t_2}} \right) + C \qquad (30)$$

where A is the amplitude, t_1 and t_2 correspond to the two lifetime values τ_Δ and τ_T, and C a constant. The iteration algorithm used to minimize the problems in the fitting is the Levenberg-Marquardt algorithm that is commonly used to solve non-linear least squares problems for non-linear curve fitting. All lifetimes extracted in the singlet oxygen data results presented in the following chapters are extracted following the fitting described using the formula above.

Chapter 4 – 1270 nm and 1590 nm singlet oxygen luminescence measurements of photosensitizer solutions

4.1 Introduction

Lately, in clinical applications, such as Photodynamic Therapy, techniques like singlet oxygen luminescence dosimetry are of strong interest. Efficient detection of singlet oxygen's signature and properties has been a subject of experimental investigation over recent decades. However, detection of singlet oxygen's luminescence in the NIR has been a challenging task due to its weak and of low probability emission. Recent advances in the single photon detection systems have enabled the engineering of sophisticated setups that greatly increase the efficiency and practicality in singlet oxygen detection. Single photon detectors, such as SNSPDs and semiconductor SPADs (described in § 3), offer unparalleled detection efficiency while as fibre-based systems they provide solution to various clinical scenarios with limited geometric collection efficiency.

In this chapter, singlet oxygen luminescence measurements are presented using the experimental setups described in the previous chapter and a variety of photosensitizers, including an FDA clinically-approved drug. § 4 starts with a brief overview on the selected photosensitizers (their structure, type, chemical and optical properties) and follow detailed measurements on the singlet oxygen luminescence in the 1270 nm and 1590 nm wavelength by various photosensitizer solutions. Experimental data on the intensity of the singlet oxygen signal and the lifetimes of singlet oxygen and photosensitizer's triplet state are presented, as well as data utilizing different bandpass filters around the 1270 nm and 1590 nm wavelength and singlet oxygen quenching agents, to validate the authenticity of the singlet oxygen signature. While the 1270 nm emission is that of highest importance and practical use, the detection of singlet oxygen's 1590 nm emission and time resolved measurements of this even weaker decay denote a brand-new singlet oxygen dataset. These measurements are of great interest regarding the photochemical nature of singlet oxygen and its decay pathways and kinetics.

4.2 Chemicals

During this project multiple photosensitizers were used to generate singlet oxygen molecules and help study its behaviour in the different microenvironments. The initial sensitizer selection was a standard photosensitizer dye, Rose Bengal, known for its high quantum yield in the singlet oxygen generation. Later, with the implementation of the versatile supercontinuum laser and its tunable single line filter, the selection of different wavelengths in the visible enabled the excitation of other photosensitizers, such as the Eosin Y, the Methylene Blue, and the Zinc Phthalocyanine. A clinically-approved photosensitizer under the trade name Visudyne was also tested in solution to give a more plausible approach. All these photosensitizer dyes were used in solutions. Solvents like distilled water (H_2O), ethanol (C_2H_5OH), methanol (CH_3OH), acetone (C_3H_6O) and dimethyl sulfoxide (DMSO - C_2H_6OS) were used to prepare PS solutions with different chemical properties and therefore different microenvironments which affect the generation and deactivation of singlet oxygen. Moreover, solutions using deuterium oxide (D_2O) were prepared, tested, and compared to other solutions as this deuterated isotope of water with different nuclear, physical, and chemical properties is known to greatly affect the singlet oxygen lifetime. All solutions were prepared by simple mixing and stirring in room temperature. For all the singlet oxygen solution experiments, a 4 ml quartz Hellma absorption cuvette was used filled with 3.5 ml of photosensitizer solution.

Verteporfin is a benzoporphyrin derivative and a clinically approved sensitizer for PDT treatments with the trade name Visudyne. The chemical formula is $C_{41}H_{42}N_4O_8$ with 1437.6 g/mol molecular mass. Verteporfin has a very broad absorption spectrum as shown in Figure 4.1a with strong peaks in the UV and visible. The targeted excitation wavelength in PDT treatments is at 689 nm, which is towards the NIR where light penetration in tissue is significantly deeper than shorter wavelengths [233]. The Visudyne solution for the SOLD experiments was prepared with methanol.

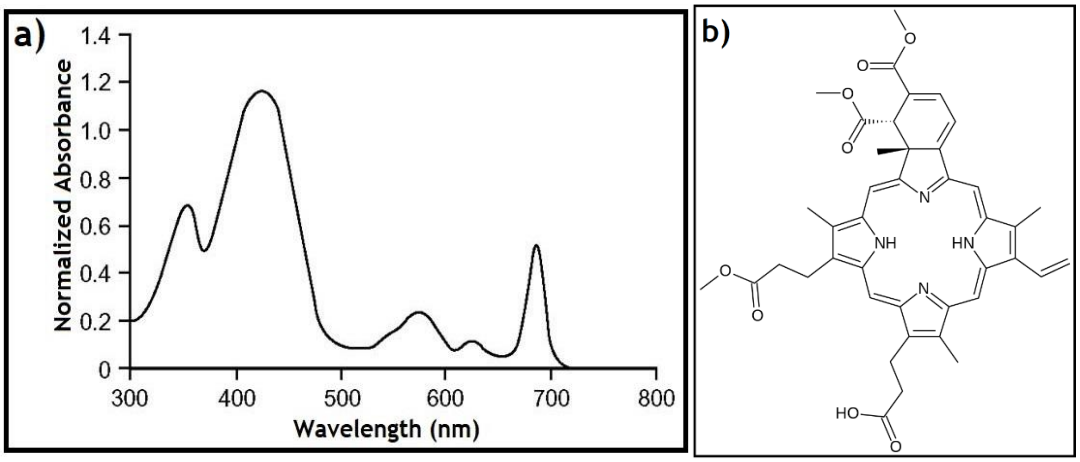

Figure 4.1. a) Absorption spectrum and b) Chemical formula of Verteporfin. From [234]

Rose Bengal is a 4,5,6,7-tetrachloro 2′,4′,5′,7′-tetraiodo derivative of fluorescein, an organic dye molecule in the xanthene class. Its chemical formula is $C_{20}H_2Cl_4I_4Na_2O_5$ with 1017.64 g/mol molecular mass. Rose Bengal has high triplet state energy and a very high quantum yield, in the order of 75% [22, 235]. Rose Bengal's peak excitation wavelength is around 550 nm, as shown in Figure 4.2a [236]. Rose Bengal's high singlet oxygen quantum yield and great solubility established it as the benchmark photosensitizer of this project. Rose Bengal solutions were made using distilled water, deuterated water, ethanol, methanol, acetone and DMSO.

Eosin Y is also a xanthene dye, 2′,4′,5′,7′-Tetrabromofluorescein**.** Chemical formula is $C_{20}H_6Br_4Na_2O_5$ with 647.89 g/mol molecular weight. Eosin Y has a quantum yield of 57% and a high excitation peak wavelength at 522 nm [22, 237]. The molecular structure and absorption spectrum of Eosin Y is shown in Figure 4.2b. Eosin Y was dissolved with distilled water, ethanol, and methanol.

Methylene Blue, also known as methylthionimium chloride, is a phenothiazinium dye with broad absorption spectrum from around 500 nm to 700 nm and a quantum yield of 52% [22, 235]. Its molecular formula is $C_{16}H_{18}ClN_3S$ with 319.85 g/mol molecular weight. The molecular structure of Methylene Blue and its broad absorption spectrum is shown in Figure 4.2c [238]. Solutions were prepared by mixing with distilled water, ethanol, methanol and DMSO. The selected excitation wavelength for the Methylene Blue solution was at 660 nm.

Zinc Phthalocyanine belongs to the big group of Metallophthalocyanines (MPcs) with chemical formula $C_{32}H_{16}N_8Zn$ with 577.91 g/mol molecular weight. Zinc Phthalocyanine (ZnPc) has a long triplet state lifetime with quantum yields reaching 53% [239-242]. ZnPc has a strong absorption peak around 650 nm as shown in Figure 4.2d [243]. ZnPc powder was only mixed with DMSO.

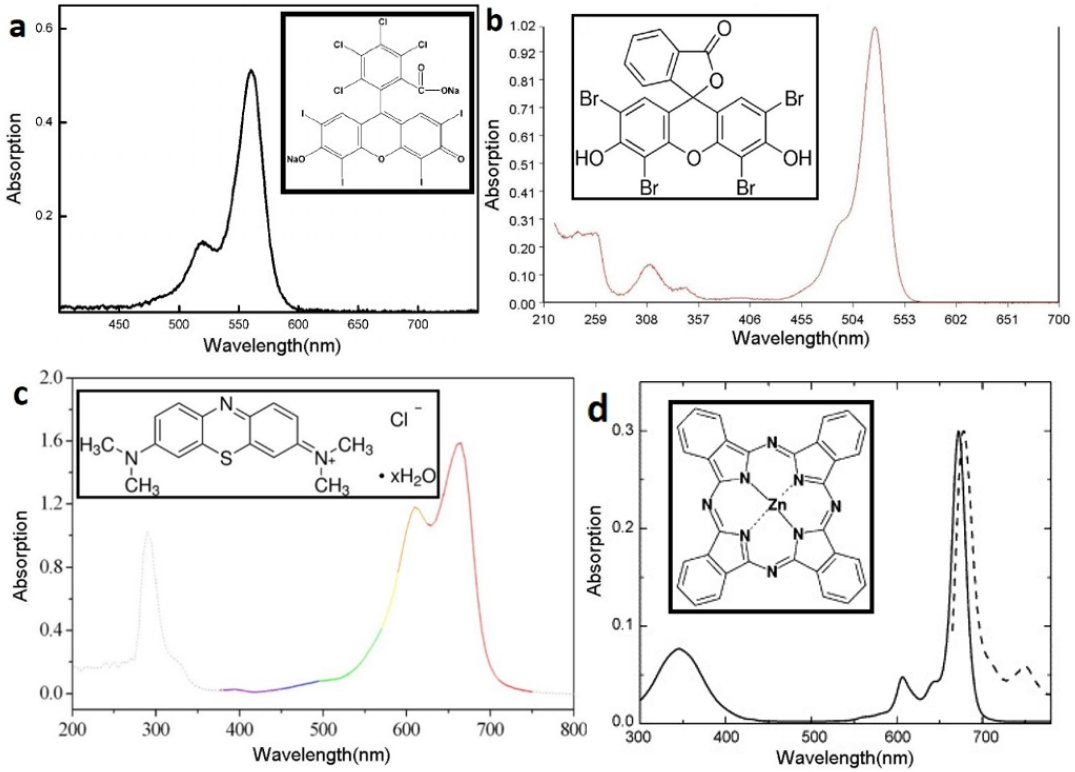

Figure 4.2. Absorption spectra and molecular structures of a) Rose Bengal, b) Eosin Y, c) Methylene Blue and, d) Zinc Phthalocyanine [236, 238, 241].

4.3 Singlet oxygen luminescence detection

The SOLD technique is based on the time resolved phosphorescence detection (TRPD) of singlet oxygen. It is a useful spectroscopic tool to monitor directly the $^1O_2$ phosphorescence transitions. TRPD gives a variety of information on the shape and intensity of the detected phosphorescence signal determined by multiple parameters. The production of singlet oxygen molecule and decay in a system is described in § 2 in equations 1 through 19. These equations lead to the conclusion that the amount of the generated singlet oxygen per absorbed photon

is determined by the ability of the photosensitizer molecules to get to the excited triplet states, the ability of the oxygen to trap these PS triplet state molecules and the efficiency of the energy transfer from the ^{3}PS to the ground state oxygen in order to excite it and produce singlet oxygen. These three factors also determine the kinetics and intensity of the singlet oxygen phosphorescence signal. The experimental detection of the $^1O_2$ phosphorescence signal derives from equation (30) and can be described in the following equation:

$$S_t = S_0 \times \frac{\tau_\Delta}{\tau_\Delta - \tau_T} \left[e^{-\frac{t}{\tau_\Delta}} - e^{-\frac{t}{\tau_T}} \right]$$

Where: $S_0 = \kappa k_{\Delta,R} [^1PS^*]_0 \times \Phi_\Delta$, τ_T is the PS triplet state lifetime and, τ_Δ is the singlet oxygen lifetime.

The singlet oxygen phosphorescence signal is defined by the S_0, τ_T and τ_Δ. In S_0, 'κ' is the instrument dependent factor, such as the detector single-photon detection efficiency and the optical collection efficiency of the system. By increasing 'κ' through increase in the sample absorbance and/or increase of the light source intensity can lead to an increase of the S_0, but not indefinitely as every setup has an optimum sample absorbance. The $k_{\Delta,R}$ is the singlet oxygen radiative rate constant and depends strongly on the electrical properties of the photosensitizer, such as the polarizability. $[^1PS^*]_0$ represents the initial concentration of all the PS excited states produced by the light pulse. Φ_Δ is the quantum yield of the singlet oxygen production. This $^1O_2$ quantum yield depends on a) the PS triplet state quantum yield Φ_T (according to eq. 18), determined by the electronic structure of the photosensitizer but can also be affected by other ^{1}PS* quenchers, the fraction of ^{3}PS* trapped by oxygen $P_T^{O_2}$, which actually reflects a competition between the ^{3}PS* natural decay and oxygen quenching. High oxygen concentrations and low-viscosity solvents mean high $P_T^{O_2}$ and, c) the efficiency of energy transfer from triplet state sensitizer molecules to ground state oxygen molecules, $f_{T,\Delta}^{O_2}$, which is determined by the electronic structure of the photosensitizer and can be affected by the polarity of the solvent.

The photosensitizer triplet state lifetime τ_T is also included in the $^1O_2$ phosphorescence signal. Photosensitizer's triplet state quenchers affect the shape of the signal. Oxygen is a very efficient triplet state quencher, so PS triplet state lifetime is decreased when oxygen concentration is higher, as shown in eq. 15. ^{3}PS lifetime is also affected by the solvent viscosity and the oxygen solubility. This leads to smaller τ_T values for organic solvents (in the nanoscale region), while in water τ_T is typically around 2 μs. By extracting τ_T kinetic information can also be gain on its precursor ^{3}PS*.

The singlet oxygen lifetime τ_Δ is mostly affected by the presence of quenchers. Solvents assist in the deactivation of singlet oxygen through electronic to vibrational energy transfer and that makes τ_Δ extremely solvent sensitive. Additionally, as mentioned in § 2, deuterated solvents are proven to lengthen the singlet oxygen lifetime.

4.3.1. 1270 nm measurements

Singlet oxygen measurements at 1270 nm wavelength were carried out using a 1200 nm long pass filter and a band pass filter centred at 1270 nm ± 4 nm (FWHM Bandwidth 20 nm ± 4 nm). To validate that the recorded signal is actually coming from the singlet oxygen decay, four more band pass filters were used bracketing the central signal at 1270 nm, at 1200 nm, 1240 nm, 1300 nm, and 1340 nm wavelength. As the 1270 nm singlet oxygen emission is quite narrow, signal from all the other band pass filters should be very weak and tend to zero as we move further from the 1270 nm wavelength. As shown in Figure 4.3, the singlet oxygen signal sensitized by Rose Bengal is strong with the 1270 nm band pass filter in place. With the 1240 nm and 1300 nm band pass filters there is still some signal coming through to the detector, which can be explained taking into consideration that $^1O_2$ emission and band pass filtering have a finite bandwidth. That means that the $^1O_2$ signal and the BP wavelength transmittance may overlap even in a small percentage and lead to some optical signal coming through the apparatus and being recorded by the detector. The 1200 nm and 1340 nm BP filters as expected

block all the singlet oxygen signal. Thus, it is reasonable to infer that the detected photons for the 1270 nm measurements come from the $^1\Delta_g \rightarrow {}^3\Sigma_g^-$(v=0) transition.

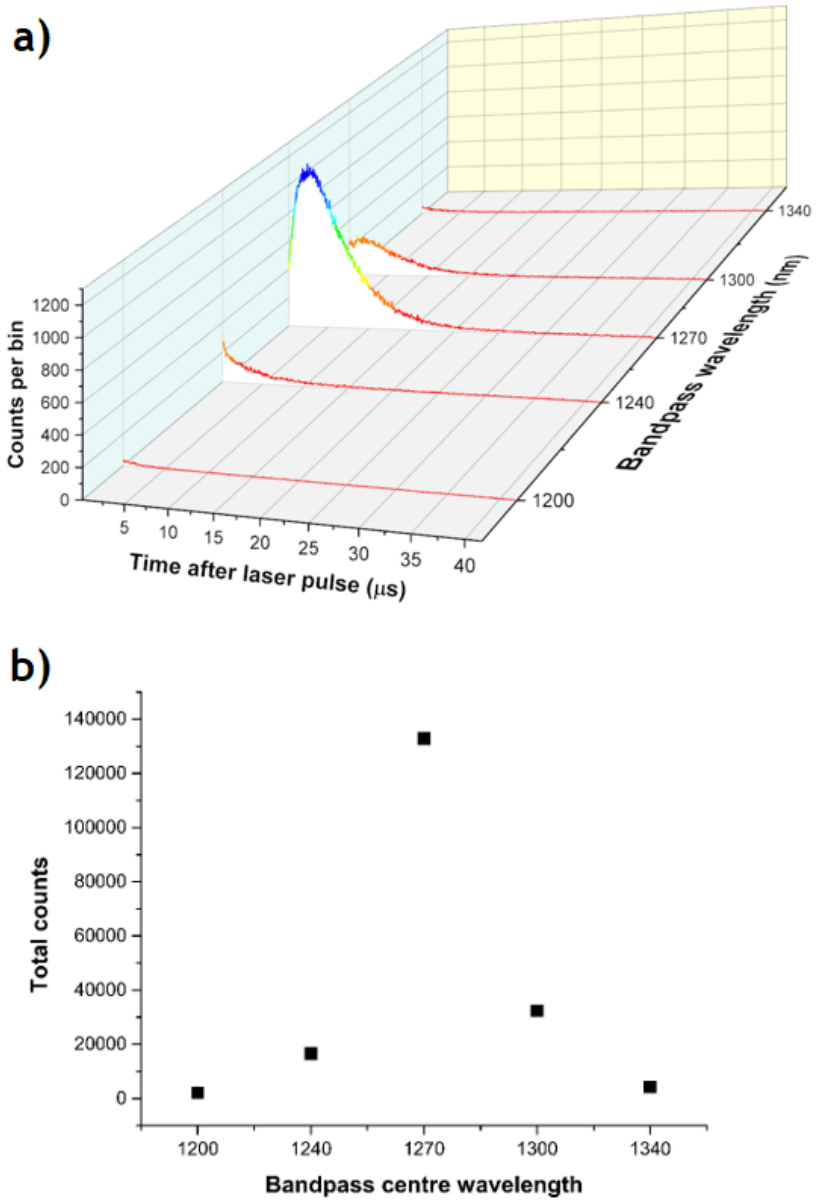

Figure 4.3. a) 3D plot comparing $^1O_2$ luminescence from 100 μg/ml of Rose Bengal in deuterated water with various BP optical filters and, b) a comparison plot of total counts integrated under the histograms versus BP optical filter centre wavelength. Acquisition time is 60 seconds and SPAD's detection efficiency set to 10%.

Three different photosensitizers were mixed with distilled water, Rose Bengal, Eosin Y and Methylene Blue. All three have different peak excitation

wavelengths, singlet oxygen quantum yields and optical properties. In Figure 4.4, the three solutions are compared in 180 second acquisition histograms and at 100 μg/ml mass concentration. The 100 μg/ml mass concentration is translated to 98.27 μM for Rose Bengal, 312.65 μM for Methylene Blue and, 154.35 μM for Eosin Y.

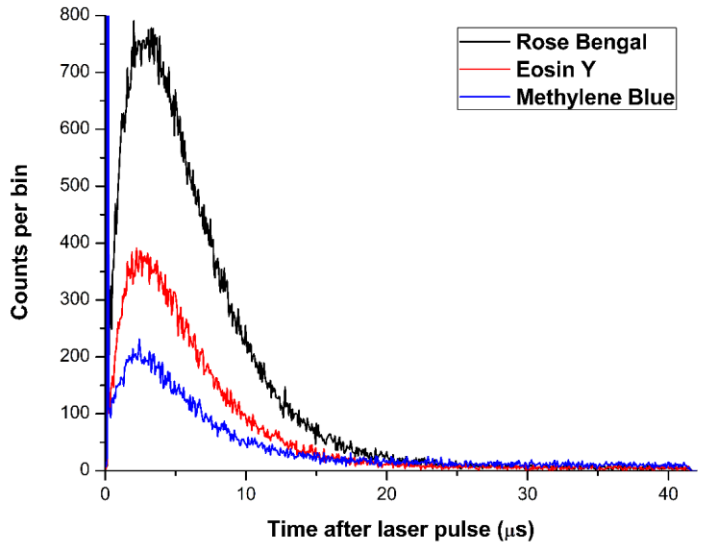

Figure 4.4. 180 second histograms comparing Rose Bengal, Eosin Y and Methylene Blue in distilled water at 100 μg/ml mass concentration. SPAD detector was set to -90 °C, 10% QE and 42 μs dead time.

Rose Bengal seems to be the more efficient photosensitizer producing the most $^1O_2$ signal from the three PSs. This was expected as Rose Bengal has the highest singlet oxygen quantum yield of all three, even though the molar concentration is lower. Next is Eosin Y and then Methylene Blue. By fitting the acquired curves with equation (30), the photosensitizer triplet state lifetime and the singlet oxygen lifetime are extracted and can be seen in Table 4.1.

Distilled water solution	**Rose Bengal**	**Eosin Y**	**Methylene Blue**
τ_T **(μs)**	2.32±0.03	1.88±0.03	1.67±0.05
τ_Δ **(μs)**	3.52±0.03	3.59±0.02	3.73±0.03

Table 4.1. Triplet state lifetimes and singlet oxygen lifetimes for Rose Bengal, Eosin Y and Methylene Blue in distilled water.

Triplet state lifetimes are close to 2 μs, while the singlet oxygen lifetimes are ~3.5-4 μs long with all three values being close to each other. Singlet oxygen lifetime (τ_Δ) should be similar regardless the photosensitizer used in each measurement. The reason of having slightly different values outside the stated error is attributed to possible fluctuations in the concentration of the prepared photosensitizer solution. Singlet oxygen decay is in the microsecond range, a long-lived decay as predicted from the theory. PS triplet state lifetime is around 2 μs as expected in water solutions. In deuterated and organic solvents, singlet oxygen lifetime is expected to be even longer and PS triplet state lifetimes even shorter with solvents of different viscosity, oxygen concentration and oxygen solubility.

Note that at the beginning of the histogram of Figure 4.4, a very strong but short (nanosecond range) emission is seen. This emission can be a few thousands up to hundreds of thousands counts stronger than the actual singlet oxygen signal and is present in every acquisition. This sharp peak is translated to the strong fluorescence of the photosensitizer emission, either emitting in the spectral window of 1270 nm or different wavelengths that pass through the optics. This emission is different depending on the experimental setup. Especially solutions made of Methylene Blue have a very strong luminescence peak which lead to very high count rates and therefore pile-up effects that distort the final shape. For that reason, in some cases the optical power coming from the supercontinuum laser is decreased to allow the setup to operate below the pile-up threshold point. Also, for solutions that exhibit strong $^1O_2$ signal, the SPAD detector is set to the lowest possible quantum efficiency value (10%) in order to decrease the input counts. For the following plots, this PS luminescence peak may be removed in order to simplify data analysis, enabling better curve fitting and more accurate lifetime extraction.

Apart from distilled water, two more polar protic solvents were tested, ethanol and methanol. These organic solvents have different properties from distilled water, so major differences in lifetimes were expected to be seen. Singlet oxygen signal from solutions by mixing ethanol and methanol with Rose Bengal, Eosin Y and Methylene Blue are compared in Figure 4.5.

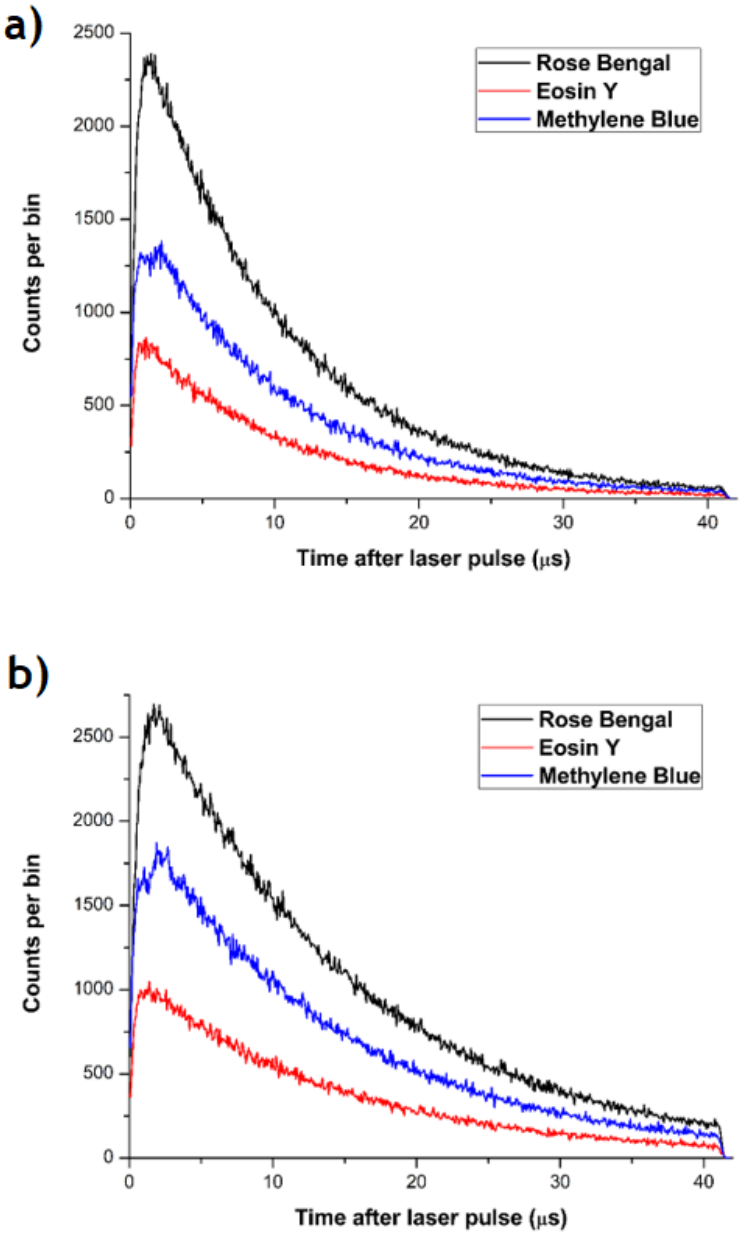

Figure 4.5. 180 second histograms comparing Rose Bengal, Eosin Y and Methylene Blue in a) methanol and, b) ethanol at 100 μg/ml mass concentration. SPAD detector set to -90 ºC, 10% QE and 42 μs dead time.

Under the same experimental conditions, the acquired singlet oxygen signal from these solutions is clearly stronger with much higher count rate. The solution with Rose Bengal is once more the one that stands on top of the other two in terms of detected counts, despite its lower concentration compared to the other two dyes. Regarding the other two solutions, the Methylene Blue with ethanol and methanol seems to generate more singlet oxygen molecules than the one with

Eosin Y, something that in the case of the water solutions was the other way around. Singlet oxygen generation is affected by the PS triplet state lifetime which in the case of organic solvent the PS triplet state lifetime is longer for Methylene Blue, in contrast to the distilled water solutions where Eosin Y triplet state lifetime is longer. The extracted lifetimes are close to theoretical values. Triplet state lifetime for all solutions is of a few hundred nanoseconds long, unlike the microsecond range lifetimes of PS solutions with distilled water. The $^1O_2$ lifetimes are significantly longer with values close to 10 μs for methanol solutions and around 14-15 μs for ethanol solutions. Lifetime values for all the solutions can be seen in Table 4.2. It is clear that both lifetimes are heavily affected by solvent properties.

Methanol solution	**Rose Bengal**	**Eosin Y**	**Methylene Blue**
τ_T **(μs)**	0.38±0.01	0.26±0.03	0.46±0.03
τ_Δ**(μs)**	9.78±0.004	9.65±0.007	10±0.008

Ethanol solution	**Rose Bengal**	**Eosin Y**	**Methylene Blue**
τ_T **(μs)**	0.49±0.02	0.31±0.03	0.59±0.03
τ_Δ**(μs)**	14.67±0.01	14.53±0.01	14.5±0.01

Table 4.2. Triplet state lifetimes and singlet oxygen lifetimes for Rose Bengal, Eosin Y and Methylene Blue in methanol (top) and ethanol (bottom).

Subsequently, two more solvents were used, dimethyl sulfoxide and acetone. These solvents are polar aprotic meaning they have high polarity which will make them more reactive and can dissolve photosensitizers that 'common' solvents cannot. Additionally, it is worth comparing their ability to generate singlet oxygen and compare the overall signal and lifetimes with the other solutions. Mixing with DMSO three solutions were prepared using Rose Bengal, Methylene Blue and Zinc Phthalocyanine, while with acetone only Rose Bengal solution was prepared. Acetone is supposed to enhance the singlet oxygen signal showing much longer singlet oxygen lifetime. Acetone was also picked as a solvent to assist in the testing of singlet oxygen quenching agents like ß-carotene which

is presented later on. A comparison plot between RB, MB and ZnPc in DMSO is shown in Figure 4.6, as well as a histogram of RB in acetone. Histograms are acquired over 3 minutes at 100 μg/ml mass concentration in order to compare to the rest of the solutions. 100 μg/ml mass concentration for ZnPc is converted to 173.04 μM.

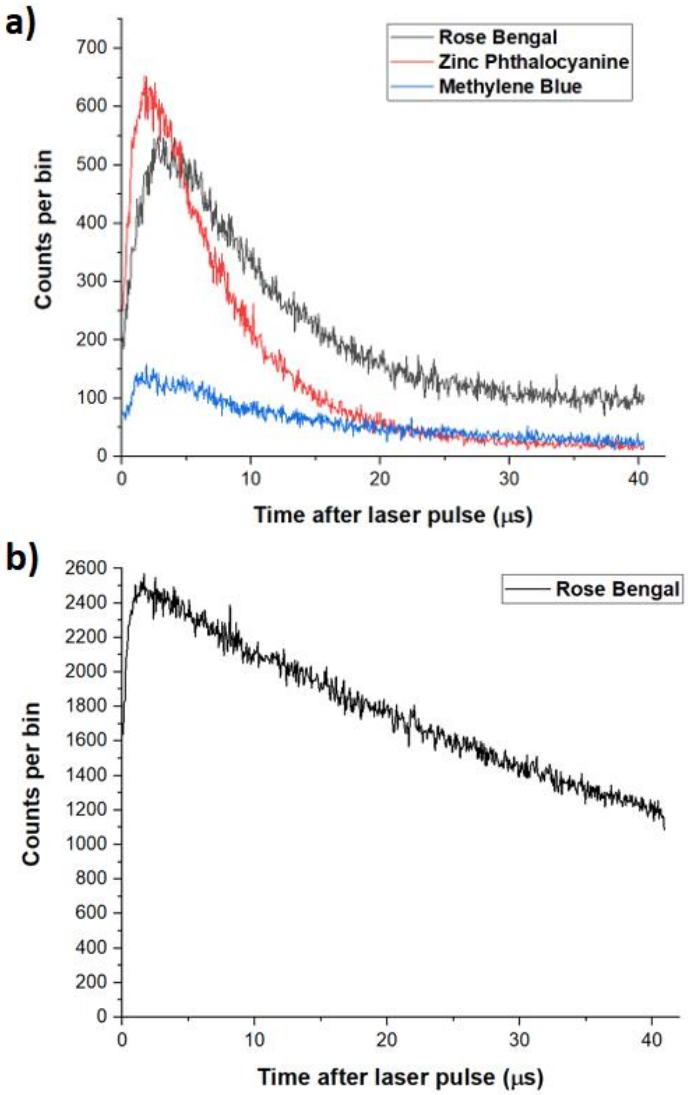

Figure 4.6. a) 180 second histograms comparing Rose Bengal, Zinc Phthalocyanine and Methylene Blue in DMSO at 100 μg/ml mass concentration and, b) 180 second histogram with Rose Bengal in acetone at 100 μg/ml mass concentration. SPAD detector set to -90 ºC, 10% QE and 42 μs dead time.

Signal intensity by ZnPc in DMSO appears to be greater than that achieved in Rose Bengal and Methylene Blue but by looking at the shape of the emission

curve it seems that singlet oxygen lifetime generated by ZnPc in DMSO is much shorter. Methylene Blue's signal in DMSO appears to be weak but the long tail of the curve indicates a long singlet oxygen lifetime. The Rose Bengal in acetone solution seems to produce not only strong $^1O_2$ signal, but also a very long lifetime. All lifetimes extracted from Figure 4.6 curves are grouped and presented in Table 4.3. While solutions in DMSO generate singlet oxygen signal weaker and similar to distilled water solutions, the lifetimes of these decays are closer to the solutions with ethanol and methanol. The PS triplet state lifetimes of the DMSO solutions, though, are in the microsecond region in comparison to solutions with ethanol and methanol which are almost an order of magnitude shorter. The Rose Bengal in acetone, however, appears to be very efficient in generating singlet oxygen molecules with long lived decay luminescence. The signal intensity is high, similar to the one produced by Rose Bengal in ethanol and methanol, but the singlet oxygen lifetime is much longer at 48.93 μs. On the other hand, the PS triplet state lifetime of RB in acetone is short in the nanosecond region at ~580 ns, very similar to the ethanol solution.

DMSO solution	**Rose Bengal**	**Zinc Phthalocyanine**	**Methylene Blue**
τ_T **(μs)**	1.76±0.04	1.08±0.02	1.64±0.08
τ_Δ**(μs)**	8.55±0.02	6.13±0.01	11.19±0.05

Acetone solution	**Rose Bengal**
τ_T **(μs)**	0.58±0.14
τ_Δ**(μs)**	48.93±0.13

Table 4.3. Triplet state lifetimes and singlet oxygen lifetimes for Rose Bengal, Zinc Phthalocyanine and Methylene Blue in DMSO (top) and Rose Bengal in acetone (bottom).

Next, a solution with Rose Bengal mixed in deuterated water was prepared to test the effect of deuterated solvent in the generation and deactivation of singlet oxygen. A comparison of singlet oxygen counts by placing various band pass

filters at and around 1270 nm wavelength was made once more for validation reasons. In Figure 4.7a is shown the acquired signal of 500 μg/ml (about 500 micromolar concentration) Rose Bengal in deuterated water by changing only the band pass filter each time and 3D plotted and in Figure 4.7b a sum of the total counts recorded for each of the band pass filters is presented.

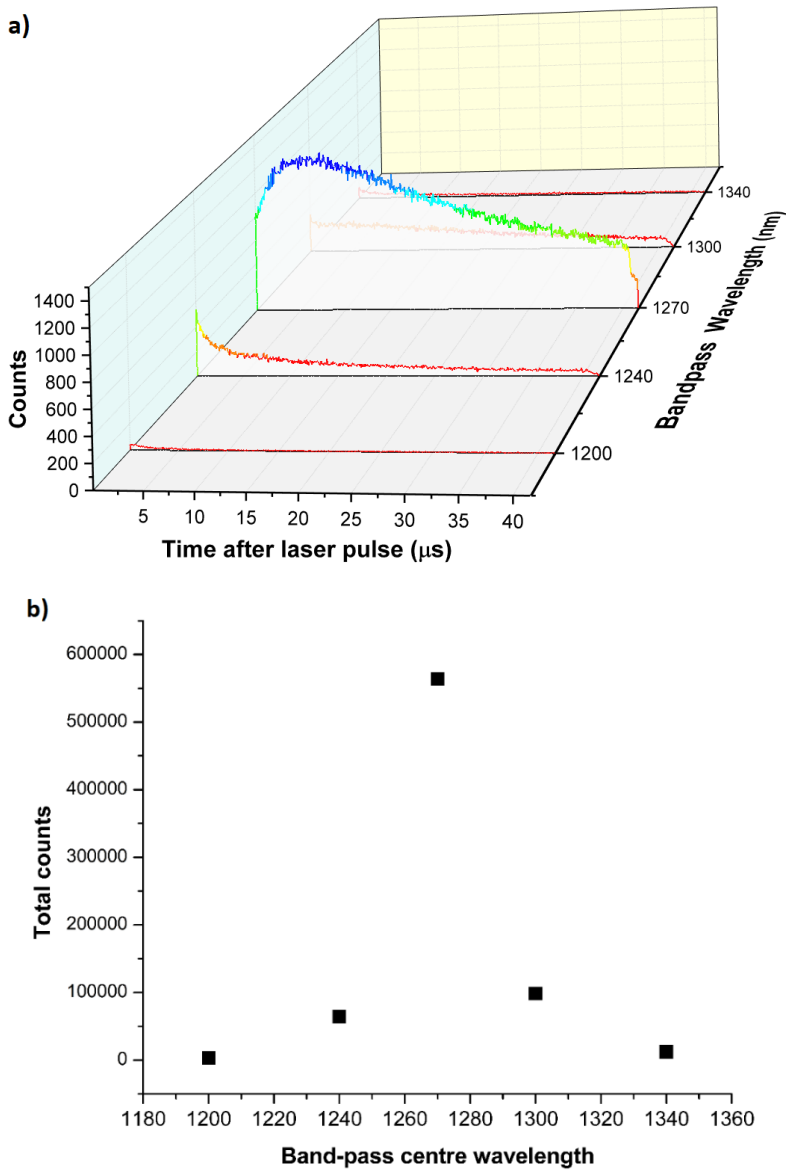

Figure 4.7. a) 3D plot comparing $^1O_2$ luminescence from 500 μg/ml of Rose Bengal in deuterated water with various BP optical filters and, b) a comparison plot of total counts integrated under the histograms versus BP optical filter centre wavelength. Acquisition time is 60 seconds and SPAD's detection efficiency set to 10%.

Similarly, a 100 μg/ml Rose Bengal in D_2O solution was prepared to compare luminescence signal and lifetimes. The shape of the curve is shown in Figure 4.8 and the lifetimes extracted are presented in Table 4.4. The most crucial comparison is between distilled water and deuterated water, pointing out the major effects of deuterated solvent in the generation of singlet oxygen. The signal intensity is much higher with the curve peak counting twice as many counts as in distilled water. The PS triplet state lifetime in heavy water is slightly shorter at 2.19 μs compared to 2.32 μs in distilled water. The major difference is expected in the singlet oxygen lifetime which is highly affected observing a 10-fold increase at 35.19 μs.

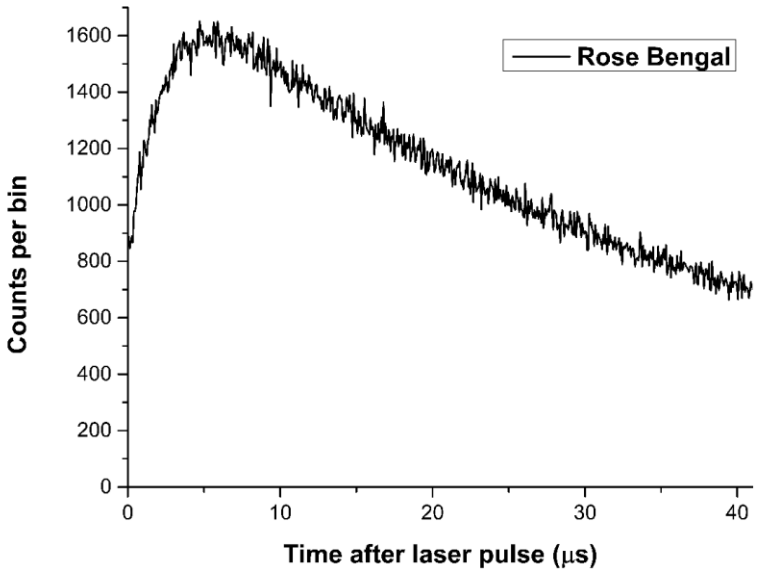

Figure 4.8. 180 second histogram with Rose Bengal in D_2O at 100 μg/ml mass concentration. SPAD detector set to -90 ºC, 10% QE and 42 μs dead time.

D_2O solution	**Rose Bengal**
τ_T (μs)	2.19±0.03
τ_Δ(μs)	35.19±0.06

Table 4.4. Triplet state lifetimes and singlet oxygen lifetimes for Rose Bengal in deuterated water.

Lastly, a solution of Visudyne in methanol was prepared at a standard concentration of 50 mg per 100 ml (500 μg/ml / 347.8 μM). Due to much weaker $^1O_2$ generation, Visudyne in methanol solution was kept at its initial concentration of 500 μg/ml so that a clear curve can be shown and proper fitted for the extraction of the two lifetimes, as shown in Figure 4.9. The engineering part of the experiment and the acquisition time of 180 seconds, though, were maintained intact so that only the one parameter (PS concentration) was changed. So, SPAD detector was cooled to -90 ºC with 10 % of quantum efficiency and 42 μs dead time.

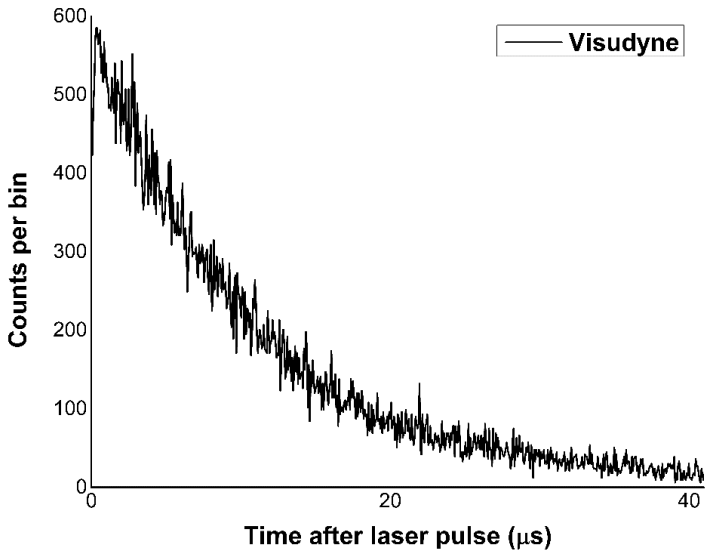

Figure 4.9. 180 second histogram with Visudyne in methanol at 500 μg/ml mass concentration. SPAD detector set to -90 ºC, 10% QE and 42 μs dead time.

methanol	**Visudyne**
τ_T **(μs)**	0.1±0.23
τ_Δ**(μs)**	10±0.01

Table 4.5. Triplet state lifetimes and singlet oxygen lifetimes for Visudyne in methanol.

Despite the fact that Visudyne's concentration is higher than the previous solutions presented above, the singlet oxygen lifetime of 10 μs is at close to the

singlet oxygen lifetimes from methanol solutions with Rose Bengal, Eosin Y and Methylene Blue. By comparing to the previous methanol solutions, the PS triplet state lifetime of Visudyne is also at the nanoscale range but slightly shorter at 100ns.

Concluding the comparison between the solutions used throughout the project, it is worth summing the registered singlet oxygen photon counts in each histogram. In Table 4.6 the total counts for each solution indicate the most efficient photosensitizer solution regarding the singlet oxygen generation capability. Most counts are detected when exciting Rose Bengal in acetone, followed by Rose Bengal in deuterated water and ethanol. Regarding the solvent effect on singlet oxygen, solutions that efficiently generate singlet oxygen molecules with long-lived luminescence are the most efficient, such as acetone, D_2O and ethanol which show long singlet oxygen lifetimes.

Photosensitizer	Solvent	Total counts
Rose Bengal	Distilled water	93.818
Eosin Y		43.707
Methylene Blue		27.340
Rose Bengal	Methanol	394.538
Eosin Y		135.786
Methylene Blue		239.083
Visudyne		92.307
Rose Bengal	Ethanol	617.612
Eosin Y		226.485
Methylene Blue		420.715
Rose Bengal	DMSO	136.840
Zinc Phthalocyanine		91.852
Methylene Blue		37.962
Rose Bengal	Acetone	1.112.940
Rose Bengal	Deuterated water	713.848

Table 4.6. Total singlet oxygen photon counts detected per 180 second histograms by all photosensitizer solutions.

Amongst the solvents, distilled water appears to be the least efficient. Solvent effect may have the biggest impact, but photosensitizer quantum yield also plays a role in the overall efficiency. Rose Bengal has the highest quantum yield amongst the photosensitizers used and that is depicted in the count difference from the rest photosensitizers.

The acquisitions presented so far are made with solutions of a specific mass concentration (100 μg/ml). This allowed the easy comparison between the samples at a concentration where singlet oxygen signal is quite strong. In real photodynamic therapy treatment scenarios, the actual photosensitizer concentration varies with the patient and the chosen type of photosensitizer. Typical dosages can vary from 0.075 mg/kg for meta-tetra(hydroxyphenyl)chlorin (mTHPC) up to 60 mg/kg for 5-aminolevulinic acid (ALA). The 100 μg/ml mass concentration is roughly translated to 126 mg/kg for organic solvents and 100 mg/kg for distilled water. Despite the fact that these photosensitizers are different and not applicable in treatments, the concentration is much higher. For that reason and for deeper understanding of the singlet oxygen behavior over the PS concentration, a follow-up experiment tests the singlet oxygen signal for various mass concentrations of the existing solutions. The initial concentration starts at 1 mg/ml down to 0.45 μg/ml for ethanol, methanol and DMSO solvents, while for distilled and deuterated water the initial mass concentration starts at 500 mg/ml down to 0.45 μg/ml. The mass concentration is reduced to half for each measurement, resulting in 12 or 11 acquisitions, respectively. This covers a broad concentration range from higher than typical concentration values down to a point that $^1O_2$ signal is almost vanished. The results are grouped by the photosensitizer type.

Starting with Rose Bengal, histograms are generated by solutions with distilled water, deuterated water, ethanol, methanol and DMSO. Unfortunately, histograms from solutions with Rose Bengal dissolved in acetone could not be efficiently acquired as acetone is a solvent with high evaporation rate, something that would alter the targeted concentration since each acquisition requires at least 1-2 minutes and also the fact that most concentration values would cause significant pile-up effects, distorting the output data. In Figure 4.10 are shown histograms comparing singlet oxygen luminescence signal from Rose Bengal in distilled water and deuterated water in decreasing concentrations from 500 μg/ml

to 0.45 µg/ml. For Rose Bengal in distilled water where the signal is relatively weak and input count rate is well below 5% of sync rate, the SPAD detector was operating at -90ºC and 25% quantum efficiency and the acquisition was over 180 seconds, while for the much stronger and long-lived luminescence from Rose Bengal in deuterated water the detector quantum efficiency was set to 10%, the supercontinuum laser output was decreased to 10 nm wavelength bandwidth (centred at 550 nm with output optical power of 122 µW), so that the input counts were not exceeding the upper limit of the timing electronics and acquisition time was 60 seconds.

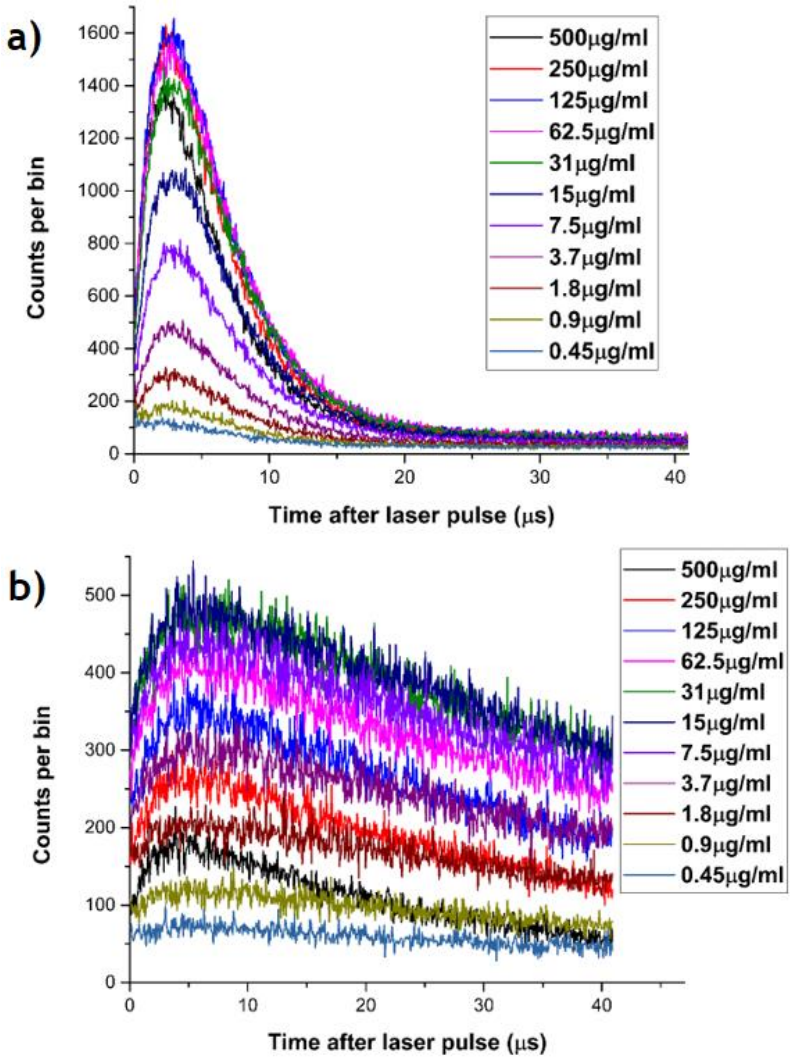

Figure 4.10. a) 180 second histogram comparing $^1O_2$ luminescence from Rose Bengal in distilled water solutions with decreasing concentrations and, b) 60 second histogram comparing $^1O_2$ luminescence from Rose Bengal in deuterated water solutions with decreasing PS concentrations.

Peak intensity alters as the concentration drops. The change in intensity, though, does not go along with the change in the concentration of the photosensitizer. From Figure 4.10 it seems that the highest mass concentration of 500 μg/ml is not the most effective. Especially for Rose Bengal in D_2O, the first concentration value appears to be inefficient with the following values producing more singlet oxygen signal with much longer lifetimes. This trend applies to both solutions with the most efficient mass concentration being the 125 μg/ml for Rose Bengal in distilled water and 31-15 μg/ml for the deuterated water solution. This can be easier noticed in Figure 4.11 where total counts are plotted as a function of PS mass concentration. The extracted lifetimes for all concentrations of each solution are presented in Table 4.7. Singlet oxygen lifetime from Rose Bengal in distilled water seems to not be affected by the change of photosensitizer concentration, while the PS triplet state lifetime shows a slight increase. However, large error values in low concentration solutions prevent us from drawing definite conclusion on the lifetime dependency of RB in water solutions.

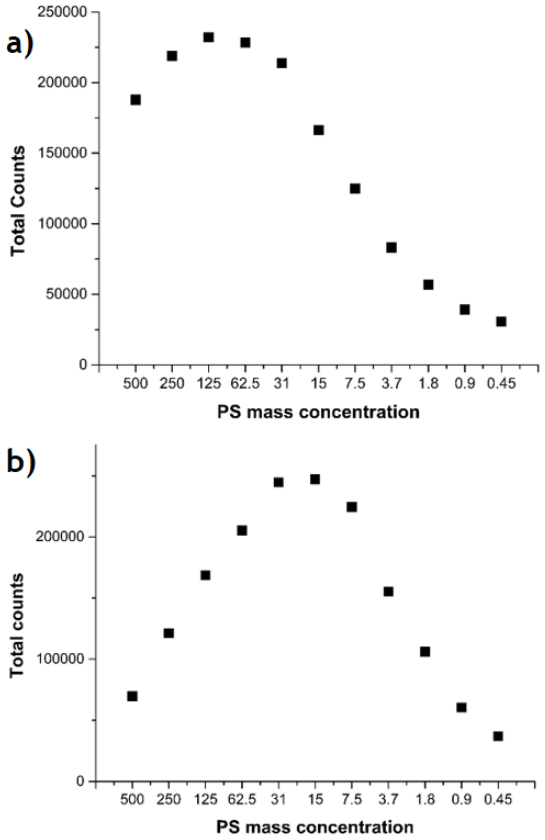

Figure 4.11. Total counts recorded versus PS mass concentration (μg/ml) for a) Rose Bengal in distilled water and, b) Rose Bengal in deuterated water.

On the other hand, due to its long singlet oxygen lifetime, Rose Bengal in deuterated water changes in concentration leads to greater changes in lifetimes. High PS concentrations appear to quench both lifetimes which start to increase as the concentration drops. Singlet oxygen lifetime shows a much bigger increase than PS triplet state lifetime as the former is about 10 times longer and is affected more. Highest recorded singlet oxygen lifetime is 70.3 μs at 15 μg/ml. After that point, decrease in mass concentration leads to shorter singlet oxygen lifetimes, while the PS triplet state lifetime seems to keep increasing, achieving more than a 2-fold increase compared to the highest mass concentration.

PS Mass concentration	Lifetime (μs)	RB in H_2O	RB in D_2O
500μg/ml	τ_Δ	3.77±0.01	23.3±0.09
	τ_T	1.72±0.02	1.88±0.08
250 μg/ml	τ_Δ	3.71±0.02	39.3±0.15
	τ_T	1.95±0.02	2.11±0.08
125 μg/ml	τ_Δ	3.74±0.02	46.8±0.2
	τ_T	2.13±0.02	2.31±0.08
62.5 μg/ml	τ_Δ	3.9±0.02	57.9±0.18
	τ_T	2.22±0.02	2.41±0.08
31 μg/ml	τ_Δ	3.88±0.02	60.5±0.28
	τ_T	2.32±0.02	2.44±0.08
15 μg/ml	τ_Δ	3.7±0.03	70.3±0.32
	τ_T	2.54±0.04	2.25±0.09
7.5 μg/ml	τ_Δ	3.79±0.04	67.3±0.3
	τ_T	2.52±0.04	2.37±0.09
3.7 μg/ml	τ_Δ	3.87±0.05	63.3±0.39
	τ_T	2.54±0.06	2.36±0.12
1.8 μg/ml	τ_Δ	3.2±276	70.5±0.59
	τ_T	3.2±274	2.86±0.19
0.9 μg/ml	τ_Δ	3.48±131	46.8±0.46
	τ_T	3.47±130	2.61±0.21
0.45 μg/ml	τ_Δ	3.93±155	20.3±0.51
	τ_T	3.93±154	4.29±0.43

Table 4.7. $^1O_2$ (τ_Δ) lifetimes and PS triplet state (τ_T) lifetimes from Rose Bengal in H_2O and D_2O at decreasing concentrations.

Similar behaviour is observed in Rose Bengal solutions with methanol, ethanol and DMSO. The PS concentration starts at 1 mg/ml down to 0.45 µg/ml. Singlet oxygen luminescence from all solutions and different PS mass concentrations are compared in 1-minute histograms and are shown in Figure 4.12.

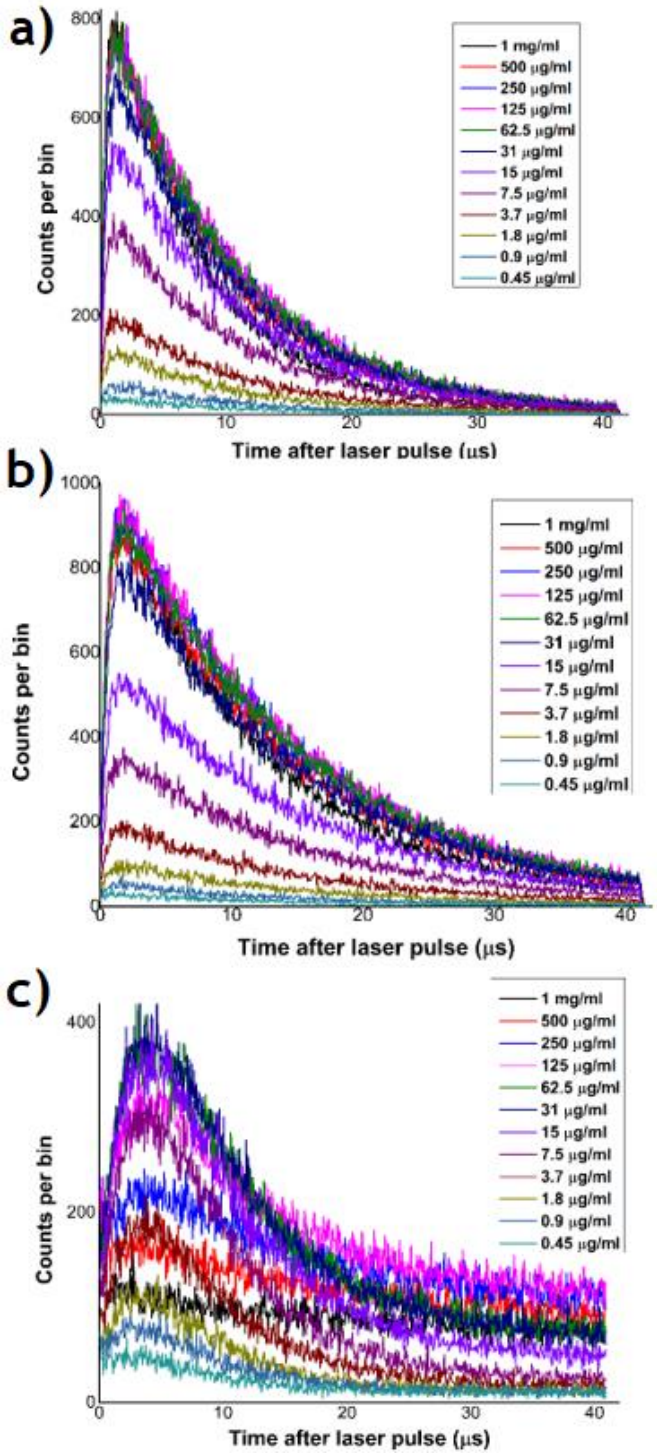

Figure 4.12. 60 second histogram comparing $^1O_2$ luminescence from Rose Bengal in a) methanol, b) ethanol and, c) DMSO with decreasing PS concentrations.

For Rose Bengal in ethanol and methanol solutions, SPAD's detection efficiency was set to 10%, while for Rose Bengal in DMSO the detection efficiency was set to 25% because of the lower singlet oxygen quantum yield. Laser source's output wavelength bandwidth was kept at 10 nm. Rose Bengal in ethanol and methanol show a similar trend with highest peaks achieved by concentrations between 250 µg/ml and 62.5 µg/ml, while Rose Bengal in DMSO despite the fact that the luminescence is weaker, the signal intensity and curve offsets indicating the convoluted lifetimes are similar to Rose Bengal in D_2O with inefficient high PS concentrations, noticeable increases in lifetime and best concentration values being between 125 µg/ml to 15 µg/ml.

PS Mass concentration	Lifetime (µs)	RB in ethanol	RB in methanol	RB in DMSO
1 mg/ml	τ_Δ	11.6±0.01	7.3±0.01	-
	τ_T	0.49±0.02	0.35±0.02	-
500µg/ml	τ_Δ	13.5±0.01	9.05±0.01	18±0.69
	τ_T	0.52±0.02	0.36±0.03	3.19±0.25
250 µg/ml	τ_Δ	14.2±0.01	9.79±0.01	10.4±0.15
	τ_T	0.51±0.03	0.36±0.03	3.58±0.2
125 µg/ml	τ_Δ	14.2±0.01	9.98±0.01	8.65±0.06
	τ_T	0.52±0.03	0.39±0.03	2.66±0.07
62.5 µg/ml	τ_Δ	14.6±0.01	9.91±0.01	7.82±0.03
	τ_T	0.48±0.02	0.36±0.03	2.43±0.04
31 µg/ml	τ_Δ	14.3±0.01	9.87±0.01	7.36±0.04
	τ_T	0.54±0.03	0.42±0.03	2.73±0.05
15 µg/ml	τ_Δ	14.7±0.02	10.2±0.01	7.08±0.03
	τ_T	0.51±0.04	0.4±0.03	2.62±0.04
7.5 µg/ml	τ_Δ	14.7±0.02	10±0.01	5.87±0.05
	τ_T	0.51±0.05	0.39±0.03	3.07±0.06
3.7 µg/ml	τ_Δ	13.6±0.03	10.3±0.01	6.06±0.05
	τ_T	0.54±0.06	0.34±0.06	2.77±0.07
1.8 µg/ml	τ_Δ	13.6±0.04	9.6±0.02	5.25±0.1
	τ_T	0.67±0.1	0.51±0.07	3.11±0.13
0.9 µg/ml	τ_Δ	1.2±0.05	10.1±0.03	5.84±0.1
	τ_T	0.47±0.2	0.39±0.14	2.82±0.14
0.45 µg/ml	τ_Δ	12.9±0.07	10.1±0.05	-
	τ_T	0.62±0.8	0.55±0.39	-

Table 4.8. $^1O_2$ (τ_Δ) lifetimes and PS triplet state (τ_T) lifetimes from Rose Bengal in ethanol, methanol and DMSO at decreasing concentrations.

Respectively, the total counts versus the PS mass concentration plots indicating the most efficient concentration for singlet oxygen generation are shown in Figure 4.13 and the extracted lifetimes in Table 4.8.

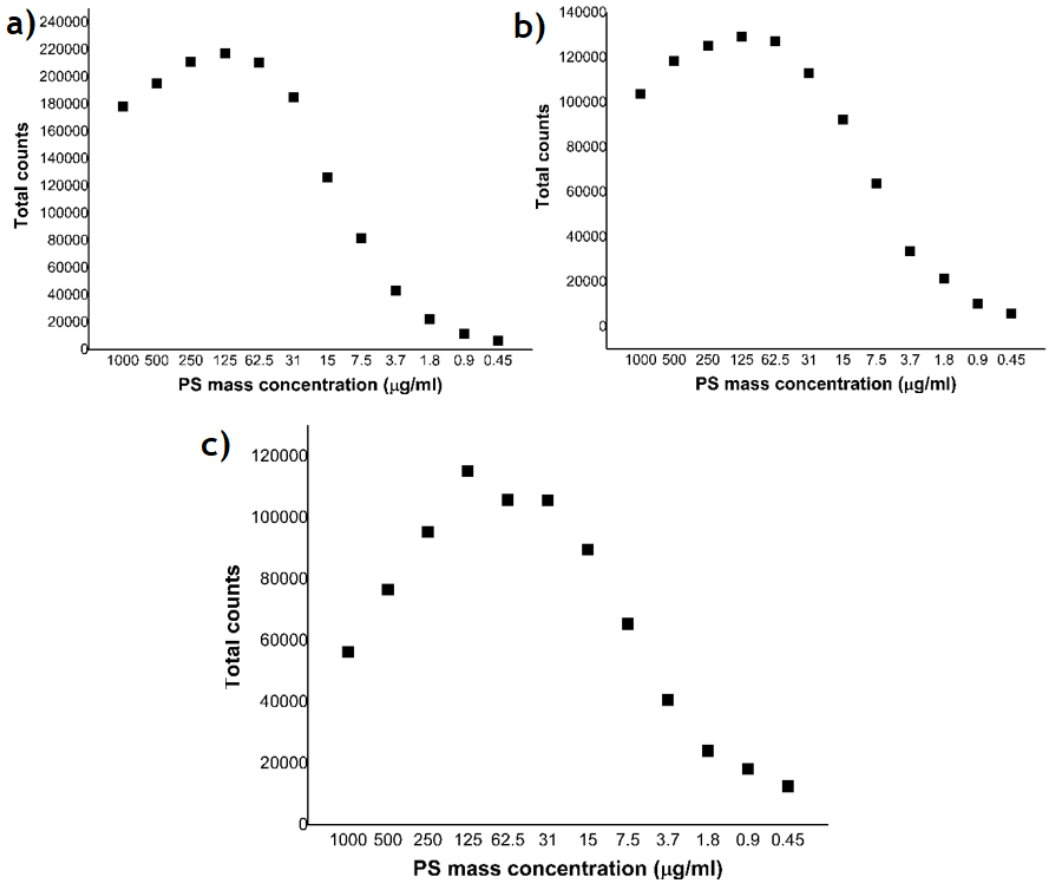

Figure 4.13. Total counts recorded versus PS mass concentration for Rose Bengal in a) ethanol, b) methanol and, c) DMSO.

Indeed, the most efficient concentrations are at 62.5 µg/ml for Rose Bengal in ethanol and methanol and, 125 µg/ml for Rose Bengal in DMSO. Above and below these optimum values overall signal decreases to a lowest point where $^1O_2$ luminescence is almost vanished. Regarding the singlet oxygen lifetime, in both Rose Bengal in ethanol and methanol solutions, the lifetime increases slightly as the concentration decreases and towards the lowest concentration values it seems to stay the same or suffer a small decrease. The PS triplet state lifetimes seem to fluctuate as this lifetime is quite short and fitting errors can be big, but it looks like it is increasing with lower concentrations. The increase is the order of 130 – 200 ns from the highest concentration value to the lowest. In the case of Rose

Bengal in DMSO solution, starting from the highest concentration the singlet oxygen lifetime decreases as the concentration drops, while it seems to stabilize as we move to the lowest concentrations. The PS triplet state lifetime seems to not be affected by the change in concentration and fluctuates between ~2.5 – 3.5 μs. Lifetimes for 1 mg/ml and 0.45 μg/ml of Rose Bengal in DMSO could not be extracted as the former lacks a clear intensity peak in order to best fit its curve (singlet oxygen lifetime though appears to be even longer than the smaller concentrations) and the latter's lifetimes are extracted with huge errors and cannot be trusted.

Next, $^1O_2$ luminescence from various concentrations of Eosin Y in distilled water, ethanol and methanol are presented. Eosin Y in distilled water is relatively weak in producing singlet oxygen compared to Rose Bengal and also, Eosin Y saturates faster in distilled water, so a 125 μg/ml mass concentration is selected as the initial concentration down to 1.8 μg/ml. Eosin Y in ethanol and methanol is significantly more efficient allowing the singlet oxygen luminescence acquisition in a wider range of concentrations starting at 1 mg/ml down to 0.45 μg/ml, although the signal from the lower concentrations is very weak. SPAD detector was set to -90ºC, 42 ps dead time and 25% of quantum efficiency for Eosin Y in distilled water solutions and 10% for Eosin Y in ethanol and methanol. Laser's output wavelength bandwidth was set to 10 nm. In Figure 4.14 are shown 60 second histograms of the Eosin Y solutions in the various concentrations. Unlike the Rose Bengal solutions, Eosin Y's singlet oxygen signal appears to be stronger with increased concentration. Therefore, at higher concentrations the peak is higher, and the tail of the curve shaped by the lifetimes does not seem to be affected much by the decrease of the concentration. However, the relative transmissivity of the two solutions is different and this observation may be due to different absorption peaks for each photosensitizer (thus different laser energy deposited within the collection volumes), as well as slightly different laser powers for each excitation wavelength. The total counts detected from each solution and concentration are presented in Figure 4.15. For Eosin Y in distilled water, the decrease in the photosensitizer concentration leads to a linear decrease in the overall singlet oxygen counts. For the other two Eosin Y solutions, this decrease in the total counts is nonlinear and appears to be reaching a plateau at

concentrations greater than 1 mg/ml and smaller than 0.9 μg/ml where luminescence signal gradually disappears.

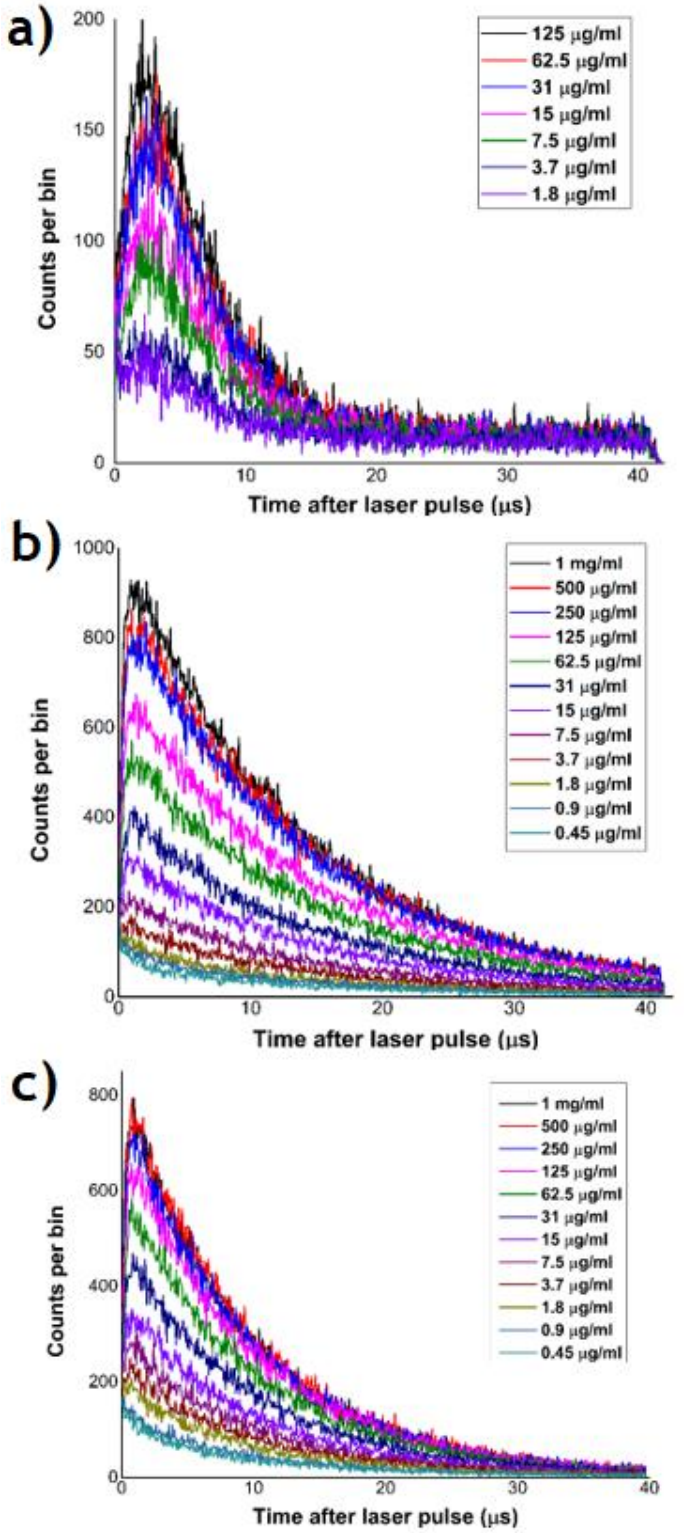

Figure 4.14. 60 second histograms comparing $^1O_2$ luminescence from Eosin Y in a) distilled water, b) ethanol and, c) methanol with decreasing PS concentrations.

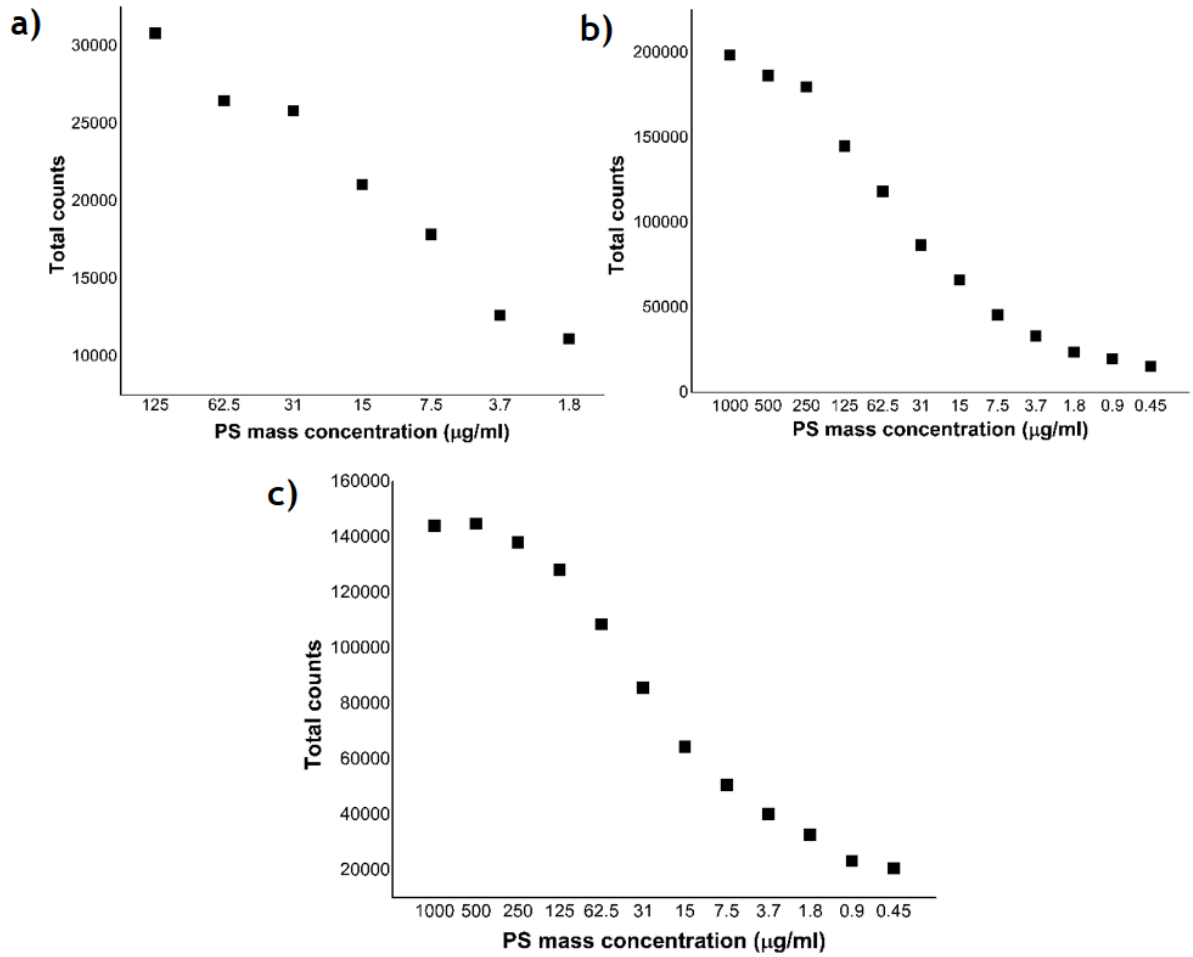

Figure 4.15. Total counts recorded versus PS mass concentration for Eosin Y in a) distilled water, b) ethanol and, c) methanol.

The lifetimes of the Eosin Y solutions as the concentration decreases are not greatly affected as seen in Table 4.9. For Eosin Y in ethanol and methanol, singlet oxygen lifetime shows a small increase, peaks at around 125 µg/ml and then decreases again. For Eosin Y in distilled water, singlet oxygen lifetime fluctuates between 3 µs and 4.3 µs. The PS triplet state lifetime for all solutions appears to be affected much by the change in concentration. A trend similar to singlet oxygen lifetime appears vaguely for Eosin Y in ethanol and methanol PS triplet state lifetime, with small changes ranging from 0.27 µs to 0.35 µs for Eosin Y in ethanol and from 0.22 µs to 0.28 µs for Eosin Y in methanol. In the case of Eosin Y in distilled water, the photosensitizer triplet state lifetime varies from 1.76 µs to 3.09 µs without distinguishing any concentration related trend.

PS Mass concentration	Lifetime (μs)	EY in ethanol	EY in methanol	EY in H_2O
1 mg/ml	τ_Δ	13.6±0.01	9.19±0.01	-
	τ_T	0.32±0.03	0.23±0.04	-
500μg/ml	τ_Δ	14.2±0.01	9.37±0.01	-
	τ_T	0.35±0.04	0.27±0.04	-
250 μg/ml	τ_Δ	14.3±0.01	9.52±0.01	-
	τ_T	0.36±0.04	0.24±0.04	-
125 μg/ml	τ_Δ	14.3±0.01	9.8±0.01	4.27±0.03
	τ_T	0.35±0.05	0.28±0.05	1.76±0.06
62.5 μg/ml	τ_Δ	14.3±0.01	9.7±0.01	3.77±0.06
	τ_T	0.31±0.06	0.26±0.05	2.07±0.08
31 μg/ml	τ_Δ	13.7±0.02	9.58±0.01	4.08±0.05
	τ_T	0.31±0.07	0.24±0.06	1.9±0.07
15 μg/ml	τ_Δ	14.1±0.02	9.3±0.01	3.53±0.15
	τ_T	0.29±0.1	0.31±0.1	2.56±0.18
7.5 μg/ml	τ_Δ	13.1±0.02	9.18±0.01	4.34±0.06
	τ_T	0.32±0.23	0.27±0.18	1.81±0.09
3.7 μg/ml	τ_Δ	13±0.03	9.17±0.01	3.1±0.02
	τ_T	0.27±1	0.22±0.21	3.09±0.02
1.8 μg/ml	τ_Δ	-	8.71±0.02	4.3±0.44
	τ_T	-	0.24±0.94	2.98±0.65

Table 4.9. $^1O_2$ (τ_Δ) lifetimes and PS triplet state (τ_T) lifetimes from Eosin Y in ethanol, methanol, and distilled water at decreasing concentrations.

Histograms of singlet oxygen luminescence with Methylene Blue show a very strong peak with short lifetime at the start of the histogram, as mentioned earlier. For this reason, for all Methylene Blue solutions the SPAD quantum efficiency was set to the lowest value 10% and the laser's wavelength bandwidth to 10 nm, so that the input counts are kept within the pile-up threshold. Methylene blue solutions used were with distilled water, ethanol and methanol at concentrations starting from 1 mg/ml down to 0.45 μg/ml, as shown in Figure 4.16. All histograms were acquired over 60 seconds. Compared to previous solutions with Rose Bengal and Eosin Y, the luminescence signal from the Methylene Blue solutions is considerably weaker, especially for the distilled water solution. However, lifetimes and total counts vs concentration plots can be extracted from the histograms to assist in

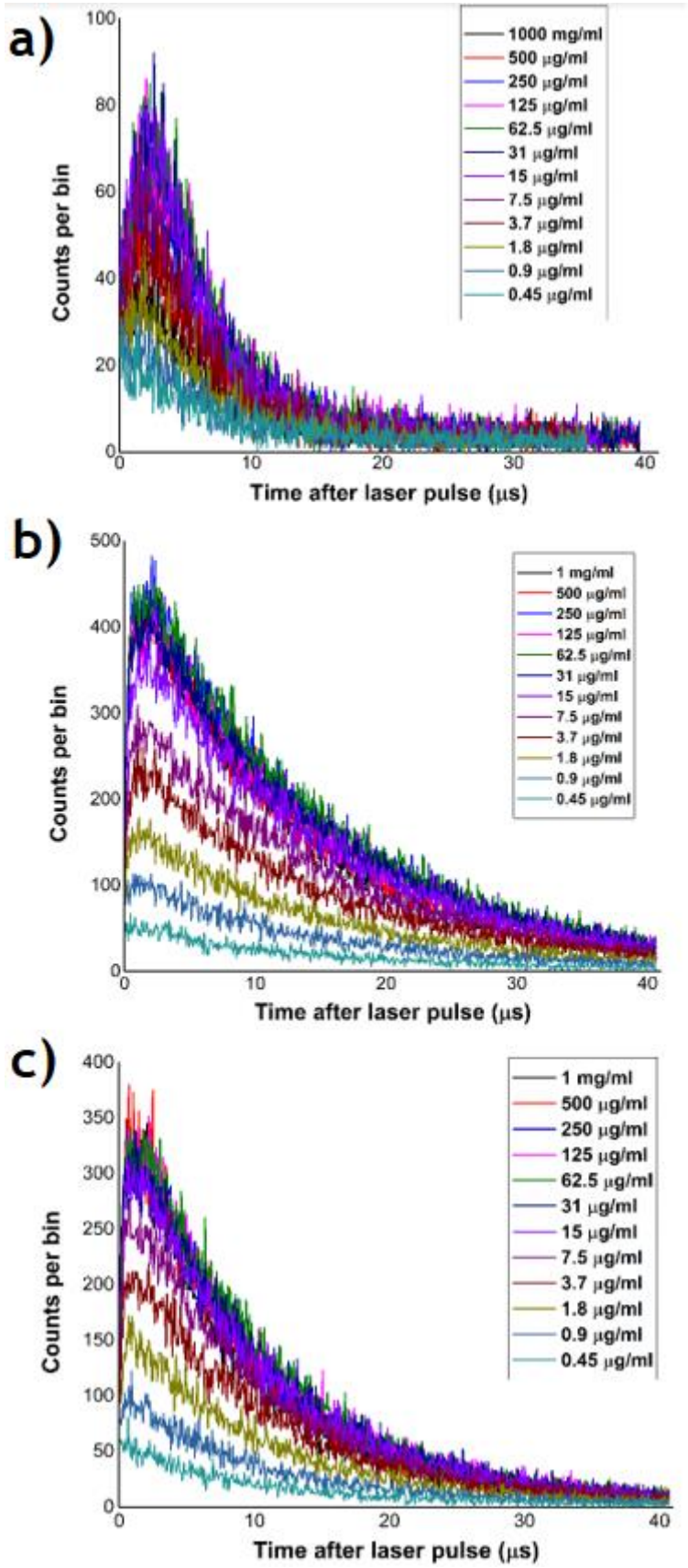

Figure 4.16. 60 second histograms comparing $^1O_2$ luminescence from Methylene Blue in a) distilled water, b) ethanol and, c) methanol with decreasing PS concentrations.

the study of these solutions. The lifetimes are shown in Table 4.10 and the total counts as a function of mass concentration in Figure 4.17. Total singlet oxygen luminescence counts recorded by Methylene Blue in distilled water vary with the PS concentration. As the photosensitizer concentration decreases the luminescence signal increases reaching an optimum value at 62.5 μg/ml where the total counts are almost double in number. After that point the signal starts to drop again. The lifetime of the singlet oxygen luminescence extracted from all concentration solutions appears to fluctuate around 4 μs with the three lowest concentrations showing an increasing trend of this lifetime. The PS triplet state lifetime seems to not be affected much as all solutions have a τ_T in the range of 1 – 1.8 μs.

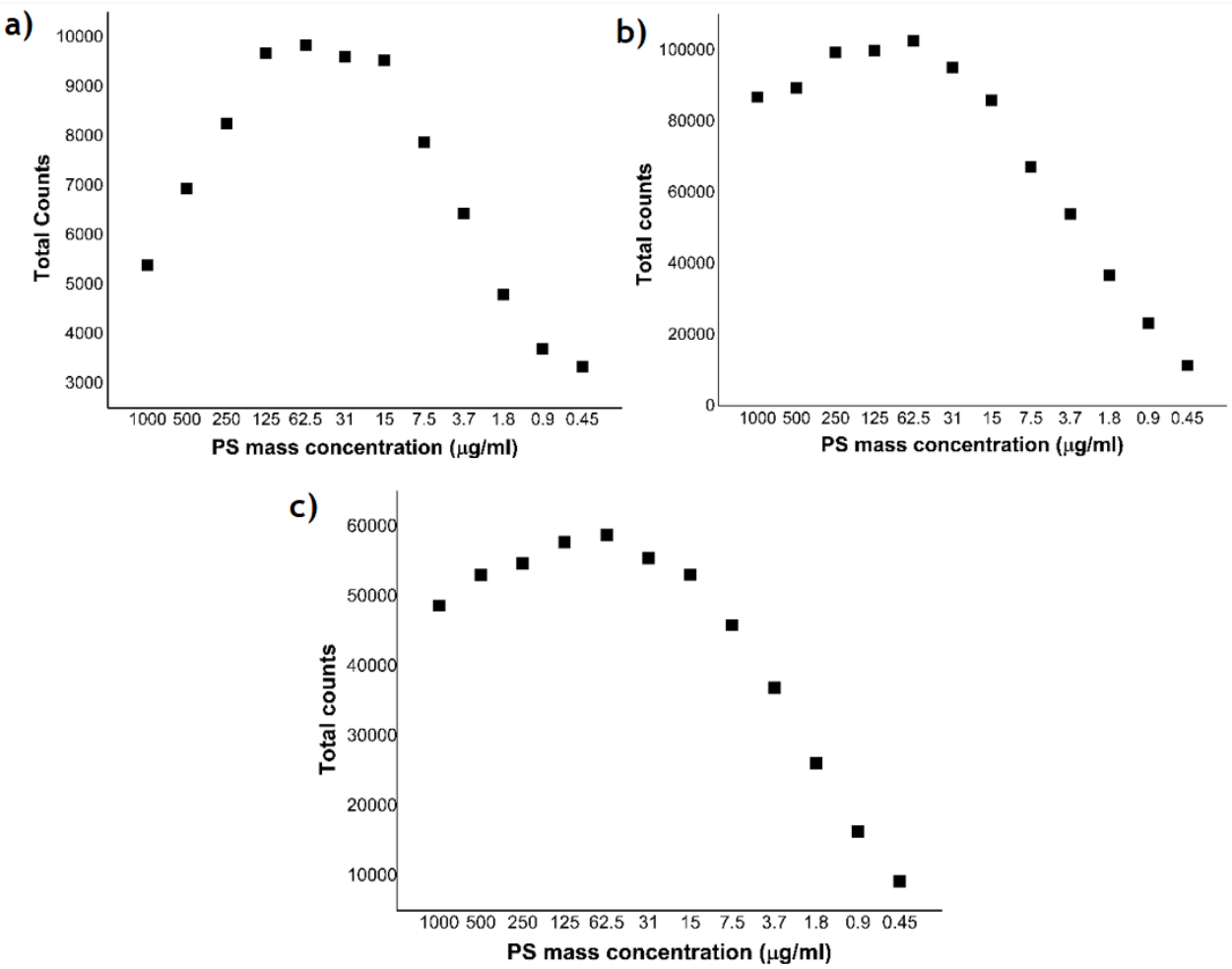

Figure 4.17. Total counts recorded versus PS mass concentration for Methylene Blue in a) distilled water, b) ethanol and, c) methanol.

The total luminescence counts from Methylene Blue in ethanol and methanol show a smaller increase in counts compared to the distilled water solution until they also reach the 62.5 μg/ml mass concentration. Then they appear to decrease again linearly. Between the two solution with the organic solvents, Methylene Blue in methanol is roughly 40% less efficient than the solution with ethanol.

PS Mass concentration	Lifetime (μs)	MB in ethanol	MB in methanol	MB in DMSO
1 mg/ml	τ_Δ	12.4±0.01	8.55±0.01	4.29±0.09
	τ_T	0.38±0.06	0.30±0.08	1.56±0.2
500μg/ml	τ_Δ	13.5±0.02	9.03±0.01	3.92±0.07
	τ_T	0.37±0.06	0.27±0.07	1.59±0.12
250 μg/ml	τ_Δ	14.2±0.16	9.59±0.01	3.9±0.07
	τ_T	0.35±0.06	0.39±0.06	1.78±0.12
125 μg/ml	τ_Δ	14.4±0.02	9.74±0.01	3.93±0.06
	τ_T	0.35±0.06	0.38±0.06	1.64±0.09
62.5 μg/ml	τ_Δ	14.7±0.02	10.3±0.01	3.58±0.07
	τ_T	0.42±0.06	0.31±0.07	1.87±0.1
31 μg/ml	τ_Δ	14.7±0.02	10.4±0.01	3.74±0.06
	τ_T	0.35±0.06	0.28±0.07	1.72±0.1
15 μg/ml	τ_Δ	15.1±0.02	10±0.01	3.52±0.07
	τ_T	0.42±0.07	0.31±0.06	1.72±0.11
7.5 μg/ml	τ_Δ	15.2±0.02	10.4±0.01	4.26±0.04
	τ_T	0.38±0.07	0.25±0.07	1.01±0.1
3.7 μg/ml	τ_Δ	14.2±0.02	10.4±0.02	3.79±0.09
	τ_T	0.35±0.09	0.29±0.08	1.66±0.16
1.8 μg/ml	τ_Δ	14.1±0.03	9.85±0.02	4.65±0.07
	τ_T	0.28±0.14	0.27±0.11	1.16±0.18
0.9 μg/ml	τ_Δ	13.2±0.03	9.42±0.02	4.47±0.12
	τ_T	0.40±0.23	0.26±0.24	1.54±0.36
0.45 μg/ml	τ_Δ	12.1±0.05	-	5.73±0.21
	τ_T	0.47±0.75	-	1.88±2.25

Table 4.10. $^1O_2$ (τ_Δ) lifetimes and PS triplet state (τ_T) lifetimes from Methylene Blue in ethanol, methanol, and distilled water at decreasing concentrations.

The singlet oxygen lifetimes of these solutions follow the same trend; increases up to a peak point (at 7.5 μg/ml for MB in ethanol and 31 – 7.5 μg/ml

for MB in methanol) and then starts decreasing again. Singlet oxygen lifetimes are very similar to the ones produced by the previous solutions with Rose Bengal and Eosin Y, around 14 μs for ethanol solutions and 10 μs for the methanol solutions. PS triplet state lifetimes from Methylene Blue are also in the nanoscale range. For solutions in ethanol τ_T is around 400 ns and around 300 ns for the methanol ones.

Next, Zinc Phthalocyanine in DMSO was tested in decreasing concentration values. Starting mass concentration was at 1 mg/ml down to 1.8 μg/ml where singlet oxygen signal is almost completely lost. SPAD detector was set to 10 % of quantum efficiency with 10 nm laser output wavelength bandwidth. 60 second histograms were acquired for all mass concentrations and are presented in Figure 4.18a, while the corresponding plot with the summed counts over the ZnPc mass concentrations is shown in Figure 4.18b.

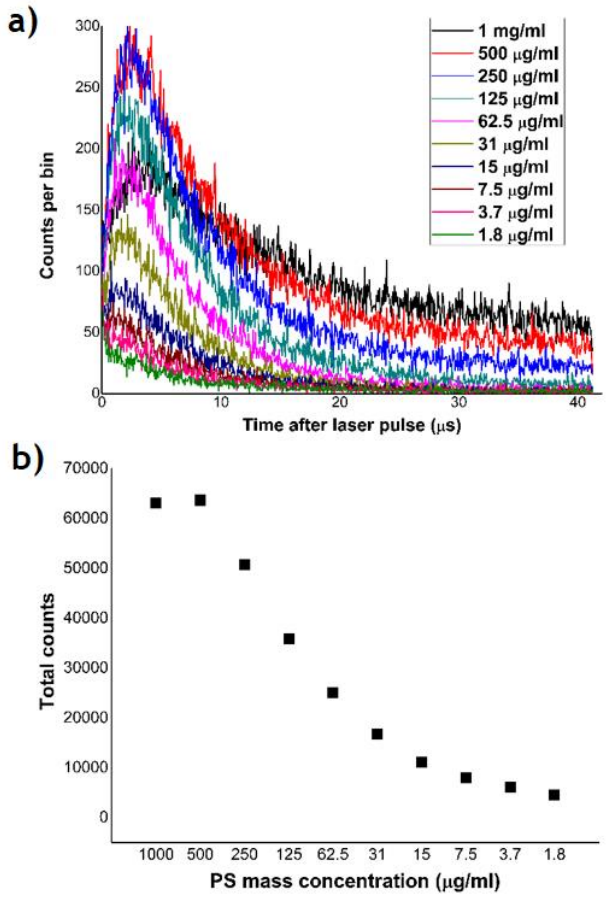

Figure 4.18. a) 60 second histograms comparing $^1O_2$ luminescence from Zinc Phthalocyanine in DMSO and, b) Total counts recorded versus PS mass concentration for Zinc Phthalocyanine in DMSO.

By looking at the shape of the curves, 1 mg/ml mass concentration solution does not seem to generate much singlet oxygen, while subsequent values at 500 μg/ml and 250 μg/ml show higher peaks and then start dropping steadily as the concentration is halved. However, the offset of these curves indicates longer lifetime for higher concentrations with the first one appearing to overcome all the following concentrations. Affected by both intensity and lifetime, the most efficient concentrations for ZnPC in DMSO are the 1 mg/ml and 500 μg/ml as shown in Figure 4.18b. Then as the concentration decreases the total counts recorded are also decreased nonlinearly. At low concentrations, the total counts seem to be slowly approaching zero.

PS Mass concentration	Lifetime (μs)	ZnPc in DMSO
1 mg/ml	τ_Δ	11.4±0.05
	τ_T	1.87±0.09
500μg/ml	τ_Δ	7.94±0.02
	τ_T	1.13±0.04
250 μg/ml	τ_Δ	6.55±0.02
	τ_T	1.17±0.04
125 μg/ml	τ_Δ	6.24±0.02
	τ_T	1.22±0.04
62.5 μg/ml	τ_Δ	5.74±0.02
	τ_T	1.05±0.04
31 μg/ml	τ_Δ	5.31±0.02
	τ_T	1.09±0.06
15 μg/ml	τ_Δ	5.5±0.03
	τ_T	1.07±0.1
7.5 μg/ml	τ_Δ	5.44±0.03
	τ_T	0.95±0.2
3.7 μg/ml	τ_Δ	-
	τ_T	-
1.8 μg/ml	τ_Δ	-
	τ_T	-

Table 4.11. $^1O_2$ (τ_Δ) lifetimes and PS triplet state (τ_T) lifetimes from Zinc Phthalocyanine in DMSO at decreasing concentrations.

Both singlet oxygen and PS triplet state lifetime appear to drop as the concentration decreases, as shown in Table 4.11. ZnPc's mass concentration at 1 mg/ml show the highest singlet oxygen lifetime being 11.4 μs long. The corresponding PS triplet state lifetime starts at 1.87 μs and decreases as well reaching to a sub-microsecond value of 950 ns. The last two mass concentrations by producing quite weak $^1O_2$ luminescence signal, the acquired curve shape could not be fitted so lifetimes where unable to extract or would give a more than acceptable error value.

Lastly, Visudyne in methanol solution was tested in various concentrations. The initial 500 μg/ml mass concentration was diluted down to half until it reaches 0.1 μg/ml. As mentioned earlier, singlet oxygen luminescence from this solution is very weak, so the SPAD detector was set to 25 % detection efficiency and the laser's output wavelength bandwidth to 100 nm to increase the optical power reaching to the solution. As shown in Figure 4.19a, the highest concentrations of 500 and 250 μg/ml seem quite efficient generating enough singlet oxygen and recorded curves have sharp peaks. The next two solutions at 125 and 62.5 μg/ml mass concentration stand out from the rest solutions, but the shape of the curves have a hint of onset and offset, tending to single exponential decay. This indicates photosensitizer's inability to efficiently generate singlet oxygen at these concentrations. Below these concentrations, the signal vanishes, and the decay is a single exponential without any certainty that the detected counts come from singlet oxygen luminescence photons. This can also be observed in Figure 4.19b where the total counts after 15 and 7.5 μg/ml reach a plateau and are stabilized at a value where solution with plain methanol also has. Therefore, the counts recorded for these solutions possibly come from methanol luminescence and not from singlet oxygen photons generated through the Visudyne photosensitizer. Also, due to weak or no luminescence signal the singlet oxygen and photosensitizer triplet state lifetimes cannot be extracted. The lifetimes for high concentration were given in Table 4.5. However, the fact that singlet oxygen luminescence signal from a clinically approved photosensitizer such as Visudyne can be efficiently monitored even at the high concentrations is very promising for future studies and eventual clinical use.

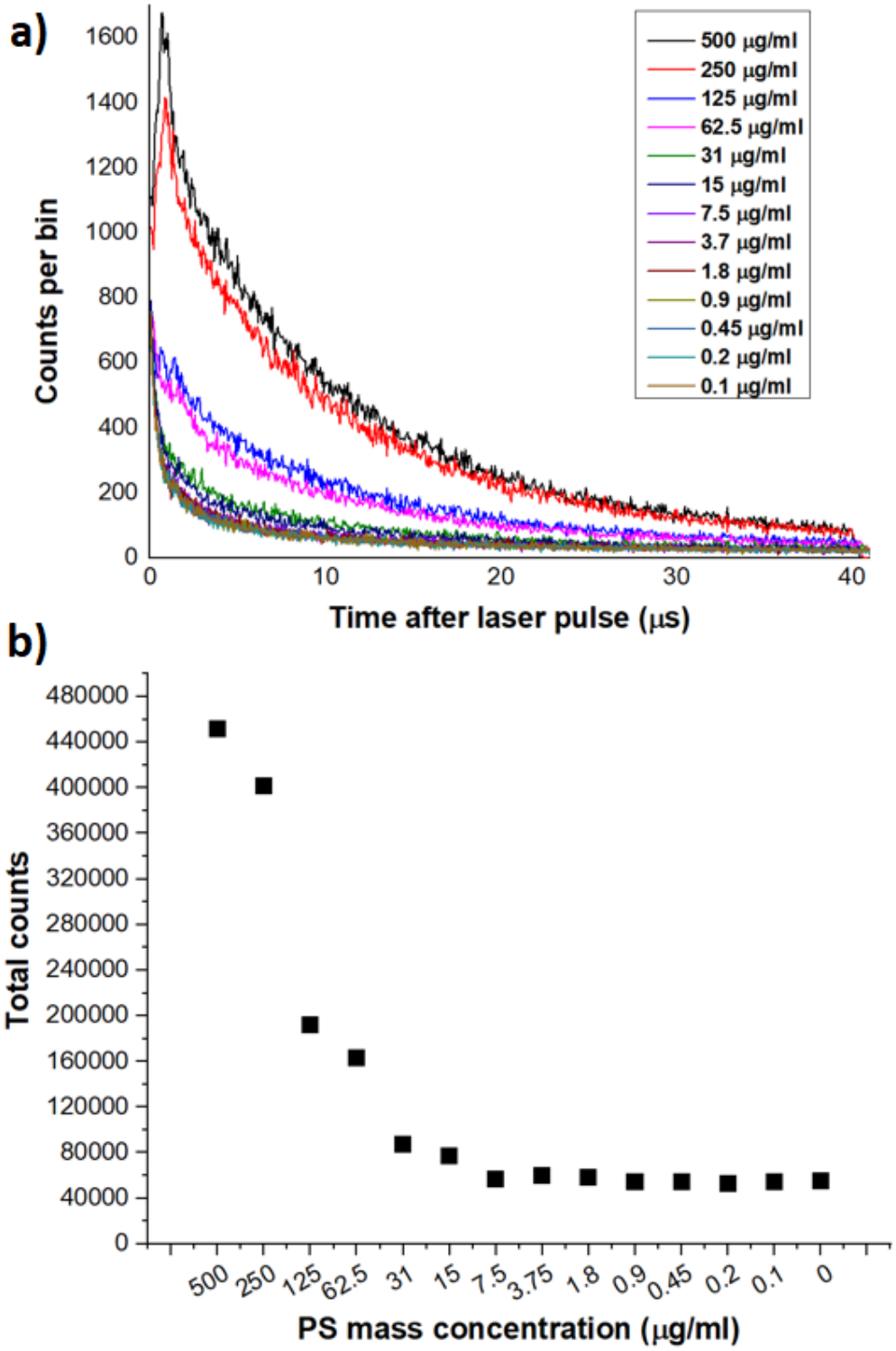

Figure 4.19. a) 60 second histograms comparing $^1O_2$ luminescence from Visudyne in methanol at decreasing concentration and, b) Total counts recorded versus PS mass concentration for Visudyne in methanol.

4.3.2 1590 nm measurements

Singlet oxygen emission at 1590 nm wavelength is also monitored, and time resolved experiments have been carried out for the first time. This emission is due to the transition $^1\Delta_g \rightarrow {}^3\Sigma_g^-$(v = 1) from the first excited singlet state to a vibrational state above the ground state. Compared to the 1270 nm emission, this 1590 nm decay is expected to be at least an order of magnitude weaker, without significant changes in the singlet oxygen and photosensitizer triplet state lifetimes. However, by being in a different spectral window in the near-infrared, various emissions from the solvents themselves are affecting the detected signal and may alter the extracted lifetimes. Regarding the optical setup, the excitation path remains intact and only the long-pass and band-pass optical filtering in the collection path change to adapt to the new wavelength. A 1500 nm cut-on long-pass optical filter is mounted to exclude all photons below 1500 nm and especially the much stronger 1270 nm singlet oxygen luminescence. The band-pass optical filter is centred at 1590 nm (FWHM Bandwidth 12 nm ± 2.4 nm), while validation experiments including band-pass optical filters spanning the 1590 nm wavelength are centred at 1560 nm, 1620 nm, 1520 nm and 1650 nm wavelengths. Due to the much weaker emission probability and intensity, all acquisitions were 10 minutes long and SPAD detector was set to maximum quantum efficiency at 25%. Because of the longer acquisition time and high quantum efficiency leading to higher dark count levels, histograms presented are dark count corrected, showing only the detected photon counts from the targeted solution.

Starting with Rose Bengal as the photosensitizer dissolved in distilled water, I observed that the recorded histogram curve is lacking the typical onset and offset of the singlet oxygen biexponential decay. Changing the solution to deuterated water whose optical properties are somehow closer to distilled water, the same decay curve was observed but with higher intensity and clearly longer lifetime, as shown in Figure 4.20. Carrying out the same acquisition with Rose Bengal in an organic solvent this time, like ethanol, the expected biexponential singlet oxygen decay was observed. This leads to the assumption that distilled and deuterated water's optical properties in the specific wavelength are affecting the output optical signal. Water's absorptance in the ~1500-1600 nm wavelength range is

much higher than in the 1200-1300 nm wavelength range. It is possible that strong absorption in water masks the singlet oxygen luminescence signature over the first microseconds.

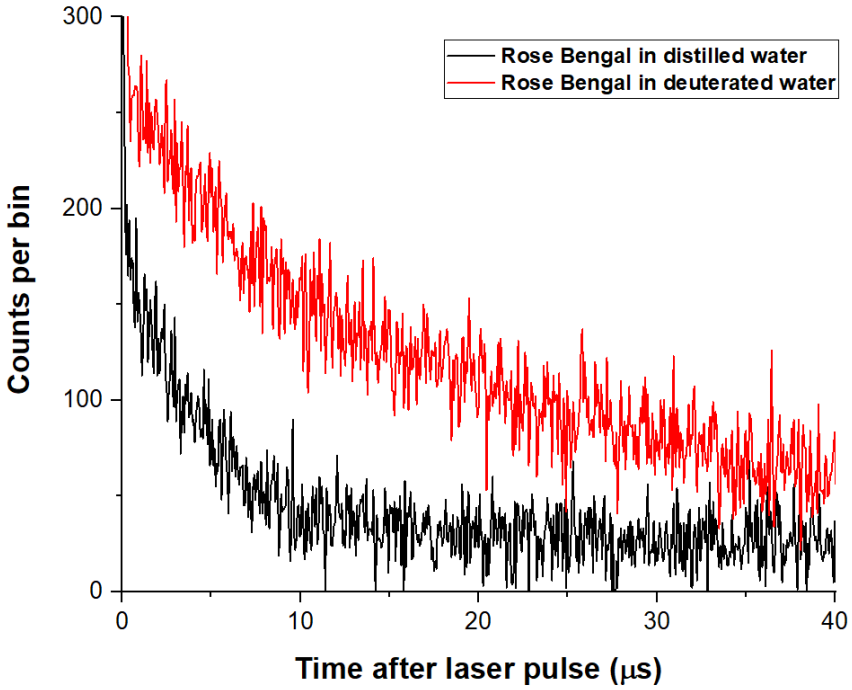

Figure 4.20. 10-minute histogram of 1590 nm wavelength luminescence signal from Rose Bengal in distilled and deuterated water.

Like with the 1270 nm emission, 1590 nm wavelength validation experiments were carried out by using different band-pass optical filters to validate that the detected photon are actually coming from the singlet oxygen 1590 nm emission. Two solutions where chosen for this type of experiment, Rose Bengal in ethanol which seems to generate enough signal and deuterated water whose luminescence decay signal may not look like the normal singlet oxygen biexponential decay curve but the detected signal is stronger and longer than that of Rose Bengal in distilled water and there is some singlet oxygen emission in that long decay. So, as can be seen in Figure 4.21, the counts recorded from Rose Bengal in ethanol with the 1590 nm bandpass optical filter clearly stand out from the rest of the bandpass filters by a factor of 4 in total counts. The corresponding comparison for the Rose Bengal in deuterated water also shows that most counts are gathered for the 1590 nm bandpass filter, with the 1560 nm wavelength evident as a secondary signal.

Photon counts at 1560 nm and 1520 nm wavelengths are more than expected, but as mentioned the luminescence from the deuterated water itself is possible to give that many counts, with the 1590 nm wavelength adding the long-lived luminescence from singlet oxygen's decay and standing out from the rest. Moreover, having in mind that this electronic to vibrational state decay is roughly 60 times weaker than the 1270 nm emission and dark count level from ambient light or electronic noise is closer to the weak singlet oxygen detected photon count level. Nevertheless, recorded counts at 1590 nm wavelength are standing out so it is reasonable to conclude that most of these photon counts arise from the $^1\Delta_g$ → $^3\Sigma_g^-$(v = 1) transition.

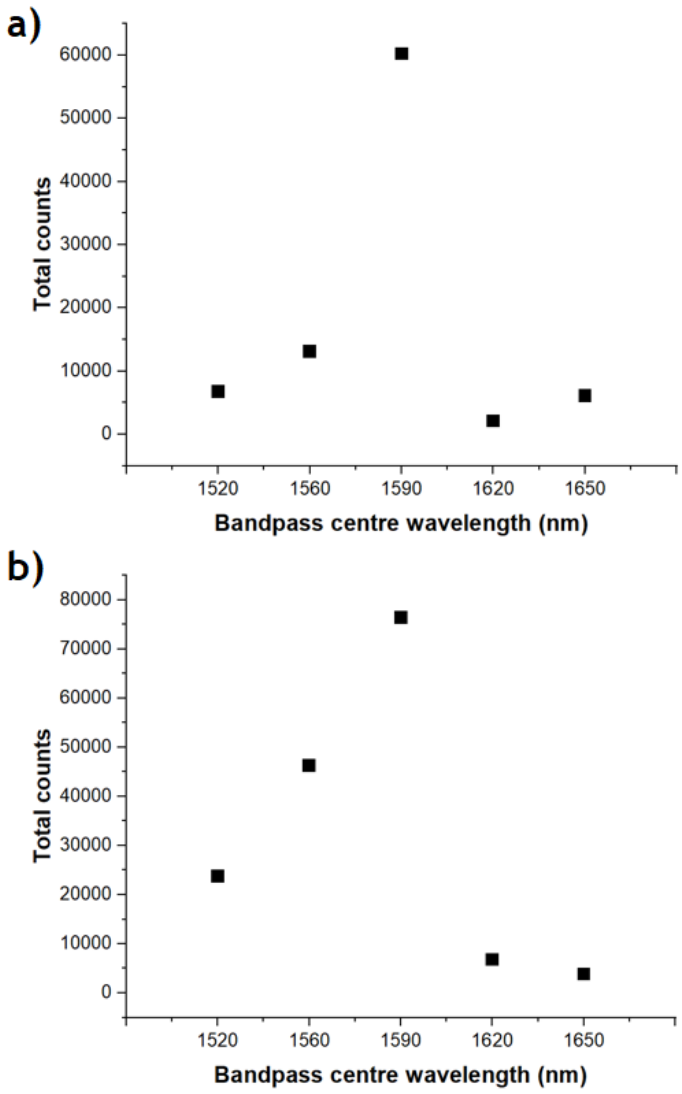

Figure 4.21. Total counts versus BP optical filter centre wavelength comparison plot from a) 500 μg/ml Rose Bengal in ethanol and, b) 500 μg/ml Rose Bengal in deuterated water.

As luminescence signal at 1590 nm wavelength is weak, solutions that are not very efficient at the 1270 nm wavelength could not generate enough singlet oxygen photons to be detected in the 1590 nm wavelength. This includes all solutions with distilled water as the solvent and also due to the lack of proper decay curve, as explained before, their data could not be properly analyzed. Therefore, time-resolved measurements were carried out for Rose Bengal, Eosin Y and Methylene Blue dissolved in ethanol and methanol. Also Rose Bengal in acetone was tested as the most efficient solution considering its ability to generate singlet oxygen molecules and long lifetimes at the 1270 nm wavelength. It should be noted that because of the high evaporation rate of acetone, the different concentrations of the Rose Bengal in acetone solutions were made separately and not diluting down the initial solution of high concentration. Starting mass concentration for all solutions tested is the same as before, diluting down to 15 μg/ml or 7.5 μg/ml. Low mass concentrations are not as low as the ones in the 1270 nm measurements, mostly because of the inability of detecting enough luminescence signal to stand above the dark count rate or generate a clear biexponential curve to be further studied.

Starting with Rose Bengal, three solutions were prepared mixed with ethanol, methanol and acetone with initial mass concentration at 1 mg/ml. Rose Bengal in ethanol and methanol were diluted down to 15 μg/ml, while Rose Bengal in acetone down to 7.5 μg/ml. Figure 4.22 shows plots of singlet oxygen luminescence produced by these three solutions at decreasing concentrations and plots correlating the total counts of each histogram with each concentration value. All histograms were acquired over 600 seconds. Solutions of Rose Bengal in ethanol and methanol in high concentrations are the most efficient. Higher than 500 μg/ml mass concentration, the total counts tend to reach a plateau, while as it gets halved the total counts drop almost linearly. For Rose Bengal in acetone, the singlet oxygen luminescence signal is much stronger with long lifetime as expected from the 1270 nm wavelength results. Unlike the other two solutions, though, total counts increase with the decrease of the mass concentration and maximizes at 125 μg/ml before it starts decreasing again. Comparing the best concentration for each solution, the Rose Bengal in ethanol produces two times the total counts of Rose Bengal in methanol, while the one in acetone is about 2.5

times the total counts of the Rose Bengal in ethanol, exhibiting similar yield to the 1270 nm measurements.

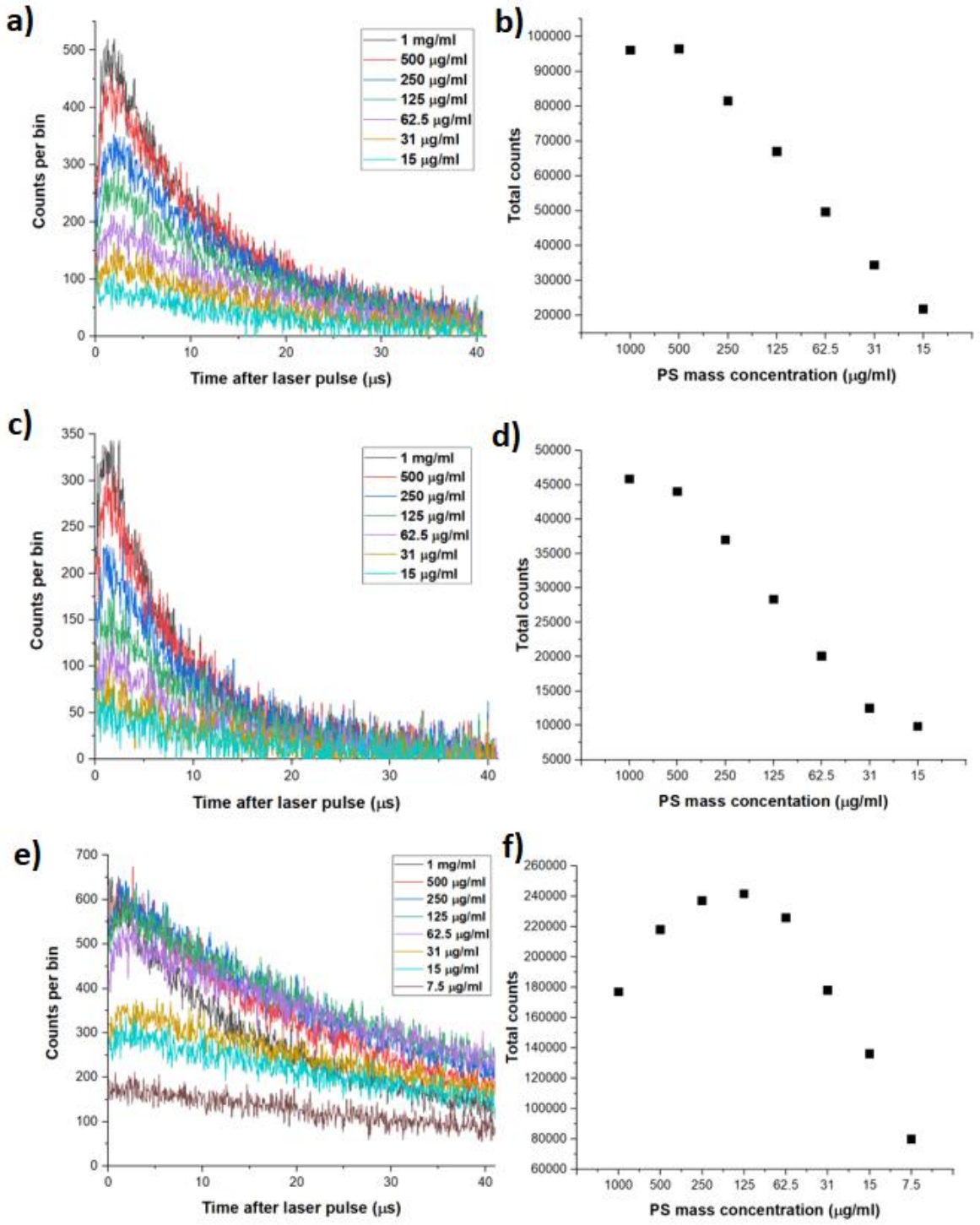

Figure 4.22. 600 second histograms comparing 1590 nm $^1O_2$ luminescence at decreasing concentration for Rose Bengal in a) ethanol, c) methanol, e) acetone and Total counts recorded versus PS mass concentration for Rose Bengal in b) ethanol, d) methanol and f) acetone.

The extracted lifetimes from the curves above are presented in Table 4.12. Singlet oxygen and PS triplet state lifetime values are similar to the 1270 nm corresponding lifetimes as expected for each solvent. In all three solutions, the singlet oxygen lifetime increases as the concentration drops, reaching a maximum value at 62.5 – 31 μg/ml and then tends to decrease again. The $^1O_2$ lifetime from Rose Bengal in methanol peaks at 10.9 μs, the Rose Bengal in ethanol as expected longer at 14.8 μs and the Rose Bengal in acetone exhibits a prolonged lifetime reaching 53.3 μs. The photosensitizer triplet state lifetime, however, appears to increase with lower concentrations. For all cases, it starts in the nanoscale range and keeps increasing, even achieving lifetimes in microseconds.

PS Mass concentration	Lifetime (μs)	RB in ethanol	RB in methanol	RB in acetone
1 mg/ml	τ_Δ	10.1±0.02	6.86±0.02	15.8±0.02
	τ_T	0.54±0.07	0.44±0.11	0.1±1.7
500μg/ml	τ_Δ	11.9±0.02	7.94±0.03	23.9±0.04
	τ_T	0.58±0.07	0.51±0.13	0.44±0.23
250 μg/ml	τ_Δ	13.9±0.03	9.41±0.03	30.4±0.55
	τ_T	0.74±0.09	0.57±0.18	0.56±0.19
125 μg/ml	τ_Δ	14.2±0.03	10.9±0.05	37±0.08
	τ_T	0.74±0.1	0.66±0.25	0.74±0.22
62.5 μg/ml	τ_Δ	14.8±0.05	10.9±0.07	43±0.07
	τ_T	0.86±0.18	0.79±0.52	0.79±0.27
31 μg/ml	τ_Δ	14.7±0.09	10±0.16	53.3±0.19
	τ_T	1.59±0.33	1.39±1.24	0.96±0.3
15 μg/ml	τ_Δ	14.1±0.19	-	48.9±0.21
	τ_T	2.5±1.23	-	0.87±0.38

Table 4.12. $^1O_2$ (τ_Δ) lifetimes and PS triplet state (τ_T) lifetimes from Rose Bengal in ethanol, methanol, and acetone at decreasing concentrations.

The singlet oxygen luminescence from Methylene Blue and Eosin Y in ethanol and methanol at decreasing concentration is shown in Figure 4.23. By looking at the luminescence peaks at histograms from Methylene Blue in ethanol and methanol, it is clear that the signal is stronger than that of Rose Bengal solutions. Eosin Y solutions appear to be very inefficient and even acquisitions

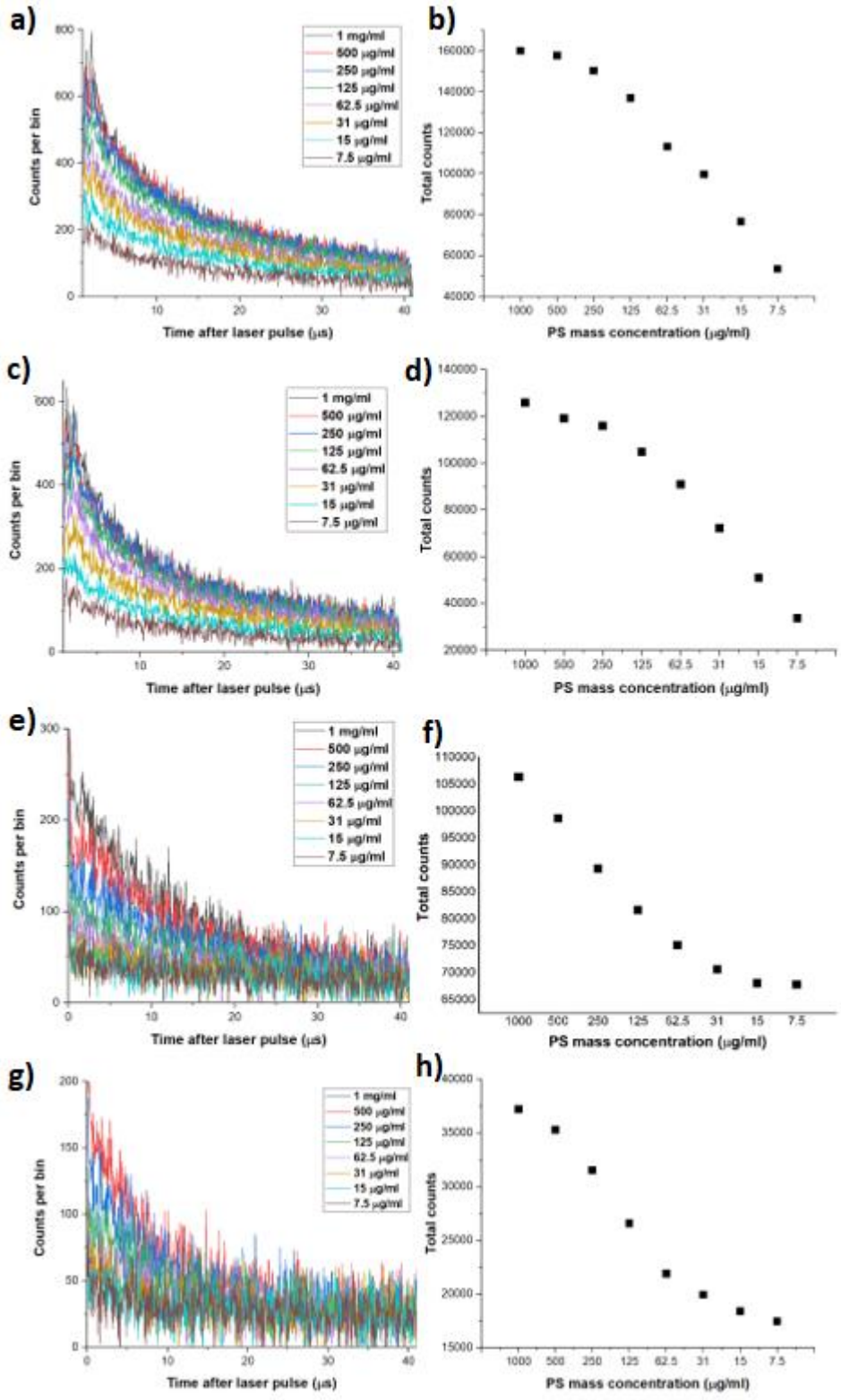

Figure 4.23. 600 second histograms comparing 1590 nm $^1O_2$ luminescence at decreasing concentration for Methylene Blue in a) ethanol, c) methanol and Eosin Y in e) ethanol, g) methanol (left hand side figures). The total counts recorded versus PS mass concentration for Methylene Blue in b) ethanol, d) methanol and Eosin Y in f) ethanol, h) methanol (right hand side figures).

over 10 minutes are not enough to produce a distinguishable curve. Comparing the total count versus photosensitizer concentration plots, total counts acquired by Methylene Blue solutions gradually decrease as the concentration decreases, while for Eosin Y total counts also decrease but seem to be reaching a plateau towards the lower mass concentrations at 15 - 7.5 μg/ml. The extracted lifetimes, shown in Table 4.13, show singlet oxygen values proportional to the solvent used for each solution, following the same trends and levels with Rose Bengal ethanol and methanol solutions. Nevertheless, the photosensitizer triplet state lifetimes do not increase with decreasing concentration like Rose Bengal solutions, they appear to slightly fluctuate between 400 – 560 ns for Methylene Blue in ethanol and 460 – 660 ns for Methylene Blue in methanol. Due to weak luminescence, though, lifetimes from low concentration solutions have big error values. Accordingly, solutions with Eosin Y in ethanol have big error values for PS triplet state lifetimes, while lifetimes from Eosin Y in methanol could not be extracted.

PS Mass concentration	Lifetime (μs)	MB in ethanol	MB in methanol	EY in ethanol
1 mg/ml	τ_Δ	9.75±0.02	8.18±0.03	11.3±0.04
	τ_T	0.56±0.34	0.66±0.8	0.56±4.29
500μg/ml	τ_Δ	10.9±0.03	8.43±0.03	12±0.06
	τ_T	0.43±0.36	0.58±0.49	0.98±0.89
250 μg/ml	τ_Δ	11±0.03	9.13±0.03	12.6±0.11
	τ_T	0.43±0.41	0.54±0.4	1.22±1.59
125 μg/ml	τ_Δ	11.9±0.03	8.96±0.03	13.1±0.03
	τ_T	0.55±0.44	0.51±0.41	1.26±2.34
62.5 μg/ml	τ_Δ	12.1±0.03	8.93±0.03	10.6±0.2
	τ_T	0.4±0.66	0.55±0.46	1.13±6.13
31 μg/ml	τ_Δ	13±0.04	9.77±0.04	1.12±0.39
	τ_T	0.41±18.24	0.54±0.58	1.93±1.58
15 μg/ml	τ_Δ	13±0.04	9.51±0.05	-
	τ_T	0.36±2.35	0.46±0.96	-
7.5 μg/ml	τ_Δ	12±0.05	10±0.07	-
	τ_T	0.1±2.22	0.56±1.98	-

Table 4.13. $^1O_2$ (τ_Δ) lifetimes and PS triplet state (τ_T) lifetimes from Methylene Blue in ethanol and methanol and, Eosin Y in ethanol at decreasing concentrations.

4.3.3 $^1O_2$ luminescence in the presence of a quencher

The behaviour of singlet oxygen in the presence of a carotenoid species, and ß-carotene in particular, was studied. B-carotene is an organic carotenoid pigment found abundant in plants, fruits, even in human serum and tissue, and is the reason why photosynthetic organisms that are photosensitized by chlorophyll are protected from the lethal effects of the sunlight and oxygen combination. ß-carotene is an efficient triplet sensitizer quencher and most importantly a singlet oxygen quencher [247]. However, ß-carotene quenching of the triplet photosensitizer is not responsible for this inhibitory effect in the photochemical reaction of singlet oxygen. Singlet oxygen interacts with ß-carotene and undergoes physical quenching through direct energy transfer between the two molecules. Energy from the excited singlet molecular oxygen is transferred to ß-carotene molecules deactivating oxygen into its ground state and producing triplet excited ß-carotene [245 - 246]. Chemical quenching of singlet oxygen by carotenoids is also possible but the contribution to the total quenching rate is minor [247].

So, to test the anti-oxidant effects of ß-carotene on photosensitized singlet oxygen, various dosages of ß-carotene powder (536.87 g/mol molecular weight) were introduced to existing photosensitizer solution. Because of ß-carotene insolubility in most common solvents, the solution chosen was 30 μg/ml Rose Bengal in acetone. Rose Bengal in acetone as shown earlier is one of the most efficient solutions for generating singlet oxygen molecules with long $^1O_2$ lifetime. The amount of ß-carotene was increased in each measurement starting with 5.7% of the total concentration up to 57.1%. The histograms were acquired over 60 seconds and the SPAD's detection efficiency was set to minimum (10%) due to the high detection rate. In Figure 4.24, the singlet oxygen luminescence from Rose Bengal in acetone with no added ß-carotene is compared to luminescence from solutions with ß-carotene in increasing concentration. Even with a small amount of ß-carotene the luminescence intensity is greatly decreased, and the singlet oxygen lifetime is obviously much shorter. As the ß-carotene concentration increases the luminescence drops and at 57.1% appears that singlet oxygen is completely quenched. The extracted lifetimes for each curve are presented in table 4.14.

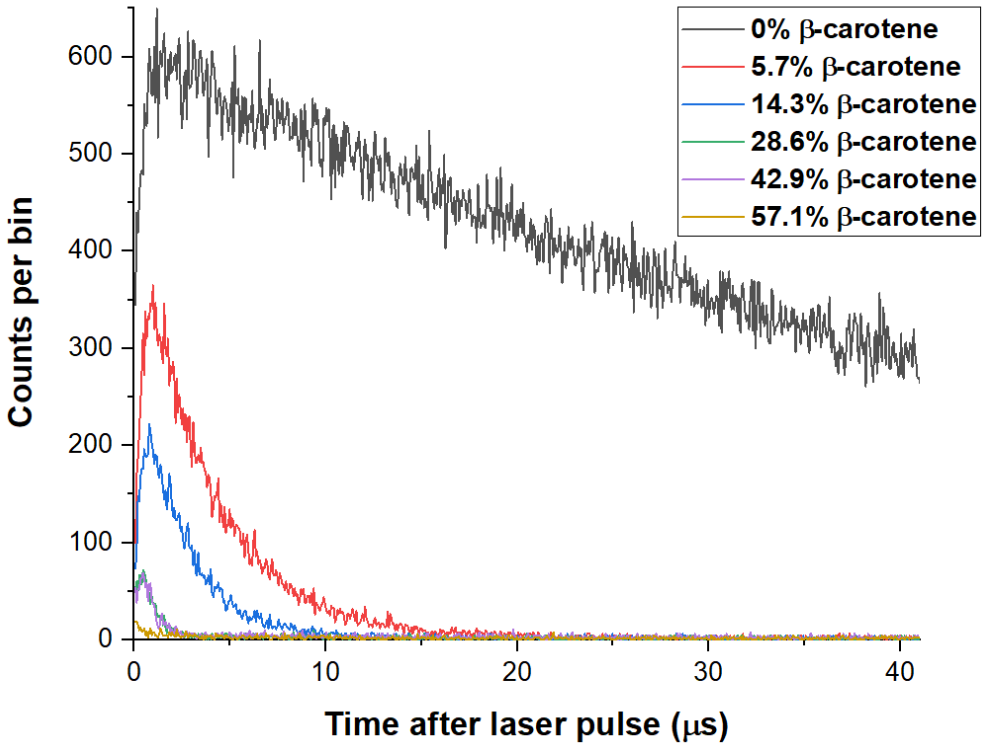

Figure 4.24. 60 second histogram comparing 1270 nm $^1O_2$ luminescence from Rose Bengal in acetone solutions with added ß-carotene. SPAD detector's detection efficiency was set to 10%.

ß-carotene in solution	Lifetime (μs)	RB in acetone
0%	τ_Δ	54.8±0.12
	τ_T	0.65±0.1
5.7%	τ_Δ	3.66±0.01
	τ_T	0.35±0.03
14.3%	τ_Δ	2.27±0.01
	τ_T	0.36±0.03
28.6%	τ_Δ	0.53±0.18
	τ_T	0.38±0.24
42.9%	τ_Δ	0.43±0.6
	τ_T	0.43±0.6
57.1%	τ_Δ	-
	τ_T	-

Table 4.14. $^1O_2$ (τ_Δ) lifetimes and PS triplet state (τ_T) lifetimes from 30 μg/ml Rose Bengal in acetone with increasing concentration of ß-carotene.

Singlet oxygen produced in Rose Bengal in acetone is long lived at 54.8 μs. With the addition of the ß-carotene quencher, the lifetime drops by an order of magnitude with small concentrations and as the quencher concentration increases, the singlet oxygen lifetime decreases by an order of magnitude more, dropping at a few hundreds of nanoseconds. The physical quenching of ß-carotene is very efficient even for small concentrations in the photosensitizer solution with the energy transfer from singlet oxygen to the quencher molecules speeding up the deactivation process. Rose Bengal's triplet state lifetime also appears to be quenched by ß-carotene with the lifetime dropping by 300 ns after the first ß-carotene addition and then stabilizing at this lifetime range of 350-430 ns.

4.4 Conclusions

Singlet oxygen luminescence was efficiently detected through photosensitizer excitation at two different singlet oxygen emission wavelengths centred at 1270 nm and 1590 nm. 1270 nm emission is much more probable with higher intensity than the 1590 nm emission which describes the deactivation of singlet oxygen into a vibrational state. In both cases, multiple photosensitizers were tested and their efficiencies in the overall singlet oxygen signal detected were compared. Also, the singlet oxygen lifetime (τ_Δ) and the photosensitizer triplet state lifetime (τ_T) were hugely affected by the environment the photodynamic process is taking place in, which in this case is the solution consisting of the photosensitizer and the solvent used each time. Organic solvents generate more singlet oxygen molecules than distilled water with singlet oxygen lifetime significantly longer, with the best one tested being the acetone. Deuterated water was also tested, with similar performance to acetone and much longer singlet oxygen lifetime compared to standard water. Subsequently, singlet oxygen luminescence was acquired by solutions with photosensitizers in different concentrations. Singlet oxygen lifetime in most cases is longer with lower PS concentrations, while the signal intensity is usually stronger with higher photosensitizer concentrations. The convolution of these two parameters lead to the optimum concentration value in terms of total singlet oxygen photon detection. Lastly, singlet oxygen was generated, and its luminescence was

acquired in the presence of a known singlet oxygen quencher, ß-carotene. Small concentrations of ß-carotene were added in a solution of Rose Bengal dissolved in acetone and the signal intensity was immediately reduced while the singlet oxygen lifetime was dramatically shortened due the physical quenching applied by the presence of the ß-carotene molecules.

Chapter 5 – Singlet oxygen optical phantom and live cell experiments

5.1 Introduction

Following the engineering of an efficient SOLD setup and the successful detection of $^1O_2$ luminescence (Chapter 4) the next development step is to move singlet oxygen monitoring closer to a PDT clinical case. Therefore, two sets of experiments were carried out and are presented in this Chapter. The first set (section 5.2) involves $^1O_2$ luminescence detection by introducing an optical phantom to the existing photosensitizer solutions in order to simulate the scattering effects of the human tissue and the second set (section 5.3) targets the detection of singlet oxygen photons from live cells. The optical phantom used was a lipoprotein suspension (Intralipid emulsion), while for the live cells two different cell lines were used, normal NIH3T3 fibroblast cells and KPC pancreatic cancer cells. Data from Rose Bengal in distilled water and deuterated solutions with increasing concentration of Intralipid emulsion are presented. Starting with low concentration and increasing towards an established milestone optical phantom concentration, the singlet oxygen behaviour is studied in the presence of the light scatterer. Thereinafter, 1270 nm singlet oxygen luminescence is monitored in live cultured cells incubated with Rose Bengal, experimenting with parameters such as well volume, incubation time, photosensitizer concentration, light exposure time and various pH levels. These initial SOLD experiments in live cells act as a benchmark for future physiological experiments, providing information and answers on the key question whether the existing SOLD setup is able to detect singlet oxygen NIR luminescence from single cells but also, to establish whether the photodynamic effect applied to these cells is capable of causing cell necrosis.

5.2 SOLD measurements in the presence of scattering

Intralipid emulsion ($C_{60}H_{115}NO_{10}P^+$, 1041.5 g/mol molecular weight) is a lipoprotein suspension based on soybean oil and is widely used as a scattering

agent to simulate the light scattering of tissue [248]. Intralipid is used as a highly diffusing optical phantom added at increasing concentration in the photosensitizer solution in order to simulate singlet oxygen generation and deactivation in an environment close to realistic biological conditions. Intralipid concentration at about 2% by mass is a point where it closely represents the optical properties and light scattering of tissue [249]. This kind of diffusion is expected *in vivo* as light and singlet oxygen molecules are interacting with proteins and other biomolecules. Therefore, sensing singlet oxygen luminescence at 2% of Intralipid concentration is crucial and could act as a benchmark for possible follow up physiological experiments.

The optical phantom was mixed with three solutions in total, Rose Bengal in distilled water, Rose Bengal in deuterated water and Visudyne in methanol. The photosensitizer mass concentration for Rose Bengal in distilled water was 100 μg/ml, 50 μg/ml for Rose Bengal in deuterated water and for the less efficient Visudyne in methanol the mass concentration was 500 μg/ml, while the InGaAs SPAD detector's quantum efficiency was set to 10% for the Rose Bengal solutions and 15% for the Visudyne solution. In addition, histogram acquisition time for Rose Bengal solutions was 60 seconds and 180 seconds for the Visudyne solution. The selection of quantum efficiency, mass concentration and acquisition time for each solution was made considering the ability of each one in generating enough singlet oxygen luminescence before and after the addition of Intralipid so that there is no pile-up effect with the initial solution and in Intralipid concentrations close to 2%, singlet oxygen luminescence would be detected. In Figure 5.1 the singlet oxygen luminescence histogram from Rose Bengal in distilled water is presented at increasing Intralipid concentration and the corresponding plot with the total histogram counts comparison of each Intralipid concentration. The dark count rate level is added as a reference. In total four concentrations of Intralipid are tested up to 2%. The luminescence intensity drops as the Intralipid concentration increases. In the 2% of Intralipid curve, the luminescence appears to be weak and the decay is not biexponential. However, the overall signal is much stronger than the corresponding from the DCR itself, meaning that this single exponential decay comes from the singlet oxygen emission through the phantom medium. This can also be verified by the long tail of the decay similar to that of the 1.14% Intralipid concentration, leading to the conclusion that the PS triplet state lifetime is too

short to assist in the formation of the onset of the typical biexponential decay. The summed counts from each solution show a decrease in the total counts as the Intralipid concentration in the mixture is increased, starting almost linearly and then decreasing at a lower rate. Despite the fact that at Intralipid concentration of 2% or higher the decay curve recorded is not biexponential, summing the counts detected we get a number much higher than the DCR level which is almost zero. This indicates that singlet oxygen luminescence signal can be detected at Intralipid concentrations of the targeted benchmark of 2% and beyond and can be further boosted with higher detector quantum efficiencies.

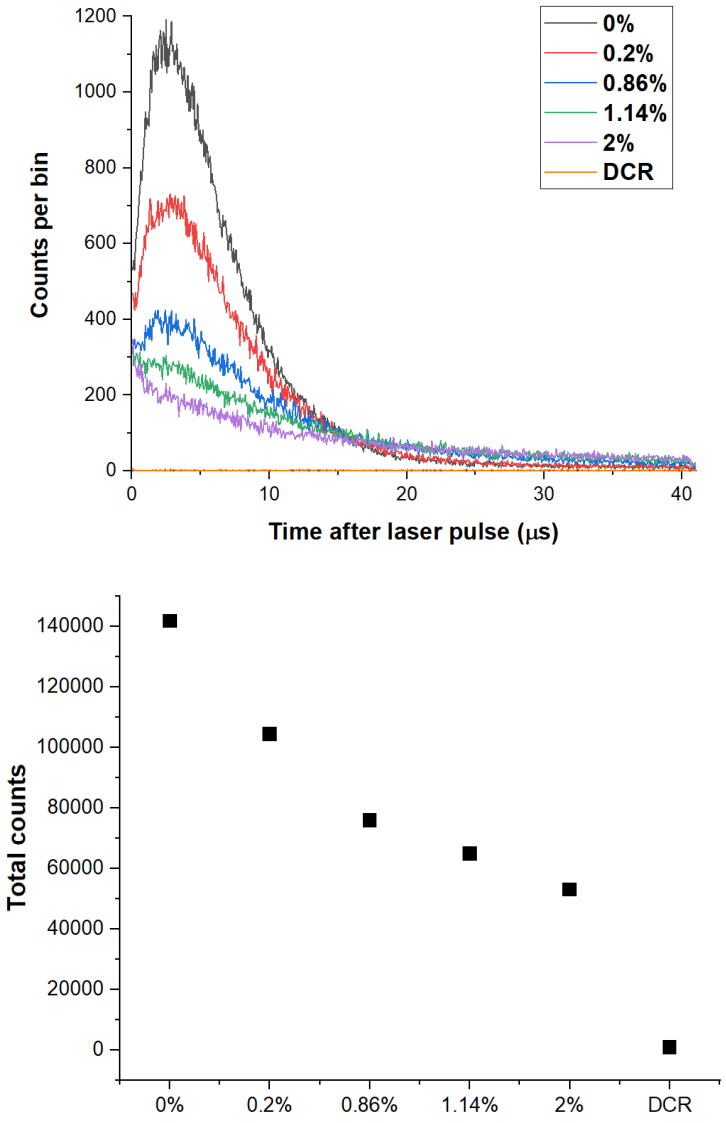

Figure 5.1. 60 second histogram of a) $^1O_2$ luminescence and b) total count comparison from 100 μg/ml Rose Bengal in distilled water with added Intralipid emulsion at increasing concentration.

More information on the effect of Intralipid emulsion in the photosensitizer solution can be obtained by extracting the lifetimes of the acquired histograms. So, in Table 5.1 can be seen that the increasing Intralipid concentration in the solution leads to lengthening of the singlet oxygen lifetime. The singlet oxygen lifetime of Rose Bengal in distilled water is extracted for the solution without the scatterer and steadily increases with added Intralipid emulsion achieving a singlet oxygen lifetime of 10.1 μs long at 2% concentration. The photosensitizer triplet state lifetime (τ_T) does not show such a dramatic change as τ_Δ. A small decrease in τ_T is observed at the first two Intralipid concentrations, while in the 1.14% concentration τ_T slightly increases with a bigger error in lifetime extraction and at 2% τ_T cannot be extracted at all.

Intralipid concentration	Lifetime (μs)	RB in distilled water
0%	τ_Δ	3.24±0.06
	τ_T	2.67±0.07
0.2%	τ_Δ	4.52±0.03
	τ_T	2.42±0.04
0.86%	τ_Δ	6.85±0.03
	τ_T	2.16±0.06
1.14%	τ_Δ	8.93±0.04
	τ_T	2.32±0.13
2%	τ_Δ	10.1±0.02
	τ_T	-

Table 5.1. $^1O_2$ (τ_Δ) lifetimes and PS triplet state (τ_T) lifetimes from 100 μg/ml Rose Bengal in distilled water with Intralipid emulsion at increasing concentration.

After the successful detection of $^1O_2$ luminescence signal from Rose Bengal in distilled water at 2% of Intralipid concentration, a solution of Rose Bengal in deuterated water was tested at increasing Intralipid concentration. As shown in Chapter 4, Rose Bengal in deuterated water is very efficient in exciting molecular oxygen which slowly decays back to triplet ground state over ~40 – 70 microseconds, depending on the photosensitizer concentration. In Figure 5.2 it is shown that luminescence intensity drops as the Intralipid concentration increases,

similar to the distilled water solution shown earlier. The Intralipid concentration for this solution was increased up to 4%. At 2% or higher concentration the decay curve loses the onset phase, while the offset seems to be longer as the Intralipid concentration increases. This lengthening of the curve tail shows an increase in the singlet oxygen lifetime, as expected after the trend observed in the Rose Bengal in distilled water with Intralipid solutions. The total counts appear to drop exponentially with increased Intralipid concentration. The dark count rate level is also added, with total counts just a few thousand fewer than the 4% concentration solution.

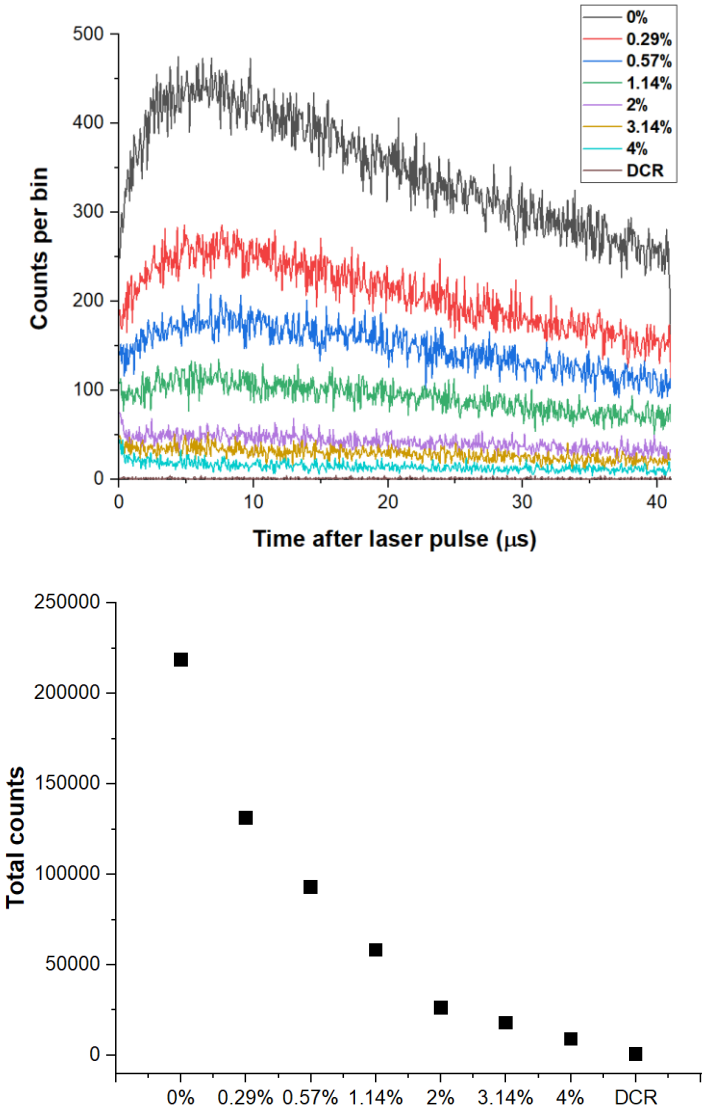

Figure 5.2. 60 second histogram of a) $^1O_2$ luminescence and b) total count comparison from 50 μg/ml Rose Bengal in deuterated water with added Intralipid emulsion at increasing concentration.

The Intralipid emulsion in Rose Bengal in deuterated water affects the singlet oxygen lifetime similarly to the distilled water solution. Because the τ_Δ in deuterated solutions is longer by more than one order of magnitude, the increases in lifetime are bigger as the Intralipid solids increase in number, compared to other solvents. As seen in Table 5.2, the singlet oxygen lifetime is about 51 μs long without any scatterer added and at 2% of Intralipid concentration the lifetime is increased to 86.5 μs. The lifetime for the curves generated by solutions with more than 2% Intralipid concentration could not be extracted as the curves could not be correctly fitted. Regarding the photosensitizer triplet state lifetime, with the addition of Intralipid shows an increase for the two first concentration values and then slightly decreases. Unfortunately, τ_T for 2% or more could not be extracted so it is hard to draw definitive conclusions on the effect of Intralipid solids on the PS triplet state lifetime.

Intralipid concentration	Lifetime (μs)	RB in deuterated water
0%	τ_Δ	51.2±0.2
	τ_T	2.2±0.07
0.29%	τ_Δ	54.5±0.29
	τ_T	3.1±0.12
0.57%	τ_Δ	61.9±0.59
	τ_T	3.52±0.17
1.14%	τ_Δ	63.8±0.78
	τ_T	3.39±0.27
2%	τ_Δ	86.5±1.16
	τ_T	-
3.14%	τ_Δ	-
	τ_T	-
4%	τ_Δ	-
	τ_T	-

Table 5.2. $^1O_2$ (τ_Δ) lifetimes and PS triplet state (τ_T) lifetimes from 50 μg/ml Rose Bengal in deuterated water with Intralipid emulsion at increasing concentration.

Next, the effect of Intralipid emulsion on a different photosensitizer was tested, Visudyne in methanol. The switch to an organic solvent for this solution

means that different optical properties should be expected compared to standard water-based solutions. Therefore, an extra acquisition was made with plain methanol to be used as a control solution. In Figure 5.3, the histogram compares the acquisition curves and total counts from 500 µg/ml Visudyne in methanol with Intralipid emulsion at increasing concentration with the control solution and the dark counts. By adding a small amount of Intralipid, the detected photons decrease dramatically and keep decreasing with increasing concentrations but with a much smaller rate. It is worth noting that a relatively clear biexponential

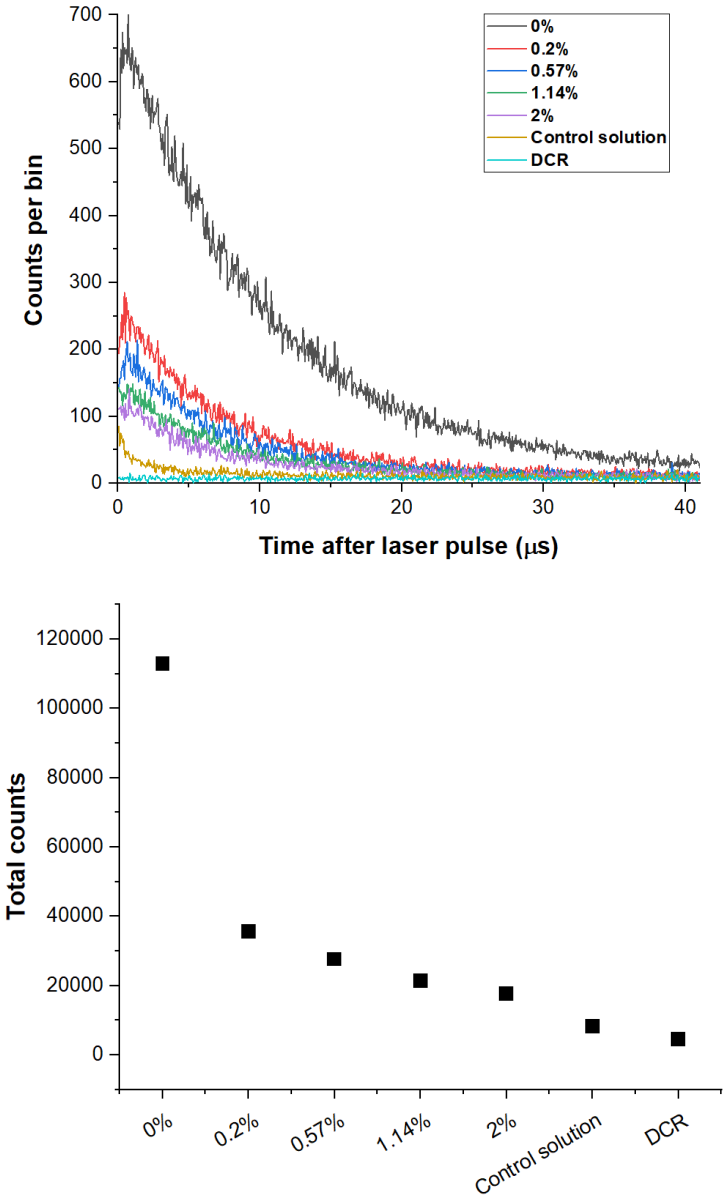

Figure 5.3. 180 second histogram of a) $^1O_2$ luminescence and b) total count comparison from 500 µg/ml Visudyne in methanol with added Intralipid emulsion at increasing concentration.

decay curve with the addition of 2% of Intralipid is obtained compared to the water solutions presented earlier. The summed counts for the 2% concentration are greater than but close to the counts recorded from the plain methanol indicating that a portion of the detected counts is coming from the solvent itself. However, the rest of the counts are actually singlet oxygen photons detected through the scattering medium. The singlet oxygen lifetime from this solution with added Intralipids behaves differently from that observed from the water solutions, as the Intralipid concentration changes. Singlet oxygen lifetime from Visudyne in methanol sees a decrease from 10 μs to 7 μs just by adding a small amount of Intralipid and then keeps getting shorter at a lower rate with higher Intralipid concentration and finally at 2% concentration this lifetime is 6.51 μs. The photosensitizer triplet state lifetime is short at 200 ns as expected from a methanol solution and shows a general increase without major changes as the concentration increases. However, the lifetime errors for τ_T is relatively big while for the 2% concentration the uncertainty is so large the lifetime cannot be extracted at all.

Intralipid concentration	Lifetime (μs)	RB in distilled water
0%	τ_Δ	10±0.01
	τ_T	0.19±0.13
0.2%	τ_Δ	7±0.01
	τ_T	0.16±0.18
0.57%	τ_Δ	6.86±0.02
	τ_T	0.24±0.16
1.14%	τ_Δ	6.76±0.02
	τ_T	0.41±0.41
2%	τ_Δ	6.51±0.02
	τ_T	-

Table 5.3. $^1O_2$ (τ_Δ) lifetimes and PS triplet state (τ_T) lifetimes from 500 μg/ml Visudyne in methanol with Intralipid emulsion at increasing concentration.

The reason for the drop in luminescence counts in all cases is the high diffusion of the excitation and singlet oxygen 1270 nm light into a larger volume caused by the Intralipid emulsion, an area bigger than the collection area leading collection optics to collect light from a much smaller fraction. Also, introducing

the Intralipid emulsion into the photosensitizer solution, the singlet oxygen signal is being quenched via additional deactivation processes and pathways enabled by its interaction with the Intralipid solids. An efficient deactivation pathway caused by Intralipids acting as a singlet oxygen quencher and interacting with Visudyne in methanol could explain the massive drop in luminescence signal and also the shortening of the singlet oxygen lifetime. In any case, the SOLD setup proved to be able to detect singlet oxygen photons even at 2% of Intralipid concentration by using some of the least efficient photosensitizer solutions like the Rose Bengal in distilled water and Visudyne in methanol. The acquired luminescence signal could be increased even more by applying higher optical power and increasing the detector's quantum efficiency, something that was avoided in the first place due to the high count rate at zero or low Intralipid concentration and for the needs of the detailed study of the effect of the scattering medium on the photosensitized singlet oxygen.

5.3 Live cells experiment

For the live cell experiment two different cell lines were cultured, NIH3T3 fibroblast cells and KPC cells. Fibroblasts are the most common mammalian connective tissue cells and the KPC model which is a pancreatic cancer cell line where KPC stands for: Kras, p53, and Cre. Kras and p53 are two genes that are often mutated in human pancreatic tumours. Cre is a special tool gene that is used to control where Kras and p53 are turned on. Cell culture was carried out by Dr. Marie Cutiongco. Microscope images of fibroblast cells and KPC cancer cells are shown in Figure 5.4.

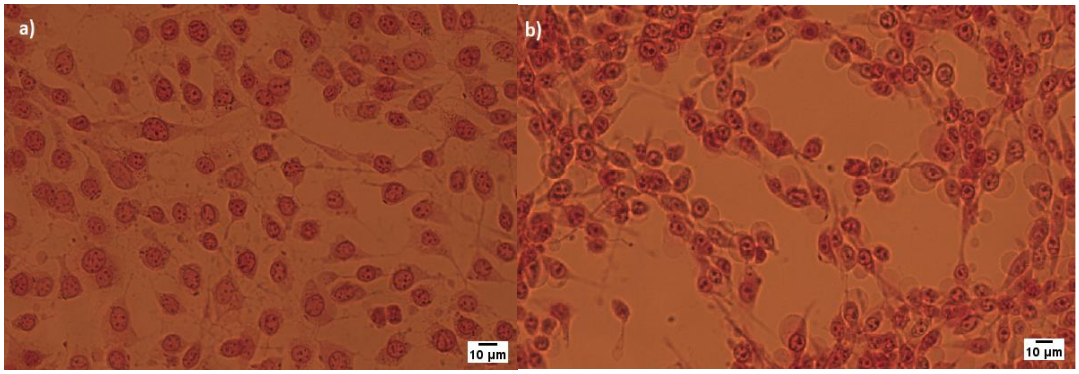

Figure 5.4. Microscope images of a) NIH3T3 fibroblast cells and, b) KPC cancer cells exposed to Rose Bengal. Images captured by Dr. Marie Cutiongco.

Cells were cultured and then incubated with Rose Bengal. For the illumination of the cells with the excitation light, the cells were placed in cell culture plates with wells of specific volume in the system shown in Figure 3.4. Since these experiments require much smaller containers compared to the standard solution cuvette, initial experiments included tests with various plates with wells of different volume containing Rose Bengal solutions in different mass concentrations. Figure 5.5 shows the total counts from the singlet oxygen luminescence acquired from the Rose Bengal in distilled water solution using three different well volumes (50 µl, 100 µl and, 200 µl). Rose Bengal's mass concentrations used were 500, 250, 100, 50, 25, 12.5 and 6.25 µg/ml.

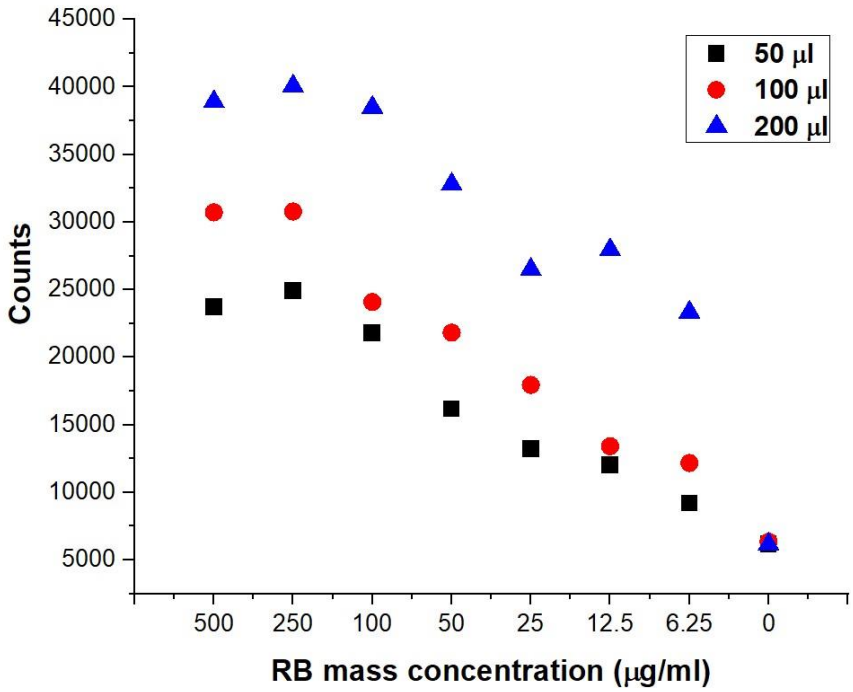

Figure 5.5. Singlet oxygen luminescence counts from Rose Bengal in distilled water solution at dropping concentrations whilst comparing signal from different solution volumes (50, 100, 200 µl). Each acquisition was 60 seconds. The SPAD detection efficiency set to 25% at -90 °C.

Next, in order to understand the incubation of the cells with Rose Bengal molecules a test was required to monitor the absorbance of Rose Bengal by the cells over time and at different mass concentrations. Therefore, cells exposed to Rose Bengal were measured after 1 hour, 3 hours, 6 hours, and 22 hours, as shown

in Figure 5.6. The absorbance measurement of the Rose Bengal uptake by the normal and the cancer cells was carried out by Dr. Marie Cutiongco. In both cell lines, the Rose Bengal uptake was higher for the 500 μg/ml mass concentration and in most

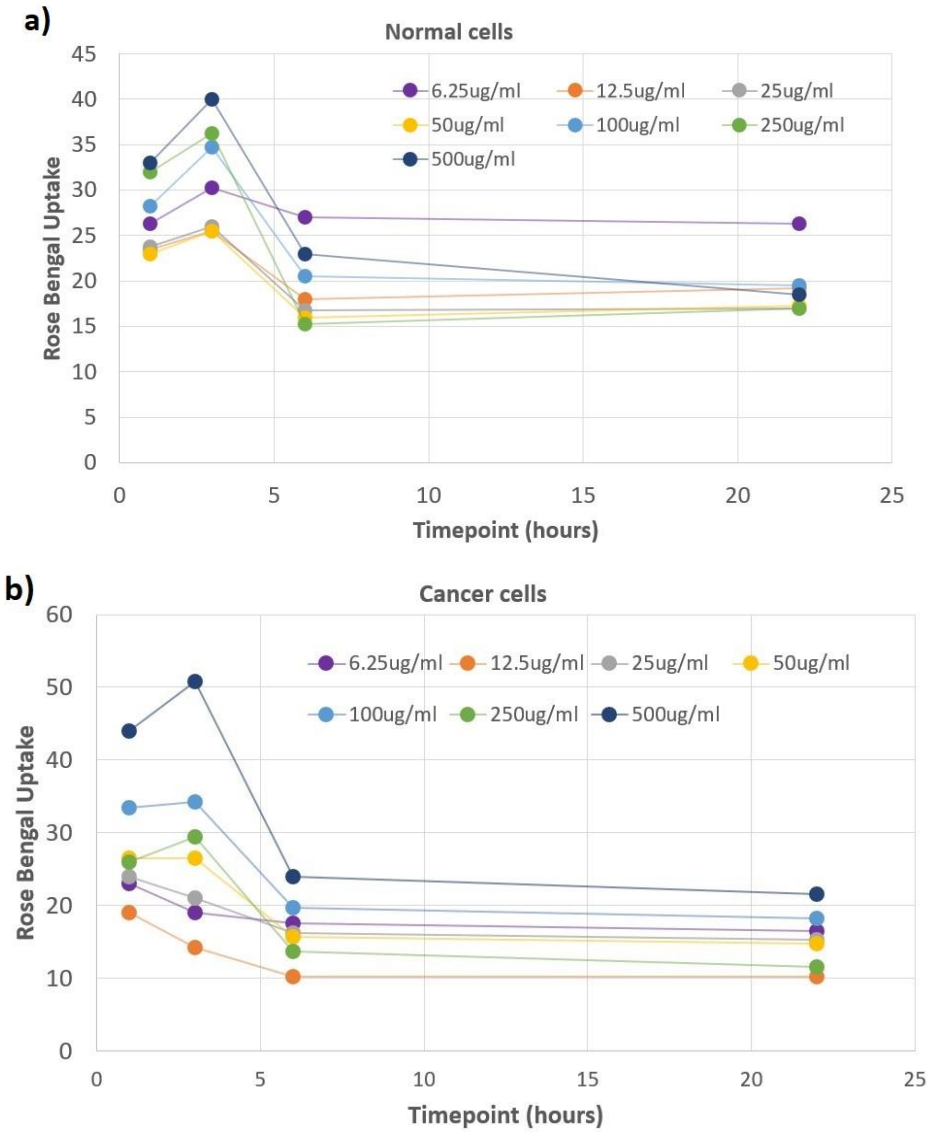

Figure 5.6. Rose Bengal absorbance by normal and cancer cells over 22 hours and at different Rose Bengal concentrations. The lines between points for each Rose Bengal concentration are a guide to the eye. Data acquired by Dr. Marie Cutiongco.

solutions the highest absorbance occurs when exposed for 3 hours. At 6 hours a significant drop is observed reaching a plateau and showing no more changes in

the photosensitizer absorbance. For normal cells, 500 μg/ml is closely followed by the 250 μg/ml solution and then the 100 μg/ml, while for cancer cells the 500 μg/ml has the highest Rose Bengal absorbance standing out from the rest of the solutions, followed by 100 μg/ml and then the 250 μg/ml. In low Rose Bengal concentration cancer cells, the highest uptake is observed during the first hour of exposure. Pictures from the Rose Bengal uptake measurements are included in Appendix B.

After determining the proper well volume and the Rose Bengal exposure time, the cells incubated with photosensitizer were taken for testing. As a start, the signal acquired by these cells at 1270 nm was compared to signal through other bandpass filters to validate that the photons detected are coming from the singlet oxygen emission. A plot comparing the total counts detected by cancer cells incubated with Rose Bengal at five different bandpass centre wavelengths is shown in Figure 5.7. Total counts detected using the 1270 nm bandpass optical filter clearly stand out from the rest of the measurements with the other bandpass filters, validating the singlet oxygen signature in the luminescence detection measurements.

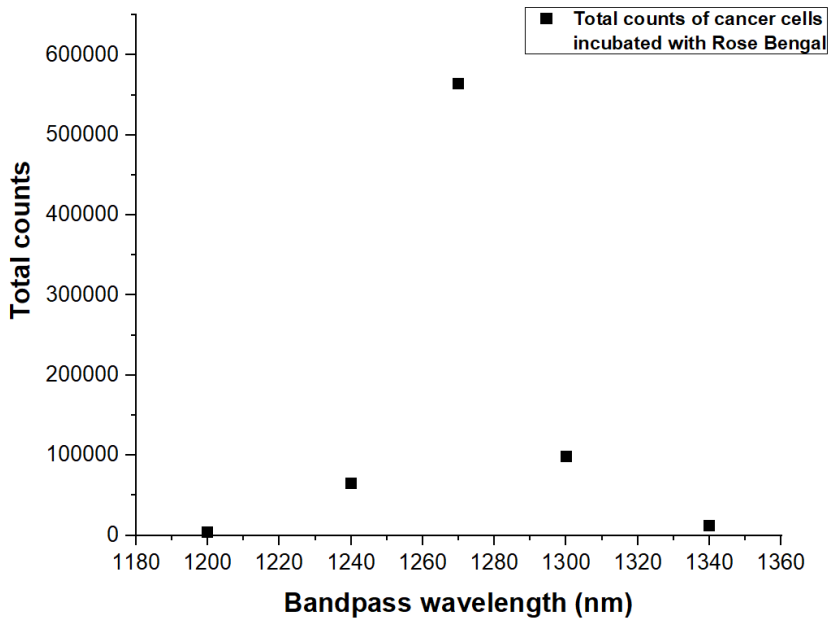

Figure 5.7. Comparison plot of total counts acquired from the cancer cells incubated with Rose Bengal versus the BP optical filter centre wavelength. Acquisition time is 60 seconds and SPAD's detection efficiency set to 25%.

The next step was to compare the counts acquired by cells incubated with Rose Bengal to other solutions with or without any photosensitizer added. Equal volume wells were filled with solutions of Rose Bengal in distilled water, Rose Bengal dissolved in standard cell culturing media (without cells), Rose Bengal with plain cells dissolved in cell media (cells were not incubated with the Rose Bengal), incubated cells with Rose Bengal in the cell media, cells in cell media without any Rose Bengal and, plain cell media. All these different solutions were illuminated and counts were recorded under the same laser and detector conditions. The total counts comparison between the different solutions are presented in Figure 5.8. As expected, Rose Bengal in distilled water solution produces the most singlet oxygen photon counts, followed by the Rose Bengal dissolved in cell media instead of the distilled water. Close to the latter is the solution with cells (not incubated with RB) in cells media and added Rose Bengal. The total singlet oxygen counts from normal cells incubated with Rose Bengal is about 50% weaker than the corresponding solution with cells and Rose Bengal without being incubated inside the cells, while the singlet oxygen signal from pancreatic cancer cells is about 30%. This decrease in the signal when Rose Bengal is incubated inside the cells is expected as the photosensitizer molecules are no longer dissolved in some solvent (cell media), but instead are located inside the cell membrane where protein and other singlet oxygen quenching components are [250]. Also, the environment where the cells are cultured, the cell media, include FBS (fetal bovine serum) a common serum type used in cell culture because of its high content of embryonic growth promoting factors. The serum is known to be an efficient singlet oxygen quencher leading to shortened singlet oxygen lifetime. The last three acquisitions from plain cell media, plain cells in cell media without any photosensitizer added and the dark count rate level are included to differentiate the singlet oxygen signal level generated by the Rose Bengal incubated cells from the signal coming from control solutions without any singlet oxygen luminescence. Between the singlet oxygen counts recorded by the normal cells and cancer cells incubated with photosensitizer, the cancer cells appear to be about 50% more efficient than the normal cells, registering ~10000 more counts as shown in Figure 5.8.

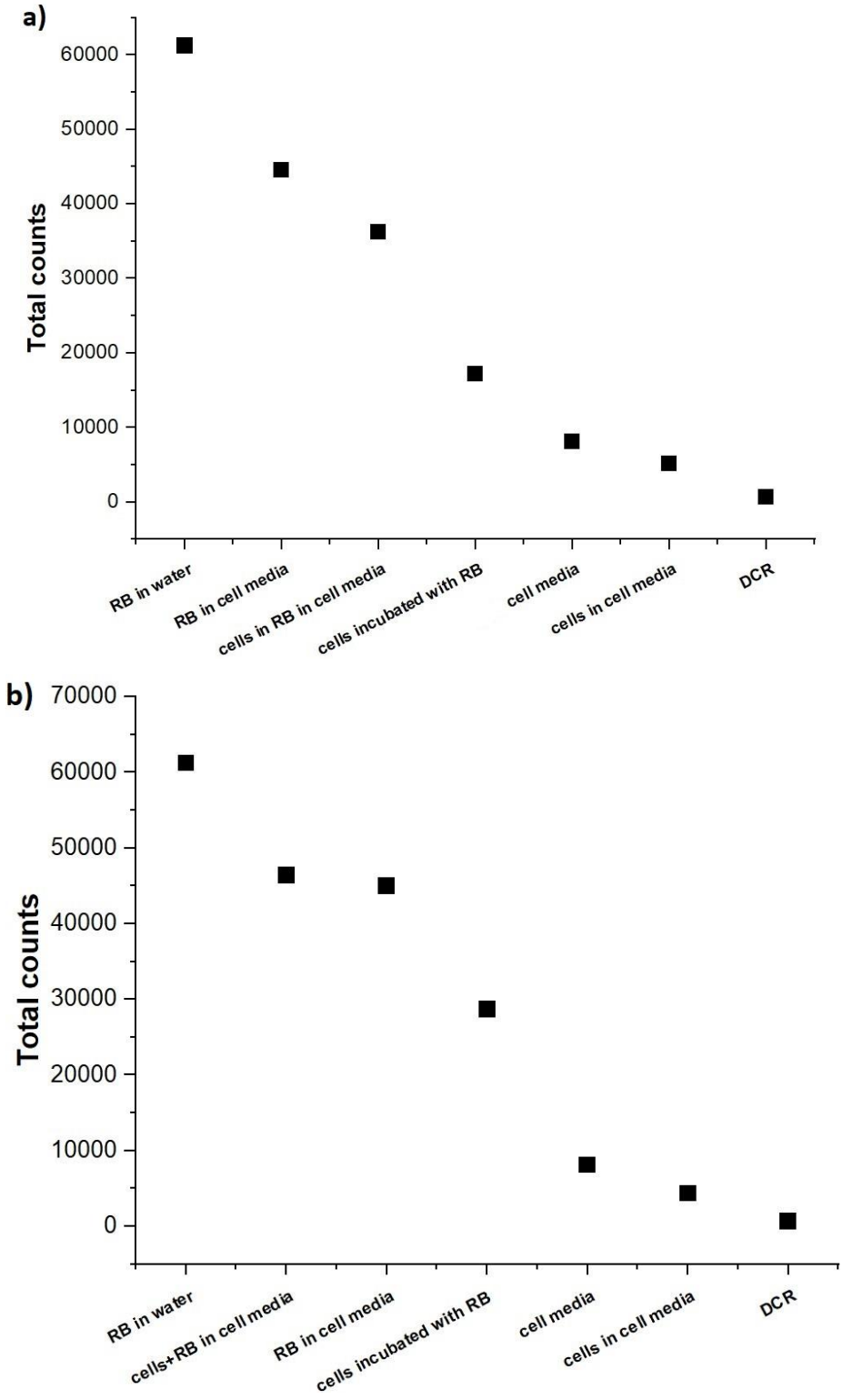

Figure 5.8. Total count comparison between a) normal, b) pancreatic cancer cells incubated with Rose Bengal and various control solutions. The conditions are presented in order maximum to minimum total counts (left to right). Rose Bengal concentration is the same for the different solutions. Acquisition time is 60 seconds and SPAD detection efficiency set to 10%.

In order to mitigate the huge quenching of the singlet oxygen signal by the serum in the cell media, the serum was removed from the solution after the growth of the cells. This allowed the efficient collection of the singlet oxygen photons generated inside the Rose Bengal incubated cells without the quenching components. As shown in Figure 5.9, the shape of the singlet oxygen signal by normal and cancer cells in cell media is very similar to the standard Rose Bengal in water solution. Both cell lines were exposed to Rose Bengal for 3 hours, washed out and then added in cell media where the serum was later removed. Luminescence from cancer cells is slightly stronger with a more distinguishable peak. This variation in the shape is depicted in the extracted lifetimes shown in Table 5.4.

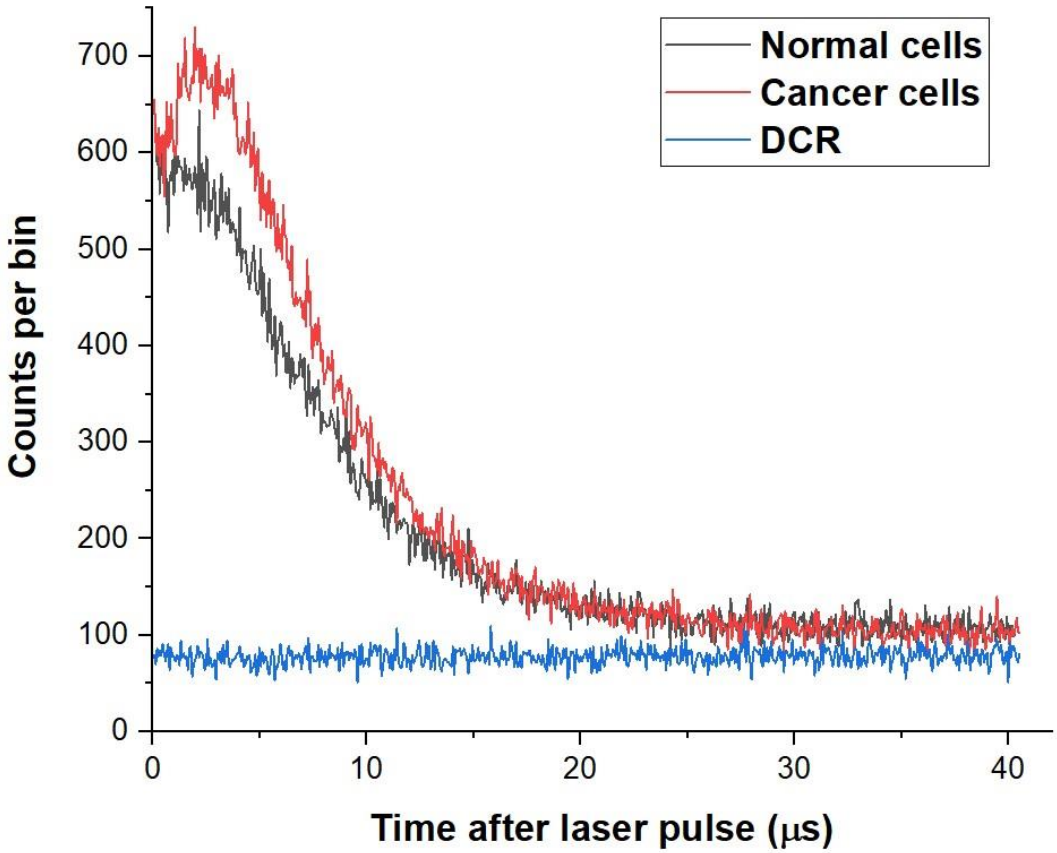

Figure 5.9. 600 second histogram of $^1O_2$ luminescence signal by normal and cancer cells incubated with Rose Bengal in cell media without serum. Cells were exposed to Rose Bengal for 3 hours. SPAD detector set to -90 ºC, 25% detection efficiency and 42 μs dead time.

The singlet oxygen luminescence signal from Rose Bengal incubated cancer cells in cell media with the serum was also recorded and is plotted in Figure 5.10 alongside the corresponding without the serum in the cell culturing media. Singlet oxygen luminescence in the presence of a serum is heavily quenched and singlet oxygen lifetime is significantly shorter.

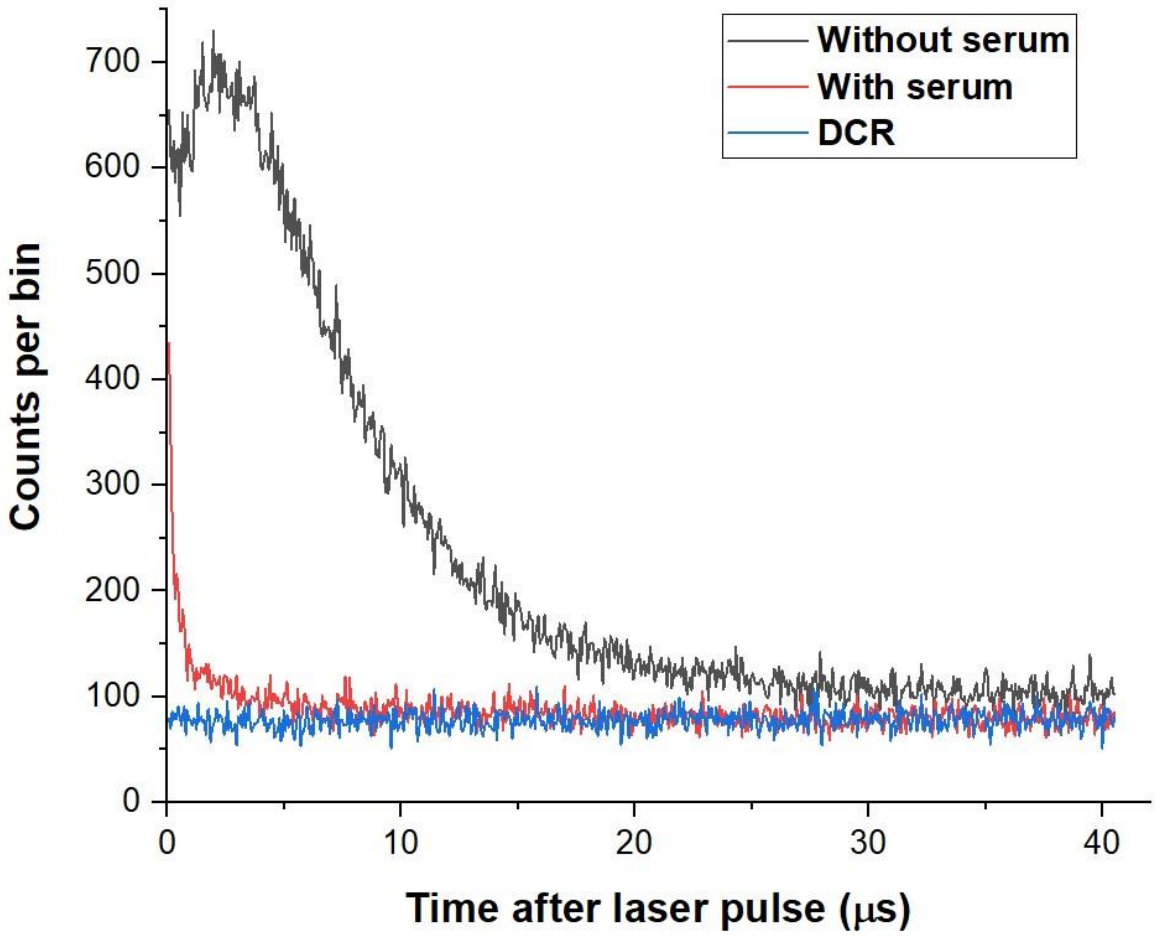

Figure 5.10. 600 second histogram of $^1O_2$ luminescence signal by cancer cells incubated with Rose Bengal in cell media with and without serum. Cells were exposed to Rose Bengal for 3 hours. SPAD detector set to -90 ºC, 25% detection efficiency and 42 μs dead time.

$^1O_2$ lifetime in a serum-free cell environment is typically in the range of τ_Δ in H_2O (~3.0–3.5 μs) or even longer depending on where the photosensitizer is located inside the cell [251]. As shown in Table 5.4, τ_Δ in serum-free cell media is very similar to the H_2O τ_Δ values at 3.55 μs for the pancreatic cancer cells and

considerably longer at 4.45 μs for the normal fibroblast cells. The difference in the τ_Δ lifetime between normal and cancer cells can be explained considering the different singlet oxygen diffusion from the cell nucleus and cell membrane over to extra-cellular environment and possible different spatial localization of the Rose Bengal. When serum is present though, the singlet oxygen lifetime is heavily affected by this extra-cellular component and is significantly shorter at 510 ns. This could also indicate that the Rose Bengal is mostly concentrated in the outer regions of the cell rather than in the cell nucleus.

Lifetime (μs)	Normal cell in cell media without serum	Cancer cell in cell media without serum	Cancer cell in cell media with serum
τ_Δ	4.45±0.09	3.55±0.2	0.51±0.04
τ_T	3.01±0.14	3.55±0.2	-

Table 5.4. $^1O_2$ (τ_Δ) lifetimes and PS triplet state (τ_T) lifetimes from normal and cancer cells incubated with Rose Bengal in cell media with and without serum.

Apart from the singlet oxygen luminescence detection, the status of the cells was also checked after a few hours or even days. Due to the photodynamic effect, the cells were expected to die after a reasonable amount of time. However, that wasn't the case for some of the cell batches. In fact, some of the cells died after the illumination period, but most of the batches were still alive even after a few days. This inconsistency in the cell necrosis after the photodynamic effect they underwent, could be due to two possible reasons. First, the cells in serum-free cell media were not able to survive without the serum. So, after the SOLD measurements the serum was added once again and that is maybe the factor that managed to keep the cells alive even after the photodynamic effect that lasted up to 30 minutes. The second reason is because of the laser beam spot size and the actual optical power applied on the cell surface. The beam spot size, as calculated in § 4, is 13.64 μm wide and covers a small portion of the overall well area. That means that only a few cells were illuminated with ~1.4 mW of optical power (at 540 nm, the excitation wavelength of Rose Bengal), an optical power value that is much smaller anyway than that applied in physiological

photodynamic therapies. An attempt to illuminate the whole well surface was made by increasing the distance between the reflective mirror and the well, so that the beam was off-focus and the spot size was increased covering a much larger area. However, this also resulted in a much weaker optical power density and it would be difficult for the applied light to generate enough singlet oxygen and cause efficient photodynamic effects. Microscope pictures from the cells are included in Appendix B, showing their status after the laser illumination and monitoring for 8 days.

5.4 Conclusions

Singlet oxygen luminescence was successfully detected in solutions containing an optical phantom in different concentrate ons, to simulate the light scattering effects of human tissue. Measurements were carried out using Rose Bengal in distilled water and deuterated water and, Visudyne in methanol adding increasing amounts of Intralipid emulsion. In all three solutions, singlet oxygen was efficiently detected even at 2% of Intralipid concentration, an established milestone optical phantom concentration simulating the optical properties of human tissue. Additionally, in some cases the SOLD setup was able to detect singlet oxygen luminescence even at concentrations greater than 2% of Intralipid. The second part of this chapter concerns experiments in which singlet oxygen is generated and its emission is detected from the inside of the cells. Two different types of cells were used, normal fibroblast and KPC cancer cells. Initially, a series of experiments were carried out to establish the ideal parameters for the SOLD measurements, including photosensitizer uptake from the cells and the volume of the well where cells are cultured. Then, singlet oxygen luminescence was efficiently detected in a variety of different solutions including solutions with plain photosensitizer, plain cell media and cells not exposed to photosensitizer, which were used as control solutions and to be compared to singlet oxygen signal from cells incubated with photosensitizer. While singlet oxygen photon counts were registered from cells incubated with photosensitizer, the time-resolved measurements appeared to be harder to record due to the high quenching from serum contained in the cell media, which is essential in the cell culturing process.

So, in order to record singlet oxygen decay histograms, serum was removed for the light exposure period of the cells and singlet oxygen biexponential decay was efficiently recorded and was compared to cell solutions with serum. Moreover, singlet oxygen lifetime (τ_{Δ}) from normal and cancer cells without serum was extracted and compared the much shorter singlet oxygen lifetime of cells in cell media with serum. After the SOLD measurements, cells were monitored for up to 8 days. The photodynamic effect should be responsible for the cell death, but that was not observed for all the cells exposed to light. The main reason for cells not dying during or after the process was attributed to the low optical power applied onto them, in combination with the overall light beam spot not being able to cover the entire well area so that all the cells are undergone the photodynamic process simultaneously.

Chapter 6 – Outlook

6.1 Conclusions

This thesis presents work on a sophisticated optical setup capable of efficient photosensitized generation of singlet oxygen and single photon detection of its luminescence. Aim of this project was the engineering of a versatile setup utilizing next generation fibre-coupled single photon detectors that can potentially be used in clinical photodynamic therapies providing valuable real time information on the dosimetry of the drug administrated to the patient.

Chapter 1 gave a brief introduction to the work and a layout of the structure of the thesis.

Chapter 2 consists of a background and literature review of the various aspects included in this thesis. The photochemistry of singlet oxygen, the photosensitizers and a brief background on the photodynamic therapy was described in the first part of this chapter. Subsequently, a background on the different single photon detectors was given focusing on the single photon avalanche diode and superconducting nanowire single photon detectors that were used in this project. Lastly, some theory on the time-correlated single photon counting techniques and modules was given, explaining the means of the singlet oxygen luminescence data acquisition described in the following chapters.

Chapter 3 gives a detailed look at all the components selected for the experimental setup. The chapter starts with a brief background on the various light sources used in photodynamic therapy and explains the selection of the supercontinuum laser source used for the experiments. Similarly, the careful selection of the optical filters and mirrors consisting the optical head were discussed and the laser's visible light delivery onto the sample and generated singlet oxygen's near-infrared light collection was explained. Then, the two types of single photon detectors used throughout the project were analysed. First, the superconducting nanowire single photon detector inside the close-cycled cooling system and the experimental configuration for the characterisation of each SNSPD device, gathering information on the I-V characteristics, the single photon detection efficiency at various wavelengths, the dark count rate and timing

properties such as the FWHM timing jitter of the device. The second single photon detector used is a commercial InGaAs SPAD characterised for the 1550 nm wavelength. Carrying out a series of measurements, its detection efficiency and dark count rate at a wider spectral range and different operation temperatures were acquired. A more general comparison was made between the SNSPD and SPAD detector and explained which detector proved to be better for obtaining the best possible results in this specific singlet oxygen project. Lastly, the TCSPC module was presented and discussed giving an insight of the singlet oxygen luminescence measurement data formats, while also it explained the fitting of the singlet oxygen biexponential curve for the extraction of the two lifetimes.

Chapter 4 focusses on the singlet oxygen luminescence detection in solution. The chapter begins by presenting the various photosensitizers used and gives information on the structure and absorption spectra of each one. The chapter continues by explaining the SOLD technique and the singlet oxygen phosphorescence signal equation. A series of measurements in the 1270 nm wavelength band is then presented, showing singlet oxygen luminescence histograms and lifetime tables extracted from solutions of different photosensitizers and solvents, and a general comparison is made between the results comparing the efficiency of each solution and the two lifetimes. Additionally, a series of measurements is presented with the same solutions but in decreasing mass concentration, discussing the effect of the concentration change in the overall luminescence signal and the lifetimes. Time-resolved measurements of singlet oxygen luminescence in the 1590 nm wavelength are presented for the first time, carrying out the same experiments performed at 1270 nm wavelength and a comparison is made regarding the luminescence signal and the lifetime values extracted. The last part of the chapter shows the singlet oxygen signal acquisition in the presence of a known quencher, β-carotene. The β-carotene is added in increasing concentration into the solution and the singlet oxygen signal and its lifetime is observed to drop dramatically.

Chapter 5 is the continuation of the singlet oxygen luminescence measurements moving the experimental conditions closer to a real biological environment. Singlet oxygen signal was generated in a solution with increasing concentration of Intralipid emulsion. This optical phantom at about 2% of concentration simulates the optical scattering properties of human tissue, in

which the singlet oxygen was activated, and its luminescence was efficiently detected. The second part of this chapter deals with singlet oxygen luminescence detection from two types of living cells, normal fibroblast cells and pancreatic cancer cells. Various measurements were carried out regarding the photosensitizer uptake time and concentration from the cells and 1270 nm luminescence detection measurements were carried out for a series of wells with different parameters so that a comparison can be made to the signal from the cells with incubated photosensitizer. Finally, histograms were generated from singlet oxygen signal inside the cells and lifetime values were extracted.

6.2 Future work

A complete optical setup optimized for singlet oxygen measurements was demonstrated through characterisation to be quite efficient. The current platform gives high collection rates and is versatile enough to try out different detector configurations and experimental scenarios. However, the existing setup can be further improved and optimised for different singlet oxygen luminescence monitoring scenarios.

6.2.1 SOLD setup configuration

As photonic technology keeps moving forward, the introduction of new components could enable the next breakthrough in the singlet oxygen sensing. Regarding the optical setup, while the optical head including all the mirrors and optical filters appear to be well designed, improvements on the light source or the near-infrared single photon detector are feasible. A drawback of the existing supercontinuum laser is the weak optical output power. Despite the fact that the centre wavelength tuning and low repetition rate offered by this supercontinuum laser are ideal for SOLD experiments, an increase in the overall optical power delivered to the sample would be able to generate much more singlet oxygen molecules leading to higher detection rate. A second improvement of the existing setup could be the replacement of the collection optical fibre (SMF-28e) with a

custom optical fibre specially optimized for the 1270 nm wavelength (ideally a multi-mode fibre for increased collection area), so that the collection will be as efficient as possible. For the single photon detector, there is plenty of room for improvement as photon counting technologies are constantly advancing. The factors that affect the overall singlet oxygen signal detection is the detection efficiency of the detector in the 1270 nm wavelength band and the active collection area of the detector chip. The latter proved to be very important in the overall light collection and is the reason the InGaAs SPAD was eventually used over the SNSPD, despite the higher detection efficiency of the SNSPD. SNSPDs offer high detection efficiencies but the active area is significantly smaller than other detector types. The ideal scenario would be a SNSPD array, consisted of 4 or more pixels that would increase the overall size of the detector, and optimized for 1270 nm wavelength photons. The case of a SNSPD array would also solve the problem with the pulse 'pile up' effect as the total count rate would be divided by the number of the detector pixels. Respectively, InGaAs SPAD arrays would potentially be a great fit in the current setup increasing further the detection area and also form a multi-pixel singlet photon camera in the near-infrared spectral region. Additionally, other types of NIR SPADs are gathering much research focus, such as the SiGe-SPAD mentioned in §2. SiGe-SPAD is a very promising alternative to the InGaAs SPAD that can eventually offer high quantum efficiency near the wanted 1270 nm wavelength.

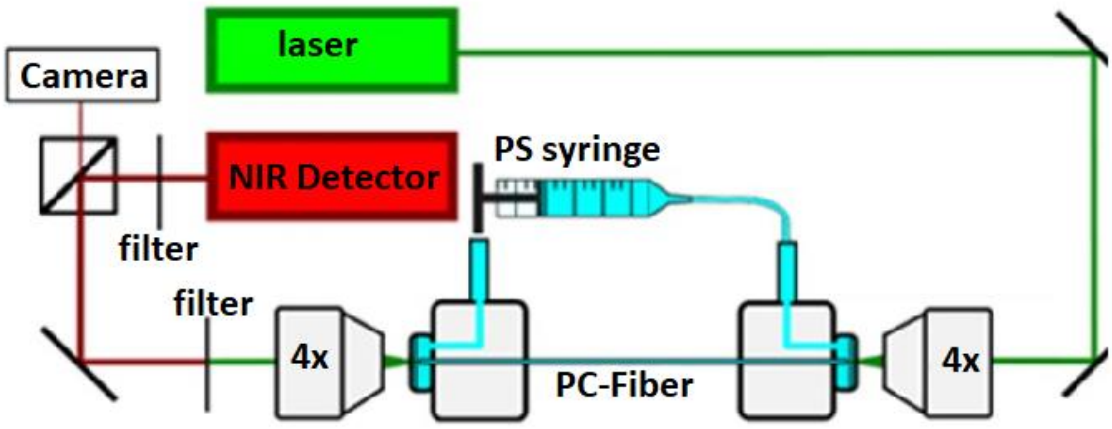

Figure 6.1. Schematic of the setup. The hollow core of the fibre can be filled with photosensitizer while illuminated to generate singlet oxygen molecules that will be detected by the other end of the fibre. Figure modified from [252].

A different approach of $^1O_2$ luminescence detection was proposed by Williams *et al.*, where the photosensitized singlet oxygen can be generated and detected inside an optofluidic system using a 15 cm hollow-core photonic crystal fibre (HC-PCF) [252]. An example diagram of a HC-PCF experimental setup is shown in Figure 6.1. This alternative could allow efficient detection of singlet oxygen even in small quantities and detection of $^1O_2$ luminescence intracellularly [253]; this approach is attractive for clinical therapy, making the optical setup less bulky with an interchangeable fibre-optic probe.

6.2.2 1590nm and 1920nm wavelength bands

An interesting area of future research was presented in this thesis, continuing fundamental studies in two different singlet oxygen emission wavelengths, at 1590nm and 1920nm. Measurements were demonstrated in this thesis on the $^1\Delta_g \rightarrow {}^3\Sigma_g^-$ (v = 1) transition, emitting at ~1590nm wavelength. Time-resolved measurements allowed a deeper understanding of this much weaker singlet oxygen emission. Additional experiments can be carried out and provide useful information on the photochemistry of singlet oxygen. An interesting experiment would involve direct excitation of molecular oxygen with powerful 1270 nm light and detection of the 1590 nm emission. Also, the optical head setup could be easily modified to a T-setup configuration where two different pathways could simultaneously detect both 1270 nm and 1590 nm emission and make a more trustworthy comparison on the intensity and probability between the two signals. Similarly, next generation fast SNSPDs with single photon sensitivity in the mid-IR could potentially be able to detect the picosecond long $^1\Sigma_g^+ \rightarrow {}^1\Delta_g$ emission at ~1920 nm wavelength [254, 255]. This would require a picosecond fast SNSPD with optical cavity tuned around 2 μm, close to 1920 nm wavelength and a couple of alterations in the current optical setup, like a 1920 nm bandpass optical filter (also maybe a long-pass optical filter with cut-on wavelength >1600 nm, to block any 1270 nm and 1590 nm light) and a more suitable collection fibre for wavelengths towards the mid-IR such as standard SMF2000. Time-resolved measurements in the singlet sigma state would be brand-new science in the photochemistry field of

molecular oxygen, like the 1590 nm emission, and could be examined as a possible alternative to 1270 nm emission for detection in future clinical trials, as 1920 nm photons are in a spectral range where there should be less absorption by the biomolecules. In this thesis time resolved singlet oxygen luminescence measurements have been carried out for the first time at 1590 nm using an SNSPD. These studies can be followed up using next generation SNSPDs. SNSPD offer a pathway to high speed low noise photon counting in the mid-infrared: this makes study of longer wavelength emission from the singlet oxygen system (for example 1920 nm wavelength) in principle feasible.

6.2.3 Singlet oxygen live cell microscope

In §5 were presented initial experiments with singlet oxygen luminescence detection in live cells. Further improvements and modifications in the whole setup could better tune it for biological experiments. An optimized singlet oxygen microscope for live cell studies would introduce new possibilities in the singlet oxygen detection from live cells. The ocular lens can be replaced with one of the fibre-coupled single-photon detectors, the illuminator (light source) with a different light source matching the photosensitizer's peak excitation wavelength, while the filters are easily replaced with others of more suitable wavelengths for SOLD experiments. A powerful addition would be a photon counting camera such as the Princeton Lightwave InGaAs SPAD camera (mentioned in section 2.4.2) or an optimized SNSPD array [177, 221, 222]. The singlet oxygen cell microscope would provide real-time monitoring of the illumination of the cells and possible cell necrosis by the photodynamic effect. It could also provide topological information on the photosensitizer accumulation and diffusion inside the cell.

6.2.4 Fibre-optic dosimetry head for PDT

The end goal of this SOLD research is the implementation of the whole optical setup in clinical trials and its test with more clinically-approved

photosensitizers in clinical trials with test animals and in the end phase with humans. The need of a direct monitoring of the PDT treatment and the efficient regulation of the drug in the patient lead to the need of practical setups that act as a routine tool and will assist the treatment in making it as efficient as possible. Current setup is ready to be incorporated in standard PDT treatments as a fibre-optic dosimetry/treatment head as it will provide direct PDT dosimetry and also, potentially a $^1O_2$ luminescence imaging system.

References

1 Nisbet E, Sleep N. The habitat and nature of early life. Nature. 2001;409(6823):1083-1091.

2 Lesser M. Oxidative stress in marine environments: Biochemistry and Physiological Ecology. Annual Review of Physiology. 2006;68(1):253-278.

3 Mulliken R. Interpretation of the Atmospheric Oxygen Bands; Electronic Levels of the Oxygen Molecule. Nature. 1928;122(3075):505-505.

4 Ogilby P. Singlet oxygen: there is indeed something new under the sun. Chemical Society Reviews. 2010;39(8):3181.

5 Paterson M, Christiansen O, Jensen F, Ogilby P. Overview of Theoretical and Computational Methods Applied to the Oxygen–Organic Molecule Photosystem. Photochemistry and Photobiology. 2006;82(5):1136.

6 Schweitzer C, Schmidt R. Physical Mechanisms of Generation and Deactivation of Singlet Oxygen. ChemInform. 2003;34(29).

7 Nonell S, Flors C. Singlet oxygen: Applications in Biosciences and Nanosciences Vol 1. Cambridge: Royal Society of Chemistry; 2016.

8 Herzberg G, Mrozowski S. Molecular Spectra and Molecular Structure. I. Spectra of Diatomic Molecules. American Journal of Physics. 1951;19(6):390-391.

9 Schmidt R, Bodesheim M. Time-Resolved Measurement of O2($^1\Sigma_g^+$)) in Solution. Phosphorescence from an Upper Excited State. The Journal of Physical Chemistry. 1994;98(11):2874-2876.

10 Turro N, Ramamurthy P, Scaiano J. Modern molecular photochemistry. 2nd ed. Mill Valley, Calif.: University Science Books; 2010.

11 Gerschman R, Gilbert D, Nye S, Dwyer P, Fenn W. Oxygen Poisoning and X-irradiation: A Mechanism in Common. Science. 1954;119(3097):623-626.

12 Gerschman R, Gilbert D, Nye S, Fenn W. Influence of X-Irradiation on Oxygen Poisoning in Mice. Experimental Biology and Medicine. 1954;86(1):27-29.

13 Nathan C, Ding A. SnapShot: Reactive Oxygen Intermediates (ROI). Cell. 2010;140(6):951-951.e2.

14 Liou G, Storz P. Reactive oxygen species in cancer. Free Radical Research. 2010;44(5):479-496.

15 Halliwell B. Oxidative stress and neurodegeneration: where are we now?. Journal of Neurochemistry. 2006;97(6):1634-1658.

16 Winterbourn C. Reconciling the chemistry and biology of reactive oxygen species. Nature Chemical Biology. 2008;4(5):278-286.

17 Abrahamse H, Hamblin M. New photosensitizers for photodynamic therapy. Biochemical Journal. 2016;473(4):347-364.

18 Ellis J, Kneser H. Kombinationsbeziehungen im Absorptionsspektrum des flüssigen Sauerstoffs. Zeitschrift für Physik. 1933;86(9-10):583-591.

19 Herzberg D. Molecular Spectra and Molecular Structure I Spectra of Diatomic Molecules, 2nd ed. Van Nostrand Reinhold, New York; 1950

20 Bregnhøj M, Blázquez-Castro A, Westberg M, Breitenbach T, Ogilby P. Direct 765 nm Optical Excitation of Molecular Oxygen in Solution and in Single Mammalian Cells. The Journal of Physical Chemistry B. 2015;119(17):5422-5429.

21 Wu H, Song Q, Ran G, Lu X, Xu B. Recent developments in the detection of singlet oxygen with molecular spectroscopic methods. TrAC Trends in Analytical Chemistry. 2011;30(1):133-141.

22 DeRosa M, Crutchley R. Photosensitized singlet oxygen and its applications. Coordination Chemistry Reviews. 2002;233-234:351-371.

23 Li B, Lin L, Lin H, Wilson B. Photosensitized singlet oxygen generation and detection: Recent advances and future perspectives in cancer photodynamic therapy. Journal of Biophotonics. 2016;9(11-12):1314-1325.

24 Paterson M, Christiansen O, Jensen F, Ogilby P. Overview of Theoretical and Computational Methods Applied to the Oxygen–Organic Molecule Photosystem. Photochemistry and Photobiology. 2006;82(5):1136.

25 Khan A, Kasha M. Red Chemiluminescence of Molecular Oxygen in Aqueous Solution. The Journal of Chemical Physics. 1963;39(8):2105-2106.

26 Brauer H, Eilers B, Lange A. Formation of singlet molecular oxygen by the Radziszewski reaction between acetonitrile and hydrogen peroxide in the absence and presence of ketones. Journal of the Chemical Society, Perkin Transactions 2. 2002;(7):1288-1295.

27 Alfano A, Christe K. Singlet Delta Oxygen Production from a Gas - Solid Reaction. Angewandte Chemie. 2002;114(17):3386-3388.

28 Khan A. Direct spectral evidence of the generation of singlet molecular oxygen (1Δg) in the reaction of potassium superoxide with water. Journal of the American Chemical Society. 1981;103(21):6516-6517.

29 Pierlot C, Nardello V, Schrive J, Mabille C, Barbillat J, Sombret B et al. Calcium Peroxide Diperoxohydrate as a Storable Chemical Generator of Singlet Oxygen for Organic Synthesis. The Journal of Organic Chemistry. 2002;67(8):2418-2423.

30 Jarvi M, Niedre M, Patterson M, Wilson B. Singlet Oxygen Luminescence Dosimetry (SOLD) for Photodynamic Therapy: Current Status, Challenges and Future Prospects. Photochemistry and Photobiology. 2006;82(5):1198.

31 Khan A. Direct spectroscopic observation of 1.27 μm and 1.58 μm emission of singlet (1Δg) molecular oxygen in chemically generated and dye-photosensitized liquid solutions at room temperature. Chemical Physics Letters. 1980;72(1):112-114.

32 Salokhiddinov K, Dzhagarov B, Byteva I, Gurinovich G. Photosensitized luminescence of singlet oxygen in solutions at 1588 nm. Chemical Physics Letters. 1980;76(1):85-87.

33 Wilkinson F, Helman W, Ross A. Quantum Yields for the Photosensitized Formation of the Lowest Electronically Excited Singlet State of Molecular Oxygen in Solution. Journal of Physical and Chemical Reference Data. 1993;22(1):113-262.

34 Nonell S, Flors C. Singlet oxygen: Applications in Biosciences and Nanosciences Vol 2. Cambridge: Royal Society of Chemistry; 2016.

35 Weldor D, Poulsen T, Mikkelsen K, Ogilby P. Singlet Sigma: The "Other" Singlet Oxygen in Solution. Photochemistry and Photobiology. 1999;70(4):369-379.

36 Scurlock R, Wang B, Ogilby P. Chemical Reactivity of Singlet Sigma Oxygen (b1Σg+) in Solution. Journal of the American Chemical Society. 1996;118(2):388-392.

37 Schmidt R, Bodesheim M. Collision-Induced Radiative Transitions $b^1\Sigma_g^+$ → a1Δ_g, $b^1\Sigma_g^+$ → $X^3\Sigma_g^-$, and a1Δ_g → $X^3\Sigma_g^-$ of O2 . The Journal of Physical Chemistry. 1995;99(43):15919-15924.

38 Minaev B. Quantum-chemical investigation of the mechanisms of the photosensitization, luminescence, and quenching of singlet 1Δg oxygen in solutions. Journal of Applied Spectroscopy. 1985;42(5):518-523.

39 Minaev B, Lunell S, Kobzev G. The influence of intermolecular interaction on the forbidden near-IR transitions in molecular oxygen. Journal of Molecular Structure: Theochem. 1993;284(1-2):1-9.

40 Fink E, Setzer K, Wildt J, Ramsay D, Vervloet M. Collision-induced emission of O2 ($b^1\Sigma_g^+$ → $a^1\Delta_g$) in the gas phase. International Journal of Quantum Chemistry. 1991;39(3):287-298.

41 Schmidt R, Bodesheim M. Radiationless Deactivation of the Second Excited Singlet State $^1\Sigma_g^+$ of O_2 in Solution. The Journal of Physical Chemistry A. 1998;102(25):4769-4774.

42 Weldon D, Wang B, Poulsen T, Mikkelsen K, Ogilby P. Solvent Effect on the O_2 ($b^1\Sigma_g^+$) → O_2 ($a^1\Delta_g$) Emission Spectrum. The Journal of Physical Chemistry A. 1998; 102(9):1498-1500.

43 Schmidt R, Bodesheim M. Time-Resolved Measurement of O_2 ($^1\Sigma_g^+$) in Solution. Phosphorescence from an Upper Excited State. The Journal of Physical Chemistry. 1994;98(11):2874-2876.

44 Macpherson A, Truscott T, Turner P. Fourier-transform luminescence spectroscopy of solvated singlet oxygen. Journal of the Chemical Society, Faraday Transactions. 1994;90(8):1065.

45 Wessels J, Rodgers M. Effect of Solvent Polarizability on the Forbidden $^1\Delta_g \rightarrow {}^3\Sigma_g^-$ Transition in Molecular Oxygen: A Fourier Transform Near-Infrared Luminescence Study. The Journal of Physical Chemistry. 1995;99(49):17586-17592.

46 Byteva M, Gurinovich P, Losev P, Mudryi V. Spectral shifts of the luminescence bands of singlet molecular oxygen in different solvents. Optics and Spectroscopy. 1990; 68(3):317-319.

47 Bromberg A, Foote C. Solvent shift of singlet oxygen emission wavelength. The Journal of Physical Chemistry. 1989;93(10):3968-3969.

48 Herzberg D. Molecular Spectra and Molecular Structure I Spectra of Diatomic Molecules, 2nd ed. Van Nostrand Reinhold, New York; 1950.

49 Noxon J. Observation of the transitions in O_2. Canadian Journal of Physics. 1961;39(8):1110-1119.

50 Chou P, Frei H. Sensitization of O_2 $^1\Sigma_g^+ \rightarrow {}^1\Delta_g$ emission in solution, and observation of O_2 $^1\Delta_g \rightarrow {}^3\Sigma_g^-$ chemiluminescence upon decomposition of 1,4-dimethylnaphthalene endoperoxide. Chemical Physics Letters. 1985;122(1-2):87-92.

51 Roelandts R. The history of phototherapy: Something new under the sun? Journal of the American Academy of Dermatology. 2002;46(6):926-930.

52 Bonnett R. Photosensitizers of the porphyrin and phthalocyanine series for photodynamic therapy. Chemical Society Reviews. 1995;24(1):19-33.

53 Gambichler T, Breuckmann F, Boms S, Altmeyer P, Kreuter A. Narrowband UVB phototherapy in skin conditions beyond psoriasis. Journal of the American Academy of Dermatology. 2005;52(4):660-670.

54 Paus S, Schmitz-Hübsch T, Wüllner U, Vogel A, Klockgether T, Abele M. Bright light therapy in Parkinson's disease: A pilot study. Movement Disorders. 2007;22(10):1495-1498.

55 Wainwright M. Photodynamic therapy - from dyestuffs to high-tech clinical practice. Review of Progress in Coloration and Related Topics. 2008;34(1):95-109.

56 Ormond A, Freeman H. Dye Sensitizers for Photodynamic Therapy. Materials. 2013;6(3):817-840.

57 McDonald I, Dougherty T. Basic principles of photodynamic therapy. Journal of Porphyrins and Phthalocyanines. 2001;05(02):105-129.

58 Zimcik P, Miletin M. Photodynamic Therapy in Dyes and Pigments: New Research. Nova Science Publishers: New York, NY, USA, 2008.

59 Lucky S, Soo K, Zhang Y. Nanoparticles in Photodynamic Therapy. Chemical Reviews. 2015;115(4):1990-2042.

60 Abrahamse H, Hamblin M. New photosensitizers for photodynamic therapy. Biochemical Journal. 2016;473(4):347-364.

61 Dougherty T, Gomer C, Henderson B, Jori G, Kessel D, Korbelik M et al. Photodynamic Therapy. JNCI Journal of the National Cancer Institute. 1998;90(12):889-905.

62 Allison R, Downie G, Cuenca R, Hu X, Childs C, Sibata C. Photosensitizers in clinical PDT. Photodiagnosis and Photodynamic Therapy. 2004;1(1):27-42.

63 Josefsen L, Boyle R. Photodynamic Therapy and the Development of Metal-Based Photosensitisers. Metal-Based Drugs. 2008; 2008:1-23.

64 Hudson R, Carcenac M, Smith K, Madden L, Clarke O, Pèlegrin A et al. The development and characterisation of porphyrin isothiocyanate–monoclonal antibody conjugates for photoimmunotherapy. British Journal of Cancer. 2005;92(8):1442-1449.

65 Malatesti N, Smith K, Savoie H, Greenman J, Boyle R. Synthesis and in vitro investigation of cationic 5,15-diphenyl porphyrin-monoclonal antibody conjugates as targeted photodynamic sensitisers. International Journal of Oncology. 2006; 28(6):1561-9.

66 Staneloudi C, Smith K, Hudson R, Malatesti N, Savoie H, Boyle R et al. Development and characterization of novel photosensitizer: scFv conjugates for use in photodynamic therapy of cancer. Immunology. 2007;120(4):512-517.

67 Taquet J, Frochot C, Manneville V, Barberi-Heyob M. Phthalocyanines Covalently Bound to Biomolecules for a Targeted Photodynamic Therapy. Current Medicinal Chemistry. 2007;14(15):1673-1687.

68 Bechet D, Couleaud P, Frochot C, Viriot M, Guillemin F, Barberi-Heyob M. Nanoparticles as vehicles for delivery of photodynamic therapy agents. Trends in Biotechnology. 2008;26(11):612-621.

69 Chatterjee D, Fong L, Zhang Y. Nanoparticles in photodynamic therapy: An emerging paradigm. Advanced Drug Delivery Reviews. 2008;60(15):1627-1637.

70 Paszko E, Ehrhardt C, Senge M, Kelleher D, Reynolds J. Nanodrug applications in photodynamic therapy. Photodiagnosis and Photodynamic Therapy. 2011;8(1):14-29.

71 Davis M, Chen Z, Shin D. Nanoparticle therapeutics: an emerging treatment modality for cancer. Nature Reviews Drug Discovery. 2008;7(9):771-782.

72 Konan-Kouakou Y, Boch R, Gurny R, Allémann E. In vitro and in vivo activities of verteporfin-loaded nanoparticles. Journal of Controlled Release. 2005;103(1):83-91.

73 Master A, Livingston M, Sen Gupta A. Photodynamic nanomedicine in the treatment of solid tumors: Perspectives and challenges. Journal of Controlled Release. 2013;168(1):88-102.

74 Allison R, Bagnato V, Sibata C. Future of oncologic photodynamic therapy. Future Oncology. 2010;6(6):929-940.

75 Huang Y, Sharma S, Yin R, Agrawal T, Chiang L, Hamblin M. Functionalized Fullerenes in Photodynamic Therapy. Journal of Biomedical Nanotechnology. 2014;10(9):1918-1936.

76 Sharma S, Chiang L, Hamblin M. Photodynamic therapy with fullerenes in vivo: reality or a dream? Nanomedicine. 2011;6(10):1813-1825.

77 Liao F, Saitoh Y, Miwa N. Anticancer Effects of Fullerene [C60] Included in Polyethylene Glycol Combined with Visible Light Irradiation Through ROS Generation and DNA Fragmentation on Fibrosarcoma Cells with Scarce Cytotoxicity to Normal Fibroblasts. Oncology Research Featuring Preclinical and Clinical Cancer Therapeutics. 2011;19(5):203-216.

78 Ikeda A, Doi Y, Nishiguchi K, Kitamura K, Hashizume M, Kikuchi J et al. Induction of cell death by photodynamic therapy with water-soluble lipid-membrane-incorporated [60] fullerene. Organic & Biomolecular Chemistry. 2007;5(8):1158.

79 Akiyama M, Ikeda A, Shintani T, Doi Y, Kikuchi J, Ogawa T et al. Solubilisation of [60] fullerenes using block copolymers and evaluation of their photodynamic activities. Organic & Biomolecular Chemistry. 2008;6(6):1015.

80 Lee U, Oh N, Kwag D, Oh K, Oh Y, Youn Y et al. Facile Synthesis of Multimeric Micelles. Angewandte Chemie. 2012;124(29):7399-7403.

81 Rozhkova E, Ulasov I, Lai B, Dimitrijevic N, Lesniak M, Rajh T. A High-Performance Nanobio Photocatalyst for Targeted Brain Cancer Therapy. Nano Letters. 2009;9(9):3337-3342.

82 Cai R, Kubota Y, Shuin T, Sakai H, Hashimoto K, Fujishima, A. Induction of cytotoxicity by photoexcited TiO_2 particles. Cancer Research. 1992;52(8):2346-2348.

83 Fujishima A, Ohtsuki J, Yamashita T, Hayakawa S. Behavior of tumor cells on photoexcited semiconductor surface. Photomedicine and Photobiology. 1986; 8:45-46.

84 Cai R, Hashimoto K, Kubota Y, Fujishima A. Increment of Photocatalytic Killing of Cancer Cells Using TiO_2 with the Aid of Superoxide Dismutase. Chemistry Letters. 1992;21(3):427-430.

85 Kubota Y, Shuin T, Kawasaki C, Hosaka M, Kitamura H, Cai R et al. Photokilling of T-24 human bladder cancer cells with titanium dioxide. British Journal of Cancer. 1994;70(6):1107-1111.

86 Huang N, Min-hua X, Yuan C, Rui-rong Y. The study of the photokilling effect and mechanism of ultrafine TiO_2 particles on U937 cells. Journal of Photochemistry and Photobiology A: Chemistry. 1997;108(2-3):229-233.

87 Xu M, Huang N, Xiao Z, Lu Z. Photoexcited TiO_2 nanoparticles through •OH- radicals induced malignant cells to necrosis. Supramolecular Science. 1998;5(5-6):449-451.

88 Zhang A, Sun P. Photocatalytic killing effect of TiO_2 nanoparticles on Ls-174-t human colon carcinoma cells. World Journal of Gastroenterology. 2004;10(21):3191.

89 Wang C, Cao S, Tie X, Qiu B, Wu A, Zheng Z. Induction of cytotoxicity by photoexcitation of TiO_2 can prolong survival in glioma-bearing mice. Molecular Biology Reports. 2010;38(1):523-530.

90 Jacques S, Weaver D, Reppert S. Penetration of light into the uterus of pregnant mammals. Photochemistry and Photobiology. 1987;45(5):637-641.

91 Li J, Guo D, Wang X, Wang H, Jiang H, Chen B. The Photodynamic Effect of Different Size ZnO Nanoparticles on Cancer Cell Proliferation In Vitro. Nanoscale Research Letters. 2010;5(6):1063-1071.

92 Hackenberg S, Scherzed A, Kessler M, Froelich K, Ginzkey C, Koehler C, Burghartz, M, Hagen R, Kleinsasser N. Zinc oxide nanoparticles induce photocatalytic cell death in human head and neck squamous cell carcinoma cell lines in vitro. International Journal of Oncology. 2010;37(6):1583-1590.

93 Hariharan R, Senthilkumar S, Suganthi A, Rajarajan M. Photodynamic action of curcumin derived polymer modified ZnO nanocomposites. Materials Research Bulletin. 2012;47(11):3090-3099.

94 Chen W, Zhang J. Using Nanoparticles to Enable Simultaneous Radiation and Photodynamic Therapies for Cancer Treatment. Journal of Nanoscience and Nanotechnology. 2006;6(4):1159-1166.

95 Chen W. Nanoparticle Self-Lighting Photodynamic Therapy for Cancer Treatment. Journal of Biomedical Nanotechnology. 2008;4(4):369-376.

96 Boyer J, Vetrone F, Cuccia L, Capobianco J. Synthesis of Colloidal Upconverting $NaYF_4$ Nanocrystals Doped with Er3+, Yb3+ and Tm3+, Yb3+ via Thermal

Decomposition of Lanthanide Trifluoroacetate Precursors. Journal of the American Chemical Society. 2006;128(23):7444-7445.

97 Auzel F. Upconversion and Anti-Stokes Processes with f and d Ions in Solids. Chemical Reviews. 2004;104(1):139-174.

98 Samia A, Chen X, Burda C. Semiconductor Quantum Dots for Photodynamic Therapy. Journal of the American Chemical Society. 2003;125(51):15736-15737.

99 Shi L, Hernandez B, Selke M. Singlet Oxygen Generation from Water-Soluble Quantum Dot−Organic Dye Nanocomposites. Journal of the American Chemical Society. 2006;128(19):6278-6279.

100 Tsay J, Trzoss M, Shi L, Kong X, Selke M, Jung M et al. Singlet Oxygen Production by Peptide-Coated Quantum Dot−Photosensitizer Conjugates. Journal of the American Chemical Society. 2007;129(21):6865-6871.

101 Hsu C, Chen C, Yu H, Lin Y, Lai P. Bioluminescence resonance energy transfer using luciferase-immobilized quantum dots for self-illuminated photodynamic therapy. Biomaterials. 2013;34(4):1204-1212.

102 Sun H, Wu L, Wei W, Qu X. Recent advances in graphene quantum dots for sensing. Materials Today. 2013;16(11):433-442.

103 Du D, Wang K, Wen Y, Li Y, Li Y. Photodynamic graphene quantum dot: Reduction condition regulated photoactivity and size dependent efficacy. ACS Applied Materials & Interfaces. 2016;8(5):3287 – 2394.

104 Ge J, Lan M, Zhou B, Liu W, Guo L, Wang H et al. A graphene quantum dot photodynamic therapy agent with high singlet oxygen generation. Nature Communications. 2014;5(1):4596.

105 Craig R, McCoy C, Gorman S, Jones D. Photosensitisers – the progression from photodynamic therapy to anti-infective surfaces. Expert Opinion on Drug Delivery. 2014;12(1):85-101.

106 Niedre M, Patterson M, Wilson B. Direct Near-infrared Luminescence Detection of Singlet Oxygen Generated by Photodynamic Therapy in Cells In Vitro and Tissues In Vivo. Photochemistry and Photobiology. 2002;75(4):382.

107 Niedre M, Secord A, Patterson M, Wilson B. In vitro tests of the validity of singlet oxygen luminescence measurements as a dose metric in photodynamic therapy. Cancer research. 2003;63(22):7986-7994.

108 Dolmans D, Fukumura D, Jain R. Photodynamic therapy for cancer. Nature Reviews Cancer. 2003;3(5):380-387.

109 Dougherty T, Gomer C, Henderson B, Jori G, Kessel D, Korbelik M et al. Photodynamic Therapy. JNCI Journal of the National Cancer Institute. 1998;90(12):889-905.

110 Weersink R, Bogaards A, Gertner M, Davidson S, Zhang K, Netchev G et al. Techniques for delivery and monitoring of TOOKAD (WST09)-mediated photodynamic therapy of the prostate: Clinical experience and practicalities. Journal of Photochemistry and Photobiology B: Biology. 2005;79(3):211-222.

111 Soto Thompson M, Johansson A, Johansson T, Andersson-Engels S, Svanberg S, Bendsoe N et al. Clinical system for interstitial photodynamic therapy with combined on-line dosimetry measurements. Applied Optics. 2005;44(19):4023-4031.

112 Wilson B, Patterson M, Lilge L. Implicit and explicit dosimetry in photodynamic therapy: A New paradigm. Lasers in Medical Science. 1997;12(3):182-199.

113 Zhu T, Finlay J, Hahn S. Determination of the distribution of light, optical properties, drug concentration, and tissue oxygenation in-vivo in human prostate during motexafin lutetium-mediated photodynamic therapy. Journal of Photochemistry and Photobiology B: Biology. 2005;79(3):231-241.

114 Kim M, Penjweini R, Gemmell N, Veilleux I, McCarthy A, Buller G, Hadfield R, Wilson B, Zhu T. A feasibility study of singlet oxygen explicit dosimetry (SOED) of PDT by intercomparison with a singlet oxygen luminescence dosimetry (SOLD) system. Proceedings of SPIE--the International Society for Optical Engineering. 2016;10.1117/12.2213236:9694.

115 Kim M, Penjweini R, Gemmell N, Veilleux I, McCarthy A, Buller G et al. A Comparison of Singlet Oxygen Explicit Dosimetry (SOED) and Singlet Oxygen Luminescence Dosimetry (SOLD) for Photofrin-Mediated Photodynamic Therapy. Cancers. 2016;8(12):109.

116 Zeng H, Korbelik M, McLean D, MacAulay C, Lui H. Monitoring Photoproduct Formation and Photobleaching by Fluorescence Spectroscopy Has the Potential to Improve PDT Dosimetry with a Verteporfin-like Photosensitizer. Photochemistry and Photobiology. 2002;75(4):398.

117 Georgakoudi I, Nichols M, Foster T. The Mechanism of Photofrin Photobleaching and Its Consequences for Photodynamic Dosimetry. Photochemistry and Photobiology. 1997;65(1):135-144.

118 Robinson D, de Bruijn H, van der Veen N, Stringer M, Brown S, Star W. Fluorescence Photobleaching of ALA-induced Protoporphyrin IX during Photodynamic Therapy of Normal Hairless Mouse Skin: The Effect of Light Dose and Irradiance and the Resulting Biological Effect. Photochemistry and Photobiology. 1998;67(1):140-149.

119 Dysart J, Singh G, Patterson M. Calculation of Singlet Oxygen Dose from Photosensitizer Fluorescence and Photobleaching During mTHPC Photodynamic Therapy of MLL Cells. Photochemistry and Photobiology. 2005;81(1):196-205.

120 Dysart J, Patterson M. Photobleaching kinetics, photoproduct formation, and dose estimation during ALA induced PpIX PDT of MLL cells under well oxygenated and hypoxic conditions. Photochem Photobiol Sci. 2006;5(1):73-81.

121 Molckovsky A, Wilson B. Monitoring of cell and tissue responses to photodynamic therapy by electrical impedance spectroscopy. Physics in Medicine and Biology. 2001;46(4):983-1002.

122 Chen B, Pogue B, Goodwin I, O'Hara J, Wilmot C, Hutchins J et al. Blood Flow Dynamics after Photodynamic Therapy with Verteporfin in the RIF-1 Tumor. Radiation Research. 2003;160(4):452-459.

123 Yu G, Durduran T, Zhou C, Wang H, Putt M, Saunders H et al. Noninvasive Monitoring of Murine Tumor Blood Flow During and After Photodynamic Therapy Provides Early Assessment of Therapeutic Efficacy. Clinical Cancer Research. 2005;11(9):3543-3552.

124 Vitkin A, Gordon M, Yang V, Jones G, Hayward J, Wilson B. Doppler optical coherence tomography for monitoring subsurface micro-structural and micro-vascular effects of cancer therapies. International Journal of Radiation Oncology Biology Physics. 2004;60: S585-S586.

125 Lapointe D., Brasseur N, Cadorette J, La Madeleine C, Rodrigue S, Van Lier J, Lecomte R. High-resolution PET imaging for in vivo monitoring of tumor response after photodynamic therapy in mice. Journal of Nuclear Medicine. 1999; 40: 876–882.

126 Gemmell N, McCarthy A, Liu B, Tanner M, Dorenbos S, Zwiller V et al. Singlet oxygen luminescence detection with a fibre-coupled superconducting nanowire single-photon detector. Optics Express. 2013;21(4):5005-5013.

127 Gemmell N, McCarthy A, Kim M, Veilleux I, Zhu T, Buller G et al. A compact fibre-optic probe-based singlet oxygen luminescence detection system. Journal of Biophotonics. 2016;10(2):320-326.

128 Boso G, Ke D, Korzh B, Bouilloux J, Lange N, Zbinden H. Time-resolved singlet-oxygen luminescence detection with an efficient and practical semiconductor single-photon detector. Biomedical Optics Express. 2015;7(1):211-224.

129 Tsimvrakidis K, Gemmell N, Erotokritou K, Miki S, Yabuno M, Yamashita T et al. Enhanced Optics for Time-Resolved Singlet Oxygen Luminescence Detection. IEEE Journal of Selected Topics in Quantum Electronics. 2019;25(1):1-7.

130 Patterson M, Madsen S, Wilson B. Experimental tests of the feasibility of singlet oxygen luminescence monitoring in vivo during photodynamic therapy. Journal of Photochemistry and Photobiology B: Biology. 1990;5(1):69-84.

131 Chou P, Chen Y, Wei C, Lee M. Evidence on the O2($^1\Delta_g$) Dimol-Sensitized Luminescence in Solution. Journal of the American Chemical Society. 1998;120(19):4883-4884.

132 Snyder J, Zebger I, Gao Z, Poulsen L, Frederiksen P, Skovsen E et al. Singlet Oxygen Microscope: From Phase-Separated Polymers to Single Biological Cells. Accounts of Chemical Research. 2004;37(11):894-901.

133 Niedre M, Yu C, Patterson M, Wilson B. Singlet oxygen luminescence as an in vivo photodynamic therapy dose metric: validation in normal mouse skin with topical amino-levulinic acid. British Journal of Cancer. 2005;92(2):298-304.

134 11. Hirano T, Kohno E, Nishiwaki M. Detection of Near Infrared Emission from Singlet Oxygen in PDT with an Experimental Tumor Bearing Mouse. The Journal of Japan Society for Laser Surgery and Medicine. 2001;22(3):99-108.

135 Einstein A. On a heuristic point of view about the creation and conversion of light. Annalen der Physik. 1905;322(6):132-148.

136 Hadfield R. Single-photon detectors for optical quantum information applications. Nature Photonics. 2009;3(12):696-705.

137 Natarajan C, Tanner M, Hadfield R. Superconducting nanowire single-photon detectors: physics and applications. Superconductor Science and Technology. 2012;25(6):063001.

138 Lita A, Miller A, Nam S. Counting near-infrared single-photons with 95% efficiency. Optics Express. 2008;16(5):3032.

139 Silberhorn C. Detecting quantum light. Contemporary Physics. 2007;48(3):143-156.

140 Jiang L, Dauler E, Chang J. Photon-number-resolving detector with 10 bits of resolution. Physical Review A. 2007;75(6).

141 Divochiy A, Marsili F, Bitauld D, Gaggero A, Leoni R, Mattioli F et al. Superconducting nanowire photon-number-resolving detector at telecommunication wavelengths. Nature Photonics. 2008;2(5):302-306.

142 Knill E, Laflamme R, Milburn G. A scheme for efficient quantum computation with linear optics. Nature. 2001;409(6816):46-52.

143 Iams H, Salzberg B. The Secondary Emission Phototube. Proceedings of the IRE. 1935;23(1):55-64.

144 Zworykin V, Morton G, Malter L. The Secondary Emission Multiplier-A New Electronic Device. Proceedings of the IRE. 1936;24(3):351-375.

145 Morton G. Photomultipliers for Scintillation Counting. RCA Review. 1949; 10: 525-553.

146 [Internet]. Hamamatsu.com. 2007 [cited 10 October 2019]. Available from: https://www.hamamatsu.com/resources/pdf/etd/PMT_handbook_v3aE.pdf

147 Cova S, Longoni A, Andreoni A. Towards picosecond resolution with single-photon avalanche diodes. Review of Scientific Instruments. 1981;52(3):408-412.

148 Haitz R. Mechanisms Contributing to the Noise Pulse Rate of Avalanche Diodes. Journal of Applied Physics. 1965;36(10):3123-3131.

149 Brown R, Jones R, Rarity J, Ridley K. Characterization of silicon avalanche photodiodes for photon correlation measurements 2: Active quenching. Applied Optics. 1987;26(12):2383.

150 Hayat M, Itzler M, Ramirez D, Rees G. Model for Passive Quenching of SPADs. Quantum Sensing and Nanophotonic Devices Vii 7608, 2010.

151 Pellegrini S, Warburton R, Tan L, Ng J, Krysa A, Groom K et al. Design and Performance of an InGaAs–InP Single-Photon Avalanche Diode Detector. IEEE Journal of Quantum Electronics. 2006;42(4):397-403.

152 Tosi A, Acerbi F, Anti M, Zappa F. InGaAs/InP Single-Photon Avalanche Diode with Reduced Afterpulsing and Sharp Timing Response With 30 ps Tail. IEEE Journal of Quantum Electronics. 2012;48(9):1227-1232.

153 Dash W, Newman R. Intrinsic Optical Absorption in Single-Crystal Germanium and Silicon at 77°K and 300°K. Physical Review. 1955;99(4):1151-1155.

154 Buller G, Fancey S, Massa J, Walker A, Cova S, Lacaita A. Time-resolved photoluminescence measurements of InGaAs/InP multiple-quantum-well structures at 1.3-μm wavelengths by use of germanium single-photon avalanche photodiodes. Applied Optics. 1996;35(6):916.

155 Vines P, Kuzmenko K, Kirdoda J, Dumas D, Mirza M, Millar R et al. High-performance planar germanium-on-silicon single-photon avalanche diode detectors. Nature Communications. 2019;10(1).

156 Lacaita A, Zappa F, Cova S, Lovati P. Single-photon detection beyond 1 μm: performance of commercially available InGaAs/InP detectors. Applied Optics. 1996;35(16):2986.

157 Stevens M, Hadfield R, Schwall R, Nam S, Mirin R, Gupta J. Fast lifetime measurements of infrared emitters using a low-jitter superconducting single-photon detector. Applied Physics Letters. 2006;89(3):031109.

158 Cova S, Ghioni M, Lotito A, Rech I, Zappa F. Evolution and prospects for single-photon avalanche diodes and quenching circuits. Journal of Modern Optics. 2004;51(9-10):1267-1288.

159 Kim Y, Makarov V, Jeong Y, Kim Y. Silicon Single-Photon Detector with 5 Hz Dark Counts. Conference on Lasers and Electro-Optics and Quantum Electronics and Laser Science Conference (CLEO. /QELS. 2009). 2009;1-5:2523-2524.

160 [Internet]. Perkinelmer.com. 2019 [cited 9 October 2019]. Available from: https://www.perkinelmer.com/cmsresources/images/44-3477dts_c30902.pdf

161 Zang K, Jiang X, Huo Y, Ding X, Morea M, Chen X et al. Silicon single-photon avalanche diodes with nano-structured light trapping. Nature Communications. 2017;8(1).

162 Buller G, Collins R. Single-photon generation and detection. Measurement Science and Technology. 2009;21(1):012002.

163 Eisaman M, Fan J, Migdall A, Polyakov S. Invited Review Article: Single-photon sources and detectors. Review of Scientific Instruments. 2011;82(7):071101.

164 Hall D, Liu Y, Lo Y. Single photon avalanche detectors: prospects of new quenching and gain mechanisms. Nanophotonics. 2015;4(1).

165 Ghioni M, Gulinatti A, Rech I, Zappa F, Cova S. Progress in Silicon Single-Photon Avalanche Diodes. IEEE Journal of Selected Topics in Quantum Electronics. 2007;13(4):852-862.

166 Charbon E, Donati S. SPAD Sensors Come of Age. Optics and Photonics News. 2010;21(2):34.

167 Niclass C, Inque D, Matsubara H, Ichikawa T, Soga M. Development of Automotive LIDAR. Electronics and Communications in Japan. 2015;98(5):28-33.

168 Gyongy I, Dutton N, Henderson R. Single-Photon Tracking for High-Speed Vision. Sensors. 2018;18(2):323.

169 Takai I, Matsubara H, Soga M, Ohta M, Ogawa M, Yamashita T. Single-Photon Avalanche Diode with Enhanced NIR-Sensitivity for Automotive LIDAR Systems. Sensors. 2016;16(4):459.

170 Pellegrini, S. et al. Industrialised SPAD in 40 nm technology. In 2017 IEEE Int. Electron Dev. Meeting, San Francisco, CA, https://doi.org/10.1109/IEDM.2017.8268404 (2017).

171 Itzler M, Ben-Michael r, Hsu C, Slomkowski K, Tosi A, Cova S et al. Single photon avalanche diodes (SPADs) for 1.5 μm photon counting applications. Journal of Modern Optics. 2007;54(2-3):283-304.

172 Itzler M, Jiang X, Entwistle M, Slomkowski K, Tosi A, Acerbi F et al. Advances in InGaAsP-based avalanche diode single photon detectors. Journal of Modern Optics. 2011;58(3-4):174-200.

173 Restelli A, Bienfang J, Migdall A. Single-photon detection efficiency up to 50% at 1310 nm with an InGaAs/InP avalanche diode gated at 1.25 GHz. Applied Physics Letters. 2013;102(14):141104.

174 Tosi A, Calandri N, Sanzaro M, Acerbi F. Low-Noise, Low-Jitter, High Detection Efficiency InGaAs/InP Single-Photon Avalanche Diode. IEEE Journal of Selected Topics in Quantum Electronics. 2014;20(6):192-197.

175 ID230 Infrared Single-Photon Detector [Internet]. Marketing.idquantique.com. 2019 [cited 10 October 2019]. Available from: https://marketing.idquantique.com/acton/attachment/11868/f-0234/1/-/-/-/-/ID230_Brochure.pdf

176 Verghese S, Donnelly J, Duerr E, McIntosh K, Chapman D, Vineis C et al. Arrays of InP-based Avalanche Photodiodes for Photon Counting. IEEE Journal of Selected Topics in Quantum Electronics. 2007;13(4):870-886.

177 Jiang X, Itzler M, ODonnell K, Entwistle M, Owens M, Slomkowski K et al. InP-Based Single-Photon Detectors and Geiger-Mode APD Arrays for Quantum Communications Applications. IEEE Journal of Selected Topics in Quantum Electronics. 2015;21(3):5-16.

178 Lacaita A, Francese P, Zappa F, Cova S. Single-photon detection beyond 1 μm: performance of commercially available germanium photodiodes. Applied Optics. 1994;33(30):6902-6918.

179 Lu Z, Kang Y, Hu C, Zhou Q, Liu H, Campbell J. Geiger-Mode Operation of Ge-on-Si Avalanche Photodiodes. IEEE Journal of Quantum Electronics. 2011;47(5):731-735.

180 Aminian M, Sammak A, Qi L, Nanver K, Charbon E. A Ge-on-Si single-photon avalanche diode operating in Geiger mode at infrared wavelengths. SPIE Defense, Security, and Sensing (international society for optics and photonics) 2012:83750Q-83750Q-83710.

181 Warburton R, Intermite G, Myronov M, Allred P, Leadley D, Gallacher K et al. Ge-on-Si Single-Photon Avalanche Diode Detectors: Design, Modeling, Fabrication, and Characterization at Wavelengths 1310 and 1550 nm. IEEE Transactions on Electron Devices. 2013;60(11):3807-3813.

182 Vines P, Kuzmenko K, Kirdoda J, Dumas D, Mirza M, Millar R et al. High-performance planar germanium-on-silicon single-photon avalanche diode detectors. Nature Communications. 2019;10(1).

183 Onnes K. Electrical Resistance of Pure Metal at Very Low Temperatures. Scientific American. 1911;72(1863supp):178-179.

184 Meissner W, Ochsenfeld R. Ein neuer Effekt bei Eintritt der Supraleitfähigkeit. Die Naturwissenschaften. 1933;21(44):787-788.

185 London F, London H. The electromagnetic equations of the supraconductor. Proceedings of the Royal Society of London Series A - Mathematical and Physical Sciences. 1935;149(866):71-88.

186 Landau L, Ginzburg V. On the theory of superconductivity. Journal of Experimental and Theoretical Physics 1950; 20:1064.

187 Bardeen J, Cooper L, Schrieffer J. Theory of Superconductivity. Physical Review. 1957;108(5):1175-1204.

188 Cabrera B, Clarke R, Colling P, Miller A, Nam S, Romani R. Detection of single infrared, optical, and ultraviolet photons using superconducting transition edge sensors. Applied Physics Letters. 1998;73(6):735-737.

189 Miller A, Nam S, Martinis J, Sergienko A. Demonstration of a low-noise near-infrared photon counter with multiphoton discrimination. Applied Physics Letters. 2003;83(4):791-793.

190 Rosenberg D, Lita A, Miller A, Nam S. Publisher's Note: Noise-free high-efficiency photon-number-resolving detectors [Phys. Rev. A71, 061803 (2005)]. Physical Review A. 2005;72(1).

191 Lita A, Miller A, Nam S. Counting near-infrared single-photons with 95% efficiency. Optics Express. 2008;16(5):3032.

192 Fukuda D, Fujii G, Numata T, Amemiya K, Yoshizawa A, Tsuchida H et al. Titanium-based transition-edge photon number resolving detector with 98% detection efficiency with index-matched small-gap fibre coupling. Optics Express. 2011;19(2):870.

193 Rosenberg D, Harrington J, Rice P, Hiskett P, Peterson C, Hughes R et al. Long-Distance Decoy-State Quantum Key Distribution in Optical Fibre. Physical Review Letters. 2007;98(1):010503.

194 Lamas-Linares A, Calkins B, Tomlin N, Gerrits T, Lita A, Beyer J et al. Nanosecond-scale timing jitter for single photon detection in transition edge sensors. Applied Physics Letters. 2013;102(23):231117.

195 Fukuda D, Fujii G, Numata T, Yoshizawa A, Tsuchida H, Fujino H et al. Photon number resolving detection with high speed and high quantum efficiency. Metrologia. 2009;46(4): S288-S292.

196 Di Giuseppe G, Atatüre M, Shaw M, Sergienko A, Saleh B, Teich M et al. Direct observation of photon pairs at a single output port of a beam-splitter interferometer. Physical Review A. 2003;68(6).

197 Rosenberg D, Nam S, Hiskett P, Peterson C, Hughes R, Nordholt J et al. Quantum key distribution at telecom wavelengths with noise-free detectors. Applied Physics Letters. 2006;88(2):021108.

198 Gol'tsman G, Okunev O, Chulkova G, Lipatov A, Semenov A, Smirnov K et al. Picosecond superconducting single-photon optical detector. Applied Physics Letters. 2001;79(6):705-707.

199 Verevkin A, Zhang J, Sobolewski R, Lipatov A, Okunev O, Chulkova G et al. Detection efficiency of large-active-area NbN single-photon superconducting detectors in the ultraviolet to near-infrared range. Applied Physics Letters. 2002;80(25):4687-4689.

200 Miki S, Fujiwara M, Sasaki M, Baek B, Miller A, Hadfield R et al. Large sensitive-area NbN nanowire superconducting single-photon detectors fabricated on single-crystal MgO substrates. Applied Physics Letters. 2008;92(6):061116.

201 Il'in K, Lindgren M, Currie M, Semenov A, Gol'tsman G, Sobolewski R et al. Picosecond hot-electron energy relaxation in NbN superconducting photodetectors. Applied Physics Letters. 2000;76(19):2752-2754.

202 Słysz W, Węgrzecki M, Bar J, Grabiec P, Górska M, Zwiller V et al. Fibre-coupled NbN superconducting single-photon detectors for quantum correlation measurements. Applied Physics Letters. 2006;88(26):261113.

203 Anant V, Kerman A, Dauler E, Yang J, Rosfjord K, Berggren K. Optical properties of superconducting nanowire single-photon detectors. Optics Express. 2008;16(14):10750-10761.

204 Dorenbos S, Reiger E, Akopian N, Perinetti U, Zwiller V, Zijlstra T et al. Superconducting single photon detectors with minimized polarization dependence. Applied Physics Letters. 2008;93(16):161102.

205 Verma V, Marsili F, Harrington S, Lita A, Mirin R, Nam S. A three-dimensional, polarization-insensitive superconducting nanowire avalanche photodetector. Applied Physics Letters. 2012;101(25):251114.

206 Kerman A, Dauler E, Yang J, Rosfjord K, Anant V, Berggren K et al. Constriction-limited detection efficiency of superconducting nanowire single-photon detectors. Applied Physics Letters. 2007;90(10):101110.

207 Kerman A, Dauler E, Keicher W, Yang J, Berggren K, Gol'tsman G et al. Kinetic-inductance-limited reset time of superconducting nanowire photon counters. Applied Physics Letters. 2006;88(11):111116.

208 Ejrnaes M, Cristiano R, Quaranta O, Pagano S, Gaggero A, Mattioli F et al. A cascade switching superconducting single photon detector. Applied Physics Letters. 2007;91(26):262509.

209 Heath R, Tanner M, Casaburi A, Webster M, San Emeterio Alvarez L, Jiang W et al. Nano-optical observation of cascade switching in a parallel superconducting nanowire single photon detector. Applied Physics Letters. 2014;104(6):063503.

210 Marsili F, Najafi F, Dauler E, Bellei F, Hu X, Csete M et al. Single-Photon Detectors Based on Ultranarrow Superconducting Nanowires. Nano Letters. 2011;11(5):2048-2053.

211 Kadin A, Johnson M. Nonequilibrium photon-induced hotspot: A new mechanism for photodetection in ultrathin metallic films. Applied Physics Letters. 1996;69(25):3938-3940.

212 Yang J, Kerman A, Dauler E, Anant V, Rosfjord K, Berggren K. Modeling the Electrical and Thermal Response of Superconducting Nanowire Single-Photon Detectors. IEEE Transactions on Applied Superconductivity. 2007;17(2):581-585.

213 Semenov A, Gol'tsman G, Korneev A. Quantum detection by current carrying superconducting film. Physica C: Superconductivity. 2001;351(4):349-356.

214 Holzman I, Ivry Y. Superconducting Nanowires for Single-Photon Detection: Progress, Challenges, and Opportunities. Advanced Quantum Technologies. 2019;2(3-4):1800058.

215 Marsili F, Verma V, Stern J, Harrington S, Lita A, Gerrits T et al. Detecting single infrared photons with 93% system efficiency. Nature Photonics. 2013;7(3):210-214.

216 Reddy D, Nerem R, Lita A, Nam S, Mirin R, Verma V. Exceeding 95% system efficiency within the telecom C-band in superconducting nanowire single photon detectors. 2019 Conference on Lasers and Electro-Optics (CLEO), IEEE. 2019; 18863734

217 Shibata H, Shimizu K, Takesue H, Tokura Y. Ultimate low system dark-count rate for superconducting nanowire single-photon detector. Optics Letters. 2015;40(14):3428-3431.

218 Korzh B, Zhao Q-Y, Frasca S, Allmaras J, Autry T, Bersin E et al. Demonstrating sub-3 ps temporal resolution in superconducting nanowire single photon detector. Nature Photonics. 2020;14(4):250-255.

219 Vetter A, Ferrari S, Rath P, Alaee R, Kahl O, Kovalyuk V et al. Cavity-Enhanced and Ultrafast Superconducting Single-Photon Detectors. Nano Letters. 2016;16(11):7085-7092.

220 Doerner S, Kuzmin A, Wuensch S, Charaev I, Boes F, Zwick T et al. Frequency-multiplexed bias and readout of a 16-pixel superconducting nanowire single-photon detector array. Applied Physics Letters. 2017;111(3):032603.

221 Miki S, Yamashita T, Wang Z, Terai H. A 64-pixel NbTiN superconducting nanowire single-photon detector array for spatially resolved photon detection. Optics Express. 2014;22(7):7811.

222 Ota K, Naruse M, Taino T, Chen J, Kang L, Wu P et al. SFQ amplified circuit for photon number resolving SNSPD array. 15th International Superconductive Electronics Conference (ISEC), IEEE. 2015; 15721061.

223 Becker W. Advanced Time-Correlated Single Photon Counting Applications. Cham: Springer International Publishing; 2015.

224 Becker, W. (2019). The bh TCSPC handbook. 8th ed. Berlin: Becker & Hickl.

225 Mang T. Lasers and light sources for PDT: past, present and future. Photodiagnosis and Photodynamic Therapy. 2004;1(1):43-48.

226 Brancaleon L, Moseley H. Laser and Non-laser Light Sources for Photodynamic Therapy. Lasers in Medical Science. 2002;17(3):173-186.

227 NKT Photonics [Internet]. NKT Photonics. 2019 [cited 19 October 2019]. Available from: https://www.nktphotonics.com/

228 Gobby C, Yuan Z, Shields A. Quantum key distribution over 122 km of standard telecom fibre. Applied Physics Letters. 2004;84(19):3762-3764.

229 McColl J. Oxford Dictionary of Statistics. Edited by Graham Upton and Ian Cook. Oxford University Press, Oxford, 2002. 420pp. ISBN: 0-19-280100-7. Psycho-Oncology. 2004;13(10):753-753.

230 Hadfield R, Stevens M, Gruber S, Miller A, Schwall R, Mirin R et al. Single photon source characterization with a superconducting single photon detector. Optics Express. 2005;13(26):10846.

231 Sumitomo (SHI) 4 K Refrigerator cold head model RDK-101J [Internet]. Janis.com. 2019 [cited 29 October 2019]. Available from: https://www.janis.com/Products/productsoverview/4KCryocooler/RDK-101DClosedCycleRefrigerator.aspx#

232 Gemmell N, Hills M, Bradshaw T, Rawlings T, Green B, Heath R et al. A miniaturized 4 K platform for superconducting infrared photon counting detectors. Superconductor Science and Technology. 2017;30(11):11LT01.

233 Scott L, Goa K. Verteporfin. Drugs & Aging. 2000;16(2):139-146.

234 Ratkay L, Waterfield J, Hunt D. Photodynamic Therapy in Immune (Non-Oncological) Disorders. BioDrugs. 2000;14(2):127-135.

235 Redmond R, Gamlin J. A Compilation of Singlet Oxygen Yields from Biologically Relevant Molecules. Photochemistry and Photobiology. 1999;70(4):391.

236 Cheng J, Yen M, Young T. Crack-free micromachining on glass using an economic Q-switched 532 nm laser. Journal of Micromechanics and Microengineering. 2006;16(11):2420-2424.

237 Amat-Guerri F, López-González M, Martínez-Utrilla R, Sastre R. Singlet oxygen photogeneration by ionized and un-ionized derivatives of Rose Bengal and Eosin Y in diluted solutions. Journal of Photochemistry and Photobiology A: Chemistry. 1990;53(2):199-210.

238 Whang T, Huang H, Hsieh M, Chen J. Laser-Induced Silver Nanoparticles on Titanium Oxide for Photocatalytic Degradation of Methylene Blue. International Journal of Molecular Sciences. 2009;10(11):4707-4718.

239 Spiller W, Kliesch H, Worhle D, Hackbarth S, Roder B, Schnurofeil G. Singlet Oxygen Quantum Yields of Different Photosensitizers in Polar Solvents and Micellar Solutions. Journal of Porphyrins and Phthalocyanines. 1998;02(02):145-158.

240 Ogunsipe A, Chen J, Nyokong T. Photophysical and photochemical studies of zinc(ii) phthalocyanine derivatives—effects of substituents and solvents. New J Chem. 2004;28(7):822-827.

241 Beeby A, FitzGerald S, Stanley C. Protonation of Tetrasulfonated Zinc Phthalocyanine in Aqueous Acetonitrile Solution. Photochemistry and Photobiology. 2007;74(4):566-569.

242 Zhang X, Xu H. Influence of halogenation and aggregation on photosensitizing properties of zinc phthalocyanine (ZnPC). Journal of the Chemical Society, Faraday Transactions. 1993;89(18):3347.

243 Sharma D, Huijser A, Savolainen J, Steen G, Herek J. Active and passive control of zinc phthalocyanine photodynamics. Faraday Discussions. 2013;163:433.

244 Foote C, Denny R. Chemistry of singlet oxygen. VII. Quenching by beta-carotene. Journal of the American Chemical Society. 1968;90(22):6233-6235.

245 Edge R, McGarvey D, Truscott T. The carotenoids as anti-oxidants — a review. Journal of Photochemistry and Photobiology B: Biology. 1997;41(3):189-200.

246 Stahl W, Sies H. Antioxidant activity of carotenoids. Molecular Aspects of Medicine. 2003;24(6):345-351.

247 Ramel F, Birtic S, Cuiné S, Triantaphylidès C, Ravanat J, Havaux M. Chemical Quenching of Singlet Oxygen by Carotenoids in Plants. Plant Physiology. 2012;158(3):1267-1278.

248 Flock S, Jacques S, Wilson B, Star W, van Gemert M. Optical properties of intralipid: A phantom medium for light propagation studies. Lasers in Surgery and Medicine. 1992;12(5):510-519.

249 Troy T, Thennadil S. Optical properties of human skin in the near infrared wavelength range of 1000 to 2200 nm. Journal of Biomedical Optics. 2001;6(2):167.

250 Snyder J, Skovsen E, Lambert J, Poulsen L, Ogilby P. Optical detection of singlet oxygen from single cells. Physical Chemistry Chemical Physics. 2006;8(37):4280.

251 Snyder J, Skovsen E, Lambert J, Ogilby P. Subcellular, Time-Resolved Studies of Singlet Oxygen in Single Cells. Journal of the American Chemical Society. 2005;127(42):14558-14559.

252 Williams G, Euser T, Russell P, MacRobert A, Jones A. Highly Sensitive Luminescence Detection of Photosensitized Singlet Oxygen within Photonic Crystal Fibres. ChemPhotoChem. 2018;2(7):616-621.

253 Unterkofler S, Garbos M, Euser T, Russell P. Long-distance laser propulsion and deformation- monitoring of cells in optofluidic photonic crystal fibre. Journal of Biophotonics. 2012;6(9):743-752.

254 Prabhakar S, Shields T, Dada A, Ebrahim M, Taylor G, Morozov D et al. Two-photon quantum interference and entanglement at 2.1 μm. Science Advances. 2020;6(13):eaay5195.

255 Taylor G, Morozov D, Gemmell N, Erotokritou K, Miki S, Terai H et al. Photon counting LIDAR at 23μm wavelength with superconducting nanowires. Optics Express. 2019;27(26):38147.

Appendix A

- Transmission data for the filters and mirrors used in the optical setup.

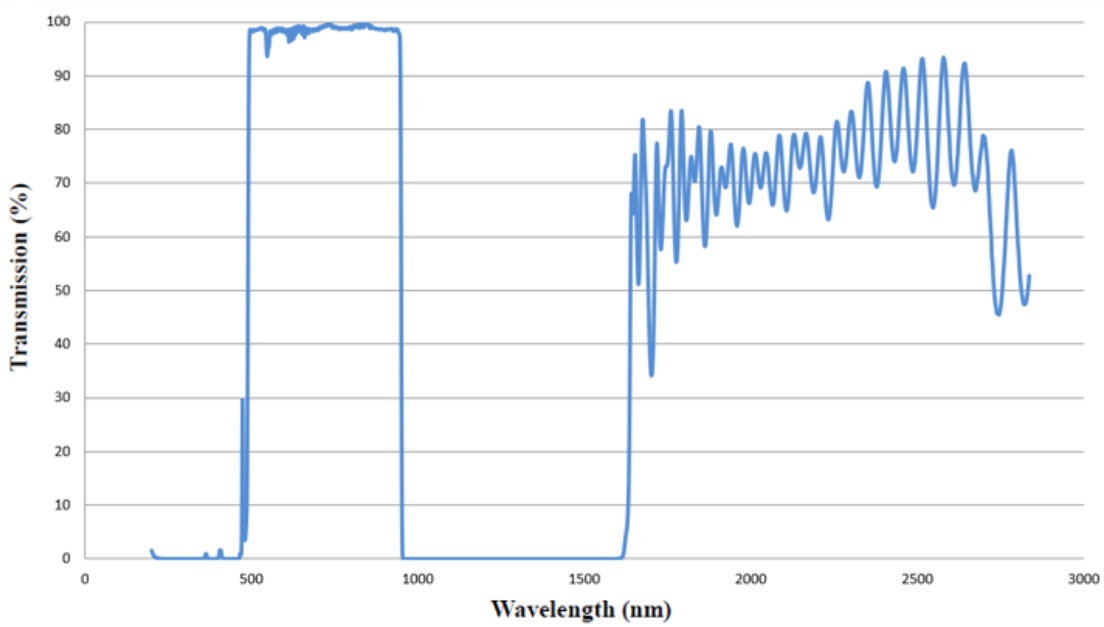

A.1. Transmission of short pass optical filter Thorlabs (FESH0950).

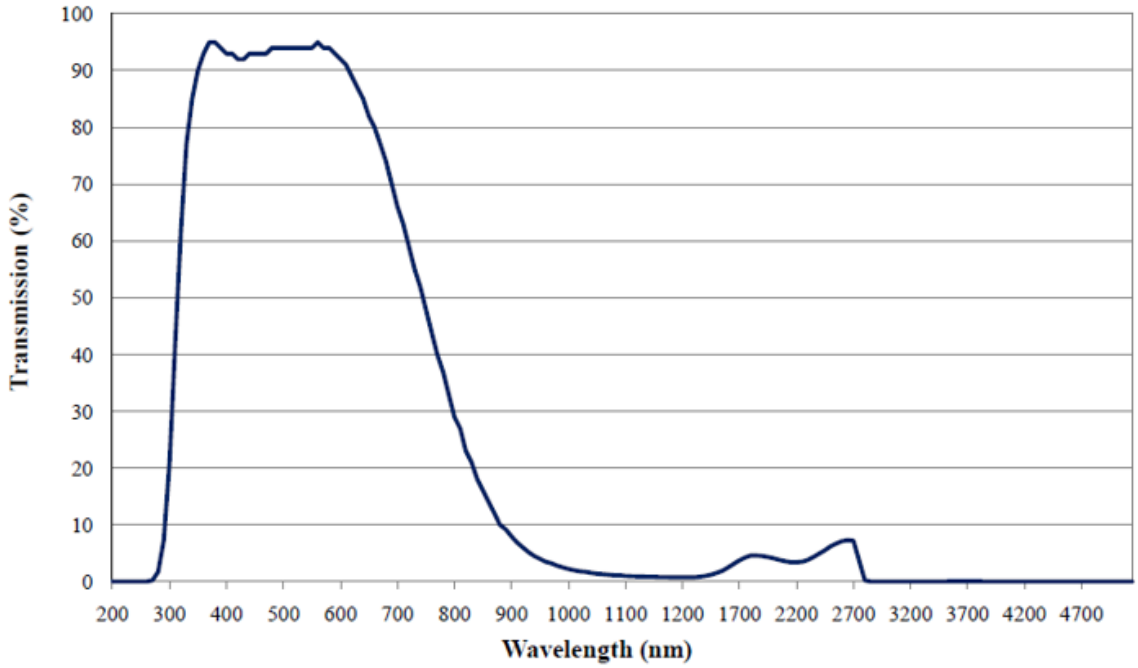

A.2. Transmission of short pass optical filter Edmund Optics (KG-1).

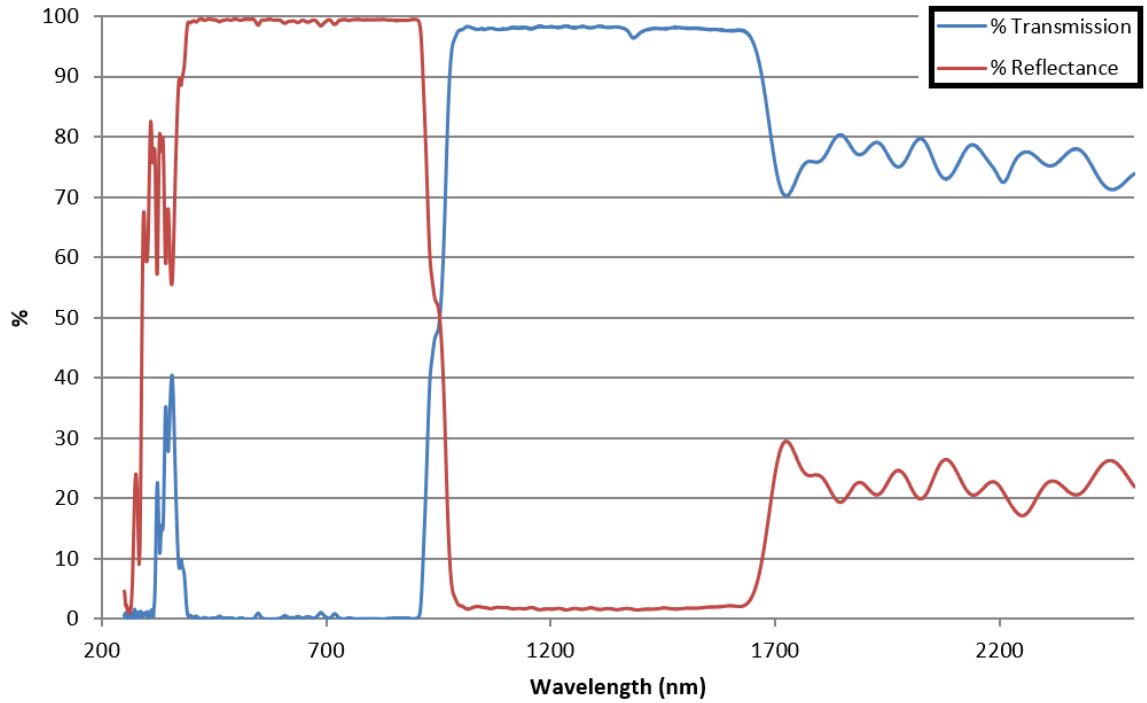

A.3. Transmission and reflectance of the dichroic mirror Thorlabs DMLP950.

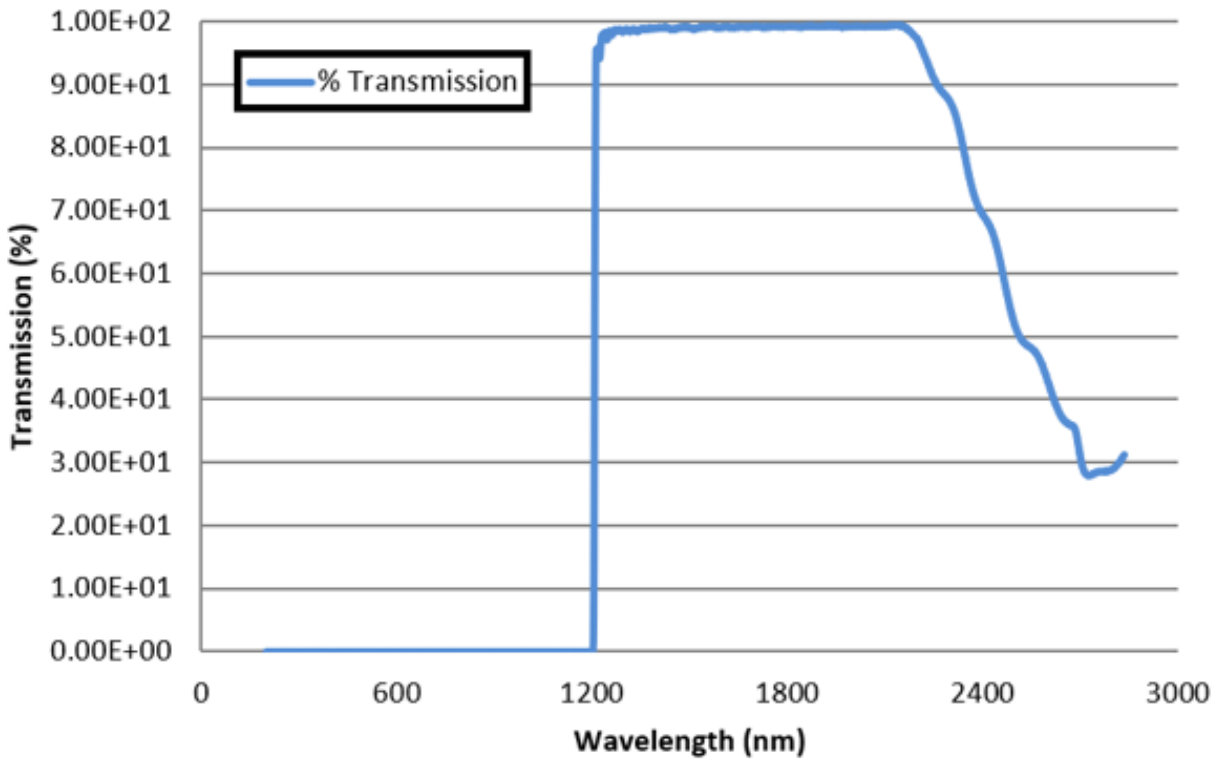

A.4. Transmission of long pass optical filter Thorlabs FELH1200.

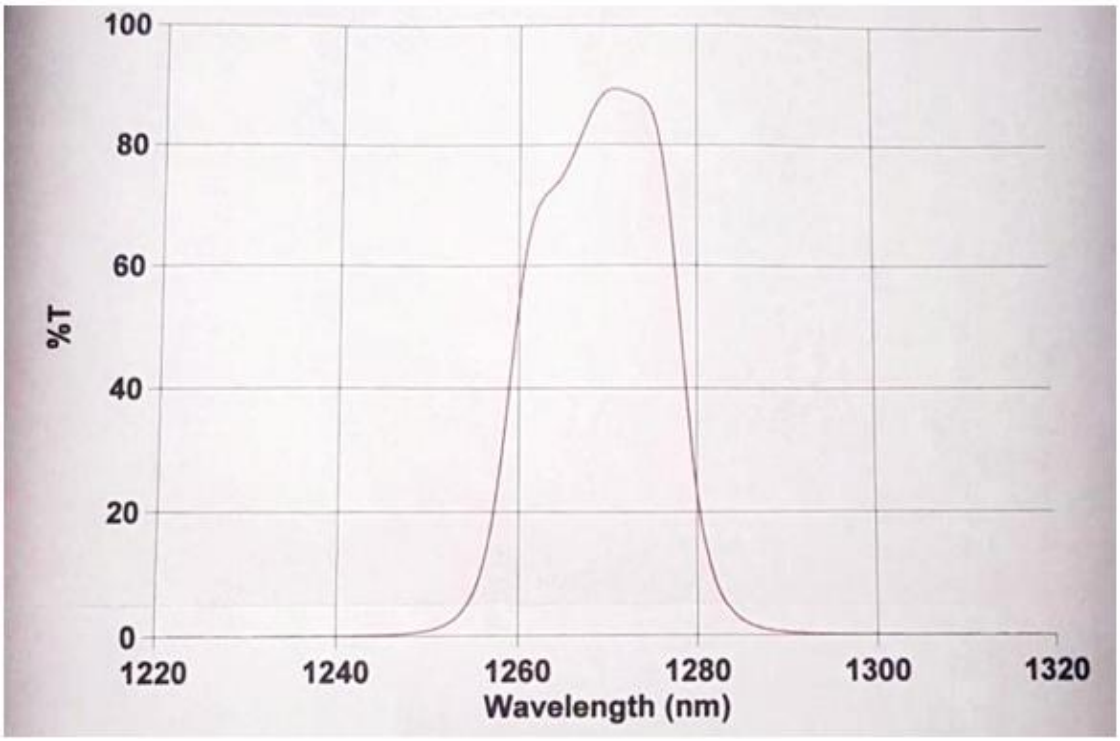

A.5. Transmission of custom band pass optical filter Omega Optical (1270±4nm).

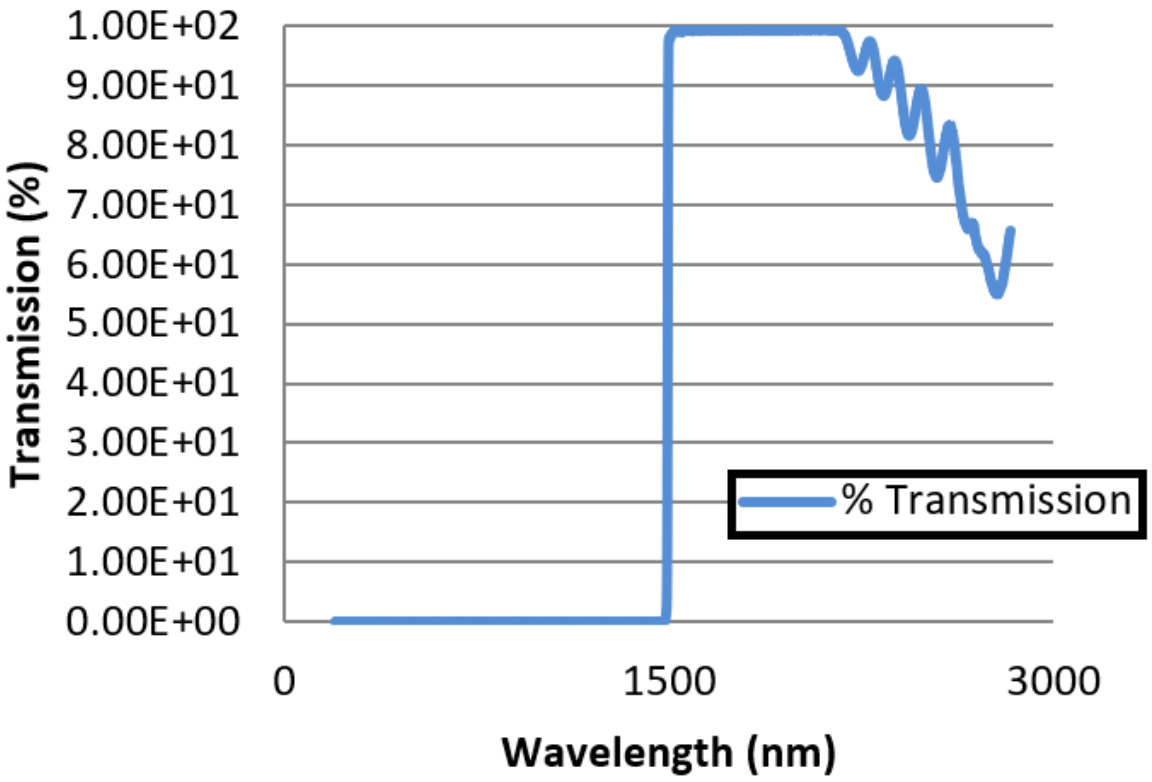

A.6. Transmission of long pass optical filter Thorlabs FELH1500.

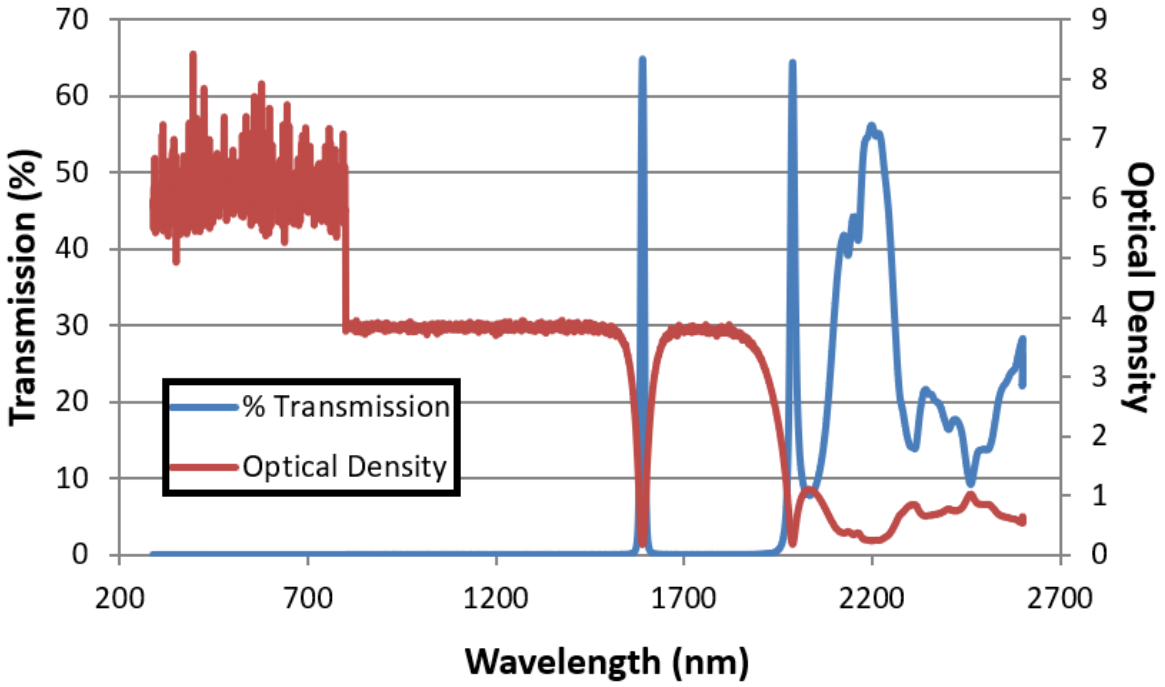

A.7. Transmission and Optical density of band pass optical filter Thorlabs FB1590-12.

Appendix B

- Microscope images from normal fibroblast cells with incubated Rose Bengal in decreasing concentration. Cell exposure time to Rose Bengal was 3 hours.

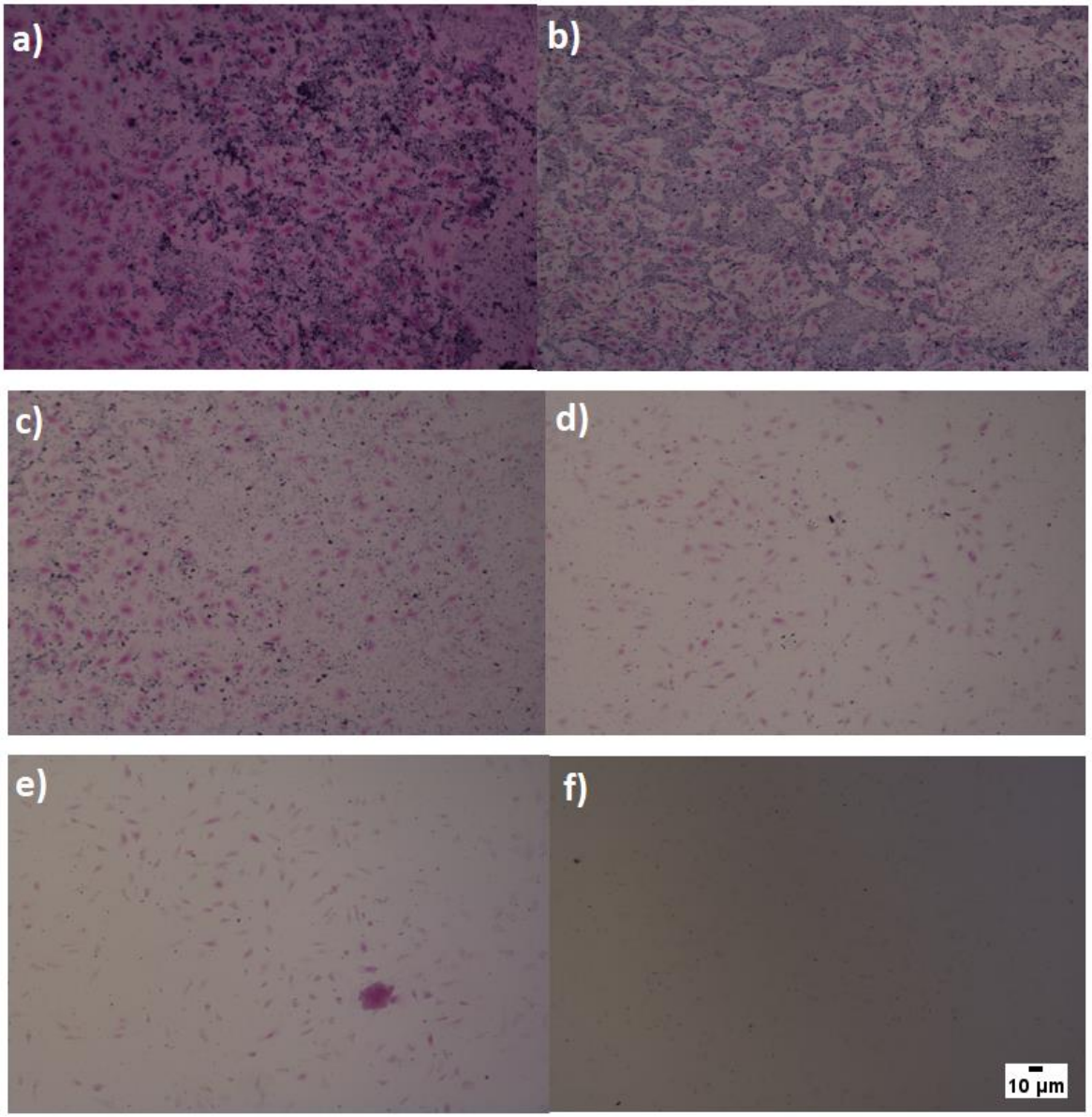

B.1. Images of Rose Bengal uptake by NIH3T3 fibroblast cells. Rose Bengal concentration is a) 500 µg/ml, b) 250 µg/ml, c) 100 µg/ml, d) 50 µg/ml, e) 25 µg/ml and, f) 12.5 µg/ml. Scale bar applies to all images. Microscope images captured by Dr. Marie Cutiongco.

- Microscope images from KPC cancer cells with incubated Rose Bengal in decreasing concentration. Cell exposure time to Rose Bengal was 3 hours.

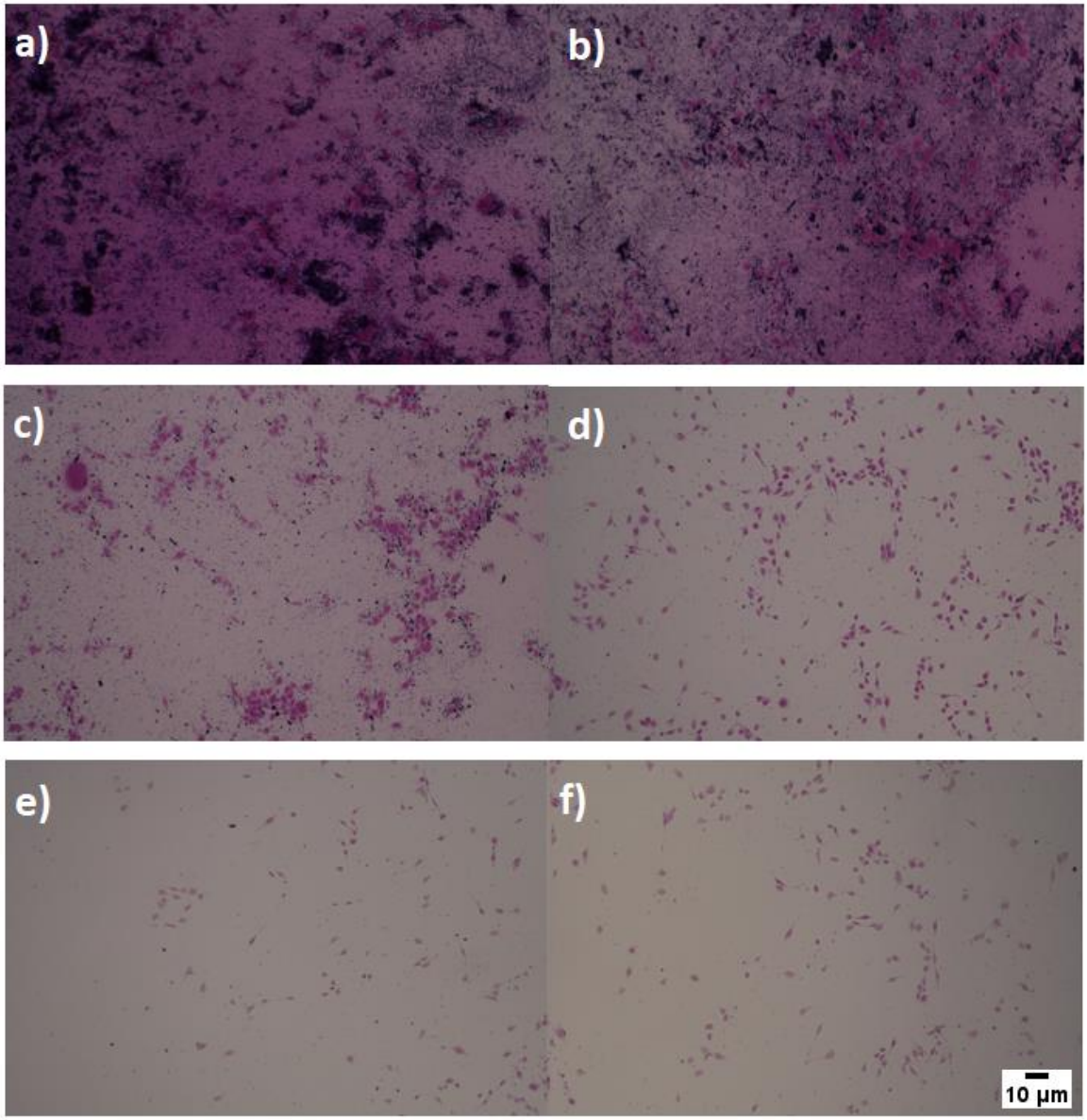

B.2. Images of Rose Bengal uptake by KPC cancer cells. Rose Bengal concentration is a) 500 µg/ml, b) 250 µg/ml, c) 100 µg/ml, d) 50 µg/ml, e) 25 µg/ml and, f) 12.5 µg/ml. Scale bar applies to all images. Microscope images captured by Dr. Marie Cutiongco.

- Microscope images of KPC cancer cells exposed to different durations of laser illumination. Cells were exposed to Rose Bengal for 3 hours and the final concentration is 100 µg/ml.

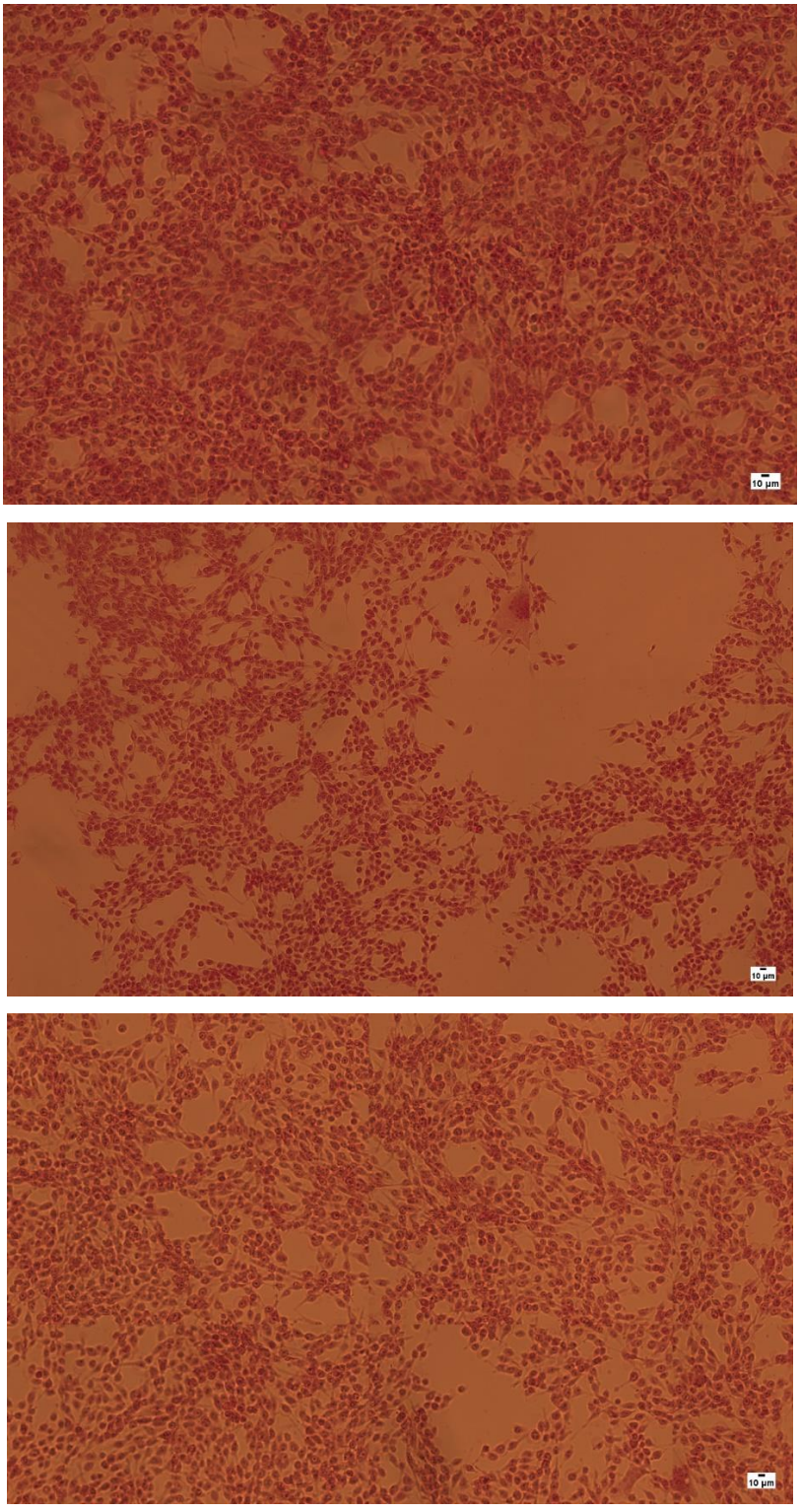

B.3. Microscope images of KPC cancer cells exposed to laser light for 0, 5 and 15 minutes (top to bottom). Microscope images captured by Dr. Marie Cutiongco directly after the experiment.

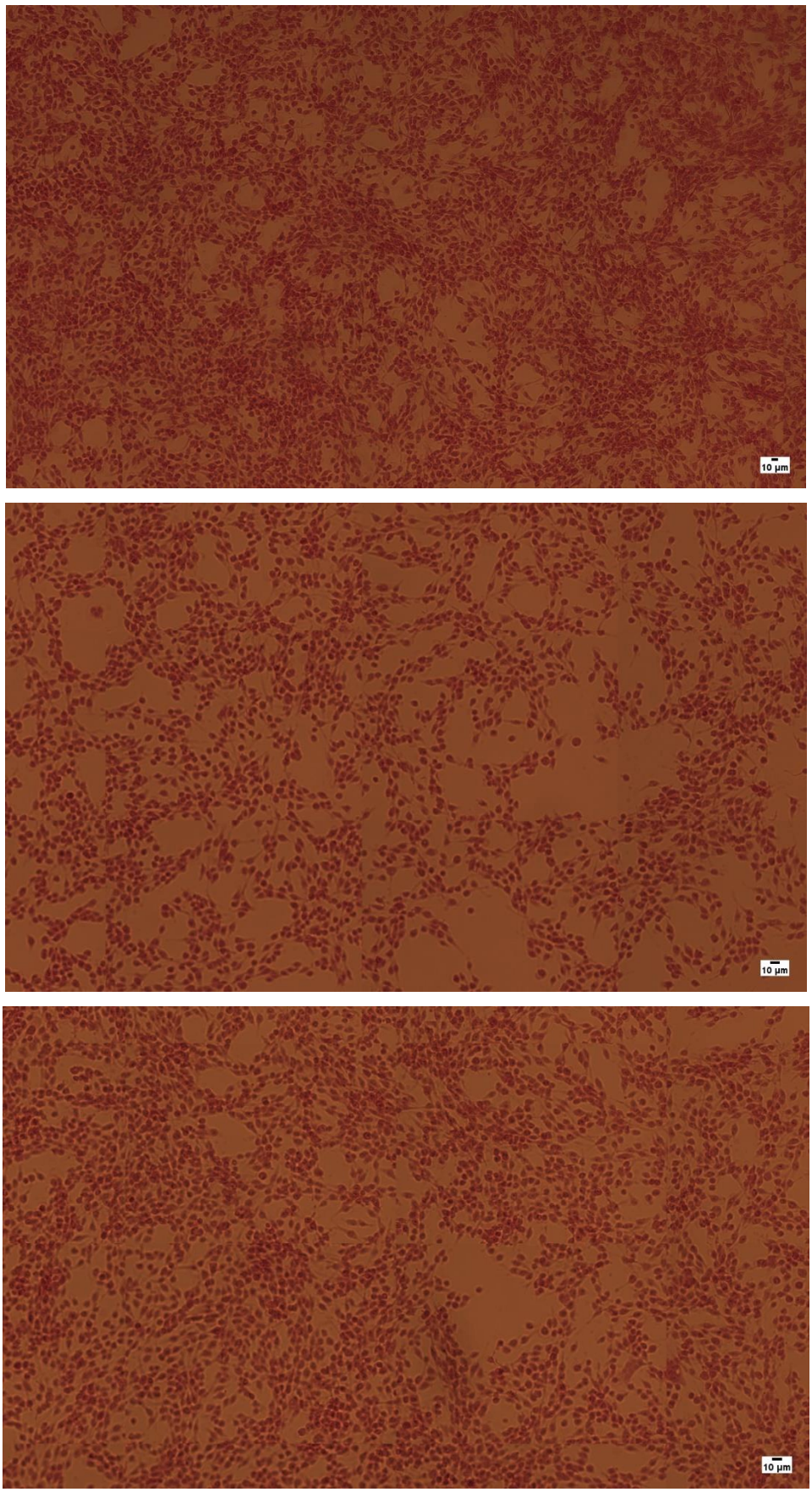

B.4. Microscope images of KPC cancer cells exposed to laser light for 0, 5 and 15 minutes (top to bottom). Microscope images captured by Dr. Marie Cutiongco 1 day after the experiment.

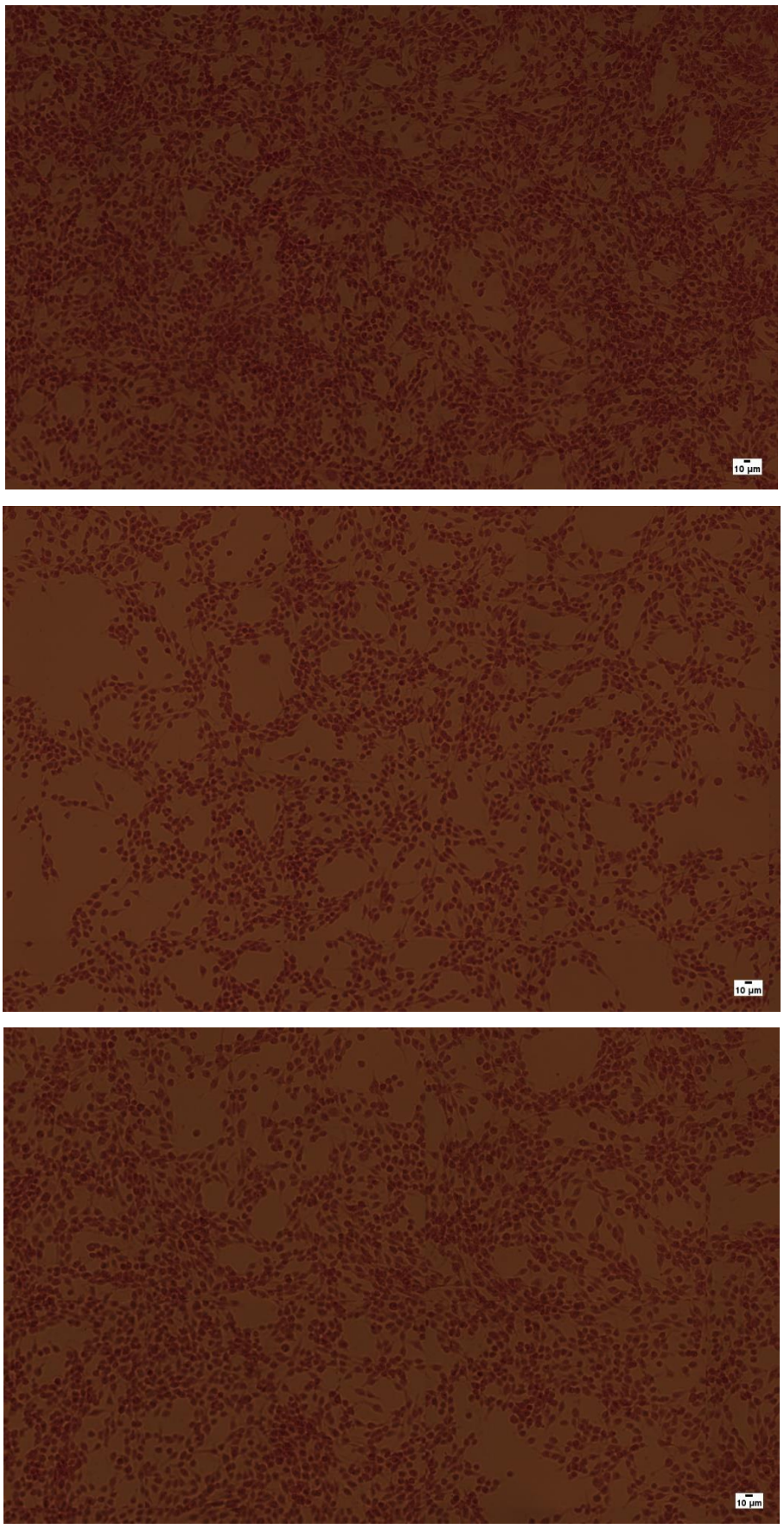

B.5. Microscope images of KPC cancer cells exposed to laser light for 0, 5 and 15 minutes (top to bottom). Microscope images captured by Dr. Marie Cutiongco 2 days after the experiment.

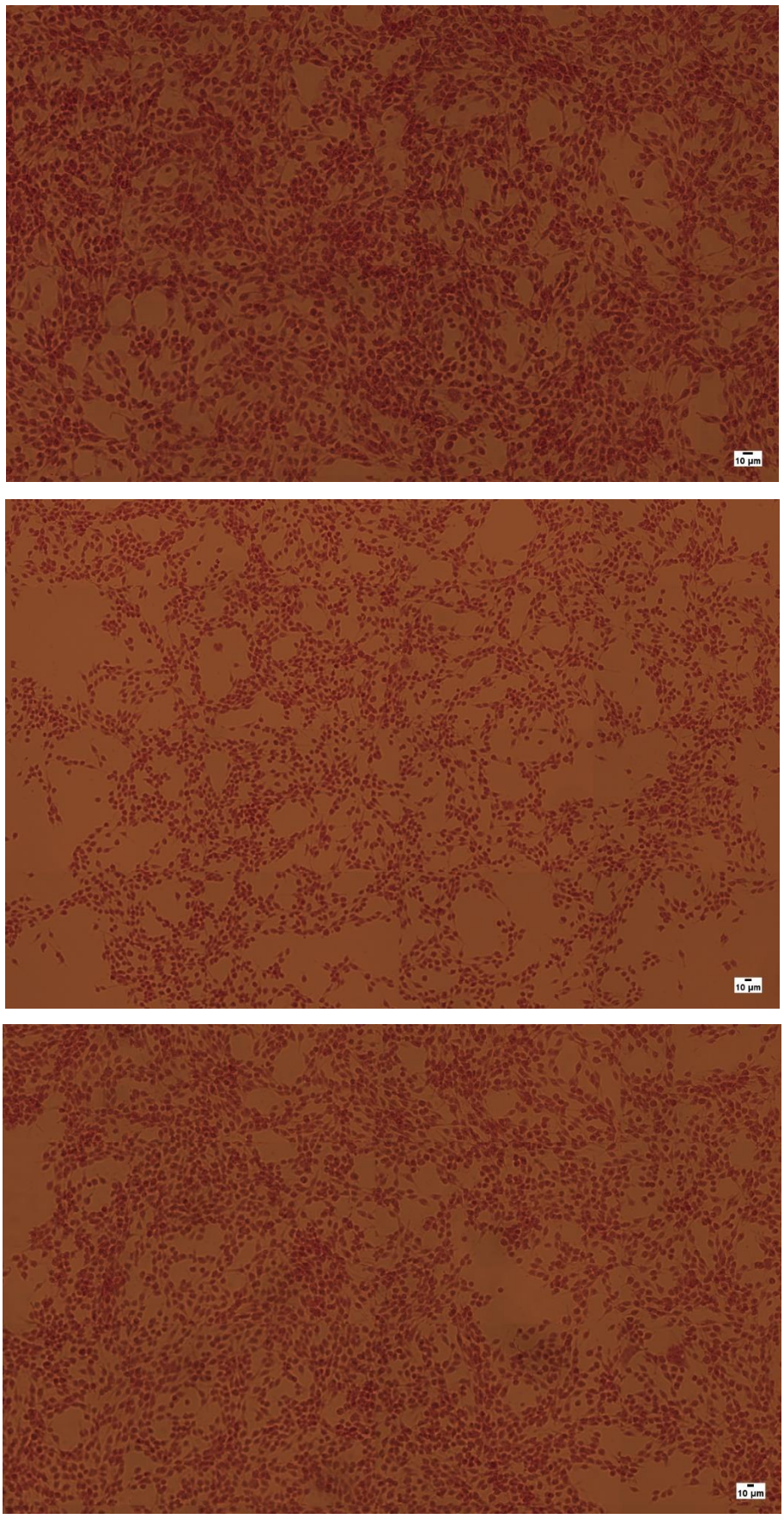

B.6. Microscope images of KPC cancer cells exposed to laser light for 0, 5 and 15 minutes (top to bottom). Microscope images captured by Dr. Marie Cutiongco 3 days after the experiment.

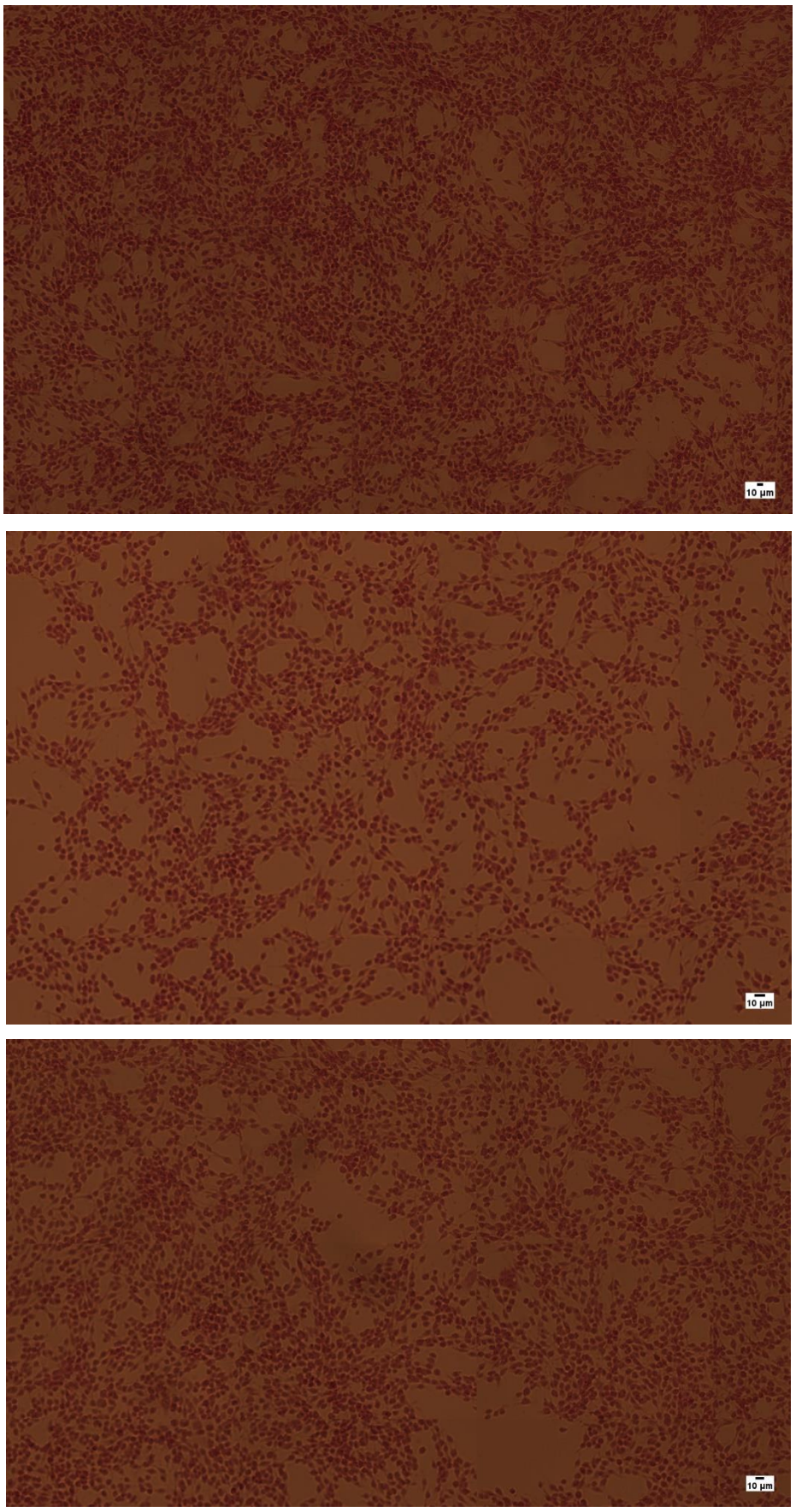

B.7. Microscope images of KPC cancer cells exposed to laser light for 0, 5 and 15 minutes (top to bottom). Microscope images captured by Dr. Marie Cutiongco 5 days after the experiment.

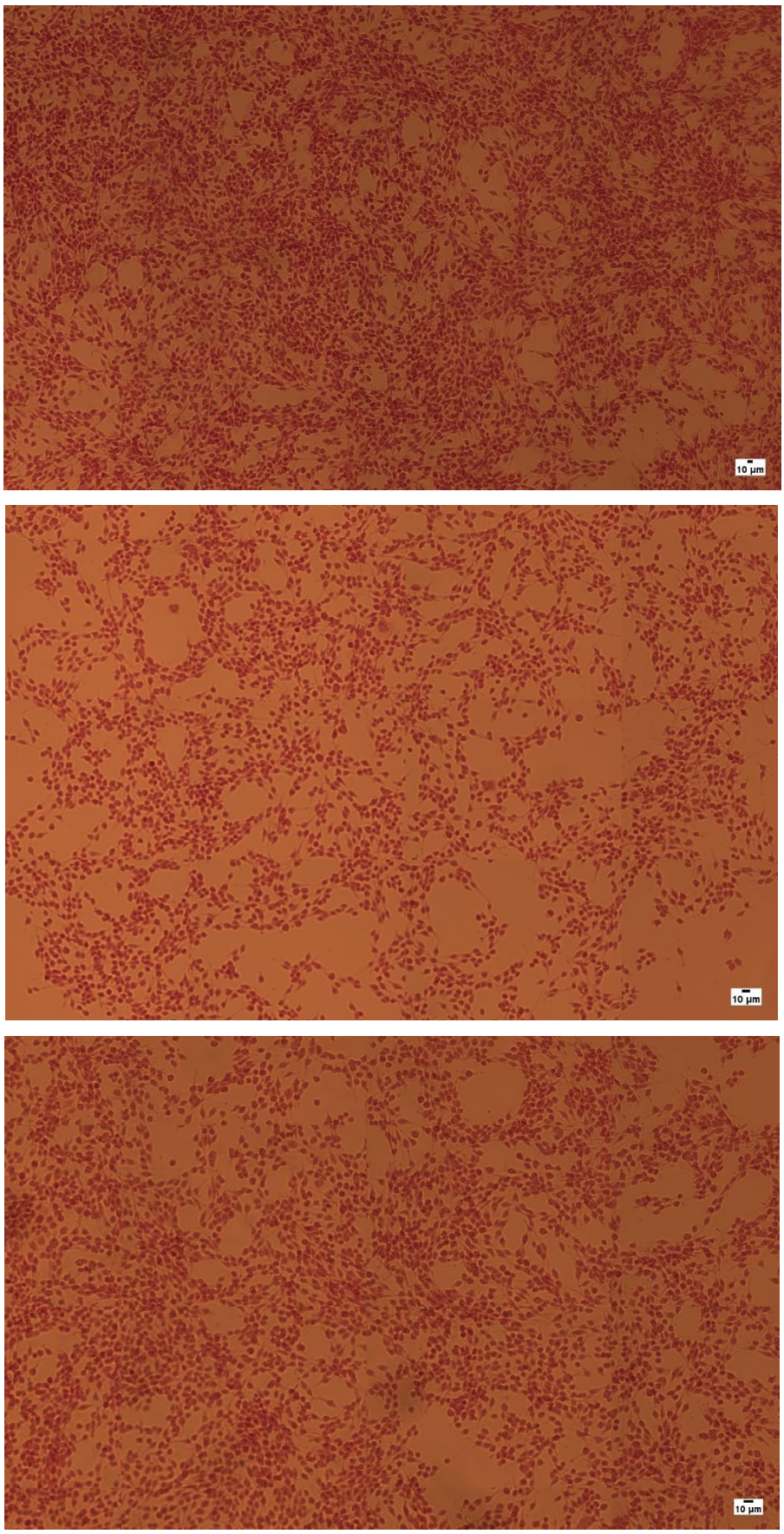

B.8. Microscope images of KPC cancer cells exposed to laser light for 0, 5 and 15 minutes (top to bottom). Microscope images captured by Dr. Marie Cutiongco 8 days after the experiment.